

Ministry of Education and Science of the Russian Federation
Saint Petersburg National Research University of Information
Technologies, Mechanics, and Optics

NANOSYSTEMS:
PHYSICS, CHEMISTRY, MATHEMATICS

2016, volume 7(3)

Наносистемы: физика, химия, математика

2016, том 7, № 3



NANOSYSTEMS:

PHYSICS, CHEMISTRY, MATHEMATICS

ADVISORY BOARD MEMBERS

Chairman: V.N. Vasiliev (*St. Petersburg, Russia*),
V.M. Buznik (*Moscow, Russia*); V.M. Ievlev (*Voronezh, Russia*), P.S. Kop'ev (*St. Petersburg, Russia*), N.F. Morozov (*St. Petersburg, Russia*), V.N. Parmon (*Novosibirsk, Russia*),
A.I. Rusanov (*St. Petersburg, Russia*),

EDITORIAL BOARD

Editor-in-Chief: I.Yu. Popov (*St. Petersburg, Russia*)

Section Co-Editors:

Physics – V.M. Uzdin (*St. Petersburg, Russia*),
Chemistry, material science – V.V. Gusarov (*St. Petersburg, Russia*),
Mathematics – I.Yu. Popov (*St. Petersburg, Russia*).

Editorial Board Members:

V.M. Adamyan (*Odessa, Ukraine*); O.V. Al'myasheva (*St. Petersburg, Russia*);
A.P. Alodjants (*Vladimir, Russia*); S. Bechta (*Stockholm, Sweden*); J. Behrndt (*Graz, Austria*);
M.B. Belonenko (*Volgograd, Russia*); V.G. Bepalov (*St. Petersburg, Russia*); J. Brasche (*Clausthal, Germany*);
A. Chatterjee (*Hyderabad, India*); S.A. Chivilikhin (*St. Petersburg, Russia*); A.V. Chizhov (*Dubna, Russia*);
A.N. Enyashin (*Ekaterinburg, Russia*), P.P. Fedorov (*Moscow, Russia*); E.A. Gudilin (*Moscow, Russia*);
V.K. Ivanov (*Moscow, Russia*), H. Jónsson (*Reykjavik, Iceland*); A.A. Kiselev (*Madison, USA*); Yu.S. Kivshar (*Canberra, Australia*);
S.A. Kozlov (*St. Petersburg, Russia*); P.A. Kurasov (*Stockholm, Sweden*); A.V. Lukashin (*Moscow, Russia*);
V.A. Margulis (*Saransk, Russia*); I.V. Melikhov (*Moscow, Russia*); G.P. Miroshnichenko (*St. Petersburg, Russia*);
I.Ya. Mittova (*Voronezh, Russia*); H. Neidhardt (*Berlin, Germany*); K. Pankrashkin (*Orsay, France*);
A.V. Ragulya (*Kiev, Ukraine*); V. Rajendran (*Tamil Nadu, India*); A.A. Rempel (*Ekaterinburg, Russia*);
V.Ya. Rudyak (*Novosibirsk, Russia*); D Shoikhet (*Karmiel, Israel*); P Stovicek (*Prague, Czech Republic*);
V.M. Talanov (*Novocherkassk, Russia*); A.Ya. Vul' (*St. Petersburg, Russia*); V.A. Zagrebnov (*Marseille, France*).

Editors:

I.V. Blinova; A.I. Popov; A.I. Trifanov; E.S. Trifanova (*St. Petersburg, Russia*),
R. Simoneaux (*Philadelphia, Pennsylvania, USA*).

Address: University ITMO, Kronverkskiy pr., 49, St. Petersburg 197101, Russia.

Phone: +7(812)232-67-65, **Journal site:** <http://nanojournal.ifmo.ru/>,

E-mail: popov1955@gmail.com

AIM AND SCOPE

The scope of the journal includes all areas of nano-sciences. Papers devoted to basic problems of physics, chemistry, material science and mathematics inspired by nanosystems investigations are welcomed. Both theoretical and experimental works concerning the properties and behavior of nanosystems, problems of its creation and application, mathematical methods of nanosystem studies are considered.

The journal publishes scientific reviews (up to 30 journal pages), research papers (up to 15 pages) and letters (up to 5 pages). All manuscripts are peer-reviewed. Authors are informed about the referee opinion and the Editorial decision.

Content

MATHEMATICS

G.I. Botirov

Functional equations for the Potts model with competing interactions on a Cayley tree 401

D.K. Durdiev, U.D. Durdiev

The problem of kernel determination from viscoelasticity system integro-differential equations for homogeneous anisotropic media 405

PHYSICS

M.B. Belonenko, N.N. Konobeeva, E.N. Galkina

Quick introduction into AdS/CFT correspondence in physics of strongly correlated systems 410

N.N. Konobeeva, M.B. Belonenko

Negative differential conductivity in Fermi liquid in the presence of magnetic field 422

V.G. Zavodinsky, O.A. Gorkusha

Development of an orbital-free approach for simulation of multi-atomic nanosystems with covalent bonds 427

CHEMISTRY AND MATERIAL SCIENCE

Zh.I. Bespalova, A.V. Khramenkova

The use of transient electrolysis in the technology of oxide composite nanostructured materials: review 433

K.I. Bryukhanova, G.E. Nikiforova, K.S. Gavrichev

Synthesis and study of anhydrous lanthanide orthophosphate (Ln=La, Pr, Nd, Sm) nanowhiskers 451

A.T. Nguyen, Ph.H.Nh. Phan, I.Ya. Mittova, M.V. Knurova, V.O. Mittova

The characterization of nanosized ZnFe₂O₄ material prepared by coprecipitation 459

D.V. Pikhurov, V.V. Zuev

Synthesis and mechanical characterization of nanoparticle-infused polyurethane foams. Statistical analysis of foam morphology 464

E.S. Shapoval, V.V. Zuev

Dielectric properties of polyamide 12- chromium(III) oxide nanocomposites 472

Papers, presented at NANO-2015

In this issue we start to publish works presented at International Conference on Nanomaterials and Nanotechnology (NANO 2015), 7-10 December 2015, Tamil Nadu, India.

Hem Bhatt

Magnetic field dependent resonant light scattering by magnetic spheres in a magnetizable medium 479

M. Balasubramaniam, S. Balakumar

Effect of precipitating agent NaOH on the preparation of copper oxide nanostructures for electrochemical applications 482

N. Shukla, A. Saxena, V. Gupta, A.S. Rawat, V. Kumar, S. Shrivastava, C. Rajagopal, P.K. Rai

Magnetic silica nanoparticles for the removal of Pb⁺² from water 488

Khurshed A. Shah

Chemically treated multi-walled carbon nanotubes for sensor applications 492

P. Venkateswara Reddy, S. Venkatramana Reddy, B. Sankara Reddy, R.P. Vijayalakshmi

Investigation on structural and photoluminescence properties of (Co, Al) co-doped SnO₂ nanoparticles 494

Kishorkumar V. Khot, Vishvanth B. Ghanwat, Pallavi B. Patil, Chaitali S. Bagade, Rahul M. Mane, Dadaso B. Shinde, Sandip K. Jagadale, Ji-hyung Jang, P.N. Bhosale	
Synthesis and characterization of highly ordered nanosized PbS thin films: modified silar	499
A. Deepak, P. Shankar	
Exploring the properties of lead oxide and tungsten oxide based graphene mixed nanocomposite films	502
A.K. Prasad, S. Dhara	
Effect of substrate temperature on microstructural, vibrational and electrical properties of ZnO nanostructured thin films	506
Chinnaiyah Sripan, Annamraju Kasi Viswanath, Ganesan. R	
Effect of excess selenium in the formation of $\text{Cu}_2\text{Zn}_{1.5}\text{Sn}_{1.2}(\text{S}_{0.9}+\text{Se}_{0.1})_4$ alloys for solar cell applications	509
Praveenkumar Ramprakash Upadhyay, Vivek Srivastava	
Titanium dioxide supported ruthenium nanoparticles for carbon sequestration reaction	513
R. Irene Hepzibah, G. Geethalakshmi, R.Ida Malarselvi	
Mathematical modeling for the evaluation of various parameters of 5-methyl salicylaldehyde aniline nano composite using fuzzy evidence theory	518
S.K. Jagadale, D.B. Shinde, R.M. Mane, K.V. Khot, V.B. Ghanwat, P.N. Bhosale, R.K. Mane	
Chemosynthesis, characterization and PEC performance of $\text{CdZn}(\text{SSe})_2$ thin films by arrested precipitation technique (APT)	523
A.S. Chinchole, P.P. Kulkarni, A.K. Nayak	
Experimental investigation of quenching behavior of heated zircaloy rod in accidental condition of nuclear reactor with water and water based nanofluids	528
Pratik Deshmukh, S. Satapathy, M.K. Singh, P.K. Gupta	
Effect of surfactant concentration and solvent used for washing in the preparation of $\text{Yb}:\text{Y}_2\text{O}_3$ transparent ceramics	534
P. Naveen., K. Gomathi., A. Senthilkumar, S. Thangavel	
Sitting posture health monitoring for scoliosis patients using capacitive micro accelerometer	538
N. Bhuvanesh, K.Velmurugan, S. Suresh, T. Sakthivel, R. Nandhakumar	
A graphene-organic composite as a fluorescent chemosensor for Ag^+	542
D. Rachel Malini, R. Sivakumar, C. Sanjeeviraja	
Annealing effects on V_2O_{5-x} thin films deposited by non reactive sputtering	547
Chaitali. S. Bagade, Vishvnath. B. Ghanwat, Kishorkumar. V. Khot, Pallavi. B. Patil, Rahul. M. Mane, P.N. Bhosale	
Facile synthesis of $(\text{CdZn})\text{Se}$ nanocrystalline thin films via arrested precipitation technique (APT) for photovoltaic application	553
P. Chithralekha, C. Murugeswari, K. Ramachandran, R. Srinivasan	
The study on ultrasonic velocities of $\text{Co}_x\text{Fe}_{3-x}\text{O}_4$ nanoferrofluid prepared by co-precipitation method	558
P. Rubalajyothi, L.C. Nehru	
Photoluminescence characteristics of nanocrystalline $\text{Ba}_{0.97}\text{Ca}_{0.03}\text{SO}_4$: EU by combustion method	561
V. Gunasekaran, G.H. Park, K.S. Kim, M. Suemitsu, H. Fukidome	
Observation of insulating and metallic-type behavior in Bi_2Se_3 transistor at room temperature	565
A. Mallaiiah, G.N. Swamy, K. Padmapriya	
Asymmetric molecular diode energy calculation using Extended Hückel and Parametric method	569

Functional equations for the Potts model with competing interactions on a Cayley tree

G. I. Botirov

Institute of Mathematics, National University of Uzbekistan

botirovg@yandex.ru

PACS 05.50.+q, 05.70.Fh, 02.30.-f, 02.50.Ga

DOI 10.17586/2220-8054-2016-7-3-401-404

In this paper, we consider an infinite system of functional equations for the Potts model with competing interactions of radius $r = 2$ and countable spin values $0, 1, \dots$, and non-zero-filled, on a Cayley tree of order two. We describe conditions on h_x guaranteeing compatibility of distributions $\mu^{(n)}(\sigma_n)$.

Keywords: Cayley tree, Potts model, Gibbs measures, functional equations.

Received: 23 March 2016

Revised: 13 April 2016

1. Introduction

The Potts model is related to and generalized by several other models, including the XY model, the Heisenberg model and the N -vector model. The infinite-range Potts model is known as the Kac model. When the spins are taken to interact in a non-Abelian manner, the model is related to the flux tube model, which is used to discuss confinement in quantum chromodynamics. Generalizations of the Potts model have also been used to model grain growth in metals and coarsening in foams. A further generalization of these methods by James Glazier and Francois Graner, known as the cellular Potts model, has been used to simulate static and kinetic phenomena in foam and biological morphogenesis. In this model, introduced by Askin and Teller (1943) and Potts (1952), the energy between two adjacent spins at vertices i and j is taken to be zero if the spins are the different and equal to a constant J_{ij} if they are same.

In [1], the Potts model with countable set Φ of spin values on Z^d was considered and it was proved that with respect to Poisson distribution on Φ , the set of limiting Gibbs measure is not empty. In [2], the Potts model with a *countable* set of spin values on a Cayley tree was considered and it was shown that the set of translation-invariant splitting Gibbs measures of the model contains at most one point, independent of parameters for the Potts model with countable set of spin values on the Cayley tree. This is a crucial difference from models with a finite set of spin values, since those may have more than one translation-invariant Gibbs measures.

The work initiated in [4] was continued in [3] and a model was considered with nearest-neighbor interactions and local state space given by the uncountable set $[0, 1]$ on a Cayley tree Γ^k of order $k \geq 2$. The translation-invariant Gibbs measures are studied via a non-linear functional equation and we prove the non-uniqueness of translation-invariant Gibbs measures in the right parameter regime for all $k \geq 2$ and not only for $k \in \{2, 3\}$ as in [3]. In [5], models (Hamiltonians) with-nearest-neighbor interactions and with the set $[0, 1]$ of spin values, on a Cayley tree Γ^k of order $k \geq 1$ were studied.

In this letter, we consider Potts model with competing interactions and countable spin values and we derive an infinite system of functional equations for the Potts model on a second order Cayley tree.

2. Preliminaries

The Cayley tree (Bethe lattice) Γ^k of order $k \geq 1$ is an infinite tree, i.e., a graph without cycles, such that exactly $k + 1$ edges originate from each vertex. Let $\Gamma^k = (V, L)$ where V is the set of vertices and L the set of edges. Two vertices x and y are called *nearest neighbors* if there exists an edge $l \in L$ connecting them and we denote $l = \langle x, y \rangle$. A collection of nearest neighbor pairs $\langle x, x_1 \rangle, \langle x_1, x_2 \rangle, \dots, \langle x_{d-1}, y \rangle$ is called a *path* from x to y . The distance $d(x, y)$ on the Cayley tree is the number of edges of the shortest path from x and y .

For a fixed $x^0 \in V$, called the root, we set:

$$W_n = \{x \in V | d(x, x^0) = n\}, \quad V_n = \bigcup_{m=1}^n W_m,$$

and denote:

$$S(x) = \{y \in W_{n+1} : d(x, y) = 1\}, \quad x \in W_n,$$

the set of direct successors of x .

The vertices x and y are called *next-nearest-neighbor* (NNN) which is denoted by $\langle x, y \rangle$, if there exists a vertex $z \in V$ such that x, z and y, z are nearest-neighbor. We consider NNN $\langle x, y \rangle$, for which there exists n such that $x \in W_n$ and $y \in W_{n+2}$, this kind of NNN is considered with the three states Potts model (see [6]).

We consider a Potts model with competing nearest-neighbor and prolonged next-nearest-neighbor interactions on a Cayley tree where the spin takes values in the set $\Phi := 0, 1, 2, \dots$. A configuration σ on V is then defined as a function $x \in V \mapsto \sigma(x) \in \Phi$; the set of all configurations is Φ^V .

The Hamiltonian for the Potts model with competing interactions has the form:

$$H(\sigma) = -J \sum_{\substack{\langle x, y \rangle \\ x, y \in V}} \delta_{\sigma(x)\sigma(y)} - J_1 \sum_{\substack{\langle x, y \rangle \\ x, y \in V}} \delta_{\sigma(x)\sigma(y)}, \tag{2.1}$$

where $J, J_1 \in \mathbb{R}$ are coupling constants and δ is the Kronecker's symbol.

Let λ be the Lebesgue measure on $[0, 1]$. For the set of all configurations on A , the a priori measure λ_A is introduced as the $|A|$ fold product of the measure λ . Here and subsequently, $|A|$ denotes the cardinality of A . We consider a standard sigma-algebra \mathbb{B} of subsets of $\Omega = [0, 1]^V$ generated by the measurable cylinder subsets. A probability measure μ on (Ω, \mathbb{B}) is called a Gibbs measure (with Hamiltonian H) if it satisfies the Dobrushin-Lanford-Ruelle (DLR) equation, namely for any $n = 1, 2, \dots$, and $\sigma_n \in \Omega_{V_n}$:

$$\mu(\{\sigma \in \Omega : \sigma|_{V_n} = \sigma_n\}) = \int_{\Omega} \mu(d\omega) \nu_{\omega|_{W_{n+1}}}^{V_n},$$

where $\nu_{\omega|_{W_{n+1}}}^{V_n}$ is the conditional Gibbs density:

$$\nu_{\omega|_{W_{n+1}}}^{V_n}(\sigma_n) = \frac{1}{Z_n(\omega|_{W_{n+1}})} \exp\left\{-\beta H(\sigma_n | \omega|_{W_{n+1}})\right\},$$

and $\beta = \frac{1}{T}$, $T > 0$ is the temperature.

Let $L_n = \{\langle x, y \rangle \in L : x, y \in V_n\}$ and Ω_{V_n} is the set of configurations in V_n (and Ω_{W_n} that in W_n). Furthermore, $\sigma|_{V_n}$ and $\omega|_{W_n}$ denote the restrictions of configurations $\sigma, \omega \in \Omega$ to V_n and W_{n+1} , respectively. Next, $\sigma_n : x \in V_n \mapsto \sigma_n(x)$ is a configuration in V_n and $H(\sigma_n | \omega|_{W_{n+1}})$ is defined as the sum $H(\sigma_n) + U(\sigma_n, \omega|_{W_{n+1}})$ where:

$$H(\sigma_n) = -J \sum_{\langle x, y \rangle \in L_n} \xi_{\sigma_n(x)\sigma_n(y)},$$

$$U(\sigma_n, \omega|_{W_{n+1}}) = -J \sum_{\substack{\langle x, y \rangle: \\ x \in V_n, y \in W_{n+1}}} \xi_{\sigma_n(x)\omega(y)}.$$

Finally, $Z_n(\omega|_{W_{n+1}})$ represents the partition function in V_n , with the boundary condition $\omega|_{W_{n+1}}$:

$$Z_n(\omega|_{W_{n+1}}) = \int_{\Omega_{V_n}} \exp\left\{-\beta H(\tilde{\sigma}_n | \omega|_{W_{n+1}})\right\} \lambda_{V_n}(d\tilde{\sigma}_n).$$

We write $x < y$ if the path from x^0 to y goes through x . We call vertex y a direct successor of x if $y > x$ and x, y are nearest neighbors. We denote by $S(x)$ the set of direct successors of x and observe that any vertex $x \neq x^0$ has k direct successors and x^0 has $k + 1$.

Let $h : x \in V \mapsto h_x = (h_{t,x}, t \in [0, 1]) \in \mathbb{R}^{[0,1]}$ be a mapping of $x \in V \setminus \{x^0\}$. Given $n = 1, 2, \dots$, consider the probability distribution $\mu^{(n)}$ on Ω_{V_n} defined by:

$$\mu^{(n)}(\sigma_n) = Z_n^{-1} \exp\left\{-\beta H(\sigma_n) + \sum_{x \in W_n} h_{\sigma(x), x}\right\}. \tag{2.2}$$

Here, as before, $\sigma_n : x \in V_n \mapsto \sigma(x)$ and Z_n is the corresponding partition function:

$$Z_n = \int_{\Omega_{V_n}} \exp\left\{-\beta H(\tilde{\sigma}_n) + \sum_{x \in W_n} h_{\tilde{\sigma}(x), x}\right\} \lambda_{V_n}(d\tilde{\sigma}_n). \tag{2.3}$$

The probability distributions $\mu^{(n)}$ are called compatible if for any $n \geq 1$ and $\sigma_{n-1} \in \Omega_{V_{n-1}}$:

$$\int_{\Omega_{W_n}} \mu^{(n)}(\sigma_{n-1} \vee \omega_n) \lambda_{W_n}(d(\omega_n)) = \mu^{(n-1)}(\sigma_{n-1}). \tag{2.4}$$

Here, $\sigma_{n-1} \vee \omega_n \in \Omega_{V_n}$ is the concatenation of σ_{n-1} and ω_n . In this case, because of the Kolmogorov extension theorem, there exists a unique measure μ on Ω_V such that, for any n and $\sigma_n \in \Omega_{V_n}$, $\mu\left(\left\{\sigma|_{V_n} = \sigma_n\right\}\right) = \mu^{(n)}(\sigma_n)$. Such a measure is called a splitting Gibbs measure corresponding to Hamiltonian (2.1) and function $x \mapsto h_x, x \neq x^0$.

The following theorem describes conditions on h_x guaranteeing compatibility of distributions $\mu^{(n)}(\sigma_n)$.

3. Functional Equations

Theorem 3.1 Probability distributions $\mu^{(n)}(\sigma_n), n = 1, 2, \dots$, in (2.2), for a Cayley tree of order two, are compatible iff for any $x \in V \setminus \{x^0\}$ the following equation holds:

$$h_{i,x}^* = F_i(h_y^*, h_z^*, \beta, J), \quad i = 1, 2, \dots, \tag{3.1}$$

where $S(x) = \{y, z\}, h_x^* = \left(h_{1,x} - h_{0,x} + \ln \frac{\nu(1)}{\nu(0)}, h_{2,x} - h_{0,x} + \ln \frac{\nu(2)}{\nu(0)}, \dots\right)$ and

$$F_i(h_y^*, h_z^*, \beta, J) = \ln \frac{1 + \sum_{\substack{p,q=0 \\ p+q \neq 0}}^{\infty} \exp\left\{\beta J(\delta_{ip} + \delta_{iq}) + J_1 \beta \delta_{pq} + h_{p,y}^* + h_{q,z}^*\right\}}{1 + \sum_{\substack{p,q=0 \\ p+q \neq 0}}^{\infty} \exp\left\{\beta J(\delta_{0p} + \delta_{0q}) + J_1 \beta \delta_{pq} + h_{p,y}^* + h_{q,z}^*\right\}}.$$

Proof. *Necessity* Assume that (2.4) holds; we will prove (3.1). Substituting (2.2) in (2.4), obtain that for any configurations $\sigma_{n-1} : x \in V_{n-1} \mapsto \sigma_{n-1}(x) \in \Phi$:

$$\begin{aligned} & \frac{1}{Z_n} \sum_{\sigma^{(n)} \in \Phi^{W_n}} \exp\left\{-\beta H_n(\sigma_n) + \sum_{x \in W_n} h_{\sigma(x),x}\right\} \times \prod_{y \in W_n} \nu(\sigma(y)) \\ &= \frac{1}{Z_{n-1}} \exp\left\{-\beta H_{n-1}(\sigma_{n-1}) + \sum_{x \in W_{n-1}} h_{\sigma_{n-1}(x),x}\right\}. \\ & \frac{Z_{n-1}}{Z_n} \sum_{\sigma^{(n)} \in \Phi^{W_n}} \exp\left\{-\beta H_{n-1}(\sigma_{n-1}) + J\beta \sum_{\substack{x \in W_{n-1} \\ y,z \in S(x)}} (\delta_{\sigma(x)\sigma(y)} + \delta_{\sigma(x)\sigma(z)}) + J_1 \beta \sum_{\substack{x \in W_{n-1} \\ y,z \in S(x)}} \delta_{\sigma(y)\sigma(z)} + \sum_{x \in W_n} h_{\sigma(x),x}\right\} \\ & \quad \times \prod_{y \in W_n} \nu(\sigma(y)) = \exp\left\{-\beta H_{n-1}(\sigma_{n-1}) + \sum_{x \in W_{n-1}} h_{\sigma_{n-1}(x),x}\right\}. \end{aligned}$$

After some abbreviations, we obtain:

$$\begin{aligned} & \frac{Z_{n-1}}{Z_n} \prod_{x \in W_{n-1}} \sum_{\sigma_x^{(n)} = \{\sigma(y), \sigma(z)\}} \exp\left\{J\beta (\delta_{\sigma(x)\sigma(y)} + \delta_{\sigma(x)\sigma(z)}) + J_1 \beta \delta_{\sigma(y)\sigma(z)} + h_{\sigma(y),y} + h_{\sigma(z),z} + \ln \nu(\sigma(y)) + \ln \nu(\sigma(z))\right\} \\ &= \prod_{x \in W_{n-1}} \exp\left\{h_{\sigma_{n-1}(x),x}\right\}. \end{aligned}$$

Consequently, for any $i \in \Phi$,

$$\begin{aligned} & \frac{\exp\left\{h_{0,y} + h_{0,z} + 2 \ln \nu(0)\right\} + \sum_{\substack{p,q=0 \\ p+q \neq 0}}^{\infty} \exp\left\{J\beta(\delta_{ip} + \delta_{iq}) + J_1 \beta \delta_{pq} + h_{p,y} + h_{q,z} + \ln \nu(p) + \ln \nu(q)\right\}}{\exp\left\{h_{0,y} + h_{0,z} + 2 \ln \nu(0)\right\} + \sum_{\substack{p,q=0 \\ p+q \neq 0}}^{\infty} \exp\left\{J\beta(\delta_{0p} + \delta_{0q}) + J_1 \beta \delta_{pq} + h_{p,y} + h_{q,z} + \ln \nu(p) + \ln \nu(q)\right\}} \\ &= \exp\left\{h_{i,x} - h_{0,x}\right\}, \end{aligned}$$

such that:

$$h_{i,x}^* = \ln \frac{1 + \sum_{\substack{p,q=0 \\ p+q \neq 0}}^{\infty} \exp \left\{ J\beta(\delta_{ip} + \delta_{iq}) + J_1\beta\delta_{pq} + h_{p,y}^* + h_{q,z}^* \right\}}{1 + \sum_{\substack{p,q=0 \\ p+q \neq 0}}^{\infty} \exp \left\{ J\beta(\delta_{0p} + \delta_{0q}) + J_1\beta\delta_{pq} + h_{p,y}^* + h_{q,z}^* \right\}},$$

where:

$$h_{i,x}^* = h_{i,x} - h_{0,x} + \ln \frac{\nu(i)}{\nu(0)}.$$

Sufficiency. Let (3.1) is satisfied we will prove (2.4).

$$\sum_{p,q=0}^{\infty} \exp \left\{ J\beta(\delta_{ip} + \delta_{iq}) + J_1\beta\delta_{pq} + h_{p,y} + h_{q,z} + \ln \nu(p) + \ln \nu(q) \right\} = a(x) \exp \left\{ h_{i,x} \right\}, \tag{3.2}$$

here $i = 0, 1, \dots$

We have:

$$\begin{aligned} \text{LHS of (2.4)} &= \frac{1}{Z_n} \exp \left\{ -\beta H_{n-1}(\sigma_{n-1}) \right\} \prod_{x \in W_{n-1}} \nu(\sigma(x)) \times \\ &\sum_{\substack{x \in W_{n-1} \\ y,z \in S(x)}} \exp \left\{ J\beta(\delta_{\sigma(x)\sigma(y)} + \delta_{\sigma(x)\sigma(z)}) + J_1\beta\delta_{\sigma(y)\sigma(z)} + h_{\sigma(y),y} + h_{\sigma(z),z} \right\}. \end{aligned} \tag{3.3}$$

Substituting (3.2) into (3.3) and denoting $A_n = \prod_{x \in W_{n-1}} a(x)$, we get:

$$\text{RHS of (3.3)} = \frac{A_{n-1}}{Z_n} \exp \left\{ -\beta H_{n-1}(\sigma_{n-1}) \right\} \prod_{x \in W_{n-1}} h_{\sigma_{n-1}(x),x}. \tag{3.4}$$

Since $\mu^{(n)}$, $n \geq 1$ is a probability, we should have:

$$\sum_{\sigma_{n-1}} \sum_{\sigma}^{(n)} \mu^{(n)}(\sigma_{n-1}, \sigma^{(n-1)}) = 1.$$

Hence, from (3.4) we obtain $Z_{n-1}A_{n-1} = Z_n$, and (2.4) holds.

References

[1] Ganikhodjaev N.N. The Potts model on Z^d eith countable set of spin values. *J. Math. Phys.*, 2004, **45**, P. 1121–1127.
 [2] Ganikhodjaev N.N., Rozikov U.A. The Potts model with countable set of spin values on a Cayley tree. *Letters in Math. Phys.*, 2006, **75**, P. 99–109.
 [3] Eshkabilov Yu.Kh., Rozikov U.A., Botirov G.I. Phase transition for a model with uncountable set of spin values on Cayley tree. *Lobachevskii Journal of Mathematics*, 2013, **V.34** (3), P. 256–263.
 [4] Eshkobilov Yu.Kh., Haydarov F.H., Rozikov U.A. Non-uniqueness of Gibbs Measure for Models with Uncountable Set of Spin Values on a Cayley Tree. *J. Stat. Phys.*, 2012, **147** (4), P. 779–794.
 [5] Rozikov U.A., Eshkabilov Yu.Kh. On models with uncountable set of spin values on a Cayley tree: Integral equations. *Math. Phys. Anal. Geom.*, 2010, **13**, P. 275–286.
 [6] Ganikhodjaev N.N., Mukhamedov F.M., Pah C.H. Phase diagram of the three states Potts model with next nearest neighbour interactions on the Bethe lattice. *Phys. Lett. A*, 2008, **373**, P. 33–38.

The problem of kernel determination from viscoelasticity system integro-differential equations for homogeneous anisotropic media

D. K. Durdiev¹, U. D. Durdiev²

¹Bukhara State University, Bukhara, Uzbekistan

²Kazan Federal University, Kazan, Russia

durdiev65@mail.ru, umidjan93@mail.ru

PACS 02.30.Zz

DOI 10.17586/2220-8054-2016-7-3-405-409

We consider the problem of reconstructing the time-dependent history of the viscoelasticity medium from the viscoelasticity system of equations for an homogeneous anisotropic medium. As additional information, the Fourier image of the displacement vector for values $\nu = \nu_0 \neq 0$ of transformation parameter is given. It is shown that if the given functions satisfy some conditions of agreement and smoothness, the solution for the posed problem is uniquely defined in the class of a continuous functions and it continuously depends on given functions.

Keywords: inverse problem, integro-differential equation, delta function, Fourier transformation, agreement condition.

Received: 8 March 2016

Revised: 20 April 2016

1. Setting up the problem and main result

We consider the integro-differential system for $x = (x_1, x_2, x_3) \in R^3$, $t \in R$:

$$\rho \frac{\partial^2 u_i}{\partial t^2} = \sum_{j=1}^3 \frac{\partial T_{ij}}{\partial x_j} + f(x, t), \quad i = 1, 2, 3, \quad (1)$$

at the initial conditions

$$u_i |_{t < 0} \equiv 0. \quad (2)$$

Here, $u(x, t) = (u_1(x, t), u_2(x, t), u_3(x, t))^*$ is the displacement vector function, $*$ is the sign of transposition, T_{ij} denotes the stress tensor related to the viscoelastic medium. More exactly, we have:

$$T_{ij}(x, t) = \sum_{k,l=1}^3 c_{ijkl} \left\{ \frac{\partial u_k}{\partial x_l}(x, t) + \int_0^t K_i(\tau) \frac{\partial u_k}{\partial x_l}(x, t - \tau) d\tau \right\}, \quad (3)$$

$f(x, t) = (f_1(x, t), f_2(x, t), f_3(x, t))^*$ is the external force; $\rho > 0$ is the density of the medium. In equality (3), coefficients c_{ijkl} are the elastic moduli of the medium. It is convenient and customary to describe the elastic moduli in the terms of a 6×6 matrix according to the following conventions relating a pair (i, j) of indices $i, j = 1, 2, 3$ to a single index $\alpha = 1, 2, \dots, 6$: $(11) \rightarrow 1$, $(22) \rightarrow 2$, $(33) \rightarrow 3$, $(23) = (32) \rightarrow 4$, $(13) = (31) \rightarrow 5$, $(12) = (21) \rightarrow 6$. This correspondence is possible due to the symmetry properties $c_{ijkl} = c_{jikl} = c_{ijlk}$. The additional symmetry property $c_{ijkl} = c_{klij}$ implies that the matrix $C = (c_{\alpha\beta})_{6 \times 6}$ of all moduli is symmetric, where $\alpha = (ij)$, $\beta = (kl)$. We will also assume that $\rho > 0$, c_{ijkl} are constants and the matrix $C = (c_{\alpha\beta})_{6 \times 6}$ is positive definite.

Many important materials used in modern technologies (such as nanotechnology) are viscoelastic and anisotropic. Viscoelastic materials have the properties of viscosity and elasticity upon deformation. Some mathematical models in the field of nanotechnology are contained, for example, in articles [1, 2] (see also references in them). In mathematical modeling of processes taking place in viscoelastic materials, there is a so-called system with memory, whose behavior is not completely determined by the state at the moment, but depends on the systems entire history, and therefore, describes an integro-differential equation that contains the corresponding integral with respect to the time variable. The system of equations (1), taking into account the integral term (3) is the basic in the linear theory of viscoelastic anisotropic media.

A study of inverse problems for hyperbolic integro-differential equations and systems is the subject of research by many authors. Among the problems that are closer to the present work can be identified [3–9]. In papers [3, 4], the unique solvability and stability of the solution for the inverse problem for the identification of a memory kernel from Maxwell's system integro-differential equations for a homogeneous anisotropic media are studied. In

work [5], the inverse problem for a second order hyperbolic equation with an integral member of convolution type with respect to one-dimensional time - dependent memory function of the medium and solution of the direct problem is investigated. By Fourier's method, this problem is reduced to solving the Volterra integral equations with respect to the unknown functions of the time-dependent variable. In papers [6, 7] (see also references therein) the problem of determining the multidimensional kernel in viscoelasticity equation for an inhomogeneous isotropic medium is investigated. In [8, 9], the problem of the one-dimensional kernel reconstruction from viscoelasticity equation in the bounded and unbounded domains has been studied. The theorems for the global unique solvability of these problems in the class of continuous functions with weighted norms were proved. The basic feature inherent in [3, 4, 6–9] and this paper is to use a boundary-localized and/or a fixed point of the spatial domain source, for the initiation of the physical process of wave propagation. Finally, we recall that the papers [10–13] are concerned with the problems of kernel determination from integro-differential equations with an integral of the convolution type. In the present paper, the approach of the works [3, 4] will be used.

We will consider the problem (1) – (2) for the case in which the function $f(x, t)$ has the form:

$$f(x, t) = \vec{e}\delta(x)\delta'(t), \tag{4}$$

where $\vec{e} = \left(\frac{1}{\sqrt{3}}, \frac{1}{\sqrt{3}}, \frac{1}{\sqrt{3}}\right)$ is unit vector; $\delta(x) = \delta(x_1)\delta(x_2)\delta(x_3)$ is the Dirac delta function of the space variable concentrated at $x_1 = 0, x_2 = 0, x_3 = 0$; $\delta'(t)$ is the derivative of Dirac delta function of the time variable concentrated at $t = 0$.

The problem in which the vector $u(x, t) = (u_1, u_2, u_3)(x, t)$ should be determined from (1) – (4) for given matrices $K(t) = \text{diag}(K_1, K_2, K_3)(t)$, $C = (c_{\alpha\beta})_{(6 \times 6)}$ and number $\rho > 0$ will be called the *direct problem*.

Let $U(\nu, t) = (U_1, U_2, U_3)(\nu, t)$ be the Fourier image of $u(x, t)$ with respect to $x = (x_1, x_2, x_3) \in R^3$, respectively, i.e.:

$$U_j(\nu, t) = \int_R u_j(x, t)e^{i(x, \nu)} dx, \quad \nu = (\nu_1, \nu_2, \nu_3) \in R^3, \quad (x, \nu) = \sum_{\lambda=1}^3 x_\lambda \nu_\lambda, \quad j = 1, 2, 3,$$

where ν is the parameter of transformation. We pose the following inverse problem: find the matrix function $K(t) = \text{diag}(K_1, K_2, K_3)(t)$, $t \geq 0$ occurring in the integral in equations (3) from the information on the Fourier image $U(\nu, t)$ at an arbitrary time $t \geq 0$ for the values $\nu = \nu_0$ of the Fourier transformation:

$$U(\nu_0, t) = g(t), \quad g(t) = (g_1, g_2, g_3). \tag{5}$$

Definition. A solution of the inverse problem is a matrix function $K(t) = \text{diag}(K_1, K_2, K_3)(t)$ such that the corresponding solution of problem (1) – (4) satisfies condition (5).

The main results of the present paper are the following theorems:

Theorem 1. Let us fix some arbitrary $T, T > 0$. Suppose that $g(t) \in C^3[0, T]$ and the agreement conditions:

$$g(0) = \frac{\vec{e}}{\rho}, \quad g'(0) = 0, \quad g''(0) = \frac{1}{\rho^2}Q(\nu_0)\vec{e},$$

holds. Besides, $\det Q(\nu_0) \neq 0, \nu_0 \neq 0$, where $Q(\nu)$ is matrix definite by formula (12). Then, the inverse problem (1) – (5) has a unique solution $K(t) = \text{diag}(K_1, K_2, K_3)(t) \in C[0, T]$.

Let $G(\gamma)$ be the set of functions $g(t)$, satisfying the conditions of theorem 1 and $\|g_i(t)\|_{C^3[0, T]} \leq \gamma < \infty, t \in [0, T], i = 1, 2, 3, \gamma$ – the given number.

Theorem 2. Let $K^m(t) = \text{diag}(K_1^m(t), K_2^m(t), K_3^m(t))$ be solution to the inverse problem (1) – (5) with $g^m(t) \in G(\gamma), m = 1, 2$, respectively. Then, there exists positive constant C , depending on numbers T, ρ, γ and elements of matrix $Q(\nu_0)$ so that the following estimate of stability is valid:

$$\sum_{i=1}^3 \|K_i^1 - K_i^2\|_{C[0, T]} \leq C \sum_{i=1}^3 \|g_i^1 - g_i^2\|_{C^3[0, T]}. \tag{6}$$

2. The main equations with respect to Fourier's image

Denote

$$\bar{T}_{ij} := \sum_{k,l=1}^3 c_{ijkl} \frac{\partial v_k}{\partial x_l}(x, t). \quad (7)$$

Then, (3) can be written as the following:

$$T_{ij}(x, t) = \bar{T}_{ij}(x, t) + \int_0^t K_i(\tau) \bar{T}_{ij}(x, t - \tau) d\tau, \quad i = 1, 2, 3; j = 1, 2, 3.$$

Using the symmetry properties of the elastic moduli and the rule of the renumbering of indices, accepted above, relation (7) obtains the form:

$$\bar{T}_\alpha = c_{\alpha 1} \frac{\partial v_1}{\partial x_1} + c_{\alpha 6} \frac{\partial v_1}{\partial x_2} + c_{\alpha 5} \frac{\partial v_1}{\partial x_3} + c_{\alpha 6} \frac{\partial v_2}{\partial x_1} + c_{\alpha 2} \frac{\partial v_2}{\partial x_2} + c_{\alpha 4} \frac{\partial v_2}{\partial x_3} + c_{\alpha 5} \frac{\partial v_3}{\partial x_1} + c_{\alpha 4} \frac{\partial v_3}{\partial x_2} + c_{\alpha 3} \frac{\partial v_3}{\partial x_3}, \quad \alpha = 1, 2, \dots, 6. \quad (8)$$

Therefore, for each $i = 1, 2, 3$, the first terms on the right side of (1) can be written as:

$$\begin{aligned} \sum_{j=1}^3 \frac{\partial \bar{T}_{1j}}{\partial x_j} &= \frac{\partial \bar{T}_1}{\partial x_1} + \frac{\partial \bar{T}_6}{\partial x_2} + \frac{\partial \bar{T}_5}{\partial x_3}, \\ \sum_{j=1}^3 \frac{\partial \bar{T}_{2j}}{\partial x_j} &= \frac{\partial \bar{T}_6}{\partial x_1} + \frac{\partial \bar{T}_2}{\partial x_2} + \frac{\partial \bar{T}_4}{\partial x_3}, \\ \sum_{j=1}^3 \frac{\partial \bar{T}_{3j}}{\partial x_j} &= \frac{\partial \bar{T}_5}{\partial x_1} + \frac{\partial \bar{T}_4}{\partial x_2} + \frac{\partial \bar{T}_3}{\partial x_3}. \end{aligned} \quad (9)$$

Formulae (8) and (9) will be used for computing the Fourier's transformation with respect to the variable x of the right sides in (1).

We apply the Fourier transformation to both parts of (1) – (4). The Fourier transform of the vector function $u(x, t)$ exists at any finite t , since the vector function $u(x, t)$, as the solution of the direct problem (1) – (4), is the sum of a certain singular generalized vector function and a regular vector function, the support of the vector function $u(x, t)$ being finite [14, chapter 4]. At any fixed ν , the vector function $U(\nu, t)$, $U(\nu, t)$ – the Fourier transformation of $u(x, t)$ with respect to x satisfies differential equation:

$$\rho I \frac{\partial^2 U}{\partial t^2} = Q(\nu) U(\nu, t) + \int_0^t K(t - \tau) Q(\nu) U(\nu, \tau) d\tau + \vec{e} \delta'(t), \quad \nu \in R^3, t \in R, \quad (10)$$

for the initial conditions:

$$\tilde{V}|_{t \leq 0} = 0. \quad (11)$$

In equation (10), we denoted I – the unit matrix of third order, $U(\nu, t) = (U_1, U_2, U_3)^*(\nu, t)$, $\vec{e} = (e_1, e_2, e_3) = \left(\frac{1}{\sqrt{3}}, \frac{1}{\sqrt{3}}, \frac{1}{\sqrt{3}} \right)$,

$$Q(\nu) = \begin{pmatrix} Q_{11} & Q_{12} & Q_{13} \\ Q_{21} & Q_{22} & Q_{23} \\ Q_{31} & Q_{32} & Q_{33} \end{pmatrix}, \quad (12)$$

$Q_{ij}(\nu)$, $1 \leq i \leq 3, 1 \leq j \leq 3$ – uniform polynomials of second order with respect to ν :

$$\begin{aligned}
 Q_{11}(\nu) &= c_{11}\nu^2 + 2c_{16}\nu_1\nu_2 + c_{66}\nu_2^2 + 2c_{15}\nu_1\nu_3 + 2c_{56}\nu_2\nu_3 + c_{55}\nu_3^2; \\
 Q_{12}(\nu) &= c_{16}\nu_1^2 + (c_{12} + c_{66})\nu_1\nu_2 + c_{62}\nu_2^2 + (c_{14} + c_{56})\nu_1\nu_3 + (c_{52} + c_{64})\nu_2\nu_3 + c_{54}\nu_3^2; \\
 Q_{13}(\nu) &= c_{15}\nu_1^2 + (c_{14} + c_{65})\nu_1\nu_2 + c_{64}\nu_2^2 + (c_{13} + c_{55})\nu_1\nu_3 + (c_{63} + c_{54})\nu_2\nu_3 + c_{53}\nu_3^2; \\
 Q_{21}(\nu) &= c_{61}\nu_1^2 + (c_{21} + c_{66})\nu_1\nu_2 + c_{26}\nu_2^2 + (c_{41} + c_{65})\nu_1\nu_3 + (c_{25} + c_{46})\nu_2\nu_3 + c_{45}\nu_3^2; \\
 Q_{22}(\nu) &= c_{66}\nu_1^2 + 2c_{26}\nu_1\nu_2 + c_{22}\nu_2^2 + 2c_{64}\nu_1\nu_3 + 2c_{24}\nu_2\nu_3 + c_{44}\nu_3^2; \\
 Q_{23}(\nu) &= c_{65}\nu_1^2 + (c_{64} + c_{25})\nu_1\nu_2 + c_{24}\nu_2^2 + (c_{45} + c_{63})\nu_1\nu_3 + (c_{23} + c_{44})\nu_2\nu_3 + c_{43}\nu_3^2; \\
 Q_{31}(\nu) &= c_{51}\nu_1^2 + (c_{41} + c_{56})\nu_1\nu_2 + c_{46}\nu_2^2 + (c_{31} + c_{55})\nu_1\nu_3 + (c_{36} + c_{45})\nu_2\nu_3 + c_{35}\nu_3^2; \\
 Q_{32}(\nu) &= c_{56}\nu_1^2 + (c_{46} + c_{52})\nu_1\nu_2 + c_{42}\nu_2^2 + (c_{54} + c_{36})\nu_1\nu_3 + (c_{32} + c_{44})\nu_2\nu_3 + c_{34}\nu_3^2; \\
 Q_{33}(\nu) &= c_{55}\nu_1^2 + 2c_{45}\nu_1\nu_2 + c_{44}\nu_2^2 + 2c_{35}\nu_1\nu_3 + 2c_{34}\nu_2\nu_3 + c_{33}\nu_3^2,
 \end{aligned}$$

Thus, the inverse problem (1) – (4) is reduced to the problem of determining the kernel $K(t)$, $t > 0$ of the integral part in the equation (10) on the bases of equalities (10), (11) and (5).

3. Proof of the main results

Taking into consideration the fact that $t\theta(t)$, where $\theta(t)$ – the Heavyside step function, is the fundamental solution of differential operator $\partial^2/\partial t^2$, the solution to the direct problem (10), (11) can be represented in the form:

$$\begin{aligned}
 U(\nu, t) &= \int_R (t - \tau)\theta(t - \tau) \left[\frac{1}{\rho} Q(\nu) \left(U(\nu, t) + \int_0^\tau K(\alpha)U(\nu, \tau - \alpha)d\alpha \right) + \frac{\vec{e}}{\rho} \delta'(\tau) \right] d\tau \\
 &= \theta(t) \left[\frac{\vec{e}}{\rho} + \frac{1}{\rho} \int_0^t (t - \tau)Q(\nu) \left(U(\nu, t) + \int_0^\tau K(\alpha)U(\nu, \tau - \alpha)d\alpha \right) d\tau \right].
 \end{aligned}$$

To prove Theorem 1, we begin by setting $\nu = \nu_0$ in this equation and using supplementary condition (5). This results in the following equality:

$$g(t) = \frac{\vec{e}}{\rho} + \frac{1}{\rho} \int_0^t (t - \tau)Q(\nu_0) \left(g(t) + \int_0^\tau K(\alpha)g(\tau - \alpha)d\alpha \right) d\tau. \tag{13}$$

Differentiating equation (13) twice with respect to the variable t , we have the following equalities:

$$\begin{aligned}
 g'(t) &= \frac{Q(\nu_0)}{\rho} \left[\int_0^t g(\tau)d\tau + \int_0^t \int_0^\tau K(\alpha)g(\tau - \alpha)d\alpha d\tau \right], \\
 g''(t) &= \frac{Q(\nu_0)}{\rho} g(t) + \frac{Q(\nu_0)}{\rho} \int_0^t K(\alpha)g(t - \alpha)d\alpha.
 \end{aligned}$$

To obtain an integral equation for $K(t)$, we differentiate the last relation again with respect to t . Multiplying the left-hand side of result equality by $Q^{-1}(\nu_0)$, after easily transforming, one gets:

$$K(t) = \sqrt{3}\rho^2 Q^{-1}(\nu_0)g'''(t) - \sqrt{3}\rho g'(t) - \sqrt{3}\rho \int_0^t K(\alpha)g'(t - \alpha)d\alpha. \tag{14}$$

For each fixed i (14), is a linear integral second-order equation with respect to the unknown vector function $K(t)$. As is known, these equations have unique solutions.

We now prove Theorem 2. Consider the integral equation (14) for each i for $g^m(t)$, $m = 1, 2$. Corresponding to these functions, the solutions of the integral equation (14) are denoted by $K_i^m(t)$, $m = 1, 2$, making the difference $K_i^1(t) - K_i^2(t)$, from which we estimate it. From (14), one gets:

$$|K_i^1(t) - K_i^2(t)| \leq C_1 \|g_i^1 - g_i^2\|_{C^3[0,T]} + C_2 \int_0^t |K_i^1(\tau) - K_i^2(\tau)| d\tau, \quad i = 1, 2, 3.$$

Therefore, taking into account Gronwall's inequality, we have:

$$|K_i^1(t) - K_i^2(t)| \leq C_3 \|g_i^1 - g_i^2\|_{C^3[0,T]}, \quad i = 1, 2, 3.$$

Constants C_j , $j = 1, 2, 3$ depend on the numbers T , ρ , γ and elements of matrix $Q(\nu_0)$. The last equalities yield estimate (6).

References

- [1] Dvurechenskii A., Alfimov M., et al. IV Nanotechnology International Forum (RUSNANOTECH 2011). *J. Phys.: Conf. Series*, 2012, **345** (1), 011001.
- [2] Chivilikhin S.A., Gusarov V.V., Popov I.Yu. Flows in nanostructures: hybrid classical-quantum models. *Nanosystems: Physics, Chemistry, Mathematics*, 2012, **3** (1), P. 7–26.
- [3] Durdiev D.K. Inverse problem for the identification of a memory kernel from Maxwell's system integro-differential equations for a homogeneous anisotropic media. *Nanosystems: Physics, Chemistry, Mathematics*, 2015, **6** (2), P. 268–273.
- [4] Durdiev D.K., Durdiev U.D. Stability of the inverse problem solution for Maxwell's system integro-differential equations in a homogeneous anisotropic media. *Uzbek Mathematical Journal*, 2014, **2**, P. 25–34. (in Russian)
- [5] Janno J., Von Welfersdorf L. Inverse problems for identification of memory kernels in viscoelasticity. *Math. Methods in Appl. Sciences*, 1997, **20** (4), P. 291–314.
- [6] Romanov V.G. Stability estimates for the solution in the problem of determining the kernel of the viscoelasticity equation. *Sib. Zh. Ind. Mat.*, 2012, **15** (1), P. 86–98. (in Russian)
- [7] Durdiev D.K., Totieva Zh.D. The problem of determining the multidimensional kernel of viscoelasticity equation. *Vladikavkaz. Mat. Zh.*, 2015, **17** (4), P. 18–43. (in Russian)
- [8] Durdiev D.K., Safarov Zh.Sh. Inverse problem of determining the one-dimensional kernel of the viscoelasticity equation in a bounded domain. *Mat. Zametki*, 2015, **97** (6), P. 855–867. (in Russian)
- [9] Durdiev D.K., Totieva Zh.D. The problem of determining the one-dimensional kernel of the viscoelasticity equation. *Sib. Zh. Ind. Mat.*, 2013, **16** (2), P. 72–82. (in Russian)
- [10] Jaan J., Von Welfersdorf L. An inverse problem for identification of a time- and space-dependent memory kernel in viscoelasticity. *Inverse Problems*, 2001, **17**, P. 13–24.
- [11] Colombo F., Guidetti D. A global in time existence and uniqueness result for a semilinear integrodifferential parabolic inverse problem in Sobolev spaces. *Math. Methods Appl. Sciences*, 2007, **17**, P. 1–29.
- [12] Colombo F., Guidetti D. Some results on the Identification of memory kernels. *Oper. Theory: Adv. Appl.*, 2011, **216**, P. 121–138.
- [13] Favaron A. Identification of Memory Kernels Depending on Time and on an Angular Variable. *Zeitschrift für Analysis und ihre Anwendungen*, 2005, **24** (4), P. 735–762.
- [14] Romanov V.G. *Inverse problems of mathematical physics*. Nauka, Moscow, 1984. (in Russian)

Quick introduction into AdS/CFT correspondence in physics of strongly correlated systems

M. B. Belonenko^{1,2}, N. N. Konobeeva², E. N. Galkina^{1,3}

¹Laboratory of Nanotechnology, Volgograd Institute of Business, 400048, Volgograd, Russia

²Volgograd State University, 400062, Volgograd, Russia

³Volgograd State Medical University, 400131, Volgograd, Russia

mbelonenko@yandex.ru, yana.nn@inbox.ru, galkina@mail.com

PACS 71.10-Ay, 71.27.+a

DOI 10.17586/2220-8054-2016-7-3-410-421

The basic ideas of the AdS/CFT correspondence in physics of strongly correlated systems are briefly discussed. The application of the AdS/CFT correspondence for the Green's functions derivation are shown.

Keywords: AdS/CFT correspondence, Green's function.

Received: 22 January 2016

1. Introduction

The AdS/CFT correspondence appeared at the end of the 1990s as an approach established a connection between the string theory and conformal field theory models. In general, the existence of such relation could be expected if both model types have the same origin [1–8]. The evolution of hadron physics models has evolved in different ways over time. It was mandated by the fact that hadrons interact strongly, and in theory, there is no a small parameter on which it would be possible to make an expansion similar to the well-known quantum electrodynamics diagram approach. Initially, string theory was provided with phenomenological foundations in the form of Regge trajectories and conformal field theory got its essential evolution as a consequence of the phase transitions theory development [9]. When coming close to the phase-transition point, the physical value fluctuations have an increasing characteristic length. This fact requires scale invariance, and thus, conformal transformations and conformal theories immediately appear. From this, further development of such an approach has allowed the establishment experimentally testable theory corollaries as well. Note that these theories were divergent from one another increasingly not only in corollaries, but also in mathematical techniques, until a certain consistency between their parameters were established.

The basic concept of the AdS/CFT correspondence is in the formulae establishing a correspondence for average values [2, 6, 8, 10–14]:

$$\left\langle \exp \left\{ i \int_{\partial M} \phi_0 \widehat{O} \right\} \right\rangle = \exp \{ i S_{cl}(\phi) \}. \quad (1)$$

Indeed, formula (1) consists of a variety of conceptions which must be deciphered. Thus:

1. Formula (1) maintains that the average values of operators \widehat{O} on the boundary of some manifold ∂M , which are taken with classic field values ϕ on the boundary of a manifold ϕ_0 , will be coincident with the imaginary exponential of classic field action ϕ in a volume of manifold .
2. Operators \widehat{O} cannot be chosen randomly and must be dual with field values ϕ (this choice will be shown in the part 2).
3. Manifold in a certain sense must be “good”, have a boundary (or boundaries) and have a dimensionality one greater than the space for which we are going to construct the Green's function.
4. The formula (1) was given for Minkowsky space. It is necessary to make the Wick rotation of time axis for Euclidean space often used in Green's temperature functions calculation.

Note that after the average values are estimated, the problem for the Green's functions calculation becomes amply obvious. For example, the following expression can be used for the retarded Green's function [15]:

$$G^R(\vec{k}) = -i \int d^4 \bar{x} \theta(t) \left\langle \left[\widehat{O}(\vec{x}), \widehat{O}(0) \right] \right\rangle, \quad (2)$$

where $\theta(t)$ is Heaviside function as usual.

Summarizing what was stated above, we can say that the AdS/CFT correspondence is a method for Green’s function calculation apart from formulae (1,2) for further use of these functions in applications. It is important to emphasize that concepts of AdS/CFT correspondence are not only limited to Green’s function construction, but can also be applied for direct calculation of kinetic coefficient relations (for example, the well-known relation between viscosity and entropy density $\eta/s = 1/4\pi$) [3,4,16–25].

In accordance with the above-stated, we build a plan of the present mini review. In the second chapter it will be briefly specified what kind of operators \hat{O} are dual with fields ϕ and how to choose a manifold . In the third part of this paper, a detailed case study for the scalar field will be analyzed. The basic formulae for Green’s function calculation for fermions will be given in the fourth chapter and examples of the main Green’s functions will be given. In the fifth chapter, a summary of the major scientific works expanding the primary models will be presented.

2. Choice of operators and space

Here and subsequently, a convention will be applied in which Greek indices correspond to the conformal field theory space on the boundary and Latin indices accord with field theory space of dimension one unit greater.

The choice of operators, \hat{O} , as noted above, is not spontaneous and determined by the fact that operators must be dual. Since the primary role in this theory is played by fields ϕ , which are defined by their transformation property under coordinate transformations; it is easier to bring the correspondence in a tabular form (Table 1).

TABLE 1. Correspondence of the classic field theory operators to the boundary operators

Field properties under transformations of coordinates	Classic field theory in a bulk	Operator on the boundary
scalar	ϕ	boson operator \hat{O}_B
vector	A_a	current operator \hat{J}^μ
second-rank tensor	g_{ab}	energy operator $\hat{T}^{\mu\nu}$
spinor	ψ	fermion operator \hat{O}_F

Note that well-known Green’s fermion and boson functions can be constructed directly for fermion and boson operators, but for applications, there are important relations which result from Kubo formulae.

Thus, under calculation of shear viscosity (η), it is easier to use expressions which follow from Kubo theory:

$$\eta = - \lim_{\varpi \rightarrow 0} \frac{\text{Im} \Xi(\varpi)}{\varpi},$$

$$\Xi(\varpi) = -i \frac{\hbar}{v} \int d^4 \bar{r} e^{i\varpi t} \theta(t) \langle [\Pi_{xy}(\bar{r}, t), \Pi_{xy}(0, 0)] \rangle, \tag{3}$$

where v is a normalization volume, and $\Pi_{xy}(\bar{r}, t)$ is a momentum flow density. It is convenient to carry out an analysis by reference to the second-rank tensor and general energy operator $\hat{T}^{\mu\nu}$ in this case. Similarly, we can use vector A_a and current operator \hat{J}^μ for Hall conductivity calculation.

The choice of a space plays no less important role than the operator choice. A fundamental point lies with the fact that at absolute zero, theories will be correspond to the classic De Sitter space.

$$s^2 = \frac{L^2}{z^2} (dt^2 + d\bar{x}^2 + dz^2), \tag{4}$$

where z is an additional coordinate (which will be used for corresponding boundary conditions), t is a time coordinate, \bar{x} are space coordinates, L is a parameter. Here the euclidian case is written down but proceeding to Minkowsky space can be performed by Wick rotation. In the case of theories with non-zero temperature it is necessary to consider more complicated metrics, for instance, of the following form which corresponds to a black hole type solution:

$$ds^2 = \frac{R^2}{z^2} (f(z)dt^2 + d\bar{x}^2 + dz^2/f(z)),$$

$$f(z) = 1 - \frac{z^4}{z_h^4}, \tag{5}$$

where z_h is a parameter which is directly associated with Hawking's temperature T :

$$z_h = 1/(\pi T).$$

Note that the metric (5) is applicable for models with a scalar field. For models with fermions, vector fields and others, it is essential to use relevant solutions of the Einstein's equations generalized to additional spatial dimension with energy-momentum tensor introduced in field models [26–39].

As an example, we provide a solution corresponding to a model with fermions which will be used in the chapter 4:

$$\begin{aligned} ds^2 &= \frac{z^2}{R^2} (-f(z) dt^2 + d\bar{x}^2) + \frac{R^2}{z^2 f(z)} dz^2, \\ f(z) &= 1 + \frac{Q^2}{z^4} - \frac{1 + Q^2}{z^3}, \\ T &= \frac{3 - Q^2}{4\pi}. \end{aligned} \quad (6)$$

3. Generation of the Green's functions for scalar field

Let us consider in more detail the generation of the Green's functions for scalar field in pursuance of the paper [40]. We start with the case of absolute zero and De Sitter space metric defined by (4). As is well-known, the action for scalar field can be given by the following expression:

$$S = -\frac{1}{2} \int d^{d+1}x \sqrt{g} [g^{MN} \partial_M \varphi \partial_N \varphi + m^2 \phi^2].$$

Now, the corresponding motion equation will take the form:

$$\frac{1}{\sqrt{g}} \partial_M (\sqrt{g} g^{MN} \partial_N \phi) - m^2 \phi = 0.$$

It is convenient to detach instantly the dependence on additional coordinate z :

$$z^{d+1} \partial_z (z^{1-d} \partial_z \phi) + z^2 \delta^{\mu\nu} \partial_\mu \partial_\nu \phi - m^2 L^2 \phi = 0.$$

Since the coefficients of equation do not explicitly depend on other coordinates, it is naturally to produce Fourier transform:

$$\phi(z, x^\mu) = \int \frac{d^d k}{(2\pi)^d} e^{ikx} f_k(z).$$

Next, we obtain the following expression for the Fourier coefficients:

$$z^{d+1} \partial_z (z^{1-d} \partial_z f_k) - k^2 z^2 f_k - m^2 L^2 f_k = 0.$$

Let us consider the given equation at a point $z = 0$. Let us assume that $f_k \sim z^\beta$. Then, β satisfies the following expression:

$$\beta(\beta - d) - m^2 L^2 = 0,$$

where d is the conformal theory space dimension. Solution of this equation is as follows:

$$\beta = \frac{d}{2} \pm \sqrt{\frac{d^2}{4} + m^2 L^2}.$$

Thus, the solution near the border (it should be recalled that we construct the effective theory namely on the border) will be in the next form:

$$\begin{aligned} f_k(z) &\approx A(k) z^{d-\Delta} + B(k) z^\Delta, \\ \Delta &= \frac{d}{2} + \nu, \quad \nu = \sqrt{\frac{d^2}{4} + m^2 L^2}. \end{aligned} \quad (7)$$

The relation (7) gives an opportunity to correlate the irregular on the border function ϕ with regular function φ through the agency of the expression:

$$\varphi(x) = \lim_{z \rightarrow 0} z^{\Delta-d} \phi(z, x).$$

After the brief introduction that gives an insight into both field behavior on the boundary and the prominent role of the parameter β we can pass on to average calculation and the Green's function development. An average,

as in any quantum theory, can be evaluated out from the following relation (it is important that we have to apply the fields ϕ which are defined on the boundary):

$$\langle O(x) \rangle_c = \frac{\delta S_{grav}^{ren}[\phi]}{\delta \varphi(x)},$$

or to pass on to variation derivative in a bulk:

$$\langle O(x) \rangle_\varphi = \lim_{z \rightarrow 0} z^{d-\Delta} \frac{\delta S_{grav}^{ren}[\phi]}{\delta \phi(z, x)}. \quad (8)$$

Hereafter, let us recall how to perform calculations with action in a bulk (index M) and on the boundary (∂):

$$\begin{aligned} S_{grav} &= \int_{\mathcal{M}} \int dz d^d x \mathcal{L}[\phi, \partial\phi], \\ \delta S_{grav} &= \int_{\mathcal{M}} \int dz d^d x \left[\frac{\partial \mathcal{L}}{\partial \phi} \delta\phi + \frac{\partial \mathcal{L}}{\partial (\partial_\mu \phi)} \delta(\partial_\mu \phi) \right], \\ \delta S_{grav} &= \int_{\mathcal{M}} \int dz d^d x \left[\left(\frac{\partial \mathcal{L}}{\partial \phi} - \partial_\mu \left(\frac{\partial \mathcal{L}}{\partial (\partial_\mu \phi)} \right) \right) \delta\phi + \partial_\mu \left(\frac{\partial \mathcal{L}}{\partial (\partial_\mu \phi)} \delta\phi \right) \right], \\ \delta S_{grav}^{on-shell} &= \int_{\epsilon}^{\infty} \int d^d x \partial_z \left(\frac{\partial \mathcal{L}}{\partial (\partial_z \phi)} \delta\phi \right) = - \int_{\partial M} d^d x \frac{\partial \mathcal{L}}{\partial (\partial_z \phi)} \delta\phi \Big|_{z=\epsilon}. \end{aligned}$$

It is convenient to introduce an analogue of a pulse having applied the additional coordinate:

$$\Pi = - \frac{\partial \mathcal{L}}{\partial (\partial_z \phi)}.$$

Now the calculation of variation derivatives can be simplified:

$$\begin{aligned} \delta S_{grav}^{on-shell} &= \int_{\partial M} d^d x \Pi(\epsilon, x) \delta\phi(\epsilon, x), \\ \frac{\delta S_{grav}^{on-shell}}{\delta \phi(\epsilon, x)} &= \Pi(\epsilon, x) = - \frac{\partial \mathcal{L}}{\partial (\partial_z \phi)}. \end{aligned}$$

In the general case, of course, there will be divergences in the action that is why it is necessary to introduce counterterms S_{ct} :

$$S^{ren} = S_{grav}^{on-shell} + S_{ct}.$$

After that we should redefine the value Π as well:

$$\begin{aligned} \Pi^{ren}(z, x) &= \frac{\delta S^{ren}}{\delta \phi(z, x)}, \\ \Pi^{ren}(z, x) &= - \frac{\partial \mathcal{L}}{\partial (\partial_z \phi(\epsilon, x))} + \frac{\delta S_{ct}}{\delta \phi(\epsilon, x)}. \end{aligned}$$

Finally, we can get the expression for average values calculation:

$$\langle O(x) \rangle_\varphi = \lim_{z \rightarrow 0} z^{d-\Delta} \Pi^{ren}(z, x).$$

Now, we pass on to direct calculation of the Green's functions. Recall that:

$$\langle O(x) \rangle_\varphi = \int [D\psi] O(x) \exp \left(S_E[\psi] + \int d^d y \varphi(y) O(y) \right).$$

Hereinafter we write an evident expansion:

$$\langle O(x) \rangle_\varphi = \langle O(x) \rangle_{\varphi=0} + \int d^d y \langle O(x) O(y) \rangle \varphi(y) + \dots \quad (9)$$

Determining the Green's functions as follows:

$$G_E(x-y) = \langle O(x) O(y) \rangle,$$

we can rewrite the expression (9) in the form:

$$\begin{aligned}\langle O(x) \rangle_\varphi &= \langle O(x) \rangle_{\varphi=0} + \int d^d y G_E(x-y) \varphi(y), \\ \langle O(x) \rangle_\varphi &= \int d^d y G_E(x-y) \varphi(y)\end{aligned}$$

or after performing a Fourier transform we get:

$$\begin{aligned}\langle O(k) \rangle_\varphi &= G_E(k) \varphi(k), \\ G_E(k) &= \frac{\langle O(k) \rangle_\varphi}{\varphi(k)}.\end{aligned}$$

Now using (8) we can obtain the final expression for the Green's function:

$$G_E(k) = \lim_{z \rightarrow 0} z^{2(d-\Delta)} \frac{\Pi^{ren}(z, x)}{\phi(z, k)}. \quad (10)$$

We will meet a similar expression further in the ratio for Green's fermionic function. Note that such structure remains for the Green's functions of fields with other spin value.

Next remember the equation for scalar field action:

$$S = -\frac{\eta}{2} \int dz d^d x \sqrt{g} [g^{MN} \partial_M \phi \partial_N \phi + m^2 \phi^2].$$

After discrimination of the total derivative the equation becomes as follows:

$$S = -\frac{\eta}{2} \int dz d^d x \partial_M [\sqrt{g} \phi g^{MN} \partial_N \phi] + \frac{\eta}{2} \int dz d^d x \phi \sqrt{g} \left[\frac{1}{\sqrt{g}} \partial_M (\sqrt{g} g^{MN} \partial_N \phi) - m^2 \phi \right].$$

Now the action on the boundary of the manifold takes the form:

$$\begin{aligned}S^{on-shell} &= -\frac{\eta}{2} \int dz d^d x \partial_M [\sqrt{g} \phi g^{MN} \partial_N \phi], \\ S^{on-shell} &= \frac{\eta}{2} \int d^d (\sqrt{g} \phi g^{zz} \partial_z \phi)_{z=\epsilon}.\end{aligned}$$

Taking into account the expression for Π :

$$\Pi = -\frac{\partial \mathcal{L}}{\partial (\partial_z \phi)} = \eta \sqrt{g} g^{zz} \partial_z \phi,$$

it is easy to get that:

$$S^{on-shell} = \frac{1}{2} \int_{z=\epsilon} d^d x \Pi(z, x) \phi(z, x).$$

If we use the ratios for Fourier components:

$$\phi(z, x) = \int \frac{d^d k}{(2\pi)^d} e^{ikx} f_k(z), \quad \Pi(z, x) = \int \frac{d^d k}{(2\pi)^d} e^{ikx} \Pi_k(z),$$

we get that:

$$S^{on-shell} = \frac{1}{2} \int \frac{d^d k}{(2\pi)^d} \Pi_{-k}(z=\epsilon) f_k(z=\epsilon).$$

Refreshing the memory about f on the boundary, it is easy to comprehend that on the boundary Π behaves like:

$$\Pi(z, x) \approx \eta L^{d-1} [(d-\Delta)A(x)z^{-\Delta} + \Delta B(x)z^{\Delta-d}], \quad (z \rightarrow 0).$$

The same expression in Fourier components will be as follows:

$$\Pi_{-k}(z) \approx \eta L^{d-1} [(d-\Delta)A(-k)z^{-\Delta} + \Delta B(-k)z^{\Delta-d}], \quad (z \rightarrow 0).$$

This makes it possible to rewrite the expression for the action on the boundary:

$$S^{on-shell} = \frac{\eta}{2} L^{d-1} \int \frac{d^d k}{(2\pi)^d} [\epsilon^{-2\nu} (d-\Delta)A(-k) + dA(-k)B(k)].$$

Unfortunately, this action diverges (see the power of ε). It is necessary to add a counterterm to the action for its regularization. Upon the demand for invariance and simplicity an appropriate counterterm will be as follows:

$$\int_{\partial AdS} d^d x \sqrt{\gamma} \phi^2(\varepsilon, x),$$

where:

$$ds_{z=\varepsilon}^2 = \gamma_{\mu\nu} dx^\mu dx^\nu = \frac{L^2}{\varepsilon^2} \delta_{\mu\nu} dx^\mu dx^\nu.$$

It is easy to modify the counterterm and we can see that:

$$\int_{\partial AdS} d^d x \sqrt{\gamma} \phi^2(\varepsilon, x) = L^d \int \frac{d^d k}{(2\pi)^d} [\varepsilon^{-2\nu} A(-k) A(k) + 2A(-k) B(k)].$$

For now, write down the counter term with correct coefficient and we obtain:

$$s_{ct} = -\frac{\eta}{2} \frac{d-\Delta}{L} \int_{\partial AdS} d^d x \sqrt{\gamma} \phi^2,$$

$$s_{ct} = -\frac{\eta}{2} \frac{d-\Delta}{L^{1-d}} \int \frac{d^d k}{(2\pi)^d} [\varepsilon^{-2\nu} A(-k) A(k) + 2A(-k) B(k)].$$

From the last expression we finally obtain the formula for regularized action:

$$S^{ren} = \frac{\eta}{2} L^{d-1} (2\Delta - d) \int \frac{d^d k}{(2\pi)^d} A(-k) B(k).$$

Then let us represent the function f as follows (for random z):

$$f_k(z) = A(k) \phi_1(z, k) + B(k) \phi_2(z, k).$$

It is naturally that for small z we get:

$$\phi_1(z, k) \approx z^{d-\Delta}, \quad \phi_2(z, k) \approx z^\Delta.$$

Then, we introduce the following notation:

$$\chi = \frac{B}{A}.$$

Now

$$S^{ren} = \frac{\eta}{2} L^{d-1} (2\Delta - d) \int \frac{d^d k}{(2\pi)^d} \chi(k) \varphi(k) \varphi(-k).$$

For now, it is easy to write an expression for variation derivative:

$$\langle O(x) \rangle_\varphi = (2\pi)^d \frac{\delta S^{ren}}{\delta \varphi(-k)} = \eta L^{d-1} (2\Delta - d) \chi(k) \varphi(k),$$

$$\langle O(k) \rangle_\varphi = 2\nu \eta L^{d-1} B(k).$$

Wherefrom we immediately obtain that:

$$G_E(k) = 2\nu \eta L^{d-1} \frac{B(k)}{A(k)}. \quad (11)$$

This formula has an important significance and will be used hereafter and for fermions as well (but without formula derivation). Its meaning is in the fact that in the AdS/CFT correspondence for Green's function calculation it is just enough to determine coefficients at the equation's asymptotics with respect to additional coordinate for our field of interest:

$$f_k(z) = z^{d/2} g_k(z).$$

Then:

$$z^2 \partial_z^2 g_k + z \partial_z g_k - (\nu^2 + k^2 z^2) g_k = 0.$$

This equation is precisely the equation for Bessel functions and its corresponding solution for f will have a form $z^{d/2} I_{\mp\nu}(kz)$.

Taking into account the fact that Bessel functions have the following asymptotic:

$$I_{\mp\nu}(z) \approx \frac{1}{\Gamma(1 \mp \nu)} \left(\frac{z}{2}\right)^{\mp\nu}, \quad z \rightarrow 0,$$

we can obtain that:

$$\phi_1(z, k) = \Gamma(1-\nu) \left(\frac{k}{2}\right)^\nu z^{d/2} I_{-\nu}(kz), \quad \phi_2(z, k) = \Gamma(1+\nu) \left(\frac{k}{2}\right)^{-\nu} z^{d/2} I_\nu(kz),$$

$$f_k(z) = z^{d/2} \left[\Gamma(1-\nu) \left(\frac{k}{2}\right)^\nu A(k) I_{-\nu}(kz) + \Gamma(1+\nu) \left(\frac{k}{2}\right)^{-\nu} B(k) I_\nu(kz) \right].$$

Correspondingly:

$$I_{\mp\nu}(z) \approx \frac{e^z}{\sqrt{2\pi z}}, \quad (z \rightarrow \infty).$$

Now we have that:

$$f_k(z) \approx \frac{z^{d/2} e^{kz}}{\sqrt{2\pi k z}} \left[\Gamma(1-\nu) \left(\frac{k}{2}\right)^\nu A(k) + \Gamma(1+\nu) \left(\frac{k}{2}\right)^{-\nu} B(k) \right].$$

From which, we get:

$$\frac{B(k)}{A(k)} = -\frac{\Gamma(1-\nu)}{\Gamma(1+\nu)} \left(\frac{k}{2}\right)^{2\nu} = \frac{\Gamma(-\nu)}{\Gamma(\nu)} \left(\frac{k}{2}\right)^{2\nu}.$$

Finally, the expression for the scalar field Green's function take the form:

$$G_E(k) = 2\nu\eta L^{d-1} \frac{\Gamma(-\nu)}{\Gamma(\nu)} \left(\frac{k}{2}\right)^{2\nu}, \quad (12)$$

or by performing an inverse Fourier transform, we derive:

$$G_E(x) = \int \frac{d^d k}{(2\pi)^d} e^{ikx} G_E(k).$$

With account of the following:

$$\int \frac{d^d k}{(2\pi)^d} e^{ikx} k^n = \frac{2^n}{\pi^{d/2}} \frac{\Gamma\left(\frac{d+n}{2}\right)}{\Gamma\left(-\frac{n}{2}\right)} \frac{1}{|x|^{d+n}}.$$

We derive a resultant expression for average with which we have defined the Green's function.

$$\langle O(x) O(0) \rangle = \frac{2\nu\eta L^{d-1}}{\pi^{d/2}} \frac{\Gamma\left(\frac{d}{2} + \nu\right)}{\Gamma(-\nu)} \frac{1}{|x|^{2\Delta}}.$$

Note that the expression for the Green's function has the well known conformal field theory form with a power law of decrease. From the given methodical example, it is possible to retrace what is necessary to do in more complex cases.

4. Green's functions for fermion field

In this case, it is necessary to start with known models [41] that consist of not only fermion fields but also metric solutions in which a boundary naturally arises. An eligible candidate is a solution in AdS₅ for the charged black hole in IIB supergravity type with three U(1) charge, wherein Q₁ = Q₂ and Q₃ = 0.

The Lagrangian density for this model is:

$$\mathcal{L} = \frac{1}{2k^2} \left\{ R - \frac{1}{4} e^{4\alpha} F_{\mu\nu} F^{\mu\nu} - 12 \partial_\mu \alpha \partial^\mu \alpha + \frac{1}{L^2} (8e^{2\alpha} + 4e^{-4\alpha}) \right\}. \quad (13)$$

Here, k is a coupling constant, R is a crookedness, $F_{\mu\nu}$ is a density tensor of a vector field A_μ , α is a scalar field. In this case, the solution for metrics, scalar and vector fields will have the following form:

$$\begin{aligned} ds^2 &= e^{2A} (-h dt^2 + dx^2) + \frac{e^{2B}}{h} dr^2, \\ A &= \ln \frac{r}{L} + \frac{1}{3} \ln \left(1 + \frac{Q^2}{r^2} \right), \\ B &= -\ln \frac{r}{L} - \frac{2}{3} \ln \left(1 + \frac{Q^2}{r^2} \right), \\ h &= \frac{(r^2 + 2Q^2) r^2}{(r^2 + Q^2)^2}, \quad \alpha = \frac{1}{6} \ln \left(1 + \frac{Q^2}{r^2} \right), \\ A_\mu dx^\mu &= \Phi dt, \quad \Phi = \frac{\sqrt{2} Q r^2}{(r^2 + Q^2) L}, \end{aligned}$$

where r is a radial coordinate, Q is a black hole charge. Since the metrics is diagonal and depends only on r Dirac equations can be simplified by substitution:

$$\begin{aligned} \Psi &\rightarrow (-g g^{rr})^{1/4} \Psi, \\ g &= \det (g_{\alpha\beta}). \end{aligned}$$

We write down Dirac equation for fermions:

$$[\gamma^\mu (\partial_\mu - iq A_\mu) - m] \psi = 0,$$

here q and m are charge and mass as well, γ are Dirac matrices. Then, after separation of variables, on which the equation coefficients don't depend, we get:

$$\psi \rightarrow e^{-i\omega t + ikx} \psi.$$

It is easy to obtain that:

$$\left[-i \sqrt{-g^{tt}} \gamma^t (w + q A_t) + \sqrt{g^{rr}} \gamma^r \partial_r + i \sqrt{g^{xx}} \gamma^x k - m \right] \Psi = 0.$$

As in the usual Dirac theory, these equations are split into pairs. Writing through the Pauli matrices σ one pair of equations we have:

$$\left[\sqrt{-g^{tt}} \sigma_1 (w + q A_t) + \sqrt{g^{rr}} \sigma_3 \partial_r + (-1)^\alpha i \sqrt{g^{xx}} \sigma_2 k - m \right] \Psi_\alpha = 0.$$

The asymptotic behavior of Dirac spinor in AdS₅ has the following form:

$$\psi_\alpha \xrightarrow{r \rightarrow \infty} a_\alpha r^m \begin{pmatrix} 1 \\ 0 \end{pmatrix} + b_\alpha r^{-m} \begin{pmatrix} 0 \\ 1 \end{pmatrix}.$$

The expected value of the boundary spinorial operator dual to the bulk spinor ψ can be written as: $\langle O_\psi \rangle = (0, b_1, 0, b_2)^T$. In fact, $O_w = 0.5 (1 - \gamma^z) O_w$, $\gamma^z = \begin{pmatrix} \sigma_3 & 0 \\ 0 & \sigma_3 \end{pmatrix}$, which means that the boundary spinorial operator is left-handed, where σ_3 is the Pauli matrix. By imposing the in-falling boundary condition at the horizon, we can obtain the retarded Green's function as:

$$G = \begin{pmatrix} 0 & & & \\ & G_1 & & \\ & & 0 & \\ & & & G_2 \end{pmatrix}, \quad G_\alpha = \frac{b_\alpha}{a_\alpha}. \quad (14)$$

Note that if we use the alternative quantization, the Green's function has the form: $G_\alpha = -a_\alpha/b_\alpha$, then the spinor operator at the border is right-handed. If $m = 0$, G_1 and G_2 are related by $G_2 = -1/G_1$ [42]. Therefore, the alternative quantization for G_1 is the standard quantization for G_2 , and vice versa. Taking G_1 and G_2 into account, the alternative quantization gives the same Fermi momenta as the standard quantization does at $m = 0$.

The fact that the corresponding Green's functions in (14) are defined in the same manner as for the scalar field Green's functions in (11) has important significance. That is the general prescription of the Green's function construction for more complex theories as well.

Let us consider equations for $\psi_1 = (u_1, u_2)^T$ and introduce $u_{\pm} = u_1 \pm iu_2$, then we get:

$$\begin{aligned}\partial_r u_+ + h^*(r) u_+ &= f^*(r) u_-, \\ \partial_r u_- + h(r) u_- &= f(r) u_+, \\ h(r) &= i\sqrt{\frac{-g^{tt}}{g^{rr}}} (w + qA_t), \\ f(r) &= \frac{m}{\sqrt{g^{rr}}} - ik\sqrt{\frac{g^{xx}}{g^{tt}}}.\end{aligned}$$

From which, we finally obtain:

$$\begin{aligned}\partial_{rr} u_+ + p^*(r) \partial_r u_+ + q^*(r) u_+ &= 0, \\ \partial_{rr} u_- + p(r) \partial_r u_- + q(r) u_- &= 0, \\ p(r) &= -\partial_r f(r)/f(r), \\ q(r) &= |h(r)|^2 - |f(r)|^2 + p(r)h(r) + h(r).\end{aligned}$$

For massless particles $m = 0$ and for the case when $w \propto 0$ ($q > 1/2$), the solution can be written exactly:

$$\begin{aligned}u_-(r) &= \left(\frac{r}{r + i\sqrt{2}Q}\right)^{\nu(k)} \left(\frac{r + i\sqrt{2}Q}{r - i\sqrt{2}Q}\right)^{q/2} {}_2F_1\left(\nu(k) - q + 1/2, \nu(k); 2\nu(k) + 1; \frac{2r}{r + i\sqrt{2}Q}\right), \\ \nu(k) &= \frac{k}{\sqrt{2}Q}.\end{aligned}\tag{15}$$

Now, under $w \propto 0$, we finally have:

$$G_1 = \lim_{r \rightarrow \infty} \left(-i \frac{(-1)^{n+1} u_-^* - u_-}{(-1)^{n+1} u_-^* + u_-} \right), \quad n = q - \nu(k) - 1/2.$$

Further calculations are performed, assuming that we have a precise analytical solution (15) for the case $w \propto 0$, we can develop perturbation theory and derive the Green's function in the ordinary form for calculations in the frame of AdS/CFT correspondence:

$$\begin{aligned}G(w, k) &= \frac{Z}{-w + v_F(k - k_F) - c(k_F)w^{2\nu(k)}}, \\ k_F = k_F(n) &= \sqrt{2}Q(q - n - 1/2), \quad n = 0, 1, 2, \dots, |q - 1/2|.\end{aligned}\tag{16}$$

Note that the formula (16) predicts few Fermi surfaces for the case of charge $> 1/2$.

The Green's functional form, similar to the cited (16), is a typical form for computation in the framework of AdS/CFT correspondence, and appears for other metrics as well [43, 44].

5. Further development of the approach

Further development of the AdS/CFT correspondence approaches proceeds in the same manner as the already-existing solid state physics models' application, but also the way of further extension of both metric and space classes.

An approach for the Green's functions calculation in the frame of AdS/CFT correspondence was evolved in article [43], but for the case when metric was described by the metrics of the so-called Schrodinger black hole. Unfortunately, the authors could not retrieve a compact enough analytic expression for the fermions Green's function and it was thus investigated numerically.

Generalization of AdS/CFT correspondence onto the case of D-branes and the use of the given description for zero-point sound in strange metals investigation has been done in the paper [45]. This research obviously demonstrates that methods under development can also be extended to more complex mathematical objects.

Research issues important for various applications of Feynman propagators were discussed in [46]. Note that this paper is among one of the first on that subject.

In article [47], the application of AdS/CFT correspondence to study the transport in new-found Dirac semimetals was proposed [48, 49]. The authors succeeded in obtaining agreement with experimental data and explain transport characteristics' behavior in the critical zone.

In [50], the authors completed the natural generalization of the AdS/CFT correspondence for the case of two interacting subsystems. In this instance, it was assumed that one subsystem consists of strongly interacting

fermions, the Green's function of which can be found in the framework of the AdS/CFT correspondence. Another subsystem interacts with the first one quite weakly (i.e. it is possible to apply a standard diagram technique within the confines of the perturbation theory) and its Green's functions can be found by the perturbation theory.

Article [51] is dedicated to the application of the method under consideration to clarify the characteristics of so-called zero-point sound in metals. For example, in [52], the authors used the standard method to derive an expression for the zero-point sound parameters, having applied the Green's functions followed from the correspondence under discussion.

Investigation [53] is also of interest, as an approach to the Green's functions calculation in the presence of magnetic field was evolved in this work and prospects of this approach application in the Hall quantum effect physics were discussed.

In our opinion, issues surrounding the Green's function in an external magnetic field were more successfully defined in [54], in which the Green's function in an external magnetic field was obtained in the form similar to (16) with momentum quantization which is identical to Landau quantization and experimentally observed characteristics were estimated.

The important applications of cuprates physics were considered in publication [55], where an exploration of mode stability was performed and in general, the Green's function was shown to be stable and have the form similar to (16).

The possibility for AdS/CFT correspondence application in high-temperature superconducting cuprates physics was also considered in [56], where the appearance of mechanisms for Fermi arcs generation was investigated and the Green's functions were adduced with regard to strong quasiparticle decay.

The properties of universal thermal and electrical conductivity were investigated and research for Reissner-Nordstrom black hole in arbitrary dimension was performed in the scientific work [57].

Article [58] is dedicated to the generalization of AdS/CFT correspondence approaches in the case of impurities presence in system. The ways of impurity introduction and their correct description within suggested approach were discussed.

Further description of impurities combined with semi-holographic approach was given in the paper [44]. Impurities were characterized as a subsystem weakly interacting with a system from which Green's functions can be determined using the AdS/CFT correspondence.

An important approach generalization for the case of an external periodic potential presence was done in article [59]. The results can be useful for analysis of the non-Fermi liquids' transport characteristics in external periodic fields created by superstructures, for instance.

Some research [60] was dedicated to the Fermi surface structure within the framework of the proposed approach. The polar motion of Green's functions was also explored.

Detailed mathematical analysis of evolving problems in the approach under consideration and investigation of important special cases were performed in [42]. Asymptotics of arising solutions and the case of final temperatures were also analyzed in detail in this paper.

The features of non-Fermi liquids' behavior and the unique characteristics of arising Green's functions were discussed in [61]. The behavior criteria of a non-Fermi electronic liquid were also mentioned there.

Non-Fermi liquids were also considered in [62]. This article is especially valuable because the authors adjusted the calculations (analytical and numerical) to obtain the excitations dispersion laws. In particular, it was shown that excitations with dispersion law $\omega \propto k^{2.09 \pm 0.01}$ exist in Non-Fermi liquids.

A significant model of Fermi liquid was analyzed in [63]. In this article, the Luttinger relation was shown to relate the area enclosed by the Fermi surfaces to the fermion density, which was derived from Gauss's Law for the bulk electric field. All low energy modes were demonstrated to be consistent with Landau's Fermi liquid theory.

AdS/CFT correspondence was generalized for the case of M-theory in [64]. The charge transport properties of $2 + 1$ dimensional conformal field theories at non-zero temperature were considered. For the theory with Abelian $U(1)$ charges, the action of particle-vortex duality on the hydrodynamic-to-collisionless crossover function was presented, leading to powerful functional constraints for self-dual theories.

The publication [65] was devoted to quantum dot investigation and consisted of a variety of model descriptions in which AdS/CFT correspondence ideas can be used. The Kondo lattice models were also considered; they can be described by mean-field theory obtained by mapping a quantum impurity coupled to a self-consistent environment. Such a theory yields a 'fractionalized Fermi liquid' phase of conduction electrons coupled to a critical spin liquid state, and is an attractive mean-field theory of strange metals.

The research [66] is also of interest, where a general hydrodynamic theory of transport was analyzed in the vicinity of superfluid-insulator transitions in two spatial dimensions described by "Lorentz"-invariant quantum

critical points. The exact results for the null frequency transport coefficients for a supersymmetric conformal field theory, which is solvable by the AdS/CFT correspondence were also presented.

Propagation of the AdS/CFT correspondence ideas onto the case of the absolute zero phases of compressible quantum matter was investigated in [67]. Fermi surfaces with the singularities of Landau's Fermi liquid theory have several phases, while other Fermi surfaces have non-Fermi liquid singularities. Compressible phases found in models applicable to condensed matter systems were also argued to be present in models obtained by applying chemical potentials.

An important application to calculate the relation of entropy to viscosity is given in the [68]. The viscosity to entropy ratio has been shown to take on a very simple universal value in all gauge theories with the AdS/CFT correspondence. Investigators described the origin of this universal ratio, and focused on how it is modified by generic higher derivative corrections, corresponding to curvature corrections on the gravity side of the duality. In particular, certain curvature corrections are known to push the viscosity to entropy ratio below its universal value. This fact disproves a longstanding conjecture that such a universal value represents a strict lower bound for any fluid in nature.

Consideration of the ratio of entropy to viscosity is also given in [69]. The existence of a sound mode, which is described by hydrodynamics, even at energies much greater than the temperature, was shown. The authors explain how these and other properties of the field theory are consistent with those of a (3+1)-dimensional Landau Fermi liquid which is finely tuned to the Pomeranchuk critical point.

In article [70], the dynamics of few cycle optical pulses in non-Fermi liquid was considered. Energy spectrum of non-Fermi liquid was taken from the AdS/CFT correspondence. Conditions of quasi-particle excitation existence were defined. The non-Fermi liquid parameters' impact on the shape of the few cycle pulses was estimated.

Paper [71] can be mentioned as an example of another application of the approach under consideration. The indirect spin-spin interaction between impurities in a non-Fermi quantum liquid system is theoretically investigated in this paper. The poles of the Green's functions are shown to be responsible for the observed excitation spectra. Specifically, the anti-de Sitter/conformal field theory (AdS/CFT) correspondence is used to gain access to the analytical expressions of the Green's functions for our particular problem. For example, the current-voltage characteristic is determined by the imaginary part of the Green's function. Great progress in the Green's functions calculation for different systems was made by the AdS/CFT correspondence between the conformal field theory and the theory of superstrings [72].

Thus, the AdS/CFT correspondence is a powerful method to obtain Green's functions in systems of strongly interacting particles. The use of this method has made possible significant progress towards answering a number of modern physics most vital questions.

Acknowledgements

This work was supported by the Russian Foundation for Basic Research under project No. 16-32-00230.

References

- [1] Casalderrey-Solana J., Liu H., et al. Gauge/String Duality, Hot QCD and Heavy Ion Collisions. 2011, ArXiv:1101.0618.
- [2] Gubser S.S., Klebanov I.R., Polyakov A.M. Gauge theory correlators from noncritical string theory. *Phys. Lett. B*, 1998, **428**, P. 105–114.
- [3] Hartnoll S.A. Lectures on holographic methods for condensed matter physics. *Class. Quant. Grav.*, 2009, **26**, 224002.
- [4] McGreevy J. Holographic duality with a view toward many-body physics. *Adv. High Energy Phys.*, 2010, 723105.
- [5] D'Hoker E., Freedman D.Z. Supersymmetric gauge theories and the AdS/CFT correspondence. 2002, ArXiv: hep-th/0201253.
- [6] Witten E. Anti-de Sitter space and holography. *Adv. Theor. Math. Phys.*, 1998, **2**, P. 253–291.
- [7] Aharony O., Gubser S.S., et al. N field theories, string theory and gravity. *Phys. Rept.*, 2000, **323**, P. 183–386.
- [8] Maldacena J.M. The Large N limit of superconformal field theories and supergravity. *Adv. Theor. Math. Phys.*, 1998, **2**, P. 231–252.
- [9] Zee A. *Quantum Field Theory in a Nutshell*, Princeton University Press, Princeton, 2010. 608 pp.
- [10] Balasubramanian V., Giddings S.B., Lawrence A. What do CFTs tell us about anti-de Sitter spacetimes. *J. High Energy Phys.*, 1999, **03**, 001.
- [11] Balasubramanian V., Kraus P., Lawrence A., Trivedi S.P. Holographic probes of anti-de Sitter spacetimes. *Phys. Rev. D*, 1999, **59**, 104021.
- [12] Policastro G., Starinets A. On the absorption by near-extremal black branes. *Nucl. Phys. B*, 2001, **610**, P. 117–143.
- [13] Danielsson U.H., Keski-Vakkuri E., Kruczenski M. Vacua, propagators, and holographic probes in AdS/CFT. *J. High Energy Phys.*, 1999, **01**, 002.
- [14] Balasubramanian V., Kraus P., Lawrence A. Bulk versus boundary dynamics in anti-de Sitter spacetime. *Phys. Rev. D*, 1999, **59**, 046003.
- [15] Pak A.V., Belonenko M.B., Dyachkov P.N. Electrophysical properties of CNT. The augmented cylindrical wave method. *Nanosystems: physics, chemistry, mathematics*, 2013, **4**(4), P. 564–569.
- [16] Herzog C.P. Lectures on holographic superfluidity and superconductivity. *J. Phys. A*, 2009, **42**, 343001.
- [17] Cubrovic M., Zaanen J., Schalm K. String Theory, Quantum Phase Transitions and the Emergent Fermi-Liquid. *Science*, 2009, **325**, P. 439–444.
- [18] Lee S.S. A non-Fermi liquid from a charged black hole: a critical Fermi ball. *Phys. Rev. D*, 2009, **79**, 086006.
- [19] Senthil T., Vishwanath A., et al. Deconfined' quantum critical points. *Science*, 2004, **303**, P. 1490–1494.

- [20] Senthil T., Balents L., et al. Quantumcriticality beyond the Landau-Ginzburg-Wilson paradigm. *Phys. Rev. B*, 2004, **70**, 144407.
- [21] Sachdev S. Quantum magnetism and criticality. *Nature Phys.*, 2008, **4**, P. 173–185.
- [22] Jensen K., Kachru S., et al. Towards a holographic marginal Fermi liquid. *Phys. Rev. D*, 2011, **84**, 126002.
- [23] Hartnoll S.A. Horizons, holography and condensed matter. 2011, ArXiv:1106.4324.
- [24] Liu H., McGreevy J., Vegh D. Non-Fermi liquids from holography. *Phys. Rev. D*, 2011, **83**, 065029.
- [25] Horowitz G.T. Introduction to holographic superconductors. 2010, ArXiv:1002.1722.
- [26] Iqbal N., Liu H. Real-time response in AdS/CFT with application to spinors. 2009, ArXiv: 0903.2596.
- [27] Iqbal N., Liu H. Universality of the hydrodynamic limit in AdS/CFT and the membrane paradigm. *Phys. Rev. D*, 2009, **79**, 025023.
- [28] Benfatto G., Gallavotti G. Perturbation Theory of the Fermi Surface in a quantum liquid. A general quasiparticle formalism and one-dimensional systems. *Journal of Statistical Physics*, 1990, **59**, P. 541–664.
- [29] Shankar R. Statistical Mechanics and its Applications. *Physica A*, 1991, **177**, P. 530–536.
- [30] Polchinski J. Effective field theory and the Fermi surface. 1992, Arxiv: hep-th/9210046.
- [31] Romans L.J. Supersymmetric, cold and lukewarm black holes in cosmological Einstein-Maxwell theory. *Nucl. Phys. B*, 1992, **383**, P. 395–415.
- [32] Bagger J., Lambert N. Gauge symmetry and supersymmetry of multiple M2-branes. *JHEP*, 2008, **02**, P. 105.
- [33] Gustavsson A. Algebraic Structures on Parallel M2-Branes. *Nucl. Phys. B*, 2009, **811**, P. 66.
- [34] Anderson P.W. Luttinger-liquid” behavior of the normal metallic state of the 2D Hubbard model. *Phys. Rev. Lett.*, 1990, **64**, 1839.
- [35] Chamblin A., Emparan R., Johnson C.V., Myers R.C. Charged AdS black holes and catastrophic holography. *Phys. Rev. D*, 1999, **60**, 064018.
- [36] Varma C.M., Littlewood P.B., et al. Phenomenology of the normal state of Cu-O high-temperature superconductors. *Phys. Rev. Lett.*, 1989, **63**, 1996.
- [37] Varma C.M., Nussinov Z., van Saarloos W. Singular or non-Fermi liquids. *Physics Reports*, 2002, **361** (6), P. 267–417.
- [38] Shankar R. Renormalization-group approach to interacting fermions. *Rev. Mod. Phys.*, 1994, **66**, P. 129.
- [39] Gauntlett J.P. Varela. O. Consistent Kaluza-Klein reductions for general supersymmetric AdS solutions. *Phys. Rev. D*, 2007, **76**, 126007.
- [40] Ramallo A.V. Introduction to the AdS/CFT correspondence. 2013, ArXiv:1310.4319.
- [41] Gubser S.S., Ren J. Analytic fermionic Green’s functions from holography. *Phys. Rev. D*, 2012, **86**, 046004.
- [42] Faulkner T., Liu H., J. McGreevy, Vegh D. Emergent quantum criticality, Fermi surfaces, and AdS₂. *Phys. Rev. D*, 2011, **83**, 125002.
- [43] Wang J. Schrodinger Fermi Liquids. *Phys. Rev. D*, 2014, **89** (4), 046008.
- [44] Belonenko M.B., Konobeeva N.N., Galkina E.N. Dynamics of few cycle optical pulses in a non-Fermi liquid and AdS/CFT correspondence. *Mod. Phys. Lett. B*, 2015, **29** (19), 15500965.
- [45] Dey P., Roy S. Zero sound in strange metals with hyperscaling violation from holography. *Phys. Rev. D*, 2013, **88**, 046010.
- [46] Ryang S. The Hadamard function and the Feynman propagator in the AdS/CFT correspondence. *Phys. Lett. B*, 1999, **469**, P. 87–95.
- [47] Jacobs V.P.J., Vandoren S.J.G., Stoof H.T.C. Holographic interaction effects on transport in Dirac semimetals. *Phys. Rev. B*, 2014, **90**, 045108.
- [48] Wan X., Turner A.M., Vishwanath A., Savrasov S.Y. Topological semimetal and Fermi-arc surface states in the electronic structure of pyrochlore iridates. *Phys. Rev. B*, 2011, **83**, 205101.
- [49] Burkov A.A., Balents L. Weyl semimetal in a topological insulator multilayer. *Phys. Rev. Lett.*, 2011, **107**, 127205.
- [50] Faulkner T., Polchinski J. Semi-holographic Fermi liquid. *JHEP*, 2011, **06**, P. 012.
- [51] Hoyos-Badajoz C., O’Bannon A., Wu J.M.S. Zero Sound in Strange Metallic Holography. *JHEP*, 2010, **1009**, 086.
- [52] Levitov L.S., Shitov A.V. *Green’s functions. Problems with solutions*. Fizmatlit, Moscow, 2003, 392.
- [53] Basu P., Yang He J., Mukherjee A., Shieh H.H. Holographic Non-Fermi Liquid in a Background Magnetic Field. *Phys. Rev. D*, 2010, **82**, 044036.
- [54] Gubankova E., Brill J., et al. *Strongly Interacting Matter in Magnetic Fields*. Springer, Berlin, 2013, 553.
- [55] Edalati M., Leigh R.G., Lo K.W., Phillips P.W. Dynamical Gap and Cuprate-like Physics from Holography. *Phys. Rev. D*, 2011, **83**, 046012.
- [56] Vegh D. Fermi arcs from holography. 2010, Arxiv: 1007.0246.
- [57] Jain S. Universal thermal and electrical conductivity from holography. *JHEP*, 2010, **1011**, P. 092.
- [58] Hashimoto K., Iizuka N. Impurities in Holography and Transport Coefficients. 2012, ArXiv:1207.4643.
- [59] Chesler P., Lucas A., Sachdev S. Conformal field theories in a periodic potential: Results from holography and field theory. *Phys. Rev. D*, 2014, **89**, 026005.
- [60] Fan Z.-Y. Exact fermionic Green’s functions from holography. 2014, ArXiv:1407.0104.
- [61] Faulner T., Iqbal N., et al. Holographic non-Fermi-liquid fixed points. *Philosophical transaction A*, 2011, **369**, P. 1941.
- [62] Liu H., McGreevy J., Vegh D. Non-Fermi liquids from holography. *Phys. Rev. D*, 2011, **83**, 065029.
- [63] Sachdev S. A model of a Fermi-liquid using gauge-gravity duality. *Phys. Rev. D*, 2011, **84**, 066009.
- [64] Herzog C.P., Kovtun P., Sachdev S., Son D.T. Quantum critical transport, duality, and M-theory. *Phys. Rev. D*, 2007, **75**, 085020.
- [65] Sachdev S. Strange metals and the AdS/CFT correspondence. *J. Stat. Mech.*, 2010, **1011**, 11022.
- [66] Hartnoll S.A., Kovtun P.K., Mueller M., Sachdev S. Theory of the Nernst effect near quantum phase transitions in condensed matter, and in dyonic black holes. *Phys. Rev. B*, 2007, **76**, 144502.
- [67] Huijse L., Sachdev S. Fermi surfaces and gauge-gravity duality. *Phys. Rev. D*, 2011, **84**, 026001.
- [68] Cremonini S. The shear viscosity to entropy ratio: A status report. *Mod. Phys. Lett. B*, 2011, **25** (23), P. 1867–1888.
- [69] Davison R.A., Goykhman M., Parnachev M. ADS/CFT and Landau-Fermi liquids. *JHEP*, 2014, **1407**, P. 109.
- [70] Konobeeva N.N., Belonenko M.B. Propagation of few cycle optical pulses in marginal Fermi liquid and ADS/CFT correspondence. *Physica B: Condensed Matter*, 2015, **478**, P. 43–46.
- [71] Zhukov A.V., Bouffanais R., Pak A.V., Belonenko M.B. Study of the indirect interaction in a non-Fermi liquid within the AdS/CFT correspondence framework. *Mod. Phys. Lett. B*, 2015, **29** (17), 1550081.
- [72] Konobeeva N.N., Belonenko M.B. Tunneling current in carbon nanotubes with deep impurities. *Nanosystems: physics, chemistry, mathematics*, 2013, **4** (4), P. 555–558.

Negative differential conductivity in Fermi liquid in the presence of magnetic field

N. N. Konobeeva¹, M. B. Belonenko^{1,2}

¹Volgograd State University, Volgograd, Russia

²Volgograd Institute of Business, Volgograd, Russia

yana_nn@inbox.ru, mbelonenko@yandex.ru

PACS 71.10.Ay, 72.20.-i, 73.40.Gk

DOI 10.17586/2220-8054-2016-7-3-422-426

Abstract. In this paper we, study the response of a Fermi liquid under the influence of an external magnetic field applied to the external electric field. The dispersion law of the Fermi liquid is obtained via AdS/CFT correspondence. The regions of the negative differential conductivity on the current-voltage characteristic were observed. The possibility of terahertz pulse generation in such systems was shown for a wide range of magnetic field strengths.

Keywords: Fermi liquid, AdS/CFT correspondence, differential negative conductivity.

Received: 15 January 2016

Revised: 22 January 2016

1. Introduction

The impetus for writing this paper was the fact that we can control the important characteristics of an electron subsystem (including conductivity) by controlling the spectrum of charge carriers, for example with a magnetic field. From a physical point of view, the reason is a phenomenon similar to the Hall Effect, namely the deflection of electrons under the influence of an electromagnetic field pulse. It should be noted that in the last few years there has been increased interest in this area [1].

One such characteristic is the current-voltage characteristic for a well-established contact with considerable substance. In this case, as will be shown below, the current-voltage characteristic is determined by the imaginary part of the Green's function.

At the same time, great progress in the Green's functions calculation for different systems – with many transformation of the corresponding fields when the coordinates change (scalar, spinor, etc.) – was made by the AdS/CFT correspondence between the conformal field theory and the theory of superstrings [2,3]. This fact allows experimental verification for some of the associated consequences using methods of solid state physics. Usually, the research in this area is focused on the conductivity study [4]. However, studies on other characteristics, which can be subjected to experimental tests, are still lacking.

Based on the above-mentioned facts, the purpose of this paper is to study the response of a Fermi liquid under the influence of an external magnetic field applied to the external electric field in circumstances where the amplitude of the external alternating fields are small and linear response theory is not applicable. The dispersion law is obtained via AdS/CFT correspondence [2,3,5].

2. Basic equation

In order to study tunneling effects, the Hamiltonian of our model has the following form:

$$H = \sum_p E_p^A a_p^+ a_p + \sum_q E_q^B b_q^+ b_q + \sum_{pq} T_{pq} (a_p^+ b_q + b_q^+ a_q), \quad (1)$$

where a_p^+ ; a_p are the creation and annihilation operators with momentum p in the metal; E_p^A is the electron spectrum of a metal; T_{pq} is the matrix element of the tunneling operator between the states p and q ; b_q^+ ; b_q are the creation and annihilation operators with momentum q of a substance in contact with the metal; E_p^B is the electron spectrum of the substance.

Following the concepts laid out in [6], we find that the current is [7]:

$$J = 4\pi e |T|^2 \sum_{pq} \int_{-\infty}^{\infty} dE \operatorname{Im} G^A(p, E + eV) \cdot \operatorname{Im} G^B(q, E) (n_f(E) - n_f(E + eV)), \quad (2)$$

where G^A is the Green's function for a superlattice, G^B is the Green's function for a Fermi liquid, V is the voltage applied to a test substance, e is the electron charge.

The dispersion law for a superlattice has the following form [8]:

$$E_p^A = \varepsilon_0 - \Delta \cos(p), \quad (3)$$

where ε_0 is the energy of quantum well electrons, Δ is the tunneling integral determined by the overlap of the electron wave functions of neighboring wells, momentum p is directed along z -axis.

As a result, we obtain the following expression for tunneling current:

$$J = 4\pi e |T|^2 \sum_{pq} \int_{-\infty}^{\infty} dE \frac{1}{\sqrt{1 - \left(\frac{\varepsilon_0 - E - eV}{\Delta}\right)^2}} \cdot \text{Im} G^B(q, E) (n_f(E) - n_f(E + eV)). \quad (4)$$

So, after the calculation of the integral in Eq. (4), it is easy to obtain the current-voltage characteristic of the superlattice and Fermi liquid contact.

3. Excitation spectrum from the AdS/CFT correspondence

The Green's function of the systems near the quantum critical point for example "strange metals" can be found in the framework of the holographic approach. High temperature superconductors in the quantum critical region, and other similar materials, can be dual with models of superstring theory with gravity [9, 10]. Duality is understood here in the sense of the gravity theory with matter (fermions, scalar fields) in space-time with a certain dimension being equivalent (in terms of mean values) to some field theory on the boundary of space-time. This gives one the opportunity to obtain an expression for the average values of the dual variables (understood in the usual sense of the conformal field theory) at the boundary and, therefore, the Green's function [11, 12] can be calculated for the wave functions of the perturbation field in the bulk material.

The action for the vector field can be written as:

$$S = \frac{1}{2k^2} \int d^4x \sqrt{-g} \left(R + \frac{6}{R^2} - \frac{R^2}{g_f^2} F_{MN} F^{MN} \right), \quad (5)$$

here g_f^2 is the effective dimensionless calibration constant, R is the curvature radius of AdS_4 .

The motion equations following from Eq. (5) can be solved by geometry, corresponding to a dyonic black hole with electric and magnetic charge:

$$ds^2 = g_{MN} dx^M dx^N = \frac{r^2}{R^2} (-f dt^2 + dx^2 + dy^2) + \frac{R^2}{r^2} \frac{dr^2}{f}, \quad (6)$$

where f is the redshift coefficient, and:

$$f = 1 + \frac{Q^2 + H^2}{r^4} - \frac{M}{r^3}, \quad A_t = \mu \left(1 - \frac{r_0}{r} \right), \quad A_y = hx, \quad A_x = A_r = 0, \\ M = r_0^3 + \frac{Q^2 + H^2}{r_0},$$

where Q, H are the electric and magnetic charge of the black hole, μ is the black hole chemical potential, h is the magnetic field of the black hole, r_0 is the horizon radius.

The Green's function can be obtained from the Dirac equation, and near the Fermi surface, is:

$$G(\omega) = \frac{-h_1 h_2 \nu_F}{\omega - \nu_F k_{\perp} - h_2 \nu_F e^{i\theta} - i\pi \nu \omega^{2\nu}}, \quad (7)$$

where ν_F is the Fermi velocity, $k_{\perp} = k - k_F$, k_F is the Fermi momentum, k is the momentum module, ν is the conformal dimension, θ and $h_{1,2}$ are the positive constant, ω is the frequency.

The effect of the magnetic field is determined by the discretization of the momentum:

$$k \rightarrow k_{eff} = \sqrt{2|qh|l}, \quad l \in \mathbb{N},$$

l is the Landau level index. These discrete values of k are the analog of the well-known Landau levels, which occur in magnetic systems.

Following the concepts which were delineated in [2, 13], we find that the imaginary part of the Green's function is:

$$\text{Im } G(\omega) = \frac{-h_1 h_2 \nu_F^2 \omega^{2\nu} \sin(\theta - \pi\nu)}{(\omega - \nu_F k_{\perp} - h_2 \nu_F \omega^{2\nu} \cos(\theta - \pi\nu))^2 + h_2^2 \nu_F^2 \omega^{4\nu} \sin^2(\theta - \pi\nu)}. \quad (8)$$

4. The results of numerical analysis and discussion

The current-voltage characteristics of the contact between the superlattice and a Fermi liquid for different tunneling integral Δ values are shown in Fig. 1.

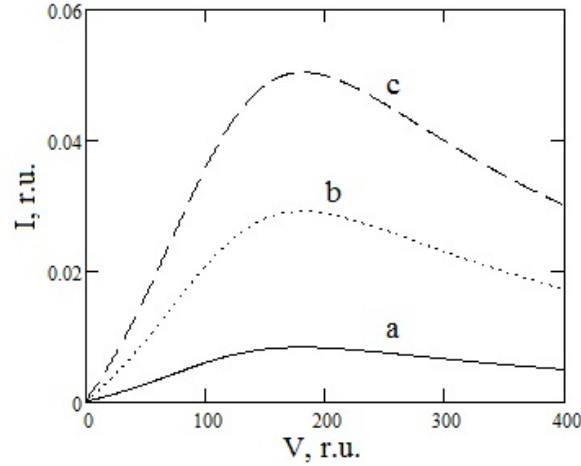


FIG. 1. Current-voltage characteristics of the tunneling contact for $h = 1.5$ r.u., $\nu = 1.3$: a) $\Delta = 0.01$ r.u.; b) $\Delta = 0.03$ r.u.; c) $\Delta = 0.05$ r.u.

A decreasing region in the CVC can be seen, which points to differential negative conductivity, which is specific for all substances having a periodical dispersion law. Behavior of the curve is determined by the tunneling integral Δ – the higher the value, the greater the current.

CVC dependence on the magnetic field is presented in Fig. 2.

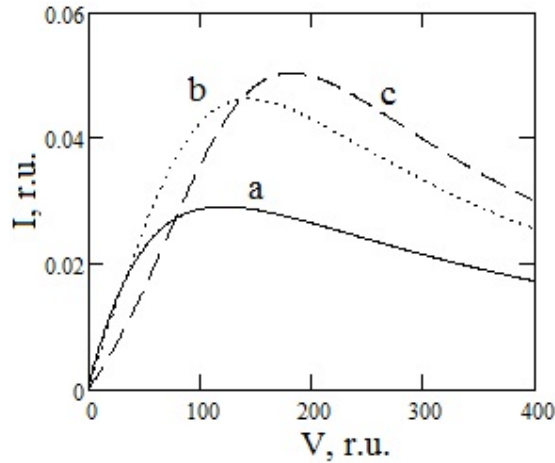


FIG. 2. Current-voltage characteristics of the tunneling contact for $\Delta = 0.05$ r.u., $\nu = 1.3$: a) $h = 1.0$ r.u.; b) $h = 1.5$ r.u.; c) $h = 2.0$ r.u.

According to the observed dependence, it can be concluded that with a stronger magnetic field, the tunneling current also increases, and hence, differential resistance decreases.

The dependence of the tunneling current on the applied voltage for different conformal dimension ν values is given in Fig. 3.

As can be seen from the graphs, for some values of parameter ν , there appear two regions with differential negative conductivity, and in the case $\nu = 1.1$, there is even a region with an absolute negative conductivity (ANC).

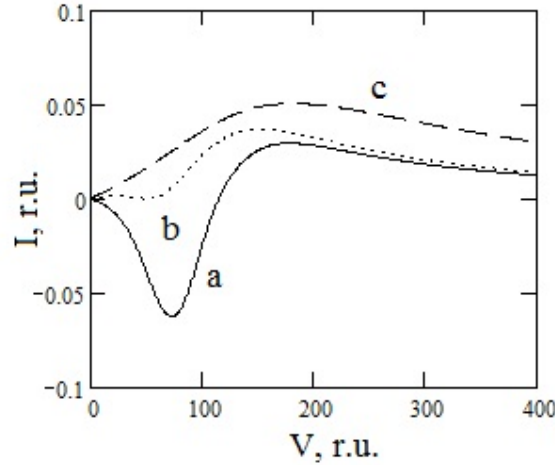


FIG. 3. Current–voltage characteristics of the tunneling contact for $\Delta = 0.05$ r.u., $h = 1.5$ r.u.: a) $\nu = 1.1$; b) $\nu = 1.2$; c) $\nu = 1.3$.

As noted in [14, 15], the uniform state system with an absolute negative conductivity is unstable due to the fact that the current–voltage characteristics with ANC has a region with negative differential conductivity of about zero field $E = 0$. This instability usually leads to the formation of the electric field domains and to the stratification of the current lines [16]. This circumstance, according to [17, 18], allows us to assume that the state with zero resistance and zero conductivity are spatially inhomogeneous, and arise from the development of instability in the initial homogeneous state with ANC. Thus, due to the value of the conformal dimension, we can control the negative differential resistance, and also the CVC's form, which significantly affects the contact properties.

Additionally, we can verify the condition for the existence of terahertz signals in our system. This condition, according to [19], can be written in the following form:

$$R_N + R_C + R_A < 0, \quad (9)$$

where R_N is the negative differential resistance of the superlattice and Fermi liquid contact; R_C is the contact resistance; R_A is the radiation resistance of the antenna. According to [19], we choose $R_C = 12.9$ k Ω , $R_A = 80$ Ω . Then, in order to satisfy the condition, we have:

$$R_{kp} = R_C + R_A = 12.98 \text{ k}\Omega, \\ |R_C| > R_{kp}.$$

For all examined values of the magnetic field, this condition is satisfied; the greater the magnetic field, the smaller the negative differential resistance.

5. Conclusion

Here, we summarize our main results:

1. A method for calculating the Fermi liquid and superlattice contact CVC in the case of magnetic fields is presented.
2. In a Fermi liquid in the presence of constant magnetic field, there are regions of differential negative conductivity and absolute negative conductivity.
3. The conductivity of such contact strongly depends on the frequency of the magnetic field and also depends on the conformal dimension.

Terahertz pulses can be generated in this system for a wide range of voltage V . These pulses may have utility in a number of practical applications.

Acknowledgements

This work was supported by the Russian Foundation for Basic Research under project No. 16-32-00230 **МОЛ_а** and project No. 16-07-01265.

References

- [1] Izyumov Yu.A., Letfulov B.M., Shipitsyn E.V., Chao K.A. A theory of ferromagnetism in the Hubbard model with infinite Coulomb interaction. *Int. J. Mod. Phys.*, 1992, **6**, P. 3479–3514.
- [2] Policastro G., Son D.T., Starinets A.O. From AdS/CFT correspondence to hydrodynamics. *J. High Energy Phys.*, 2002, **9**, P. 43.
- [3] Pal Sh.S. Model building in AdS/CMT: DC conductivity and Hall angle. *Phys. Rev. D*, 2011, **84**, P. 126009.
- [4] Sachdev S. What can gauge-gravity duality teach us about condensed matter physics. *Annual Rev. Cond. Mat. Phys.*, 2012, **3**, P. 9.
- [5] Nakayama Yu.A. A lecture note on scale invariance vs conformal invariance, 2013, <http://arxiv.org/abs/1302.0884>.
- [6] Belonenko M.B., Konobeeva N.N., et al. Tunneling characteristics of a contact between a superlattice and non-Fermi liquid using the AdS/CFT correspondence. *Mod. Phys. Let. B*, 2014, **28**, P. 1450170.
- [7] Levitov L.S., Shitov A.V. *Green's functions. Problems with solutions*, Moscow: Fizmatlit, 2003, 392 p.
- [8] Belonenko M.B., Mescheryakova N.E. Electromagnetic solitons in a system of quantum dots with taking into account the Hubbard interaction. *J. Rus. Las. Res.*, 2008, **29**, P. 544.
- [9] Witten E. Anti-de Sitter space and holography. *Adv. Theor. Math. Phys.*, 1998, **2**, P. 253.
- [10] Kulaxizi M., Parnachev A. Comments on Fermi Liquid from Holography. *Phys. Rev. D*, 2008, **78**, P. 086004.
- [11] Kulaxizi M., Parnachev A. Holographic Responses of Fermion Matter. *Nucl. Phys. B*, 2009, **815**, P. 125.
- [12] Charmousis C., Gouteraux B., et al. Effective Holographic, Theories for low-temperature condensed matter systems. *J. High Energy Phys.*, 2010, **1011**, P. 151.
- [13] Hartnol S.A. Quantum critical dynamics from black holes, 2010, <http://arxiv.org/abs/0909.3553v2>.
- [14] Gladun A.D., Ryzhij V.I. Absolute negative conductivity mechanism of the thin films in quantizing transverse field. *JETP Lett.*, 1969, **57**, P. 978.
- [15] Ignatov .A., Romanov Yu.A. Absolute negative conductivity in semiconductor with superlattice. *Radiophys. Quant. Electr.*, 1978, **21**, P. 90.
- [16] Volkov A.F., Kogan Sh.M. Physical phenomena in semiconductors with negative differential conductivity. *UFN*, 1968, **96**, P. 633.
- [17] Andreev A.V., Aleiner I.L., Millis A.J. Dynamical symmetry breaking as the origin of the zero-dc-resistance state in an ac-driven system. *Phys. Rev. Lett.*, 2003, **91**, P. 056803.
- [18] Bergeret F.S., Huckestein B., Volkov A.F. Current-voltage characteristics and the zero-resistance state in a two-dimensional electron gas. *Phys. Rev. B*, 2003, **67**, P. 241303(R).
- [19] Dragoman D., Dragoman M. Terahertz oscillations in semiconducting carbon nanotubes resonant-tunneling diodes. *Physica E*, 2004, **24**, P. 282–289.

Development of an orbital-free approach for simulation of multi-atomic nanosystems with covalent bonds

V. G. Zavodinsky¹, O. A. Gorkusha²

¹Institute for Material Science, 153 Tikhookeanskaya str., 680042 Khabarovsk, Russia

²Institute of Applied Mathematics, 54 Dzerzhinskogo str., 680000 Khabarovsk, Russia

vzavod@mail.ru, o_garok@rambler.ru

PACS 03.65.-w

DOI 10.17586/2220-8054-2016-7-3-427-432

On the example of the three-atomic clusters Al₃, Si₃, and C₃, it is shown that an orbital-free version of the density functional theory may be used for finding equilibrium configurations of multi-atomic systems with both metallic and covalent bonding. The equilibrium interatomic distances, interbonding angles and binding energies are found to be in good agreement with known data.

Keywords: Orbital-free, density functional, covalent bonding, angle dependence.

Received: 9 November 2015

Revised: 17 December 2015

1. Introduction

A number of works (for instance [1–8]) have been devoted to the development of the orbital-free (OF) version of the density functional theory (DFT) [9–13] over the last few years. This approach, in contrast to the Kohn–Sham (KS) method, does not use the wave functions (orbitals) and operates with the only electron density. The OF approach is the result of further development of the ideas of Hohenberg–Kohn [10]; i.e., that the basic state of a quantum system can be completely described by means of electronic density. There has been significant progress in the description of diatomic systems [8, 14, 15] and simple crystals [16]. However, an essential hindrance to further development of the OF method is the fact that the electronic density of a single (isolated) atom is spherical, i.e. the “orbital-free” atom has a shape of a ball, but balls form the close packed structures. For example, three identical atoms are obliged to form an equilateral triangle with corners of 60 degrees. At the same time, it is known that three atoms of silicon form an isosceles triangle with the main corner of about 80 degrees [17], atoms of carbon build a linear chain [18], and atoms of aluminum really behave like balls – they form a correct equilateral triangle [19]. The present work is an attempt to develop a technique which would allow us to adequately describe the geometry of interatomic bonds in polyatomic systems within the OF approach.

2. A general description of the OF approach

As is well-known the DFT claims that the energy E_{el} of the ground state of any quantum system can be found by minimization of some function which depends only on the electronic density of this system ρ :

$$E_{el}[\rho] = E_{kin}[\rho] + E_{ex}[\rho] + E_c[\rho] + E_H[\rho] - \int V_{ext}(\mathbf{r})\rho(\mathbf{r})d^3\mathbf{r}, \quad (1)$$

where V_{ext} is an external potential, E_{kin} is kinetic energy, E_{ex} is exchange energy, E_c is correlation energy, and E_H is Hartree energy:

$$E_H[\rho] = \frac{1}{2} \int \frac{\rho(\mathbf{r})\rho(\mathbf{r}')}{|\mathbf{r} - \mathbf{r}'|} d^3\mathbf{r}d^3\mathbf{r}'.$$

The total energy E_{tot} is given by integral:

$$E_{tot} = \int E_{el}[\rho(\mathbf{r})]d^3\mathbf{r}. \quad (2)$$

Minimization of (1) with the condition $\int \rho(\mathbf{r})d^3\mathbf{r} = N$ means solving the following equation:

$$\frac{\delta E_{el}[\rho]}{\delta \rho} - \mu = 0, \quad (3)$$

where μ is the Lagrange parameter gives one a sense of the electron chemical potential.

Introducing $F[\rho] = \frac{\delta E_{el}[\rho]}{\delta \rho} - \mu$, we obtain the equation:

$$F[\rho] \equiv -V_{ext}(\mathbf{r}) + \varphi(\mathbf{r}) + \mu_{kin}(\rho) + \mu_{ex}(\rho) + \mu_c(\rho) - \mu = 0, \quad (4)$$

where $\varphi(\mathbf{r}) = \int \frac{\rho(\mathbf{r}')}{|\mathbf{r} - \mathbf{r}'|} d^3\mathbf{r}'$, $\mu_{kin}(\rho) = \frac{\delta E_{kin}[\rho]}{\delta \rho}$, $\mu_{ex}(\rho) = \frac{\delta E_{ex}[\rho]}{\delta \rho}$, $\mu_c(\rho) = \frac{\delta E_c[\rho]}{\delta \rho}$.

There are some realistic approximations for exchange $\mu_{ex}(\rho)$ and correlation $\mu_c(\rho)$ potentials; the potential of the electron-electron repulsion $\varphi(\mathbf{r})$ may be calculated using Fourier transformations or Poisson equations; the external potential $V_{ext}(\mathbf{r})$ usually consists of atomic potentials or of pseudopotentials. The key problem is to find the potential of kinetic energy $-\mu_{kin}(\rho)$. In the Kohn–Sham approach, this problem is absent because the kinetic energy is calculated using electron orbitals (wave functions).

Quantum mechanical pseudopotentials are usually constructed for different angular states. Thus, we have to present the total density as a sum of partial densities:

$$\rho = \rho_s + \rho_p + \rho_d + \dots \quad (5)$$

For the s - p case, we may write the equations:

$$\begin{aligned} F_s[\rho_s, \rho] &\equiv -V_s(\mathbf{r}) + \varphi(\mathbf{r}) + \mu_{kin}^s(\rho_s) + \mu_{ex}(\rho) + \mu_c(\rho) - \mu_s = 0, \\ F_p[\rho_p, \rho] &\equiv -V_p(\mathbf{r}) + \varphi(\mathbf{r}) + \mu_{kin}^p(\rho_p) + \mu_{ex}(\rho) + \mu_c(\rho) - \mu_p = 0, \end{aligned} \quad (6)$$

where $V_s(\mathbf{r})$ and $V_p(\mathbf{r})$ are the s , p components of atomic pseudopotential. The electrostatic potential $\varphi(\mathbf{r})$, exchange and correlation potentials $\mu_{ex}(\rho)$ and $\mu_c(\rho)$ are calculated through the total density ρ while partial kinetic potentials $\mu_{kin}^s(\rho_s)$ and $\mu_{kin}^p(\rho_p)$ depend on corresponding partial densities ρ_s and ρ_p .

As designing of pseudopotentials is followed by the finding of equilibrium pseudo-wave functions, it is always possible to calculate partial densities of the isolated atom $\rho_s(\mathbf{r})$ and $\rho_p(\mathbf{r})$, as well as its full equilibrium electronic density $\rho(\mathbf{r}) = \rho_s(\mathbf{r}) + \rho_p(\mathbf{r})$. If we know the type of these functions we could calculate energy E_{kin} and find the total energy of a single atom using Eq. (2). However, there is no basis to believe that there are some functions for kinetic functional and energy, which could be used for atoms of any type and any quantity. Moreover, as it was recently shown [20], the Hohenberg–Kohn idea about the existence of a universal density functional leading to the energy minimum was not strictly proved, and it is possible to say only about approximate solutions for the problem. However, in our case, the problem consists not in finding of the energy of a single atom (this can be done in more traditional ways), but in calculation of the energy of the interatomic interaction, and in finding the geometry of the polyatomic system corresponding to this interaction.

3. From dimers to trimers: a role of quantum rules and restrictions

3.1. Dimers

For simplicity, we will consider dimers consisting of atoms of one type. The elementary approach for the electronic density of such dimer ρ_{dim} is the sum of densities of the atoms:

$$\rho_{dim}(\mathbf{r}) = \rho_{at}(\mathbf{r} - \mathbf{R}_A) + \rho_{at}(\mathbf{r} - \mathbf{R}_B), \quad (7)$$

where \mathbf{R}_A and \mathbf{R}_B are coordinates of points in which the A and B atoms with densities ρ_{at} are situated.

Then, the binding energy (per one atom) would be calculated as follows:

$$E_b = \frac{1}{2} (E_{dim} - 2E_{at}), \quad (8)$$

where $E_{at} = E_{at}^{tot} = \int E^{el}[\rho_{at}(\mathbf{r})] d^3\mathbf{r}$,

$$E_{dim} = \int E^{el}[\rho_{dim}(\mathbf{r})] d^3\mathbf{r} + \frac{Z_A Z_B}{|\mathbf{R}_A - \mathbf{R}_B|}, \quad (9)$$

Z_A and Z_B are the positive charges of atomic cores equal to absolute values of charges of valence electrons.

We took Al, Si, and C as test elements (for the reasons stated above: trimers of these elements have essentially different geometric configurations). For all three elements we accepted the following function $\mu_{kin}(\rho)$ as the universal function for s - and p -states and:

$$\mu_{kin}(\rho) = 0.9\rho^{1/3} - 15\rho^2. \quad (10)$$

We used the FHI98pp [21] package as a generator of pseudo-potentials. We calculated exchange and correlation potentials in the local density approach [19, 20]. The studied atoms were located in a cubic cell of the L size

TABLE 1. Equilibrium distances d and binding energies E_b (absolute values, per atom) for Si_2 , Al_2 and C_2 in comparison to known calculated data

Dimer	Source of data	d , Å	E_b , eV
Si_2	Our method	2.1	2.0
	Other calculations	2.23 ^a	1.97 ^a
		2.21 ^b	1.599 ^b
Al_2	Our method	2.4	1.2
	Other calculations	2.46 ^c	1.0 ^d
		2.95 ^e	1.23 ^e
C_2	Our method	1.3	4.8
	Other calculations	1.247 – 1.367 ^f	4.7 ^f
		1.316 ^g	3.5 ^g

Notations: ^a [17], ^b [25], ^c [23], ^d [19], ^e [27], ^f [28], ^g [29]

($L = 52$ a.u.; 1 a.u. = 0.529 Å). The cell was divided into $128 \times 18 \times 128$ elementary sub-cells for the integration with the integration step ΔL of 0.406 a.u. Results of calculations were compared to the published data.

Calculated values of interatomic distances and binding energies for the Al_2 , Si_2 , and C_2 dimers are collected in Table 1 in comparison with known published data. It is clear that agreement is rather good.

3.2. Trimers

To describe the angle dependence of interatomic bonding, we must analyze the reasons for this dependence in the standard quantum-mechanical approach, which uses wave functions and electronic states. For example, it is specified in the work [24] that the angle peculiarities of a cluster Si_3 are defined by the Yang–Teller effect, which is caused by the existence of an energy gap between the occupied and empty states. In other words, the differences in semiconductor and metal small cluster structures are connected with the difference of their bond wave functions: namely, covalent atoms have localized functions oriented between nearest atoms, while metallic atoms have dispersed functions without spatial orientation.

In our case, both wave functions and electronic states are absent, and therefore, we cannot speak about any energy gap. In the OF approach, we deal only with the electronic density which defines all energies and structures of the polyatomic system. However, the main quantum-mechanical rules still remain fair in this case. Besides the Schrödinger's (or Kohn–Sham) equations, out of which wave functions and electron states arise, we must not forget Pauli's principle which specifies that in one quantum state there can be only two electrons (without taking into account spin). In our case, this principle may be paraphrased in the following way: a covalent bond is formed by two electrons, the common wave function of which is localized in the space between two nearest atoms. It is obvious that the quantity of the electrons which are responsible for this bond doesn't change as the distance between atoms changes (if, of course, the bond isn't broken at all and the electronic structure isn't completely reconstructed). In the case of metals, the conduction states are close each other and electrons can easily “flow” from one state to another during the changing of atomic geometry.

The above-mentioned concepts may be reformulated in the language of the electronic density: the density integral (n_{int}) between atoms with covalent bonding, has to remain its value with a change of distance between atoms; in the case of metal bonding, the integral n_{int} can have any possible value.

Certainly, there is a question: on what space do we have to provide integration, and what do we have to do with intermediate cases, with atoms of different types? We will leave these questions for the future, and now we will try to explain the differences in the structures of covalent and metal systems using the following homogeneous clusters Al_3 , Si_3 and C_3 as examples.

It is obvious that the space of integration has to be rather local, and at the same time, it has to give us the information on quantity of the electrons included in a covalent bond. In the present work we used the space having a shape of the slab situated between two nearest atoms (Fig. 1) and oriented perpendicularly to the plane in which the trimer triangle is placed. The thickness of a slab was taken as $2\Delta L$. As the number of the integration points can be changed with a change in the trimer configuration, the value of n_{int} was normalized to one point.

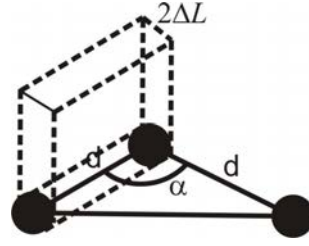


FIG. 1. The scheme for the arrangement of atoms in a trimer. Dashed lines show the space on which the electronic density is integrated for definition the number of the electrons involved in the covalent bond; α is a corner between bonds with identical lengths of d

The electronic density of the trimer ρ_{trim} may be found as follows:

$$\rho_{trim}(\mathbf{r}) = \rho_{at}(\mathbf{r} - \mathbf{R}_A) + \rho_{at}(\mathbf{r} - \mathbf{R}_B) + \rho_{at}(\mathbf{r} - \mathbf{R}_C), \quad (11)$$

where \mathbf{R}_A , \mathbf{R}_B , and \mathbf{R}_C are coordinates of points in which the A , B , and C atoms with densities ρ_{at} are situated. The binding energy is:

$$E_b = \frac{1}{3} (E_{trim} - 3E_{at}), \quad (12)$$

where

$$E_{trim} = \int E^{el}[\rho_{trim}(\mathbf{r})]d^3\mathbf{r} + \frac{Z_A Z_B}{|\mathbf{R}_A - \mathbf{R}_B|} + \frac{Z_A Z_C}{|\mathbf{R}_A - \mathbf{R}_C|} + \frac{Z_B Z_C}{|\mathbf{R}_B - \mathbf{R}_C|}, \quad (13)$$

Z_A and Z_B are the positive charges of atomic cores equal to absolute values to charges of valence electrons.

Let us take the interatomic bond in a dimer as a standard. Let us call the value $P = \frac{n_{int}^{trimer}}{n_{int}^{dimer}}$ (the relation of n_{int} of trimer to n_{int} of dimer) as “the bonding strength” and accept that for covalent bonds, the value of P shouldn’t exceed 1.0 with a change of distance between atoms. For metallic bonds, P can have any possible value.

Calculated values P for clusters Al_3 , Si_3 , and C_3 are presented in Fig. 2 as functions of the angle between interatomic bonds in the case when restrictions on these values are absent. For each angle, we found the values of interatomic distances, which corresponded to the minimum of the total energy of the cluster. One can see that P is approximately 1.0 at $\alpha = 180^\circ$ and increases when α approaches 60° . The maximum value ($P = 1.40$) is observed for carbon, which has the smallest interatomic distances. Interatomic distances in aluminum and silicon are approximately the same, therefore it should come as no surprise that the “bonding strengths” for the Al_3 and Si_3 trimers are approximately equal.

We repeated the calculations using thicker slabs ($4\Delta L$ and $8\Delta L$) for integration of $n_{int}(\text{dimer})$ and $n_{int}(\text{trimer})$ values between atoms in dimers and trimers and we found that results changed by no more than by 2 per cent.

In Figure 3 (curve A), we present the results for calculations of binding energies for the Al_3 , Si_3 and C_3 trimers without restriction of the “bonding strengths”. From these curves it is clear that in all three cases, the maxima of the binding energy (on the absolute value) correspond to triangular clusters, “bonding strengths” in which significantly exceed the corresponding values, characteristic for linear chains. This result looks natural for aluminum as its states have the metallic, not localized character; but for the clusters of Si_3 and C_3 having covalent bonds it is necessary to introduce restrictions on values of P stipulated above. We have taken into account this condition ($P = 1$) and found dependences of the binding energy on the angle between bonds in the Si_3 and C_3 clusters (Fig. 3, curve B). One can see that atoms of carbon seek to form linear chains, while for silicon, neither a linear chain, nor an equilateral triangle is energetically favorable; atoms of silicon prefer to form an isosceles triangle with the angle α of 80 degrees.

Equilibrium values for interatomic distances d , angles α , and binding energies E_b for the trimers Al_3 , Si_3 , and C_3 are collected in Table 2 (calculated for the condition $P = 1$) in comparison with known data. One can see that comparison is good. Thus, we showed that an orbital-free approach is capable of correctly describing the orientations of interatomic bonds in atomic clusters, as well as values of interatomic distances and binding energies.

Certainly, it is interesting to compare our results for interatomic densities with results of standart DFT-KS calculations. For this purpose, we calculated “bonding strenghts” P for Si_3 and Al_3 using the popular DFT-KS code FHI96md [31] for the same triangles as were studied above. We have found that P were equal 1 (± 0.02) for all cases for Si_3 , but it increased up to 1.3 for the Al_3 equilateral triangle. These results are in excellent agreement with ours.

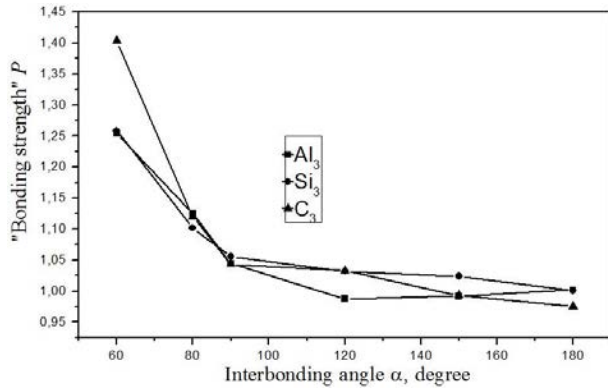


FIG. 2. “The bonding strengths” in the Al_3 , Si_3 and C_3 trimers as functions of the corner between interatomic bonds in the case when there are no restrictions on the interatomic electron density

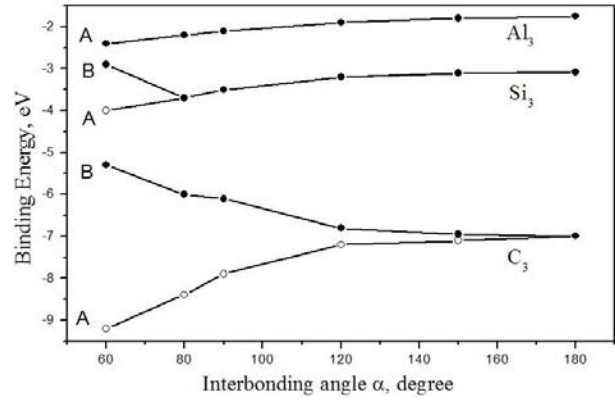


FIG. 3. Calculated dependence of binding energy (on atom) on the angle between interatomic bonds for the Al_3 , Si_3 and C_3 trimers. A) Values are obtained without restrictions on electronic density in interatomic bonds; B) values calculated with the condition $P = 1.0$

TABLE 2. Equilibrium distances d , angles α and binding energies E_b (absolute values, per atom) for Si_3 , Al_3 and C_3 in comparison with known calculated data

Trimer	Source of data	α , deg	d , Å	E_b , eV
Si_3	Our method	≈ 80	2.1	3.7
	Other calculations	77.8 ^a	2.26 ^b	2.51 ^b
		78.10 ^c	2.177 ^c	2.93 ^d
		79.6 ^e		
Al_3	Our method	60	2.3	2.4
	Other calculations	60 ^f	2.50 ^f	1.74 ^g
		60 ^h	2.55 ^h	1.96 ^f
C_3	Our method	180	1.2	7.0
	Other calculations	180 ⁱ	1.29 ^j	6.8 ⁱ
		180 ^k	1.3 ^k	5.0 ^l
		1.316 ^l		

Notations: ^a [17], ^b [25], ^c [30], ^d [31], ^e [32], ^f [27], ^g [19], ^h [33], ⁱ [18], ^j [30], ^k [28], ^l [29]

4. Conclusion

We showed that the use of the restriction principle for the interatomic density (following from Pauli’s principle) allows us to correctly describe the angular dependences of the interatomic bonding in polyatomic clusters within the orbital-free version of the density functional theory. In particular, it is possible to show that for the Al_3 cluster, the equilateral triangle is favorable; the Si_3 trimer is characterized by an isosceles triangle with angles of 80 and 50 degrees, and the three atoms of carbon are present as a linear chain. Calculated equilibrium interatomic distances and binding energy values are in fair agreement with known data. As the problem of correctly describing the angles between interatomic bonds is a key point in the modeling of polyatomic systems, it is possible to consider that our work opens a direct way to design an effective method for modeling of big nanosystems and supermolecules.

We have to note that the consideration which is carried out above is directly applicable only to the systems consisting of identical atoms and requires a special development for application to more complicated systems.

References

- [1] Wang Y.A., Carter E.A. Orbital-free kinetic-energy density functional theory. In: *Progress in Theoretical Chemistry and Physics*, Kluwer, Dordrecht, 2000, 117 p.
- [2] Huajie Chen, Aihui Zhou. Orbital-Free Density Functional Theory for Molecular Structure Calculations. *Numerical Mathematics: Theory, Methods and Applications*, 2008, **1**, P. 1–28.
- [3] Baojing Zhou, Ligneris V.L., Carter E.A. Improving the orbital-free density functional theory description of covalent materials. *Journal Chemical Physics*, 2005, **122**, P. 044103–13.
- [4] Karasiev V.V., Trickey S.B. Issues and challenges in orbital-free density functional calculations. *Computational Physics Communications*, 2012, **183**, P. 2519–2527.
- [5] Karasiev V.V., Chakraborty D., Shukruto O.A., Trickey S.B. Nonempirical generalized gradient approximation free-energy functional for orbital-free simulations. *Physical Review B*, 2013, **88**, P. 161108–13(R).
- [6] Wesolowski T.A. Approximating the kinetic energy functional $T_s[\rho]$: lessons from four-electron systems. *Molecular Physics*, 2005, **103**, P. 1165–67.
- [7] Hung L., Carter E.A. Accurate Simulations of Metals at the Mesoscale: Explicit Treatment of 1 Million Atoms with Quantum Mechanics. *Chemical Physics Letters*, 2009, **475**, P. 163–170.
- [8] Zavodinsky V.G., Gorkusha O.A. Quantum-Mechanical Modeling without Wave Functions. *Physics of the Solid States*, 2014, **56** (11), P. 2329–35.
- [9] Kohn W., Sham J.L. Self-Consistent Equations including Exchange and Correlation Effects. *Phys. Rev. A*, 1965, **140**, P. 1133–38.
- [10] Hohenbeg H., Kohn W. Inhomogeneous Electron Gas. *Physical Review B*, 1964, **136**, P. 864–871.
- [11] Sivasathya S., Thiruvadigal D.J. The effects of defects on electron transport in metallic single wall carbon nanotubes. *Nanosystems: physics, chemistry, mathematics*, 2013, **4** (3), P. 405–408.
- [12] Hariharan R.M., Thiruvadigal D.J. Effect of anchoring atoms on transport properties of a carbon-dimer based molecular junctions: a first principles study. *Nanosystems: physics, chemistry, mathematics*, 2013, **4** (2), P. 294–298.
- [13] Polyakov E.A., Vorontsov-Velyaminov P.N. Exact classical stochastic representations of the many-body quantum dynamics. *Nanosystems: physics, chemistry, mathematics*, 2015, **6** (4), P. 501–512.
- [14] Junchao Xia, Chen Huang, Ilgyou Shin, Carter E.A. Can orbital-free density functional theory simulate molecules? *The Journal of Chemical Physics*, 2012, **136**, 084102(13).
- [15] Zavodinsky V.G., Gorkusha O.A. New Orbital-Free Approach for Density Functional Modeling of Large Molecules and Nanoparticles. *Modeling and Numerical Simulation of Material Science*, 2015, **5**, P. 39–46.
- [16] Carling K.M., Carter E.A. Orbital-free density functional theory calculations of the properties of Al, Mg and Al–Mg crystalline phases. *Modelling and simulation in materials science and engineering*, 2003, **11**, P. 339–348.
- [17] Raghavachari K., Logovinsky V. Structure and bonding in small silicon clusters. *Phys. Rev. Lett.*, 1985, **55**, P. 2853–2856.
- [18] Van Orden A., Saykally R.J. Small carbon clusters: spectroscopy, structure, and energetics. *Chemical Review*, 1998, **98**, P. 2313–57.
- [19] Feng-Chuan Chuang, Wang C.Z., Ho K.H. Structure of neutral aluminum clusters Al_n ($2 \leq n \leq 23$): Genetic algorithm tight-binding calculations. *Phys. Rev. B*, 2006, **73**, 125431(7).
- [20] Sarry A.M., Sarry M.F. To the density functional theory. *Physics of Solid State*, 2012, **54** (6), P. 1315–22.
- [21] Fuchs M., Scheffler M. Ab initio pseudopotentials for electronic structure calculations of poly-atomic systems using density-functional theory. *Computational Physics Communications*, 1999, **119**, P. 67–98.
- [22] Perdew J.P., Zunger A. Self-interaction correction to density functional approximation for many-electron systems. *Physical Review B*, 1981, **23**, P. 5048–79.
- [23] Ceperley D.M., Alder B.J. Ground state of the electron gas by a stochastic method. *Physical Review Letters*, 1980, **45**, P. 566–569.
- [24] Tomanek D., Schluter M.A. Structure and bonding of small semiconductor clusters. *Phys. Rev. B*, 1987, **36**, P. 1208–17.
- [25] Mukhtarov A.P., Normurodov A.B., Sulaymonov N.T., Umarova F.T. Charge States of Bare Silicon Clusters up to Si₈ by Non-Conventional Tight-Binding Method. *Journal of nano- and electronic physics*, 2015, **7**, 01012(7).
- [26] Nayak S.K., Khanna S.N., Jena P.J. Evolution of bonding in Al_nN clusters: A transition from nonmetallic to metallic character. *Physical Review B*, 1998, **57**, P. 3787–90.
- [27] Matnez A., Vela A. Stability of charged aluminum clusters. *Physical Review B*, 1994, **49**, 17464(4).
- [28] Karton A., Tarnopolsky A., Martin J.M.L. Atomization energies of the carbon clusters C_n ($n = 2 - 10$) revisited by means of W4 theory as well as density functional, Gn, and CBS methods. *International Journal of Interface between Chemistry and Physics*, 2009, **107**, P. 977–1003.
- [29] Afshar M., Babaei M., Kordbacheh A.H. First principles study on structural and magnetic properties of small and pure carbon clusters (C_n , $n = 2 - 12$). *Journal of Theoretical and Applied Physics*, 2014, **8**, P. 103–108.
- [30] McCarthy M.C., Thaddeus P. Rotational spectrum and structure of Si₃. *Physical Review Letters*, 2003, **90**, 213003(4).
- [31] Liu B., Lu Z.Y., et al. Ionization of medium-sized silicon clusters and the geometries of the cations. *Journal of Chemical Physics*, 1998, **109**, P. 9401–09.
- [32] Raghavachari K., Rohlfing C.M. Bonding and stabilities of small silicon clusters: A theoretical study of Si₇–Si₁₀. *Journal of Chemical Physics*, 1988, **89**, P. 2219–34.
- [33] Tse J.S. Electronic structure of the dimer and trimer of aluminium. *Theoretical Chemistry (Journal of Molecular Structures)*, 1988, **165**, P. 21–24.
- [34] Beckstedte M., Kley A., Neugebauer J., Scheffler M. Density functional theory calculation for poly-atomic systems: electronic structure, static and elastic properties and ab initio molecular dynamics. *Computational Physics Communications*, 1997, **107**, P. 187–205.

The use of transient electrolysis in the technology of oxide composite nanostructured materials: review

Zh. I. Bespalova, A. V. Khramenkova

Platov South-Russia State Polytechnical University (NPI), Novocherkassk, Russia

anna.vl7@yandex.ru

PACS 81.15.-z

DOI 10.17586/2220-8054-2016-7-3-433-450

The available experimental material relating to the patterns of formation and properties of functional nanostructured transition metal oxide (Mo, Co, Mn, Ni, Fe, V) composite materials is reviewed. Advanced coatings are considered those whose formation method are simple and do not require high energy costs, expensive equipment and permit the creation of materials with desired physical and chemical properties in a specified manner. In this review, the priority of oxide composite nanostructured materials technology is given to a transient electrolysis method based on the analysis of a data set that demonstrates its advantages. The results are presented for a number of studies aimed at identifying and analyzing the nature and regularities of processes that take place when obtaining oxide composite nanostructured materials using transient electrolysis methods.

Keywords: asymmetric alternating current, composite oxide nanostructured coatings, optically selective coatings, catalytically active oxide composite coatings, metal oxides, electrolyte, solution, asymmetry parameter.

Received: 9 December 2015

1. Introduction

The research related to the enhancement of existing technologies for producing coatings and their simplification is aimed primarily at finding the most cost-efficient procedures.

Transient electrolysis, which uses periodically alternating (symmetric, asymmetric and pulsed) currents, should be referred to in such discussions. There are several data that point out the advantages for the deposition of coatings using an asymmetrical alternating current [1–3]. The successful use of current without previous rectification is undoubtedly worthwhile. The appropriate alternating current enables the deposition of coatings at lower temperatures, making the process more energy-efficient because of the possibility of using lower voltages. This increases the rate of electrolysis and, respectively, the process productivity, allowing one to change the physical and chemical properties of coatings by varying a wide range of electrolysis parameters (current density, composition and concentration of electrolyte components), and to obtain more dense and fine coatings as well as to increase the upper limit of working current density and to reduce internal stress in a coating, i.e. allows coating property regulation by a purely electrical method. Coatings that are obtained using an alternating polarity current differ from those obtained by a direct current method in microstructure, porosity, surface purity and mechanical properties.

Transient regimes, however, are considered worse as compared to conventional ones and consequently, are used much more rarely.

This is explained by the fact that transient processes are considerably more complicated than stationary ones, because both cathodic and anodic electrode reactions proceed under the periodic changes of an electrical flow and then transient processes occur.

To date, in the area of transient electrolysis, much research has been done [4–12], many factors which affect these processes have been discovered. All this gives one reason to consider it worthwhile to use an asymmetrical current in electrochemical productions.

Accumulated experimental data [13–17] show that in many cases transient electrolysis allows one to achieve effects that either cannot be achieved using a direct current or can be achieved in a much more complicated fashion. The ability to affect an electrochemical process more efficiently and flexibly due to the change of a mode and frequency variation of amplitudes for both anodic and cathodic current pulses is an undeniable advantage for transient electrolysis.

Electrochemical synthesis using a line-frequency alternating current allows one to obtain a number of metal oxides [18–21]. When using an alternating current, Dolinina et al. [22] obtained a copper-cadmium oxide system in a solution of a sodium hydroxide, and determined that in the presence of copper, the rate of cadmium oxidation rose 2- to 3-fold. Thus, predicting the operating parameters of copper electrolysis, one can obtain cadmium oxide systems of a prescribed composition. The asymmetric alternating current was successfully applied to obtain films

of barium titanate (BaTiO_3) from an aqueous suspension in the presence of 0.5 mass% polyvinyl alcohol using an electrophoresis method [23].

Under the influence of an alternating current, Jagminas et al. [24] precipitated bismuth oxide in the pores of aluminium, the size of its particles being 5 – 100 nm. The high-frequency alternating current allowed the impregnation of a nanostructured cadmium selenide (CdSe) in anodic aluminum oxide pores [25]. The development of such nanocomposite materials, including metamaterials [26] is very promising for applications in electronic, optical and magnetic devices [26,27]. Nano-scale particles of a cerium oxide (CeO_2) were obtained [28] from 0.1 M $\text{Ce}(\text{NO}_3)_2$ aqueous solution under polarization using an alternating current on the surface of a platinum electrode, the size of a particle being regulated by electrolysis conditions (pH and component electrolyte composition, temperature, current density), which set this method apart from other precipitation [29,30], pyrolysis [31], hydrothermal [32–36] and sonochemical [37–39] synthetic methods. Nanostructured coatings based on titanium oxide were obtained as a result of electrophoretic deposition under the influence of an asymmetrical alternating current [16]. This method also has a number of advantages compared to other widely-used nanocrystal titanium dioxide methods [40–45]. It should be noted that the use of an asymmetric alternating current for these purposes allowed suppression of gas bubble formation due to the absence of electrolysis of water on electrodes, and obviated the need for using organic stabilizers in the electrolyte-suspension. The electrophoretic coatings using an asymmetric alternating current thus was shown to be favorable both environmentally and economically.

Because the use of an alternating current suggests a whole number of electrode reactions and the change of electrode capacity occurs under conditions which are far from an equilibrium state, the formation of metal oxide products having different degrees of oxidation with defective structure are predetermined. The cyclicity of the polarizing voltage leads to two consecutive processes on the surface of an electrode: the first one is the formation of oxide phases in an anodic current half-cycle, and the second one is the discharge of protons, hydrogen being emitted in a cathodic current half-cycle. Thus, the alternating current allows one to influence the most important property of oxide films, i.e. their porosity.

To obtain composite materials on the basis of metal oxides deposited from aqueous solutions of their salts under polarization using an asymmetric alternating current is equally promising, but still somewhat unexplored. The formation of such composite materials relates to the area of nanotechnologies and nanomaterials because the substance of a matrix of a composite material is finely dispersed. Such systems, compared with similar monolithic objects, have specific and in some cases unique physical and chemical properties.

In recent years there has been increased interest in composite materials based on polymer matrix with nano-sized metal oxide particles [46–53]. This is due to their wide application ranging from membranes, catalysts to constructive materials and materials that are used in information technology. So, methods of synthesis of nanoparticles and nanostructures play an important role while determining their quality characteristics. Among the methods for nanoparticle and nanostructure synthesis, [54–71] electrochemical methods have not been thoroughly explored. At the same time, the use of electrochemical methods to obtain nanoparticles and nanostructured materials is very attractive, as they do not require complex equipment, they are easy and economical compared to other methods, and in some cases they allow one to obtain oxide films of specified morphology and composition by controlling the composition of electrolyte and electrolysis modes.

The transient electrolysis allows the formation of coatings which differ in their properties from similar ones that are formed using a direct current due to the cycling of surface layers, irreversibility of electrode reactions of oxidation and reduction.

This method gives tremendous opportunities to control electrode processes by current modes and allows the deposition of nanostructured coatings on substrates of various chemical natures and geometries.

A significant contribution to the development of transient electrolysis as a research area of technical electrochemistry was made at the Novochoerkassk electrochemical school [72–81].

In works [72, 73], the behaviors of a number of metals (platinum, nickel, iron, silver, gold, lead, cobalt and others) were studied in alkaline and neutral solutions during transient electrolysis, and the mechanism of their destruction was determined. Additionally, a whole series of works on an accelerated charge, the formation of alkaline accumulators and the definition of their degree of charge was carried out. [72, 73].

The development of directed synthetic methods for new composite materials on the basis of transition metal oxides is one of the promising directions in modern science. The wide interest in composite materials on the basis of Mo, Co, Ni, Fe, V oxides is determined by the complexity of areas of their use: as catalytically active materials, sensor, solion, photo and electrocatalytic devices, solid-phase converters of light energy and anti-corrosion materials.

2. Composite oxide materials

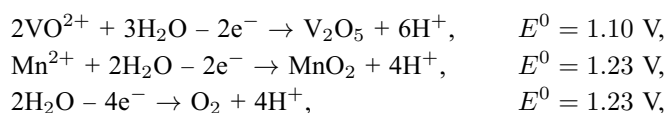
Metal oxidation is one of most widely used methods of metal corrosion protection. In this case the oxide film is formed, mainly, due to oxidation of a substrate material during its anodic polarization. However, the electrochemical synthesis of complex oxide materials by anodic deposition from mixed aqueous solutions of salts of co-precipitated metals is of great interest [82,83]. The positive aspect of electrolytic synthesis is the opportunity to obtain homogeneous structured systems which components (unlike conventional mechanical mixtures) can interact at a molecular level and have higher electrochemical characteristics. Legagneur et al. [84] showed that complex vanadium-manganese oxides, which are obtained by electrolytic deposition from aqueous solutions, have higher electrochemical activity in comparison to the individual components.

2.1. Electrolytic composite oxide materials

The interest in composite oxide coatings is largely a result of the potential to obtain composite materials on their basis and the opportunity to develop thin film ballastless cathodes of lithium cells by direct deposition of oxide material as a compact coating on a conductive substrate [85–87].

Nagirnyj et al. [88] found that during electrolysis, vanadium and manganese oxides codeposit as the $V_2O_5 - MnO_2$ double oxide system from mixed aqueous solutions containing the ions VO^{2+} and Mn^{2+} .

The kinetics of these processes are largely determined by concurrent oxidation and reduction reactions between ions involved in an electrode process and products of anodic oxidation formed during different stages. Comparison of the standard electrode potentials for reactions occurring on electrodes show that their values are close [89].



Therefore, the above oxidation and reduction reactions can occur at intermediate and final stages of an anodic process when shifting equilibrium to one or another direction due to changes of the ratio of concentrations of original components.

In [90], complex binary systems were obtained as a result of electrolytic codeposition of oxides of manganese, cobalt, nickel, and chromium from mixed aqueous solutions of salts of codeposited metals under different electrolytic conditions. Electrodeposition was carried out on anodes made of Type 12189 (12H12N9T) stainless steel at $j_a = 7.5 - 25.0 \text{ mA}\cdot\text{cm}^{-2}$ and 85°C . The presence of a basal oxide which can be deposited by itself on an anode having quite a high yield, for example, oxides of manganese and cobalt, is a necessary condition for electrolytic synthesis of such materials.

Nagirnyj et al. [91] reported that during electrolytic deposition of cobalt(III) oxide in the presence of nickel(II) and chromium(III) ions from aqueous sulfate solutions the Co – Ni and Co – Cr. complex binary oxide systems are deposited on the anode. The most favorable conditions for quantitative deposition of oxides on an anode are achieved at $80 - 85^\circ\text{C}$, pH 2.5 – 3.0 and an anodic current density $j_a = 10 \text{ mA}\cdot\text{cm}^{-2}$.

The anodic deposition of a vanadium oxide from vanadium(IV) oxide sulfate solutions in the presence of nickel ions results in the formation of complex vanadium-nickel oxide systems, which are characterized by increased electrochemical activity [92]. To obtain anodic deposits as V-Ni binary systems with the content of alloying phase 0.10 – 20 (mass.-%), the electrolysis is carried out using vanadium(IV) oxide sulfate and nickel sulfate solutions with total concentration of $40 - 45 \text{ g}\cdot\text{l}^{-1}$, at $80 - 85^\circ\text{C}$, pH 2.0 – 2.2 and $j_a = 7.5 - 10 \text{ mA}\cdot\text{cm}^{-2}$. Transition metal oxides enable one to obtain electrical materials, ranging from high resistance dielectrics to high temperature superconductors.

The possibility of obtaining molybdenum oxide both as fine deposits and as compact coatings on a surface of stainless steel and aluminum should be referred to the benefits of a method of its electrosynthesis [90,93–98]. The scientific and technological foundations for quantitatively obtaining vanadium, cobalt oxides and two-phase systems based on manganese dioxide as dispersed deposits by electrolytic anodic deposition from aqueous solutions of the corresponding salts are reviewed in work [98].

Nickel and cobalt oxides obtained by electrolytic deposition on the surface of steel from aqueous solutions [99] can be used as electrode materials [100,101], in heterogeneous catalysis [102,103] and as an active element of gas sensors [104,105].

Composite coatings based cobalt and nickel oxides are used in electrochromic devices [106]. High efficiency and super frequency dielectrics based on complexes of cobalt and nickel oxides have also been developed [107].

The kinetics for anodic processes during electrodeposition of V_2O_5 from aqueous solutions of vanadium(IV) oxide sulfate (VO_2SO_4) in the presence of Na^+ ions is considered in [108].

During the process of electrodeposition, tungsten and molybdenum oxides are able to incorporate a metal matrix (for example, nickel) with the formation of composite films which are characterized by significant wear resistance, especially in the process of mixed oxide formation [109]. Mixed oxide systems based on vanadium and molybdenum are used either as massive or supported catalysts for the partial oxidation and oxidative dehydrogenation of organic compounds [110]. These catalysts are usually obtained by igniting a mixture of oxides in air at 650 °C and higher, by their alloying [111] or by vaporization of aqueous solutions of ammonium salts of vanadium and molybdenum with their subsequent thermolysis [112]. Such methods for obtaining catalysts are very time-consuming. At the same time, the use of an electrochemical method to obtain such oxide systems is very attractive because it does not require complex equipment; it is simple, economical unlike other methods, and in some cases it allows one to obtain oxide coatings with specified composition by controlling the electrolyte composition and electrolysis mode.

Recently, the areas of chemistry dealing with electrochemical synthesis and research of thin layer metal polymers and their composite coatings have been widely developed [113]. Metal complex polymer-immobilized systems have widely-ranging practical applications [114]. The possibility of obtaining non-porous double-layer magnetic matrices based on cobalt ferrite to immobilize biologically active substances in a silicon matrix was examined in [115].

Pimkov et al. [116] developed methods for the chemical activation of polypropylene materials and subsequent immobilization of a cobalt phthalocyanine complex in them.

The Japanese researchers [117] offered the composition of electrolyte to obtain a polymeric composite coating with high corrosion resistance and adhesion based on zinc, cobalt, nickel and iron oxides

As a result of the hemisorption process, polymer-immobilized composite coatings of Fe_3O_4 [118] that can be used in biotechnology were obtained, using polyamine-, polylactam- and polyacrylamide-based polymers.

A polymer-immobilized nickel oxide-based composite coating on a titanium surface having high anti-microbial properties was obtained by an electrochemical method using direct current [119].

Analysis of the present state of the art showed that the above electrolytic oxide materials were obtained by deposition of their salts from aqueous solutions on an anode (mostly) or on a cathode using direct current polarization. Currently, the immobilization of metal oxides and metal-complexes into different polymer arrays is carried out, mainly, by pure chemical methods [120].

2.2. Selective composite oxide coatings

The electrochemical methods which allow one to obtain anodic aluminum oxide (AOA) with specified functional properties are quite simple. Their properties can be changed by filling oxide pores with one or more organic or inorganic substances that are added to the electrolyte solution. To obtain selective coatings based on AOA using an asymmetric alternating current seems to be a promising line of research.

Special units, called “solar collectors”, are used to convert solar electromagnetic radiation into thermal energy. The main element of a collector is an absorbing panel (an absorber or a heat receiver). This captures the energy in sunlight by converting it into heat and transmits it to a heat transfer agent. The panels are usually made of aluminium, copper or steel.

The ideal surface of a heat receiver should be able to absorb in the visible part of the electromagnetic (EM) spectrum well and radiate little if any of the absorbed energy in the infrared region. Such an ideal surface is called a selective surface and a coating which allows one to obtain such a surface is called selective or optically selective.

Selective coatings must meet certain criteria. Their effectiveness is characterized by:

- integrated solar energy absorption coefficient, α_{sol} , which should be high;
- relative integrated intrinsic radiation coefficient, ε , which should be low throughout the whole spectral range of solar radiation;
- selectivity expressed by the ratio of absorptivity to radiation, α_{sol}/ε . The higher this ratio is, the higher the quality of a selective coating is because the collector converts EM radiation of the Sun into heat more efficiently.

Current state-of-the-art collectors have α_{sol} values that approach 94.0 – 96.0 % (0.94 – 0.96), and ε values that do not exceed 12.0 – 16.9 % (0.12 – 0.16). To minimize energy losses, it is essential that the α_{sol} coefficient value tends to unity in the visible and near infrared regions of the EM spectrum, and the reflection coefficient value for the surface should tend to unity in the wavelength region intrinsic to thermal radiation [121].

A layer with a large reflection coefficient in the long-wavelength region of spectrum, for example, copper, nickel, molybdenum, silver, aluminium is usually applied on a surface which must be given selective properties. Another translucent layer with a high absorption coefficient in the visible and near infrared regions is also applied to this layer. Many oxides have such properties. Thus, in the UV and visible regions, the optical properties

of selective coatings should be very close to properties of an absolute black-body, and in the infrared region of spectrum they should be very close to properties of an absolutely white one. The development of such coatings is quite a difficult task, so the technology of their production is commercially confidential. Multilayer selective coatings are known for solar collectors having two layers, one of which is made as an aluminum oxide film which has pores filled with metal particles, for example, nickel, and another possibility is a tin dioxide film which is placed first along the solar rays [122]. An additional layer, in the form of a hydrated Al_2O_3 film, is located between these two layers. The α_{sol}/ε ratio is about 4.0 – 5.0 for coatings of this type because of the relatively high value of the coefficient ε and the low magnitude of A_c ($A_c \geq 0.9$; $\varepsilon \geq 0.2$).

The absorbing coating consisting of a solid amorphous carbonaceous film [123] was deposited on metal electrodes from the glow discharge in organic or organoelement compounds. The coating has high adhesion characteristics but a low integrated solar energy absorption coefficient ($\alpha_{sol} = 0.85$). This is because the coating has high refraction indices, n , in the visible part of the EM spectrum. But selective coatings have optimum optical properties only at an optimum thickness, which should not exceed the λ_0/n value (λ_0 – a wavelength corresponding to maxima of solar radiation spectrum).

The method of obtaining a multilayered selective coating [124] on aluminum foil by depositing a titanium layer in vacuo and subsequent vacuum reactive evaporation of nonstoichiometric titanium metalloids is known. The latter is usually obtained by reactive evaporation of CO_2 or N_2 in the atmosphere under the partial pressure of each gas within $(2.5 - 8.0) \cdot 10^{-2}$ Pa, then amorphous carbonaceous material is precipitated in glow discharge in vacuum in organic or organoelement compound vapor under partial gas pressure within the range of 10 – 20 Pa. The selective coating obtained by this method has rather low radiation coefficient $\varepsilon = 0.035$ and $\alpha_{sol} = 0.84 - 0.87$. The latter is very low therefore to increase the absorption coefficient α_{sol} , Dyachshin et al. [124] increased the discharge current density to 0.2 – 0.3 $\text{A} \cdot \text{dm}^{-2}$ and the discharge burning voltage to 400 – 450 V of an alternating current with the frequency of 50 Hz. Only in this case did the α_{sol} value increase from 0.87 to 0.94. As is obvious, this method of obtaining a selective coating is technologically complicated and very time-consuming.

A multilayered selective coating that consists of two layers was obtained by Dyachshin et al. [125] by consistent precipitation from a glow discharge under organic or organoelement compound vapors on the metal surface of an aluminum collector. The first layer was deposited from a glow discharge in benzol vapors under a pressure of $1 \cdot 10^{-2}$ mmhg, a discharge density 0.7 $\text{A} \cdot \text{m}^{-2}$, a discharge burning voltage 4.0 kV at a frequency of 50 Hz.

The second layer of the coating is located directly on the first one and is deposited from the glow discharge in benzol vapors under a pressure of $1 \cdot 10^{-2}$ mmhg, discharge density 2 – 3 $\text{A} \cdot \text{m}^{-2}$, discharge burning voltage 400 V of AC at a frequency of 50 Hz. This type of coatings has an integrated absorption coefficient α_{sol} 0.92 – 0.94 and radiation coefficient $\varepsilon = 0.07 - 0.08$ at 100 °C. The efficiency of solar power conversion is 11.5 – 13.5.

A multilayered absorbing coating was obtained by Golovkov and Verbitsky [126]. The coating contained two dielectric layers, between which there was an operated layer made in the form of a thin sprayed graphite film and a lattice made of sprayed metal strips. The process for forming a selective coating using this method is very time-consuming and ineffective.

Multilayered absorbing coatings based on fine ferromagnetic, metal or graphite particles of inductive and capacitor elements dispersed over the entire surface can be obtained [127].

The selective coating can be obtained by an electricity-free method using PbS, black copper and black chrome, TiN_xO_y , Ni – NiO_x , Al_2O_3 in the presence of fine dispersion of Ni, Co, Mo, W, Pt [128].

When developing light absorbing coatings for space devices [129], a CuO coating on the surface of copper with a high absorption coefficient and a low reflective power was obtained. These coatings were also used as an absorber in solar collectors. To increase a solar energy absorption coefficient, however, they were deposited on rough surfaces. As a result, the light flux stayed on a surface because of its multiple re-reflection in the light traps which were formed by the surface's texture. To roughen metal substrates, they were sandblasted with 0.2 – 0.5 mm silicon carbide particles. Nevertheless, the coatings had a high radiatability.

To obtain selective copper-based coatings, the black coloring of copper in alkaline solution was used [130]. The CuO thin film obtained had properties of a filter: it absorbed the visible light and had a high reflective ability for long-wavelength infrared radiation. Such a film does not release heat which develops from solar radiation of a more short-wavelength part of spectrum in the thin layer of copper oxide.

Thus, depending on the method of surface preparation and oxidation time, it is possible to obtain selective coverings with different optical properties. Cheap light absorbing coatings in the form of BT – 577 black bituminous enamel and No. 164 black enamel can be also used as selective coatings when there is glassifying with a “thermal mirror” made of a Zr_2O_3 or SnO_2 thin film. These films are transparent in the visible range of solar radiation (λ from 400 to 800 nm) but reflect the infrared radiation rather well, which results in a more effective transformation of solar radiation to heat. However, these coatings have low A_c values and high ε values.

Moldovanov et al. [131] obtained a selective coating which consisted of aluminum particles precipitated in nitrogen-containing plasma. Atoms of nitrogen create strong covalent bonds with surrounding aluminum atoms which results in an aluminum lattice distortion and transformation of solar into thermal energy. When obtaining selective coatings which reflect or absorb optical radiation selectively, various pigments are also used [132]. They are added to the selective coatings composition in a dispersion form [133]. ZnO, TiO₂, MgO, Al₂O₃ and others are referred to pigments that reflect optical radiation in the short-wavelength region. Fe₃O₄, Sb₂O₃ and carbon-based pigments absorb optical radiation over the entire optical range from visual to infrared, therefore, they are used as solar absorbers.

Metal-based thin films that absorb visible light and passing infrared radiation are the common type of a selective coating. Among these are coatings from black chrome and black nickel which are applied on nickel, zinc, tin or copper substrates using an electrochemical method. Black chrome coatings are the most promising ones, since they allow one to obtain the required optical properties and have a high thermal stability. However, when depositing black chrome, the density of an electric current is almost a hundred times higher than that for black nickel, therefore, the cost of black chrome selective coatings is high.

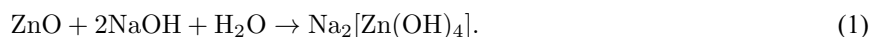
Coating selectivity can also be provided solely by geometrical factors: surface asperities should be greater than the wavelength of light in the spectrum of visible and near IR regions and less than a wavelength corresponding to its surface intrinsic radiation. Such a surface for the first of the above spectrum regions will be black, and for the second one it will be mirrored. Surfaces with a dendritic or porous structure with appropriate sizes for the dendritic needles and pores have selective properties.

Thus, the efficiency of a solar collector can be increased by using selective absorbing coatings on a heat absorber surface which absorb the visible part of the EM spectrum well and do not practically radiate in the infrared region of spectrum [134].

As it appears from the reviewed methods of obtaining selective coatings, the mature methods at present are as follows: chemical vapor deposition, vacuum dusting, galvanic and chemical ones. The methods listed have a number of disadvantages: high process energy intensity (more than 200 kW·m⁻²); multilayer coatings and their deposition time; expensive and ecologically harmful components; insufficiently high transformation efficiency for solar energy. According to the current standards [134] for good selective coatings, the absorption ability has to be not less than 92 % (0.92), and the radiation ability – no more than 30 % (0.3). Selective coatings can be deposited on such materials of a heat exchanger (absorber) as aluminum, steel, nickel, titanium, silver, copper and others. Additionally, the thickness of coatings having absorbing properties should not exceed 1 μm. While developing selective coatings, their cost is also an important factor, since the use of one type of a selective coating or another can result in either decrease of costs for the collector's other elements or increase them and, thus, make their characteristics worse.

The use of an asymmetric alternating current to obtain selective coatings has received almost no attention in the literature. Meanwhile, the use of an asymmetric alternating current, which allows one to regulate the structure of an oxide film and the amount of impurities in it, is very promising for obtaining such coatings.

When developing a technique to obtain optically selective coatings on the surface of Type AD 31 and Type A5M aluminum alloy using a transient electrolysis method, Bespalova et al. [78] paid much attention to a surface preparation to receive a developed microstructure. Therefore a stage of zinc electrodeposition was added to the surface preparation methods. As a result of interaction of the components of a zinc electrolyte, the reaction of sodium tetrahydrozincate formation proceeds as follows:



Heating the zinc solution increases the rate of the reaction (1) and the content of sodium tetrahydrozincate in the solution. While immersing a sample of aluminum alloy into a sodium tetrahydrozincate solution, the process of zinc chemical reduction takes place on its surface. The structure and the specific surface of the aluminum sample change due to a contact exchange of aluminum atoms to zinc atoms in a crystal lattice. The zinc layer was removed from the surface of an aluminum alloy using orthophosphoric acid solution [78]. When it was removed, the surface had a very developed microstructure. The latter was confirmed by the images of the surface of Type AD 31 and Type A5M aluminum alloys that were received by means of high vacuum scanning electron microscopy (Fig. 1) after its preparation. The surface consisted of pyramid-shaped projections, with their base being 0.8 – 1.5 microns and their height – 0.5 to 1.5 microns. To obtain selective coatings is difficult, and in this case, it is also complicated by the fact that the electrolytes used to oxidize aluminum and its alloys [135–142] cannot be used, as they do not allow one to obtain porous coatings with thickness not more than 1 micron, simultaneously filling pores with a highly-dispersed metal. But heavy coatings have high radiabilities.

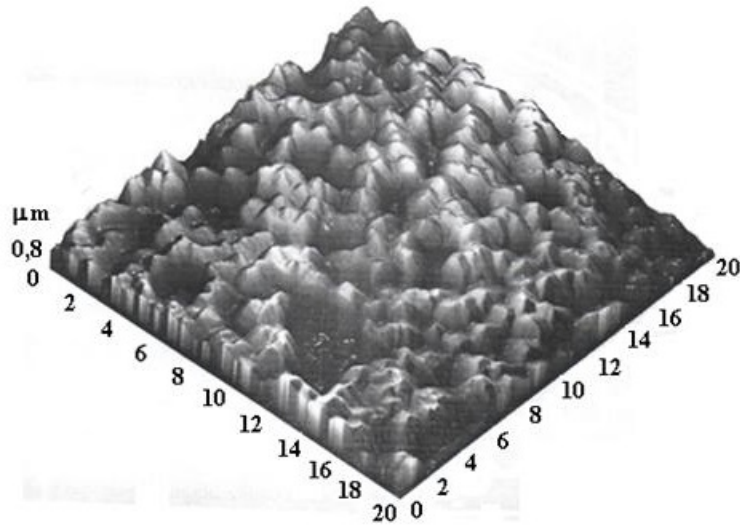
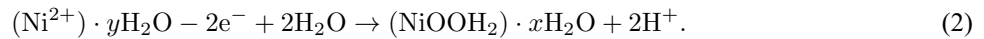


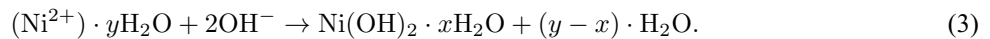
FIG. 1. Morphology of Type AD 31 and Type A5M aluminum surface after pretreatment

The composition of an electrolyte solution containing: formalin – 1.5 g/l; citric acid – 1.0 g/l; ammonium sulfate $[Al_2(SO_4)_3 \cdot 18H_2O]$ – 35.0 g/l; nickel sulfate $[NiSO_4 \cdot 7H_2O]$ – 35.0 g/l was developed [78]. The oxidation mode when obtaining selective coatings was the following: the ratio between average cathode and anode current densities was 2:1; the temperature – 25 ± 5 °C; the time – 150.0 s. During asymmetric alternating current electrolysis in aqueous solutions of nickel salts, nickel hydroxides are usually formed [72,76] which for nickel oxidation levels within the range of (“+2” ÷ “+3”), form a continuous number of solid solutions in nickel oxide [143] corresponding to the NiOOH formula x , where x changes from 2 to 1.2.

The process of deposition for hydrated nickel ion (an aquacomplex) from solution on an electrode surface in the form of a solid phase proceeds by equation:



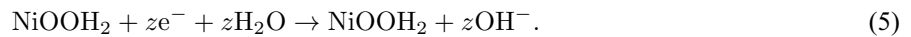
One can suggest two methods for this process development. The first one deals with the formation of coatings due to chemical precipitation of nickel hydroxides from aquacomplex solutions when basifying a near-electrode layer near the electrode surface:



While cycling under the influence of an asymmetric alternating current, the film charge in an anode semiperiod is:



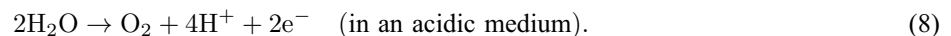
and the discharge in a cathodic semiperiod which occurs is:



The galvanic nickel deposition in aluminum oxide pores Al_2O_3 can also proceed in a cathodic semiperiod:



and the subsequent oxidation can proceed in an anode semiperiod due to oxygen evolution:



The above equations (2 – 8) represent a simplified record. In fact, an oxide film has water molecules in its composition, and ions in solution represent aquacomplexes. In addition to reaction (8), however, a nickel oxidation can proceed via:



The selective coating obtained by the method [78] consists of aluminum oxide particles having sizes ranging from 20 to 70 nm (Fig. 2). The raster electron microscopy showed that in aluminum oxide particles, there is highly-dispersed nickel which is evenly distributed on the entire surface (Fig. 3).

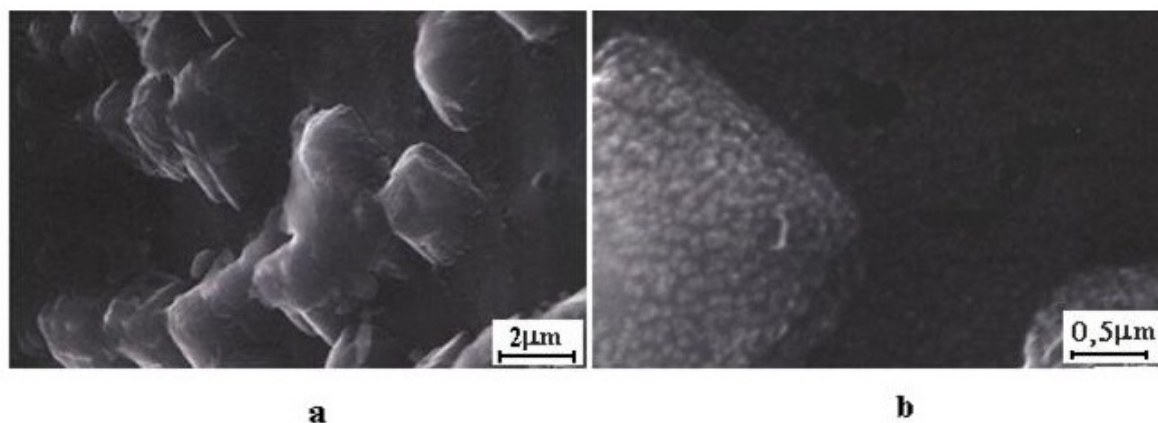


FIG. 2. SEM – image of the selective coating on the surface of aluminum: a – general view of the surface at the angle of 45° , b – image of fine-dispersed nickel in nanoscale hollows of aluminum oxide

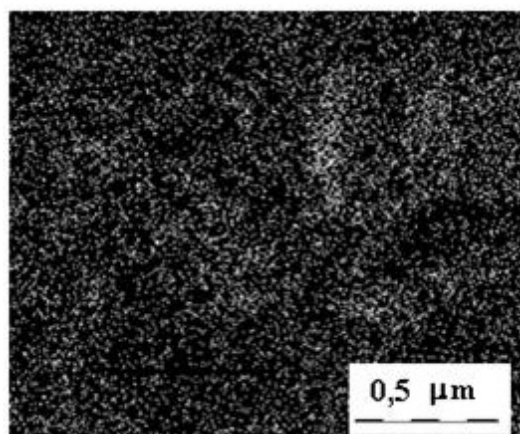
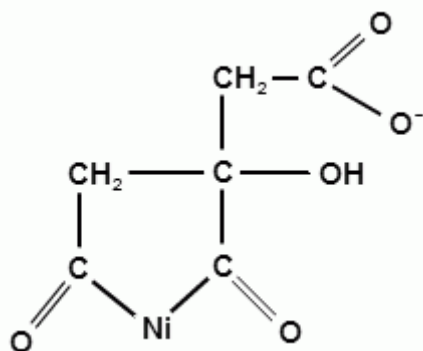


FIG. 3. Image of a selective coating surface in the X-ray radiation of NiK_α -line. Density of white points is proportional to the nickel content

This suggests that the coating represents aluminum oxide nanotubes filled with nickel nanoparticles. Thus, in pores of oxides, a highly-dispersed nickel is deposited in a cathodic semiperiod according to reaction (6).

Gnedenkov et al. found [144] that in solutions and in powder samples complex compounds in an anion form of aluminum with carboxylic acids can be formed by carboxy groups at $\text{pH} = 2 - 4$, carboxyl groups and hydroxy groups at $\text{pH} = 4 - 9$ and only hydroxy groups at $\text{pH} = 9 - 10$. The similar complex formation of nickel with citric acid is likely to take place to obtain selective coatings in an electrolyte solution.



This process enables one to suppress the formation of nickel hydroxide in a cathodic semiperiod because of alkalizing near-cathode space and makes the lifting of nickel to an electrode surface easier where it is deposited in the form of highly-dispersed nickel in aluminum oxide pores.

The presence of a citric acid in the composition of an electrolyte [78] besides the processes of complex formation also provides high adhesion for an optically selective coating to a substrate, creating an acid medium in which the partial oxidation process for an aluminum alloy with formation of a thin layer of aluminum oxide takes place. Under optimum conditions, the optical selective coatings with absorption coefficient of 93.5 % and radiation coefficient of 6.0 % were obtained using the method of Type AD 31 and Type A5M aluminum alloys surface preparation developed by Bespalova et al. [78]. These data are among the best characteristics of optical selective coatings manufactured by industry for helioplants. The development of an effective surface allowed reduction of the probability for a secondary photon to leave surface coatings because of its repeated reflection in light traps formed by the surface relief.

To increase the thermoreceptor properties of optical selective coatings, it is necessary to have a transparent layer that is resistant to the impact of ultra-violet radiation on its surface. Initially, fluoroplastic (type F-3MV, F-32LN) and silicone varnishes (type KO-85) were investigated as a transparent layer by Bespalova et al. [44]. The most promising of them was the 1 – 3 mass% solution of F-32LN fluoroplastic varnish. The presence of this layer allowed them to increase the absorption coefficient to 95.0 % and slightly increased the radiating power to 9.0 %.

According to the results of the research, the developed optical selective coatings had high heat stability that confirmed the possibility of their use in helioplants.

Thus, on the surface of aluminum alloys, optically-selective coatings were obtained under polarization by an asymmetric alternating current that enabled researchers to obtain single-layer coatings with exceptional optical properties within 2.5 min; to reduce power consumption of the process to $10 \text{ kW}\cdot\text{m}^{-2}$; to exclude the use of expensive components; and to ensure ecological safety of coatings formation.

3. Catalytically-active composite materials based on transition metal oxides

The development of composite coatings based on transition metal oxides, including molybdenum oxide compounds with a wide range of practical application [145–148] is a promising trend of surface modification.

Composite coatings based on molybdenum oxides are especially attractive because of their atypical chemistry resulting from multiple valence states. In addition, they are stable, have significant activity and selectivity in different processes [149].

Molybdenum oxide compounds can be obtained by a hydrothermal method [150], pyrolysis of various oxide organic precursor molybdenum compounds [151] chemical dehydration of colloidal solutions [152] and also by an electrochemical method using a direct current from molybdate solutions [153]. Among the methods for directed synthesis of new catalytically active composite materials based on molybdenum, cobalt, nickel, iron, manganese, vanadium oxides, electrochemical methods are very promising. The electrolytic depositions of molybdenum oxides in the form of specific modifications: Mo_4O_{11} , Mo_8O_{23} , MoO_2 , MoO_3 , $\text{Mo}_{18}\text{O}_{52}$ and Mo_9O_{26} from ammonium molybdate and sodium molybdate solutions are the subject of a large number of studies [93, 97, 150, 151, 154]. Electrochemical methods for obtaining such systems from aqueous solutions have a number of specific characteristics because the state of Mo (VI) in an aqueous solution has certain impact on the mechanism of electrochemical reactions. The latter is caused by the fact that depending on the concentration of molybdenum containing particles and pH of the solution, various isopoly compounds are formed.

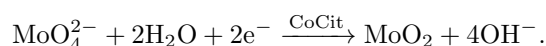
A unique feature of obtaining molybdenum-based coatings from aqueous solutions is that they cannot be obtained in pure form. The most common elements of such coatings are Co, Ni, Fe [155], which have a catalytic effect on electrochemical molybdate ions reactions. Molybdenum electrolytes are stable only at pH 3.5 – 5.0, therefore hydroxy acids or their salts are added into their composition, along with transition metal elements.

The reduction of the large molybdate- ion MoO_4^{2-} is a very complex process which involves electron and proton transfer processes. It proceeds in a stepwise manner, i.e. by individual elementary stages. In the case of low molybdate concentrations, the formation of Mo – Ni, Mo – Co, Mo – Fe alloys will occur in the solution as a result of induced co-precipitation [156–158], proceeding through the formation of intermediates. Monovalent ions, radicals (in the presence of hydroxy acids in the electrolyte solution) and complex compounds with varying degrees of stability can act as intermediates during reaction. The nature of the intermediates, however, is not adequately studied, and the evidence of their existence on the surface or in solution is indirect. Nevertheless, one must not ignore this, as they can determine the rate and direction of an electrochemical process.

The primary process in the formation of coatings from solutions containing transition metal compounds is the deposition of iron group metals, and molybdenum deposits because of its ions adsorption by hydroxy forms of

nickel, cobalt or iron (CoOH_{ads}^+ , NiOH_{ads}^+), which cover the electrode. In case of higher MoO_4^{2-} content in an electrolyte solution, the electrical deposition of alloys becomes impossible and the products of partial reduction of molybdate ions deposits on the cathode. They represent both simple and complex oxide systems which are catalysts for the discharge of protons. The oxide film formed acquires electronic conductivity; its further reduction stops and only hydrogen reduction proceeds on the surface [155].

The formation of molybdenum oxides is catalyzed by iron metal group citrate complexes, for example, by a CoCit complex [159, 160]:



The presence of cobalt in the solution determines if one obtains molybdenum oxides at low concentrations, with substoichiometric molybdenum oxides being formed, whose color is associated with the presence of oxygen vacancies [161], and the potentials which are more positive than minus 0.125 V can be attributed to the cobalt - molybdenum oxidation [158]. The high efficiency of molybdenum oxide formation in the presence of Co (II), Fe (II) and Ni in the solution may be connected with simultaneous CoCit adsorption on molybdenum and the presence of electroactive colloidal forms of $[\text{Fe}(\text{OH})_x]\text{Fe}^{2+}$, $[\text{Ni}_y\text{Fe}_z\text{OH}]^{n+}$ or $[\text{Co}_y\text{Fe}_z\text{OH}]^{n+}$ in the reaction layer which reduces hydrogen evolution [162].

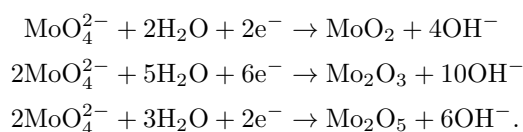
In [163], it was determined that reduction of hexavalent molybdenum in ammonium citrate electrolytes occurs mainly from heptamolybdate ions. Ammonium ions increase the percentage of heptamolybdate in the solution which increases their reduction, and the presence of citrate has a depolymerization effect on hexavalent molybdenum compounds. The citrate-ion is a hard ligand, so it could retain pentavalent molybdenum compounds in a solution and prevent its disproportionation with MoO_2 formation. The quantitative ratio of citrate ion and ammonium ion allows one to control the rate of formation of molybdenum oxide and its quantity.

The degree of molybdenum oxidation in oxide films was (IV), (V) and (VI). In the presence of ammonium ions, Mo(VI) reduction to intermediate oxidation states is facilitated. One can suggest that ammonium ions, in addition to cobalt ions serve as donors of protons that are necessary to reduce molybdenum oxygen-containing compounds. However, the main factors that affect the formation of hydroxide forms, the process of polymerization and chemisorption processes are the pH-value and the electrolyte temperature.

The deposition of molybdenum oxides takes place only when the potentials are more negative than some threshold value, which depends only on the electrolyte composition [159]. In the partial reduction of Mo(VI) during electrolysis of aqueous solutions of molybdates MoO_2 [164, 165], Mo_2O_3 [166], Mo_2O_5 , Mo_3O_8 , nonstoichiometric compounds type $\text{Mo}_3\text{O}_{R-x}$ as well as mixed Mo (IV) – Mo (V) oxides [167] are formed. These products can be subjected to further reduction, its mechanism is still not clear [165–169]. It is significant that in solutions containing Mo(VI), Co, Ni, Fe and hydroxy acids various chemical reactions that lead to the formation of a wide range of compounds, including complex ones can proceed. The identification of Mo(VI) complexes is very problematic. However, citrate complexes, for example, type $\text{HrMoO}_4\text{Cit}^{(5-r)-}$ [165, 169], $\text{H}_x\text{Mo}_7\text{O}_{24}^{(6-x)-}$, $\text{NiMoO}_{24}\text{H}_6^{4-}$, $\text{H}_x(\text{MoO}_4)_2\text{Cit}^{(7-x)-}$ and $\text{H}_x\text{MoO}_x\text{Cit}^{(5-x)-}$ [170] are documented, which confirms that complex chemical or electrochemical processes occur during the co-deposition of molybdenum with transition metals (Co, Ni, Fe) from electrolyte solutions containing hydroxy acids.

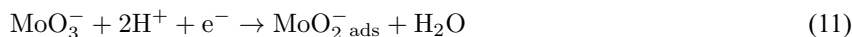
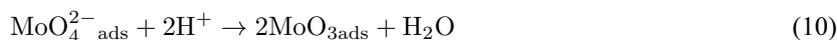
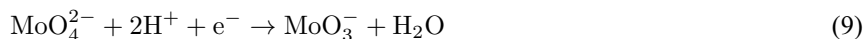
The ligand excess in the electrolyte composition is not desirable and its concentration should not be also very low. Otherwise, slightly-soluble hydroxides can be formed because of the system's stability loss in bulk solution.

The possibility of obtaining molybdenum oxides by cathodic reduction during electrolysis of aqueous solutions of sodium molybdate and ammonium heptamolybdate on the surface of steel was determined in [93, 97, 154, 171–173], where it was supposed that under investigated circumstances several parallel reactions were realized with a certain probability for proceeding:



According to [93, 97, 154, 171, 172], during formation of molybdenum oxides the main step is the discharge of the MoO_4^{2-} ion, whose rate largely depends on the intensity of its forestalling hydrogen evolution. The summary

scheme of an electrode process can be represented by a number of the following chemical equations [154]:

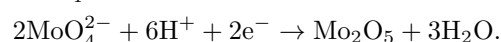
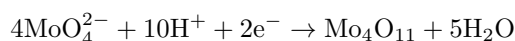
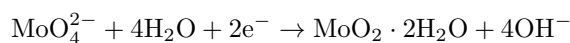


The given scheme reflects the sequential interdependence of electrochemical (9,11) and redox (10) reactions as well as the initial stage of phase transition (12). The justification for such a mechanism has not been thoroughly proven.

In addition to a MoO_3 rhomboidal main phase $\text{MoO}_3 \cdot 2\text{H}_2\text{O}$, $\text{MoO}_3 \cdot \text{H}_2\text{O}$ monoclinic phases and $\text{MoO}_x(\text{OH})_y$ crystallographic shift phase can be present in the composition of the coatings. In [174], using an electrochemical method, molybdenum oxide compounds were formed on the surface of steel, nickel and carbon from aqueous solutions containing: $(\text{NH}_4)_6\text{Mo}_7\text{O}_{24} \cdot 4\text{H}_2\text{O} - 10.0 \text{ g/l}$; $\text{HF} - 1.0 \text{ g/l}$; cathodic current density of $0.5 - 1.0 \text{ A} \cdot \text{dm}^{-2}$; electrolysis time - 10 min at room temperature. The cathodic deposits obtained represented such phases as $\text{Mo}_{3-x}(\text{OH})_x$, $\text{MoO}_3(\text{H}_2\text{O})_2$, $\text{MoO}_3(\text{H}_2\text{O})_{0.5}$, $\text{Mo}_3\text{O}_8 \cdot \text{H}_2\text{O}$.

In an aqueous electrolyte solution, some dissolved forms of molybdate ions are present, depending on its pH, which should largely determine all electrochemical processes. However, the greatest rate of molybdenum oxides formation was observed at pH 4.

In ammonium heptamolybdate acidic solutions, $(\text{NH}_4)_6\text{Mo}_7\text{O}_{24} \cdot 4\text{H}_2\text{O}$ Mo(VI) first reduces to Mo(V) and then to trivalent compounds Mo(III), and oxide $\text{Mo}_4\text{O}_{11} \cdot n\text{H}_2\text{O}$ represents an intermediate oxide compound between pentavalent Mo_2O_5 and hexavalent MoO_3 . The reactions which proceed on the cathode can be presented by the equations:



Additionally, the step below is also present:



It is also necessary to consider that molybdenum oxides formation due to a partial molybdate ion reduction proceeds with a simultaneous cycling of oxides on the surface, i.e. they are subjected to oxidation and reduction because of the changes of current direction. As a result, the spinel is formed in the active coating. A great variety of other spinel phases are considered in detail in [175–178].

When analyzing cathodic processes for the formation of molybdenum oxide phases, the processes of Mo(VI) polymerization which take place in heptamolybdate solutions with the formation of polymer cations Type $[(\text{MoO}_2)(\text{MoO}_3)_{n-1}]^{2+}$ or polyacids ($\text{H}_2\text{Mo}_2\text{O}_7$, $\text{H}_2\text{Mo}_3\text{O}_{10}$), and redox processes leading to formation of oxide radicals are excluded from consideration. In general, the formation processes for molybdenum oxide phases and complex oxide phases using an asymmetric alternating current is very complicated. Despite the complexity of a molybdenum compound's state both in aqueous solutions and in a solid phase, however, composite materials based on oxide compounds of molybdenum can be very useful as catalytically active materials, while solving applied problems of electrochemistry. The confirmation of the latter is the research [179–182] on obtaining catalytically active coatings based on transition metal oxides (Mo, Ni, Co, Fe) by depositing their salts from aqueous solutions under polarization by an asymmetric alternating current on the surface of St. 3 steel. The composition of electrolyte and electrolysis modes that allow one to obtain composite oxide catalytically-active coatings have been developed and optimized by Bespalova et al. [182].

Composite oxide coatings were formed on the surface of St. 3 steel pre-treated using a standard method [183] further comprising the stage of surface modification by galvanizing with a subsequent removal of a zinc layer. The main electrolyte aqueous solution components were iron(II) sulfate ($\text{FeSO}_4 \cdot 7\text{H}_2\text{O}$), cobalt sulfate ($\text{CoSO}_4 \cdot 7\text{H}_2\text{O}$), ammonium heptamolybdate $(\text{NH}_4)_6\text{Mo}_7\text{O}_{24} \cdot 4\text{H}_2\text{O}$, nickel sulfate ($\text{NiSO}_4 \cdot 7\text{H}_2\text{O}$), boric (H_3BO_3) and citric ($\text{C}_6\text{H}_8\text{O}_7$) acids. The device consisting of two paralleled diodes conducting a current in different directions through the adjustable resistance was used as a technological current source.

The asymmetry parameter (j_k/j_a) was equal to 1.44; the electrolyte temperature - $65 - 70 \text{ }^\circ\text{C}$; pH - 4; and coating deposition time - 60 min.

The X-ray diffraction data demonstrated that the phase composition of the coating substance is rather complex. The basic phases of the coating composition are molybdenum oxides (MoO_3 , MoO_2 , and $\text{Mo}_{18}\text{O}_{52}$), spinel (Fe_3O_4),

and cobalt, nickel, and iron molybdates (CoMoO_4 , NiMoO_4 , and FeMoO_4). Molybdenum oxide MoO_3 has a stable layered structure, consisting of 2D networks bound by vertices of $[\text{MoO}_6]$ octahedral. The weak binding between layers in the structure of a rhombic MoO_3 enables these layers to be rearranged into polymorphic modifications of MoO_{3n-x} by the crystallographic shear mechanism [184]. This accounts for the presence of $\text{Mo}_{18}\text{O}_{52}$ in the coating's substance.

The transmission electron microscopic data demonstrated that the electron diffraction patterns apart from the a.m. phases contain lines of molybdenum oxide Mo_4O_{11} and complex oxides CoFe_2O_4 and $(\text{Co,Ni})\text{Fe}_2\text{O}_4$ with an inverted spinel structure. The oxides $\text{Mo}_{18}\text{O}_{52}$ and MoO_3 are the most active catalytic phases of a composite coating with high selectivity that were obtained in [182].

Compared with the interplanar spacings (d) of the known molybdenum oxides [185], the whole set of interplanar spacings obtained using X-ray and HRTEM data suggests that the coating substance contains MoO_2 (space group $P21/n$), Mo_4O_{11} (space group $Pnma$), and $\beta\text{-MoO}_3$ (space group $P21/c$). The electron-microscopic study of oxide compounds obtained demonstrated that these compounds are present in coating composition in the form of agglomerates of particles (Fig. 4a) having a needle morphology (Fig. 4b). The coating itself has a cracked microstructure that is characteristic of oxygen compounds of molybdenum [186]. The calculation of coating crystalline particle sizes using Debye-Scherrer formula showed that their sizes range from 6.5 – 9 nm

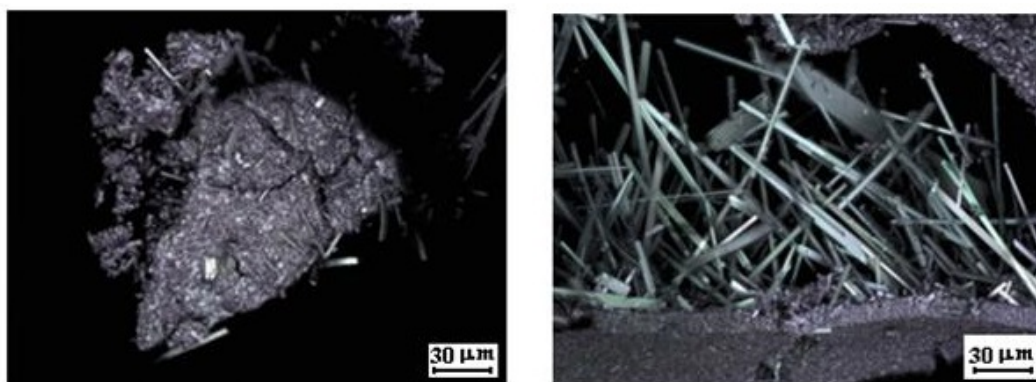


FIG. 4. Micrographs of the composite coatings substance. (a) Agglomerates of oxide compounds and (b) structure of separate particles

The oxides MoO_2 , MoO_3 , Mo_4O_{11} , $\text{Mo}_{18}\text{O}_{52}$, Fe_3O_4 , CoFe_2O_4 , $(\text{Co,Ni})\text{Fe}_2\text{O}_4$, CoMoO_4 , NiMoO_4 , FeMoO_4 that are present in composite coatings represent themselves as heterogeneous catalysts which are used in oxidation processes as cathode materials for chemical power sources and increase the protective ability in corrosive environments [187–189].

Composite oxide materials developed in [179–182] were investigated for their potential use as catalysts in liquid-phase oxidations of glyoxal to glyoxylic acid. The test results showed that their catalytic activity is greater than that of Pt- and Pd-containing catalysts: the conversion value is higher by 13 %, and the selectivity value by 20 %. Composite coatings based on transition metal oxides not only have good catalytic properties, but good performance characteristics as well. Corrosion-protective properties increase by 25- to 50-fold when the coating thickness is 15 microns, tensile strength is 3.1 MPa and microhardness is 250 MPa.

The real advantage of the above research is the fact that for the first time, composite coatings based on molybdenum oxides, complex molybdenum oxides and its oxygen compounds with iron group metals were obtained on a solid substrate by deposition of their salts from aqueous solutions using transient electrolysis.

4. Conclusion

In this review, the principles for the formation of oxide composite nanostructured materials by electrochemical methods are considered and the benefits of transient electrolysis when obtaining such materials are shown. The use of an asymmetric alternating current allows one to obtain principally new oxide nanostructured composite materials both based on metal substrate oxidation processes and metal oxides deposition from aqueous solutions of their salts. The use of an asymmetric alternating current allows the creation of principally new oxide nanostructured composite materials both based on metal substrate oxidation processes and metal oxides deposition from aqueous solutions of their salts. This approach expands the spectrum and methods of new nanostructured materials considerably [190, 191].

The development of technologies to produce oxide composite nanostructured materials by a method of transient electrolysis is one of the promising directions for nanotechnologies because of its such obvious advantages, such as availability, simplicity of experimental design, relative low costs. Nanomaterials obtained by this method can be very promising as optically selective coatings used in helioplants and as catalytically active materials in oxidation processes, cathode materials in chemical current sources, sensors for monitoring the gas content in the atmosphere, and can significantly increase corrosion resistance and protective ability in a number of corrosive environments. The method of transient electrolysis enables one to obtain composite materials based on complex oxides of molybdenum, cobalt, manganese, nickel, iron, vanadium as disordered solid solutions with a defective structure. The latter determines a large set of their various properties.

Due to the cycling processes on the surface of the substrate (steel, nickel, copper and other metals) a transition spinel layer is formed which ensures high adhesion of the obtained composite oxide material. The deposition of oxides from aqueous solutions of their salts under electrolysis by an asymmetric alternating current, as is shown in the reviewed works, occurs when an average cathodic current is more than anodic one, the electrode periodically being an anode or a cathode. The deposited composite oxide coatings are still not adequately investigated. The use of an asymmetric alternating current can lead to new, exciting and unexpected results which, undoubtedly, will find many new applications.

Acknowledgements

We thank Professor V.V. Gusarov, doctor of chemical sciences, for valuable advice in discussion of the experimental results.

References

- [1] Raeva O.V., Shestakov I.Ya. Electrochemical Method of Discharged Waters Cleaning with of Alternating Current. *Journal of Siberian University. Engineering & Technologies*, 2011, **3** (4), P. 348–355.
- [2] Kilimnik A.B., Nikiforova E.Y. Electrochemical behavior of nickel and its oxides in concentrated sodium hydroxide solutions. *Russian Journal of Electrochemistry*, 2013, **49** (12), P. 1122–1126.
- [3] Degtyareva E.E., Kilimnik A.B., Ankudimova I.A. Anodic Oxidation of Sodium 2–mercaptobenzthiazolate anion in the Presence of 5–Methyl–2– hexanol. *Russian Journal of Electrochemistry*, 2007, **43** (10), P. 1203–1205.
- [4] Klochko N.P., Volkova N.D., Starikov V.V. et al. Utilization of alternating current methods for manufacture of selective absorbing coatings for heat collectors. *Functional Materials*, 2005, **12** (3), P. 123–125.
- [5] Zhang J., Ge H., Li Z., Ding Z. Internal heating of lithium–ion batteries using alternating current based on the heat generation model in frequency domain. *Journal of Power Sources*, 2015, **273**, P. 1030–1037.
- [6] Abdulla T., Yerokhin A., Goodall R. Effect of plasma electrolytic oxidation coating of the specific strength. *Materials and design*, 2011, **32**, P. 3742–3749.
- [7] Yoshioka T., Chavez-Valdez A., Roether J.A. et al. AC electrophoretic deposition of organic-inorganic composite coatings. *Journal of colloid and interface science*, 2013, **392**, P. 167–171.
- [8] Kudryavtsev Yu.D., Bespalova Zh.I., Pyaterko I.A. et al. Optimization of anodic aluminum oxide filling with polytetrafluoroethylene in polarization with asymmetrical alternating current. *Russian Journal of Applied Chemistry*, 2000, **73** (4), P. 631–634.
- [9] Makarochkina S.M., Rozin Yu.I., Samarin K.M. et al. Electrochemical Synthesis of Tetraethyllead at a Lead Trickle–Bed Electrode. *Soviet Electrochemistry*, 1985, **21** (12), P. 1529–1533.
- [10] Alsayhen E., McLeod E. et al. Impact of AC/DC spark anodizing on the corrosion resistance of Al–Cu alloys. *Electrochimica Acta*, 2011, **56**, P. 6041–6048.
- [11] Chávez-Valdez A., Boccaccini A.R. Innovations in electrophoretic deposition: Alternating current and pulsed direct current methods. *Electrochimica Acta*, 2012, **65**, P. 70–89.
- [12] Chávez-Valdez A., Herrmann M., Boccaccini A.R. Alternating current electrophoretic deposition (EDP) of TiO₂ nanoparticles in aqueous suspensions. *Journal of Colloid and Interface Science*, 2012, **375**, P. 102–105.
- [13] Hibino T., Inoue T., Sano M. Electrochemical reduction of NO by alternating current electrolysis using yttria–stabilized zirconia as the solid electrolyte: Part II. Modification of Pd electrode by coating with Rh. *Solid State Ionics*, 2000, **130** (1–2), P. 31–39.
- [14] Klochko N.P., Volkova N.D., Starikov V.V. et al. Utilization of alternating current methods for manufacture of selective absorbing coatings for heat collectors. *Functional Materials*, 2005, **12** (3), P. 548–554.
- [15] Hekman F., Sohrabi B., Rahmanifar M.S. Growth of the cobalt using AC electrochemical deposition on anodized aluminum oxide templates. *J. Nanostruct. Chem.*, 2014, <http://link.springer.com/article/10.1007/s40097-014-0105-2>.
- [16] Karimi E.Z., Esmailzaden J., Marzbanrad E. Electrospun TiO₂ nanofibre-based gas sensors fabricated by AC electrophoresis deposition. *Bull. Mater. Sci.*, 2015, **38** (10), P. 209–214.
- [17] Sadykov N.R., Kocherga E.Y., Dyachkov P.N. Nonlinear current in modified nanotubes with exposure to alternating and constant electric fields. *Russian Journal of Inorganic Chemistry*, 2013, **58** (8), P. 951–955.
- [18] Therese G.H.A., Kamath P.V. Electrochemical Synthesis of Metal Oxides and Hydroxides. *Chem. Mater.*, 2000, **12** (5), P. 1195–1204.
- [19] Korobochkin V.V., Balmashov M.A., Gorlushko D.A. et al. Phase Composition and Pore Structure of Nanoparticulate Tin Oxides Prepared by AC Electrochemical Synthesis. *Inorganic Materials*, 2013, **49** (10), P. 993–999.
- [20] Korobochkin V.V., Kosintsev V.I., Bystritskii L.D., Kovalevskii E.P. Preparation of Aluminum Hydroxide Gel by AC Electrolysis. *Inorganic Materials*, 2002, **38** (9), P. 914–916.

- [21] Usoltseva N.V., Korobochkin V.V., Balmashnov M.A. Air Carbonisation of AC Electrochemical Copper and Aluminium Oxidation Products. *International Journal of Engeneering & Technology*, 2013, **2** (1), P. 2355–2362.
- [22] Dolinina A.S., Korobochkin V.V., Usoltseva N.V. et al. Joint destruction of cadmium and copper at alternating current electrolysis in sodium hydroxide solution. *Procedia Chemistry*, 2014, **10**, P. 369–372.
- [23] Raju K., Yoon D.H. Electrophoretic deposition of BaTiO₃ in an aqueous suspension using asymmetric alternating current. *Materials Letters*, 2013, **110**, P. 188–190.
- [24] Jagminas A., Valsiūnas I., Šimkūnaitė B., Vaitkus R. Peculiarities of Bi⁰ nanowire arrays growth within the alumina template pores by ac electrolysis. *Journal of Crystal Growth*, 2008, **310**, P. 4351–4357.
- [25] Sankar P.R., Tiwari P., Kumar R. et al. Synthesis and characterization of cadmium selenide nanostructures on porous aluminum oxide templates by frequency alternating current electrolysis. *Applied Surface Science*, 2010, **256**, P. 2097–2103.
- [26] Atrashchenko A.V., Krasilin A.A., et al. Electrochemical methods of synthesis of hyperbolic metamaterials. *Nanosystems: Physics, Chemistry, Mathematics*, 2012, **3** (3), P. 31–51.
- [27] Yoon C., Suh J.S. Electrochemical Fabrication of CdS/Co Nanowire Arrays in Porous Aluminum Oxide Templates. *Bull. Korean Chem.*, 2002, **23** (11), P. 1519–1523.
- [28] Sameshima T., Hirata Y. et al. Factors affecting formation of ceria nanoparticles by alternating current electrolysis of aqueous solutions. *Materials Chemistry and Physics*, 2012, **136**, P. 313–316.
- [29] Xu J. Synergy effect on a suspended mixture of ceria and activated carbon for the photocatalytic degradation of phenol. *Powder Tech.*, 2011, **210**, P. 1–5
- [30] Wang C., Ao Y., et al. Preparation, characterization and photocatalytic activity of a novel composite photocatalyst: Ceria-coated activated carbon. *Journal of Hazardous Materials*, 2010, **184** (1–3), P. 35–41.
- [31] Kang H.S., Kang Y.C., Koo H.Y. et al. Nano-sized ceria particles prepared by spray pyrolysis using polymeric precursor solutio. *Mater. Sci. Eng. B*, 2006, **127** (2–3), P. 99–104.
- [32] Wang Y., Zhang F., Guo Y. et al. 3D navicular ceria micro/nanocomposite structure with multi-layered arrangement and its application in CO oxidation. *Mater. Chem. Phys.*, 2010, **120** (1), P. 23–30.
- [33] Ivanov V.K., Kopitsa G.P., et al. Hydrothermal growth of ceria nanoparticles. *Russian Journal of Inorganic Chemistry*, 2009, **54** (12), P. 1857–1861.
- [34] Ivanov V.K., Polezhaeva O.S., et al. Hydrothermal microwave synthesis of nanocrystalline cerium dioxide. *Doklady Chemistry*, 2009, **426** (2), P. 131–133.
- [35] Panahi-Kalamuei M., Alizadeh S., Mousavi-Kamazani M., Salavati-Niasari M. Synthesis and characterization of CeO₂ nanoparticles via hydrothermal route. *Journal of Industrial and Engineering Chemistry*, 2015, **21**, P. 1301–1305.
- [36] Rao R., Yang M., et al. Mesoporous CeO₂ nanobelts synthesized by a facile hydrothermal route via controlling cationic type and concentration of alkali. *Microporous and Mesoporous Materials*, 2013, **169**, P. 81–87.
- [37] Pinjari D.V., Pandit A.B. Room temperature synthesis of crystalline CeO₂ nanopowder: Advantage of sonochemical method over conventional method. *Ultrason. Sonochem.*, 2011, **18** (5), P. 1118–1123.
- [38] Baranchikov A. Y., Ivanov V.K., Tretyakov Yu. D. Sonochemical synthesis of inorganic materials. *Russian Chemical Reviews*, 2007, **76** (2), P. 133.
- [39] Yin L., Wang Y., Pang G. et al. Sonochemical synthesis of cerium oxide nanoparticles—effect of additives and quantum size effect. *J. Colloid and Interface Sci.*, 2002, **246**, P. 78–84.
- [40] Ishutina Z.N., Gusarov V.V., Malkov A.A. et al. Phase Transformations in Nanosized γ -Al₂O₃-SiO₂-TiO₂. *Zhurnal Neorganicheskoy Khimii*, 1999, **44** (1), P. 16–19.
- [41] Vasilevskaya A., Almjasheva O. Features of phase formation in the ZrO₂-TiO₂ system under hydrothermal conditions. *Nanosystems: physics chemistry mathematics*, 2012, **3** (4), P. 75–78.
- [42] Baranchikov A.E., Ivanov V.K., Tretyakov Yu.D. Hydrothermal microwave synthesis of nanocrystalline anatase. *Doklady Chemistry*, 2012, **447** (1), P. 241–243.
- [43] Leyva-Porras C., Toxqui-Teran A., et al. Low-temperature synthesis and characterization of anatase TiO₂ nanoparticles by an acid assisted solgel method. *Journal of Alloys and Compounds*, 2015, **647**, P. 627–636.
- [44] Ouzzine M., Maciá-Agulló J.A., et al. Synthesis of high surface area TiO₂ nanoparticles by mild acid treatment with HCl or HI for photocatalytic propene oxidation. *Applied Catalysis B: Environmental*, 2014, **154-155**, P. 285–293.
- [45] Prakash T., Navaneethan M., et al. Synthesis of TiO₂ nanoparticles with mesoporous spherical morphology by a wet chemical method. *Materials Letters*, 2012, **82**, P. 208–210.
- [46] Kosobudsky I.D., Ushakov N.M., Yurkov G. Yu. Et al. Synthesis and Structure of Polyethylene-Matrix Composites Containing Zinc Oxide Nanoparticles. *Inorganic Materials*, 2005, **41** (11), P. 1172–1177.
- [47] Bugrov A.N., Vlasova E.N., et al. Distribution of zirconia nanoparticles in the matrix of poly(4,4'-oxydiphenylene-pyromellitimide). *Polymer Science Series B*, 2012, **54** (9–10), P. 486–495.
- [48] Yudin V.E., Otaigbe J.U., et al. Effects of nanofiller morphology and aspect ratio on the rheo-mechanical properties of polyimide nanocomposites. *Express Polymer Letters*, 2008, **2** (7), P. 485–493.
- [49] Kononova S.V., Korytkova E.N., et al. Nanocomposite based on polyamidoimide with hydrosilicate nanoparticles of varied morphology. *Russian Journal of Applied Chemistry*, 2007, **80** (12), P. 2142–2148.
- [50] Kononova S.V., Korytkova E.N., Maslennikova T.P. et al. Polymer-Inorganic Nanocomposites Based on Aromatic Polyamidoimides Effective in the Processes of Liquids Separation. *Russian Journal of General Chemistry*, 2010, **80** (6), P. 1136–1142.
- [51] Gofman I.V., Svetlichnyi V.M., Yudin V.E. et al. Modification of Films of Heat-Resistant Polyimides by Adding Hydrosilicate and Carbon Nanoparticles of Various Geometries. *Russian Journal of General Chemistry*, 2007, **77** (7), P. 1158–1163.
- [52] Golubeva O.Yu., Yudin V.E., et al. Nanocomposites on the basis of polyimide termoplasts and magnesium-silicate nanoparticles with montmorillonite structure. *Russian Journal of Applied Chemistry*, 2007, **80** (1), P. 106–110.
- [53] Ivanov V.K., Shaporev A.S., et al. Synthesis of polymer composites based on nanocrystalline ZnO and CeO₂. *Doklady Chemistry*, 2010, **431** (2), P. 109–112.

- [54] Gorelik V.S., Mikov S.V., Sokolovskii M.I., Tsuzuki T. Secondary Emission of Nanocrystalline Zinc Oxide. *Inorganic Materials*, 2006, **42** (3), P. 282–285.
- [55] Ezhovskii Yu. K., Egorov A.L. Chromium Oxide Nanolayers on Gallium Arsenide. *Inorganic Materials*, 2006, **42** (4), P. 368–373.
- [56] Yue H.M., Liu Z.L., Wang Y., Yao K.L. Electrical Properties of Nanocrystalline CeO₂-Y₂O₃ Thin Films Prepared by the Sol-Gel Method. *Inorganic Materials*, 2003, **39** (7), P. 720–724.
- [57] Almjasheva O.V., Korytkova E.N., Maslov A.V., Gusarov V.V. Preparation of nanocrystalline alumina under hydrothermal conditions. *Inorganic Materials*, 2005, **41** (5), P. 4604–67.
- [58] Pozhidaeva O.V., Korytkova E.N., Romanov D.P., Gusarov V.V. Formation of ZrO₂ nanocrystals in hydrothermal media of various chemical compositions. *Russian Journal of General Chemistry*, 2002, **72** (6), P. 849–853.
- [59] Komlev A.A., Gusarov V.V. Mechanism of Nanocrystals Formation of the Spinel Structure in the MgO–Al₂O₃–H₂O System under the Hydrothermal Conditions. *Russian Journal of General Chemistry*, 2011, **81** (1), P. 2222–230.
- [60] Tomkovich M.V., Andrievskaya E.R., Gusarov V.V. Formation under hydrothermal conditions and structural features of nanoparticles based on the system ZrO₂-Gd₂O₃. *Nanosystems: Physics, Chemistry, Mathematics*, 2011, **2** (2), P. 6–14 (In Russian).
- [61] Bugrov A.N., Almjasheva O.V. Formation of nanoparticles Cr₂O₃ in hydrothermal conditions. *Nanosystems: Physics, Chemistry, Mathematics*, 2011, **2** (4), P. 126–132 (In Russian).
- [62] Gusarov V.V., Ishitina Zh.N., Malkov A.A., Malygin A.A. Peculiarities of the solid-phase chemical reaction in formation of mullite in the nanosize film composition. *Dokl. Akad. Nauk*, 1997, **357** (2), P. 203–205 (In Russian).
- [63] Gusarov V.V. Fast Solid-Phase Chemical Reactions. *Russian J. of Gen. Chem.*, 1997, **67** (12), P. 1846–1851.
- [64] Kolenko Yu.V., Burukin A.A., Churagulov B.R. Hydrothermal synthesis of nanocrystalline powders of various crystalline phases of ZrO₂ and TiO₂. *Russian Journal of Inorganic Chemistry*, 2002, **47** (1), P. 1609–1615.
- [65] Pourmortazavi S.M., Marashianpour Z., Karimi M.S., Mohammad-Zadeh M. Electrochemical synthesis and characterization of zinc carbonate and zinc oxide nanoparticles. *Journal of Molecular Structure*, 2015, **1099**, P. 232–238.
- [66] Harra J., Nikkanen J.-P., et al. Gas phase synthesis of encapsulated iron oxidetitanium dioxide composite nanoparticles by spray pyrolysis. *Powder Technology*, 2013, **243**, P. 46–52.
- [67] Srivastava V., Gusain D., Sharma Y.C. Synthesis, characterization and application of zinc oxide nanoparticles (n-ZnO). *Ceramics International*, 2013, **39** (8), P. 9803–9808.
- [68] Haider M.A., Capizzi A.J., Murayama M., McIntosh S. Reverse micelle synthesis of perovskite oxide nanoparticles. *Solid State Ionics*, 2011, **196** (1), P. 65–72.
- [69] Bermejo E., Becue T., Lacour C., Querton M. Synthesis of nanoscaled iron particles from freeze-dried precursors. *Powder Technology*, 1997, **94** (1), P. 29–34.
- [70] Khayati G.R., Nourafkan E., Karimi G., Moradgholi J. Synthesis of cuprous oxide nanoparticles by mechanochemical oxidation of copper in high planetary energy ball mill. *Advanced Powder Technology*, 2013, **24** (1), P. 301–305.
- [71] Bayal N., Jeevanandam P. Synthesis of TiO₂-MgO mixed metal oxide nanoparticles via a sol-gel method and studies on their optical properties. *Ceramics International*, 2014, **40** (10), Part A, P. 15463–15477.
- [72] Kudryavtsev Yu.D., Fesenko L.N. Behavior of Porous Nickel during Alternating Current Electrolysis. *Sov. Electrochemistry*, 1976, **12** (3), P. 344–348.
- [73] Kudryavtsev Yu. D., Kukoz F.I., Fesenko L.N. Experimental Study Concerning the Current Distribution in a Porous Nickel Electrode During Polarization with Alternating Current. *Sov. Electrochemistry*, 1975, **11** (3), P. 352–355.
- [74] Bespalova Zh. I., Ivanov V.V., Smirnitskaya I.V. Fabrication of a Titanium Anode with an Active Coating Based on Mixed Oxides of Base Metals. *Russian Journal of Applied Chemistry*, 2010, **83** (2), P. 242–246.
- [75] Galushkin N.E., Kudryavtsev Yu.D. The Effect of External Current Frequency on Depth Distribution of the Quantity of Electricity Passed Through a Porous Electrode. *Russian Journal of Electrochemistry*, 1993, **29** (10), P. 1030–1032.
- [76] Galushkin N.E., Yazvinskaya N.N., Galushkin D.N. Generalized Model for Self-Charge Process in Alkaline Batteries. *Journal of The Electrochemical Society*, 2012, **159** (8), P. 1315–1317.
- [77] Galushkin N.E., Fesenko L.N. Simulating Decomposition of Hydrogen Sulfide in a Three-Dimensional Electrofilter. *Russian Journal of Electrochemistry*, 1997, **33** (8), P. 852–856.
- [78] Method of Making Selective Coating, Patent. 2393275 Russia: MPK C 25D 11/10, F24J 2/48, Bespalova Z.I., Klushin V.A., Djachishin A.S. No. 2009130707/02, Issue No. 18, 7 p.
- [79] Bespalova Zh.I., Lovpache Yu.A., Lipkin M.S. et al. Composite Coatings Based on Copper Oxides Electrodeposited from Solutions and on Polymers. *Russian Journal of Applied Chemistry*, 2006, **79** (7), P. 1105–1109.
- [80] Erokhin A.L., Lubimov V.V., Ashitkov R.V. Model of Oxide Coatings Formation During Plasma-Electrolytic Oxidizing of Aluminum in Silicate Solutions. *Physics and Chemistry of Materials Treatment*, 1996, **5**, P. 39–44.
- [81] Galushkin D.N., Yazvinskaya N.N., Galushkin N.E. Investigation of the process of thermal runaway in nickel-cadmium accumulators. *Journal of Power Sources*, 2008, **177** (2), P. 610–616.
- [82] Ivanova N.D., Ivanov S.V., Boldyrev E.I. et al. Thin-Film Cathode Materials Based on Chromium Oxides. *Russian Journal of Applied Chemistry*, 2003, **76** (7), P. 1067–1069.
- [83] Lukiyanchuk I.V., Rudnev V.S., Panin E.S. et al. Modification with Manganese of Anodic Layers Containing Tungsten Oxides. *Russian Journal of Applied Chemistry*, 2003, **76** (10), P. 1597–1599.
- [84] Legagneur V., Liao J.-H., et al. Li₂Mn(VO₃)₄·2H₂O: synthesis, crystal structure, thermal behavior and lithium insertion/deinsertion properties. *Solid State Ionics*, 2000, **133**, P. 161–170.
- [85] Apostolova R.D., Shembel E.M., Nagirnyi V.M. Synthesis and Investigations of Electrolytic Sodium-Vanadium Oxide Compounds for Cathodes of Lithium Batteries: The Production of Compounds with Stable Initial Characteristics. *Russian Journal of Electrochemistry*, 2000, **36** (1), P. 36–42.
- [86] Nagirnyi V.M., Apostolova R.D., Baskevich A.S., Shembel E.M. Joint Electrolytic Deposition of Vanadium (V) and Chromium (III) Oxides from Aqueous Sulfate Solutions. *Russian Journal of Applied Chemistry*, 2004, **77** (11), P. 1777–1780.
- [87] Shembel E.M., Apostolova R.D., Nagirnyi V.M. Electrochemical Synthesis of the Cathode Materials Based on Metal Oxides for Lithium Secondary Batteries. *The 197th Meeting of the Electrochemical Society: Abstracts of Papers*, 2000, Toronto, P. 105.

- [88] Nagirnyi V.M., Apostolova R.D., et al. Joint Electrolytic Deposition of Vanadium and Manganese Oxides. *Russian Journal of Applied Chemistry*, 2002, **75** (4), P. 552–557.
- [89] Zoski C.G. *Handbook of Electrochemistry*. Elsevier, 2007, 934 p.
- [90] Apostolova R.D., Kolomoets O.V., Danilov M.O., Shembel E.M. Electrolytic Co, Ni–Bimetal sulfide Composites with Hydrophilized Multi-Wall Carbon Nanotubes in a Prototype Lithium Accumulator. *Surface Engineering and Applied Electrochemistry*, 2014, **50** (1), P. 18–27.
- [91] Nagirnyi V.M., Apostolova R.D., et al. Electrolytic Deposition of Cobalts (III) Oxide in the Presence of Nickel (II) and Chromium (III) Ions. *Russian Journal of Applied Chemistry*, 2002, **75** (6), P. 905–910.
- [92] Nagirnyi V.M., Apostolova R.D., Baskevich A.S., Shembel E.M. Anodic Deposition of Vanadium (V) Oxide from Solutions in the Presence of Nickel Ions. *Russian Journal of Applied Chemistry*, **75** (12), P. 1968–1971.
- [93] Nagirnyi V.M., Apostolova R.D., Shembel E.M. Electrodeposition of Molybdenum Oxide and Its Structural Characteristics. *Russian Journal of Applied Chemistry*, 2006, **79** (9), P. 1438–1442.
- [94] Nagirnyi V.M., Apostolova R.D., Baskevich A.S., et al. Electrolytic Preparation of Vanadium (V) Oxide from Oxovanadium (IV) Sulfate Solutions in the Presence of Sodium Ions. *Russian Journal of Applied Chemistry*, 2001, **74** (9), P. 1470–1473.
- [95] Nagirnyi V.M., Apostolova R.D., Baskevich A.S., et al. Electrolytic Preparation of Vanadium (V) Oxide from Saturated Solutions of Ammonium Metavanadate. *Russian Journal of Applied Chemistry*, 2001, **74** (9), P. 1474–1478.
- [96] Nagirnyi V.M., Apostolova R.D., Baskevich A.S., et al. Electrolytic Synthesis of Binary Oxide Systems Based on Manganese (II) Oxide. *Russian Journal of Applied Chemistry*, 2002, **75** (2), P. 213–218.
- [97] Nagirnyi V.M., Apostolova R.D., Baskevich A.S., Shembel E.M. Electrolytic Deposition of Molybdenum Oxide from Aqueous Solutions at Room Temperature. *Russian Journal of Applied Chemistry*, 2004, **77** (1), P. 71–73.
- [98] Nagirnyi V.M., Apostolova R.D., Shembel E.M. Surface Morphology of Electrolytic Deposits of Vanadium, Cobalt, and Manganese Oxides. *Russian Journal of Applied Chemistry*, 2006, **79** (9), P. 1443–1446.
- [99] Belous A.G., Yanchevskii O.Z., Kramarenko A.V. Synthesis of Nanosize Particles of Cobalt and Nickel Oxides from Solutions. *Russian Journal of Applied Chemistry*, 2006, **79** (3), P. 345–350.
- [100] Poizot P., Laruelle S., et al. Nano-sized transition-metal oxides as negative-electrode materials for lithium-ion batteries. *Nature*, 2000, **407**, P. 496–499.
- [101] Nuli Y.N., Zhao S.L., Qin Q.Z. Nanocrystalline tin oxides and nickel oxide film anodes for Li-ion batteries. *J. Power Sources*, 2003, **14**, P. 113–120.
- [102] Ahmad A.S., El-Shobaky G.A., Al-Noaimi A.N., El-Shobaky H.G. Surface and catalytic properties of gamma-irradiated CuO and NiO catalysts. *Mater. Lett.*, 1996, **26**, P. 107–112.
- [103] Curri M.L., Agostiano A., Mavelli F. et al. Reverse micellar systems: self organized assembly as effective route for the synthesis of semiconductor nanocrystals. *Mater. Sci. Eng. C. Biomim. Mater., Sens. Syst.*, 2002, **22**, P. 423–426.
- [104] Dirksen J.A., Duval K., Ring T.A. NiO thin-film formaldehyde gas sensor. *Sensors and Actuators B: Chemical*, 2001, **80** (2), P. 106–115.
- [105] Hotový, I., Huran J., et al. Preparation and characterization of NiO thin films for gas sensor applications. *Vacuum*, 2000, **58**, P. 300–307.
- [106] Svegl F., Orel B., Hutchins M.G. et al. Structural and spectroelectrochemical investigations of sol-gel derived electrochromic spinel Co₃O₄ films. *J. Electrochem. Soc.*, 1996, **143**, P. 1532–1539.
- [107] Takashi T. First-principles Investigation of the Phase Stability for Ba_{1/3}Ba_{2/3}B₂O₇ Microwave Dielectrics with the Complex Perovskite Structure. *Jpn. J. Appl. Phys.*, 2000, **39**, P. 5637–5641.
- [108] Nagirnyi V.M., Apostolova R.D., Shembel E.M. Anodic Processes Occurring upon V₂O₅ Electrodeposition. *Russian Journal of Applied Chemistry*, 2007, **80** (1), P. 71–73.
- [109] Stepanova L.I., Ivashkevich L.S., Branitskii G.A. Hydrothermal Synthesis of Tungsten Molybdenum Mixed Oxides. *Russian Journal of Inorganic Chemistry*, 2009, **54** (10), P. 1553–1558.
- [110] Švachula J., Tichý J., Machek J. Oxidation of Propanal on Molybdenum–Vanadium Oxide Catalyst. *Catalysis Letters*, 1989, **3**, P. 257–262.
- [111] Neiman A.Ya., Trafieva M.F., Kostikov Yu.P. Chemism and mass–transfer routes during phase formation in the V₂O₅ – MoO₃. *Russian Journal of Inorganic Chemistry*, 2005, **50** (10), P. 1472–1484.
- [112] Sviridova T.V., Antonova A.A., Kokorin A.I. et al. Nanostructured Vanadium – Molybdenum Mixed Oxides Prepared by the Solvothermal Method. *Russian Journal of Physical Chemistry*, 2015, **9** (1), P. 22–28.
- [113] Shagisultanova G.A., Ardasheva L.P., Orlova I.A. Electro- and Photoelectroactivity of Thin-Layer Polymers Based on [NiSalen] and [NiSalphen] Complexes. *Russian Journal of Applied Chemistry*, 2003, **76** (10), P. 1631–1636.
- [114] Mikhailov O.V. Immobilization of (dd)heteronuclear hexacyanoferrates (II) in a gelatin matrix. *Russian Chemical Bulletin*, 2008, **57** (1), P. 8–17.
- [115] Airapetyan S.S., Balayan G.G., Khachatryan A.G. Synthesis and Some Characteristics of Magnetic Matrices for Fixation of Biologically Active Substances. *Russian Journal of Applied Chemistry*, 2001, **74** (3), P. 519–521.
- [116] Pimkov I.V., Lutsenko O.G., Golubchikov O.A. Immobilization of Cobalt Disulfophthalocyanine Complex on Polypropylene. *Russian Journal of Applied Chemistry*, 2007, **80** (5), P. 828–832.
- [117] Electroplating solution composition for organic polymer-zinc alloy composite plating and plated metal material using such composition. Patent EP 1719826 A1, MPK C 25D 5/26, C 25 D 15/02, C 25 D 3/56, Haruta Y., Hiraki T., Kubota K., N 04801689.3, 2006/45, 14 p.
- [118] Polymer coated particles having immobilized metal ions on the surfaces thereof. Patent 4677027 A US: MPK 32 B 15/08, B 32 B 19/02; B 32 B 19/04, Lindahl M., Porath J. N 06/786,857, N 788,857, 5 p.
- [119] Process for the surface-immobilization of anti-microbial polymers by metal deposition. Patent 0144657 US: MPK 25 D 9/02, C 25 D 205/316, Inhester M., Ottersbach P. N 10/645,553.
- [120] Pomogailo A.D. *Catalysis by polymer – immobilized metal complexes*. Gordon & Breach Science Publishing. Amsterdam, 1998, 322 p.
- [121] Tamizhevskij B.V. Assessment of the Effectiveness of Operating Solar Heating Installation in Russia. *Thermal Engineering*, 1996, **43** (5), P. 373–376.
- [122] Multilayer Selective Absorbing Coating for Solar Collector and Method of Making Said Coating. Patent 2407958 Russia: MPK F 24 J 2/48, Djachishin A.S., Jazvina I.M., Stadnik A.V. N 2008149287/06.

- [123] Alturaif H.A., ALOthman Z.A., Shapter J.G., Wabaidur S.M. Use of Carbon Nanotubes (CNTs) with Polymers in Solar Cells. *Molecules*, 2014 (<http://www.mdpi.com/journal/molecules>).
- [124] Multi-layer selective coating for solar collector. Patent 93028687 Russia: MPK F 24J2/02, Dyachshin A.S., Dremlyuga A.A., Saksonsky V.A., 93028687/06, Bull. No. 10.
- [125] Multi-Layer Selective Coating For Solar Collector. Patent 2044964 Russia: P6 F24J2/48, Dyachshin A.S., Dremlyuga A.A., Saksonsky V.A. N 93028687/06, Bull. No. 15.
- [126] Absorbing Coating. Patent 2271058 Russia: P H01Q17/00, Golovkov A.A., Verbitskij A.V. N 2004122349.09, Bull. No. 6.
- [127] Absorbing Coating For Attenuation of Reflected Electromagnetic Waves; Capacitance Element For Absorbing Coating; Inductance Element For Absorbing Coating. Patent 2125327 Russia: 6 H01Q17/00, Marushkin V.A. N 96102682/09, Bull. No. 8.
- [128] Absorbermaterial für solarthermische Anwendung Gew. 202006011147U1 DE, F24J2/48, NARVA Lichtquellen GmbH + Co. KG, 09618 Brand-Erbisdorf, N 202006011147U1; filed Sep.21.2006, date of patent Oct.26.2006.
- [129] Moldovanov K.A., Hecceck R., Skrynnikov A.M. Reflectivities of Light-Absorptive coatings Within Visible Wavelengths Range. *Proceeding of SPIE*, 2000, **4093**, P. 181–192.
- [130] Fredj N., Burleigh T.D. Transpassive Dissolution of Copper and Rapid Formation of Brilliant Colored Oxide Films. *Journal of Electrochemical Society*, 2011, **158** (4), P. 104–110.
- [131] Moldovanov K.A., Anisimova I.A., Skrynnikov A.M. Reflectivity of Al coating sputtered by using the nitrogencontaining plasma. *Proceeding of SPIE*, 2001, **4447**, P. 98–108.
- [132] Pigments Reflecting Optical Emission with Specified Long-Wave Border and Absorbing Emission with Specified Short-Wave Border or at Specified Wavelength. Patent 2127747 Russia: P6 C09C1/00, C09D5/32, C09D5/33Egorov Ju. P., Malinovskaja T.D. N 95110119/04, Bull. No. 9.
- [133] Singh S.M. Paints and Painting Procedures for Solar Energy Collectors. *Proceedings of "the Workshop on Solar Water Heating Systems"*, 1985, New Delhi, India, 6–10 May, P. 153–158.
- [134] ISO/CD 12592,2 Solar Energy-Materials for Flat-Plate Collectors. Qualification Test Procedure for Solar Surface Durability.
- [135] Mozalev A., Surganov A., Magaino S. Anodic Process for Forming Nanostructured Metal-Oxide Coatings for Large-Value Precise Microfilm Resistor Fabrication. *Electrochimica Acta*, 1999, **44** (21–22), P. 2891–3898.
- [136] Skoneczny W., Bara M. Aluminium Oxide Composite Layers Obtained by the Electrochemical Method in the Presence of Graphite. *Material Science – Poland*, 2007, **25** (4), P. 1053–1062.
- [137] Stojanov E., Popov D., Stoychev D. Bildung und Schutzwirkung von Oxidschichten and of Aluminum. *Galvanotechnik*, 1994, **85** (10), P. 3240–3247.
- [138] Yang S., Aoki Y., Skeldon P. et al. Growth of porous anodic alumina films in hot phosphate-glycerol electrolyte. *J. Solid State Electrochem.*, 2011, **15**, P. 689–696.
- [139] Patemarakis G., Moussoutzakis K. Aluminium anodizing in ultra-dense sulfate baths: discovery by overall kinetic and potentiometric studies of the critical role of interface colloidal $Al_2(SO_4)_3$ nanoparticles in the mechanism of growth and nanostructure of porous oxide coatings. *J. Solid State Electrochem.*, 2005, **9**, P. 205–233.
- [140] Koyama S., Aoki Y., Nagata S., Habazaki H. Formation and dielectric properties of anodic oxide films on Zr-Al alloys. *J. Solid State Electrochem.*, 2011, **15**, P. 2221–2229.
- [141] Henley V.F. *Anodic Oxidation of Aluminium and Its Alloys*. Pergamon Press, Oxford, 1982, 170 p.
- [142] Dolgovesova I.P., Bakovets V.V., Nikiforova G.L., Royak A.Ya. Distribution of Alloying Components During The Anodic-Spark Oxidation of Aluminum Alloys in Concentrated Sulfuric Acid. *Protection of Metals*, 1987, **23** (4), P. 515–518.
- [143] Korolev Y.A., Greish A.A., Kozlova L.M. et al. Glycerol Dehydroxylation in Hydrogen on a Raney Cobalt Catalyst. *Catalysis in Industry*, 2010, **2** (3), P. 287–289.
- [144] Gnedenkov S.V., Khrisanfova O.A., Ignateva L.N. et al. Aluminum Complexation with Metal Tartrates. *Russian Journal of Inorganic Chemistry*, 2005, **50** (12), P. 1925–1932.
- [145] Clark A. Oxides of the Transition Metals as Catalysts. *Ind. Eng. Chem.*, 1953, **45** (7), P. 1476–1480.
- [146] Temperoni G., Gignini P., Icovi M., Panero S. Non-stoichiometric molybdenum oxides as cathodes for lithium cells: Part III. cells based on $Mo_{18}O_{52}$. *J. Electroanal. Chem.*, 1980, **108** (2), P. 169–180.
- [147] Li Y.B., Bando Y., Golberg D., Kurasima K. Field emission from MoO_3 nanobelts. *Appl. Phys. Lett.*, 2002, **81**, P. 5048–5052.
- [148] Ressler T., Walter A., Huang Z.D., Bensch W. Structure and properties of a supported MoO_3 /SBA-15 catalyst for selective oxidation of propene. *Journal of catalysis*, 2008, **254** (2), P. 170–179.
- [149] Gervasini A., Wahba L., Finol M.D., Lamonier J.-F. Property and activity of molybdates dispersed on silica obtained from various synthetic procedures. *Materials Sciences and Applications*, 2012, **3**, P. 195–212.
- [150] Wang G., Ji Y., et al. Synthesis of molybdenum oxide nanoplatelets during crystallization of the precursor gel from its hybrid nanocomposites. *Chem. Mater.*, 2007, **19**, P. 979–981.
- [151] Prasada A.K., Kubinskin D.J., Gouma P.I. Comparison of sol-gel and ion beam deposited MoO_3 thin film gas sensors for selective ammonia detection. *Sensors and Actuators B*, 2003, **93**, P. 25–30.
- [152] Ivanovskaya M.I., Gurlo A. Ch., Lutynskaya E.V., Romanovskaya V.V. Effect of Heat Treatment Conditions on Formation of Paramagnetic Centers of Molybdenum in MoO_3 . *Russian Journal of General Chemistry*, 1997, **67** (11), P. 1683–1688.
- [153] Ivanova N.D., Boldyrev E.I., Stadnic O.A., Zheleznova L.I. Composition and Catalytic Properties of Co (II) Anodic Oxidation Products. *Ukrainskij Khimicheskij Zhurnal*, 2004, **70** (5–6), P. 51–53.
- [154] Tsyachny V.P., Shembel E.M., Apostolova R.D. et al. Chronovoltammetry of Electrolytic Molybdenum Oxides at the Electrochemical Intercalation/Deintercalation of Lithium Ions. *J. Solid State Electrochem.*, 2003, **8** (1), P. 20–22.
- [155] Beltowska-Lehman E. Kinetic Correlations in Codeposition of Coatings of Molybdenum-Iron Metal Alloys. *Journal of Applied Electrochemistry*, 1990, **20** (1), P. 132–138.
- [156] Podlaha E.J., Landolt D. Induced codeposition. I. An experimental investigation of Ni-Mo alloys. *J. Electrochem. Soc.*, 1996, **143** (3), P. 885–892.
- [157] Podlaha E.J., Landolt D. Induced codeposition. II. A mathematical model describing the electrodeposition of Ni-Mo alloys. *J. Electrochem. Soc.*, 1996, **143**, P. 893–899.

- [158] Podlaha E.J., Landolt D. Induced codeposition. III. Molybdenum alloys with nickel, cobalt and iron. *J. Electrochem. Soc.*, 1997, **144** (5), P. 1672–1680.
- [159] Gomez E., Pellicer E., Valles E. Detection and characterization of molybdenum oxides formed during the initial stages of cobalt-molybdenum electrodeposition. *Journal of Applied Electrochemistry*, 2003, **33**, P. 245–252.
- [160] Gomez E., Kipervaser Z.G., Pellice E., Valles E. Extracting deposition parameters for cobalt-molybdenum alloy from potentiostatic current transients. *Phys. Chem.*, 2004, **6**, P. 1340–1344.
- [161] Sabhapathi V.K., Hussain O.Md., et al. Optical absorption studies in molybdenum trioxide films. *Physica status solidi (a)*, 1995, **148** (1), P. 167–173.
- [162] Kuznetsov V.V., Pshenichkina T.V. Kinetics of Cathodic Reactions in the Electrodeposition of Cobalt-Molybdenum Alloy. *Russian Journal of Electrochemistry*, 2010, **46** (4), P. 401–410.
- [163] Kuznetsov V.V., Pavlov M.R., Kuznetsov K.V., Kudryavtsev V.N. Kinetics of Cathodic Processes of Deposition of Nickel-Molybdenum Alloys from an Ammonia-Citrate Electrolyte. *Russian Journal of Electrochemistry*, 2003, **39** (12), P. 1338–1341.
- [164] Gomez E., Pellicer E., Valles E. An approach to the first stages of cobalt-nickel-molybdenum electrodeposition in sulphate-citrate medium. *Journal of Electroanalytical Chemistry*, 2005, **580**, P. 222–230.
- [165] Gomez E., Pellicer E., Valles E. Developing plating baths for the production of cobalt-molybdenum films. *Surface and Coatings Technology*, 2005, **197** (2–3), P. 238–246.
- [166] Obradovic M.D., Stevanovic R.M., Despic A.R. Electrochemical deposition of Ni-W alloys from ammonia-citrate electrolyte. *Journal of Electroanalytical Chemistry*, 2003, **552**, P. 185–196.
- [167] McEvoy T.M., Stevenson K.J. Electrochemical quartz crystal microbalance study of the electrodeposition mechanism of molybdenum oxide thin films from peroxy-polymolybdate solution. *Analytica Chimica Acta*, 2003, **496** (1–2), P. 39–51.
- [168] Ibrahim M.A.M., Rehim Abd El, Moussa S.O. Electrodeposition of noncrystalline cobalt-tungsten alloys from citrate electrolytes. *Journal of Applied Electrochemistry*, 2003, **33** (7), P. 627–633.
- [169] Gomez E., Pellicer E., Valles E. Influence of the bath composition and the pH on the induced cobalt-molybdenum electrodeposition. *Journal of Electroanalytical Chemistry*, 2003, **556**, P. 137–145.
- [170] Murase K., Ando H., et al. Determination of Mo(VI) species and composition in Ni-Mo alloy plating baths by raman spectra factor analysis. *J. Electrochem. Soc.*, 2000, **147** (6), P. 2210–2217.
- [171] Nagirnyi V.M., Apostolova R.D., Shembel E.M. Electrodeposition of Molybdenum Oxide and Its Structural Characteristics. *Journal of Applied Electrochemistry*, 2006, **79** (9), P. 1438–1442.
- [172] Nagirnyi V.M., Apostolova R.D., Baskevich A.S., Shembel E.M. Electrolytic Synthesis of Complex Oxide Systems by Cathodic Deposition of Molybdenum Oxide from Aqueous Solutions in the Presence of Nickel (II) and Thiosulfate Ions. *Russian Journal of Applied Chemistry*, 2003, **76** (9), P. 1438–1443.
- [173] Sinkeviciute D., Baltrusaitis J., Dukstiene N. Layered molybdenum oxide thin films electrodeposited from sodium citrate electrolyte solution. *J. Solid State Electrochem.*, 2011, **15**, P. 711–723.
- [174] Danilov M.O., Ivanova N.D., Boldyrev E.I. et al. Nanostructured Composites for Power Cells Based on Molybdenum-modified Carbon Nanotubes. *Proceeding of Conference "11th Advanced Batteries, Accumulators and Fuel Cells, ABAF 2010"*, University of Technology, Faculty of Electrical Engineering Brno, Czech Republic, 19 September 2010 through 22 September 2010, P. 39–43.
- [175] Talanov V.M., Shirokov V.B. Tilting structures in spinels. *Acta Cryst.*, 2012, **A68**, P. 595–606.
- [176] Talanov V.M., Shirokov V.B. Atomic order in spinel structure – a group-theoretical analysis. *Acta Cryst.*, 2014, **A70**, P. 49–63.
- [177] Talanov V.M. Anion ordering in spinels. *Physica Status Solidi (A)*, 1989, **115** (1), K1–K4.
- [178] Talanov V.M. Calculation of structural parameters of spinels. *Physica Status Solidi (B)*, 1981, **106** (1), P. 99–106.
- [179] Bespalova Zh.I., Khramenkova A.V. Preparation of Oxide and Metal-Complex Polymer-Immobilized Composite coatings on the Steel Surface. *Russian Journal of Applied Chemistry*, 2012, **85** (11), P. 1681–1685.
- [180] Bespalova Zh.I., Khramenkova A.V. A study of the possibility of obtaining catalytically active oxide compounds on a solid support by transient electrolysis. *Russian Journal of Applied Chemistry*, 2013, **86** (4), P. 539–544.
- [181] Bespalova J.I., Khramenkova A.V., Abdala R.M., Dmitriev V.P. Study of the phase composition and structure of composite coatings based on transition- metal oxide compounds via X-ray diffraction and X-ray absorption fine structure spectroscop. *Journal of Surface Investigation. X-ray, Synchrotron and Neutron Techniques*, 2014, **8** (1), P. 60–65.
- [182] Method for Obtaining Coating from Metal Oxides on Steel. Patent 2449061 Russia: P C25D 11/34, C25D 3/56, Bespalova Zh.I., Smiritskaia I.V., Khramenkova A.V. N 2010142537/02, Bull. No. 12.
- [183] Cohen E., Gutoff E. *Modern Coating and Drying Technology*. Wiley-VCH, 1992, 336 p.
- [184] Delmon B. Catalyst Deactivation. *Proceeding of the 7th International Symposium "Studies in Surface Science and Catalysis"*, Cancun, Mexico, 1997, p. 39.
- [185] Atuchin V.V., Gavrilova T.A., Kostrovsky V.G. et al. Morphology and Structure of Hexagonal MoO₃ Nanorods. *Inorganic Materials*, 2008, **44** (6), P. 62–627.
- [186] Majumdar S., Sharma I.G. Oxidation Behavior of MoSi₂ and Mo(Si,Al)₂ Coated Mo–0.5Ti–0.1Zr–0.02C Alloy. *Intermetallics*, 2011, **19**, P. 541–545.
- [187] Tamizhmani G., Capuano G. Improved Electrocatalytic Oxygen Reduction Performance of Platinum Ternary Alloy-Oxide in Solid-Polymer-Electrolyte Fuel Cells. *J. Electrochem. Soc.*, 1994, **141** (4), P. 968–975.
- [188] Kuznetsov V.V., Kalinkina A.A., Pshenichkina T.V. Electrochemical Properties of Composite Materials Based on Platinum Modified with Molybdenum Compounds. *Russian Journal of Electrochemistry*, 2007, **43** (7), P. 776–781.
- [189] Wang Y., Fachini E.R., et al. Effect of Surface Composition of Electrochemically Codeposited Platinum/Molybdenum Oxide on Methanol Oxidation. *J. Electrochem. Soc.*, 2001, **148**, P. 222–226.
- [190] Talanov, V.M., Ereyskaya, G. P. *Fundamentals of Nanochemistry and Nanotechnology*, edited by V.M. Talanov. Novocherkassk: South-Russian State Polytechnical University. 2014, 524 p.
- [191] Talanov V.M., Ereyskaya G.P., Yuzyuk Y.I. *Introduction to Chemistry and Physics of Nanostructures and Nanostructured Materials*, edited by V.M. Talanov. Moscow: Academy of Natural Science, 2008, 389 p.

Synthesis and study of anhydrous lanthanide orthophosphate (Ln = La, Pr, Nd, Sm) nanowhiskers

K. I. Bryukhanova, G. E. Nikiforova, K. S. Gavrichev

Kurnakov Institute of General and Inorganic Chemistry of the Russian Academy of Sciences, Leninsky prospect 31, Moscow, 119991, Russia
bryuhanova@igic.ras.ru

PACS 61.46.-w, 81.20.-n

DOI 10.17586/2220-8054-2016-7-3-451-458

The effect of hydrothermal synthetic conditions on the obtaining of lanthanide orthophosphates LnPO_4 (Ln = La, Pr, Nd, Sm) with different structure, size and shape of particles was revealed. The optimum conditions for preparation of anhydrous nanoscale lanthanide orthophosphates with monoclinic structure were determined. The prepared nanowhiskers had lengths ranging from 0.4 μm (for LaPO_4) to 5 μm (for SmPO_4), and the diameter – from 30 nm (for LaPO_4) to 200 nm (for SmPO_4). The size of particles synthesized under similar conditions increased with decreased of lanthanide ion radius.

Keywords: nanowhisiker, lanthanides, orthophosphates, hydrothermal synthesis, size factor.

Received: 12 February 2016

1. Introduction

A preparation of inorganic materials containing nanosized particles (up to 100 nm) with a geometrical dimension below 3 is the actual task of the modern materials science. Nanoscale substances' properties, such as electronic, optical, chemical, thermal and mechanical properties [1–6] differ sufficiently from those of the bulk phase material. Usually, nanoparticles contain a significant quantity of substances adsorbed on their surface and the measurement of its own properties (in part, thermal and thermodynamic) is difficult. So the necessity arises to elaborate experimental routes for the synthesis of nanocrystalline substances without detectable amounts of adsorbed impurities.

Lanthanide orthophosphates of cerium subgroup (Ln = La – Gd) can be found in nature in the form of crystal hydrates $\text{LnPO}_4 \cdot (x + 0.5)\text{H}_2\text{O}$ [7] with hexagonal structure (space group P6_222 , mineral rhabdophane) or in the anhydrous form LnPO_4 with the monoclinic structure (space group $\text{P2}_1/c$, mineral monazite) [8, 9].

Lanthanide orthophosphates with these structures can be synthesized in the laboratory by different methods: a precipitation from the solutions, a sol-gel technique, a hydrothermal synthesis, a solid state reaction (ceramic method) [14], as well as by the application of microwave [10], sonochemical [11, 12] and mechanical treatments (high-energy milling) [13].

The precipitation from solutions and sol-gel methods allow preparation of mostly hexagonally-structured crystalline substances with the isometric micro- [15, 16] and nanoparticles [17, 18]. In rare instances an amorphous phase [19–21] or nanowhiskers [16] can also be obtained by above-mentioned ways. Subsequent sintering of these samples at temperatures above 700 °C leads to the formation of an anhydrous monoclinic phase [17, 19, 20, 22]. Moreover, it is noted that annealing can cause an increase in the particle size [23] that does not permit one to unambiguously attribute measured properties to nanoscale crystals. According to a literature review, the hydrothermal method is preferable for the synthesis of lanthanide orthophosphates with low-dimensional particles (the particles for whose the size in one direction is sufficiently larger than in the remaining directions), because this method makes it possible to obtain the completely uniform particles size avoiding an additional high-temperature sintering and a multi-stage treatment. By varying the hydrothermal synthesis parameters (temperature and time of treatment, ratio of initial reagents, pH), one can promote a preparation of final products with the controlled chemical composition, dimension, morphology and crystal structure.

The ratio of initial reagents, including a rare earth cation and a phosphate anion plays a key role in the phosphorous coordination generation [21] and, as a consequence, allows one to adjust the composition [20, 24] and morphology [16, 25] of the forming phase. An excess of phosphorous in the reagent mixture always leads to polyphosphates formation, and for this reason, an equimolar ratio of La:P is optimal for the preferred orthophosphate synthesis. Different compounds H_3PO_4 , $\text{NH}_4\text{H}_2\text{PO}_4$, $\text{Na}_3\text{PO}_4 \cdot 12\text{H}_2\text{O}$, P_2O_5 , organic compounds [26] are usually used as the phosphate group containing precursors.

The pH value plays a significant role in the formation of the final product, since it has an impact not only on the phase composition of the product, but also on the preferential growth of particles in one direction or

another [27]. It was noted [1,28–30] that an increasing of pH value from 0 to 10 leads to the change of a particle shape from nanowhiskers to isometric nanoparticles and, moreover, to the formation of rare earth (RE) hydroxide impurities [8,28,31]. The pH value near 1 leads to the formation of unidimensional structure samples.

A great deal of attention in the literature is devoted to the influence of synthetic parameters on the phase composition and the morphology of the obtained particles, however, this information is fragmented. Thus, authors [1, 6, 8, 25, 29, 34] describe the influence of the synthesis temperature not only on the phase composition (hexagonal or monoclinic phase), and also on the change of the shape and dimension of the particles. While the influence of hydrothermal processing time on the final phase composition is described in articles [25,32], the information regarding the morphology changes in the particles is missing. In [33], only the effect of synthesis time on particle size of the obtained substances is reported.

The goal of this research is the elaboration of a synthesis route to one-dimensional anhydrous cerium subgroup lanthanide orthophosphates (nanowhiskers) for subsequent studies of its thermal and thermodynamic properties.

2. Experimental

2.1. Synthesis

High-purity RE oxides La_2O_3 , Pr_6O_{11} , Nd_2O_3 , Sm_2O_3 (99.99 mass%), ammonium dihydrogenphosphate $\text{NH}_4\text{H}_2\text{PO}_4$ (“pure for analysis” grade), hydrochloric acid (“pure” grade) concentration 34.68 mass% and distilled water were used as the initial reagents.

RE Oxides were dissolved in hydrochloric acid and mixed with ammonium dihydrogenphosphate in a 1:1 Ln:P ratio. Hydrothermal synthesis was conducted under “soft” conditions, varying the temperature (120 °C, 160 °C and 200 °C) and time of processing (55 and 100 hours) in a stainless steel autoclave with Teflon liner ($V = 7$ mL). The autoclave filling coefficient was 0.75 – 0.80 and pH = 0 – 1. The rate of cooling after hydrothermal treatment to temperatures of 40 – 60 °C was ~ 1 °C/min. The obtained sediments were washed with distilled water from mother liquor at room temperature using the blue tape ash-free filters and was then aerobically dried at 80 °C for 6 h.

2.2. Samples characterization

X-ray powder diffraction (XRD) patterns were performed on a BrukerAdvance D8 diffractometer (Cu $K\alpha_{cp}$ radiation, $\lambda = 1.5418$ Å, reflection geometry, $2\theta = 10 - 60$ degree, step 0.02).

The size and morphology of the formed particles were evaluated by the scanning electron microscopy (SEM) CrossBeam Zeiss NVision 40 ($U = 1$ kV).

The water content and the thermal stability of the lanthanide orthophosphates were studied by differential scanning calorimetry and thermogravimetric analysis (DSC/TG) using Netzsch STA 449F1 Jupiter® in the inert gas (helium 6.0) flow.

The surface specific area of powder was determined by low-temperature nitrogen adsorption method in ATX.06 Katakonusing the BET model.

3. Result and discussion

Synthesis parameters, structure type and particles size of the lanthanide orthophosphates with the general formula LnPO_4 (Ln = La – Sm) are presented in Table 1. The XRD patterns of the LnPO_4 samples prepared at 200 °C/55 h by hydrothermal method are shown in Fig. 1. All reflections can be readily indexed to a pure monoclinic phase (space group $P2_1/c$) and are in agreement with data for RE orthophosphates from ICDD PDF2 (JCPDS 84-0600, 83-0653, 83-0654 and 46-1329 for orthophosphates of La, Pr, Nd and Sm, respectively). But hexagonal phase peaks are also detected in diffractograms of the LaPO_4 and PrPO_4 samples synthesized at 120 °C and 160 °C (these data are not shown). The peak shapes show that the samples were well-crystallized. Unit cell parameters calculated from X-ray patterns are given in Table 2. There are only unit cell parameters for isometric particles or single crystals of La, Pr, Nd and Sm orthophosphates in the literature. Comparison of crystallographic characteristics for particles with different morphologies allows one to understand the nucleation process better. As is shown in the Table 2, the parameters a , b and angle β is slightly larger for nanowhiskers than what is typical for anisotropic crystal growth [8,27].

Figure 2 displays the thermal behavior for monoclinic LnPO_4 (Ln = La, Pr, Nd, Sm) nanowhiskers obtained at 200 °C/55 h. All samples were shown to not contain adsorbed water and volatile impurities. Specimens synthesized at 120 °C and 160 °C (La4, Pr3 and Pr4) contain a small amount of water, which confirms the presence of hexagonal phase substances in the final product (data are not given). These results are in good agreement with the results of XRD.

TABLE 1. Synthesis conditions (pH = 0 – 1), crystal structures and morphology of LnPO₄ (Ln = La, Pr, Nd and Sm) nanowhiskers

Sample	t, °C	τ, h	Crystal system*	Particle size, μm (length/diameter)	S _{surf} , m ² /g
LaPO₄					
La1	200	55	M	0.5 – 0.7 / 0.045	12.0
La2	200	100	M	0.4 – 0.6 / 0.08 – 0.10	8.9
La3	160	55	M	0.6 – 0.8 / 0.05	—
La4	120	55	M + H	—	—
PrPO₄					
Pr1	200	55	M	1.0 – 1.5 / 0.03 – 0.06	15.7
Pr2	200	100	M	1.0 – 2.0 / 0.05 – 0.10	11.0
Pr3	160	55	M + H	0.2 – 2.0 / 0.04 – 0.09	—
Pr4	160	100	M + H	—	—
NdPO₄					
Nd1	200	55	M	0.2 – 2.0 / 0.05	19.9
Nd2	200	100	M	0.8 – 1.5 / 0.04 – 0.10	9.3
Nd3	160	100	M	—	—
SmPO₄					
Sm1	200	55	M	1.0 – 5.0 / 0.12 – 0.25	4.9
Sm2	200	100	M	0.8 – 3.0 / 0.12 – 0.25	5.3
Sm3	160	100	M	—	—
*M – monoclinic form, H – hexagonal form.					

The average size of particles presented in Table 1 is determined from SEM images. Figs. 3–6 show the particles have the shape of whiskers with diameter from 30 nm (for La-, Pr- and NdPO₄) to 120 nm (for SmPO₄) and length up to several microns.

Increasing the hydrothermal treatment time leads to particle growth and, as a consequence, a decreasing in the surface area (Table 1, Figs. 3–6). This is a typical for La1 and La2, Pr1 and Pr2, Nd1 and Nd2 samples. The exception is samarium orthophosphate, whose particles are larger in diameter and their size doesn't appreciably change with prolonged treatment time.

The analysis of obtained data shows that decreased treatment temperature results in the formation of a biphasic product which can be associated both with the formation of numerous nucleation centers and the thermodynamic factors. It should be noted that an increase of the treatment time, even up to 100 hours at “low” temperature, does not result in the formation of a pure monoclinic phase (Pr3 and Pr4).

The influence of the synthesis temperature on the morphology and size of lanthanum orthophosphate particles can be traced in more details. Lowering the temperature (with constant treatment time) from 200 °C (La1) – 160 °C (La3) to 120 °C (La4) leads to a decrease in the particle size, the origination of more defective particle surface and the large deviation in the grain size and, finally, the formation of a second phase (see Table 1, Fig. 3). From SEM images, we can visualize the transformation of the product morphologies over several treatment times and temperatures.

To summarize the results of the given “time-temperature” treatment, one can conclude that the final phase composition strongly depends on the treatment temperature, while the particle size and the degree of crystallinity for the samples are equally influenced by both the synthesis temperature and the time.

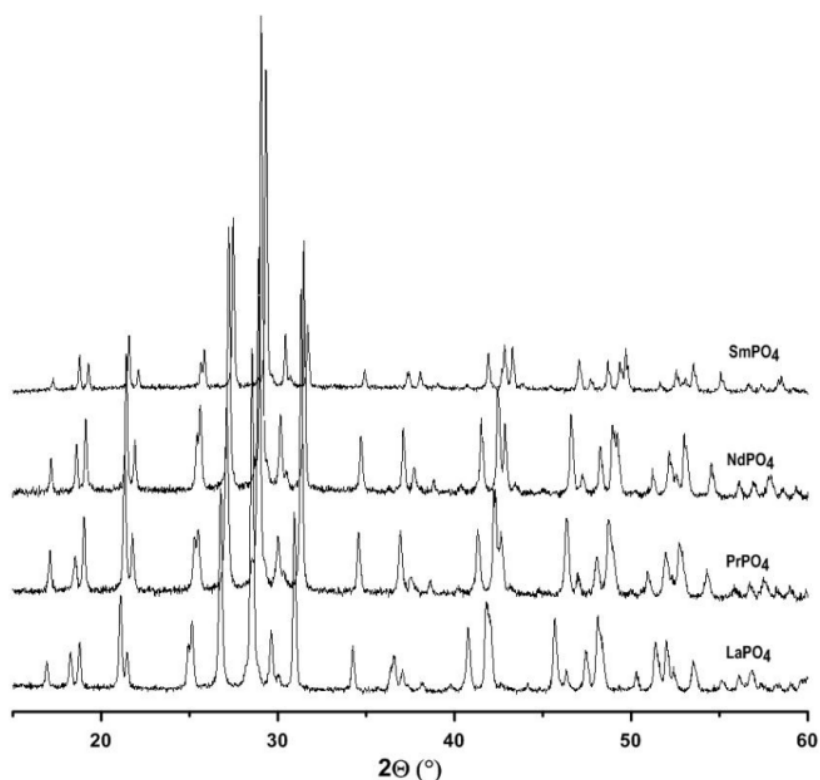


FIG. 1. X-ray diffraction patterns of LnPO_4 ($\text{Ln} = \text{La}, \text{Pr}, \text{Nd}, \text{Sm}$) synthesized at $200\text{ }^\circ\text{C}/55\text{ h}$

TABLE 2. The comparison of unit cell parameters of samples synthesized at $200\text{ }^\circ\text{C}/55\text{ h}$ with literature data

Substance	a , Å	b , Å	c , Å	B , °	V , Å ³	Reference
LaPO₄	6.8485(31)	7.0818(40)	6.5085(31)	103.431(37)	307.02(27)	La1
Isometric	6.8406(1)	7.0736(1)	6.5126(1)	103.310(1)	306.7(3)	[35]
Isometric	6.841(2)	7.079(3)	6.508(4)	103.33(7)	306.7(4)	[36]
Single crystal	6.8313(10)	7.0705(9)	6.5034(9)	103.27(1)	305.7(5)	[9]
PrPO₄	6.7721(42)	6.9938(34)	6.4374(49)	103.728(58)	296.18(33)	Pr1
Isometric	6.7687(5)	6.9900(3)	6.4439(4)	103.5(1)	296.0(5)	[37]
Single crystal	6.4304(4)	6.9785(5)	6.7623(5)	103.516(1)	295.05(4)	[38]
Single crystal	6.741(3)	6.961(4)	6.416(3)	103.63(3)	292.6(5)	[39]
NdPO₄	6.7546(69)	6.9725(79)	6.4169(65)	103.770(79)	293.53(54)	Nd1
Isometric	6.7392(9)	6.9621(6)	6.4053(6)	103.6(1)	292.1(4)	[37]
Isometric	6.7426(3)	6.9574(2)	6.4097(3)	103.6624(3)	292.2(3)	[40]
Single crystal	6.722(1)	6.933(1)	6.390(2)	103.72(2)	289.3(2)	[39]
SmPO₄	6.7027(38)	6.9068(24)	6.3723(30)	103.930(50)	286.33(24)	Sm1
Isometric	6.6891(3)	6.8958(3)	6.3770(6)	103.9(1)	285.5(3)	[37]
Single crystal	6.6818(12)	6.8877(9)	6.3653(9)	103.86(1)	284.4(5)	[9]
Single crystal	6.669(1)	6.868(2)	6.351(1)	103.92(2)	282.4(2)	[41]

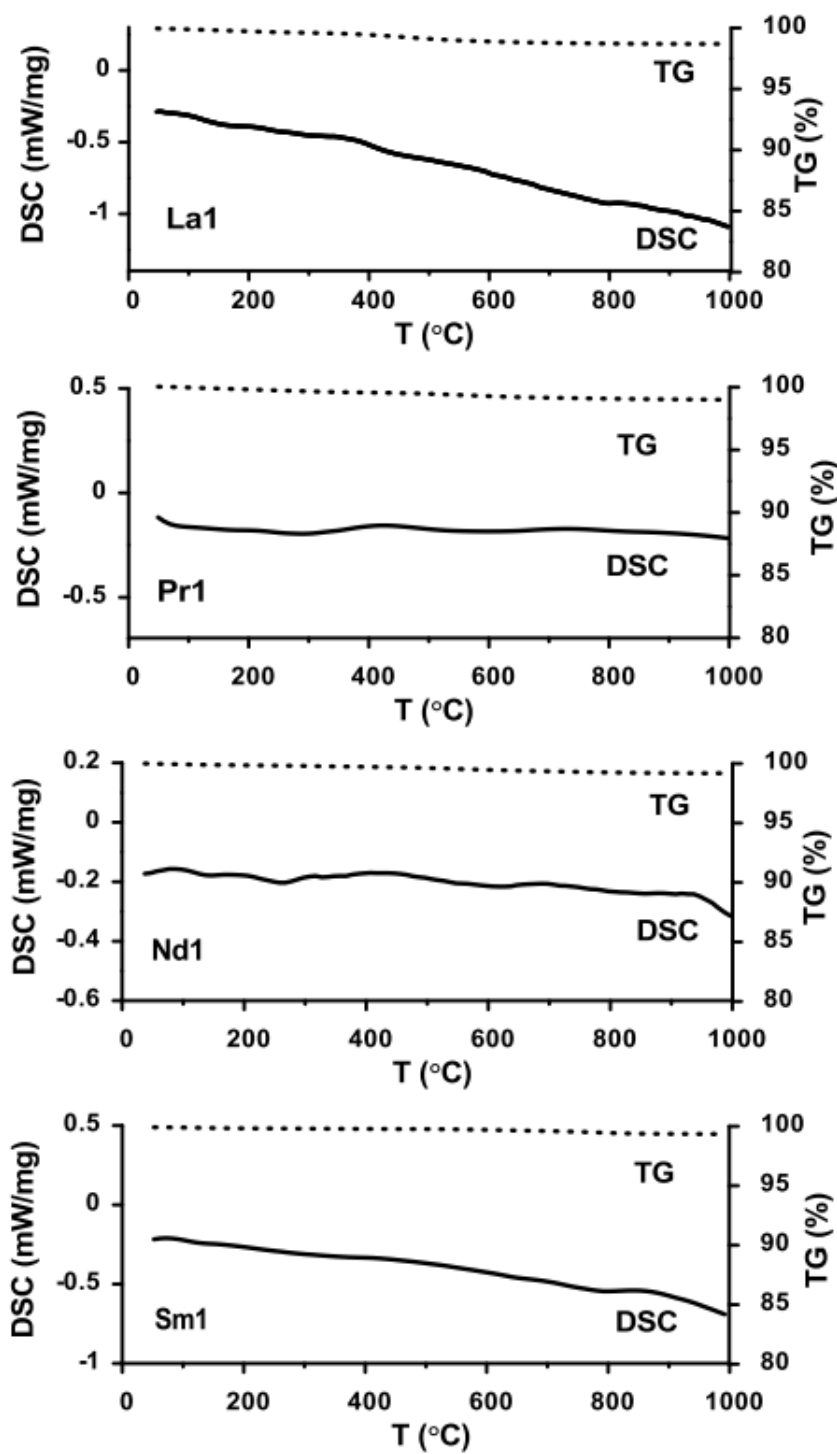


FIG. 2. DSC/TG plots of LnPO_4 (Ln = La, Pr, Nd, Sm) synthesized at 200 °C/55 h

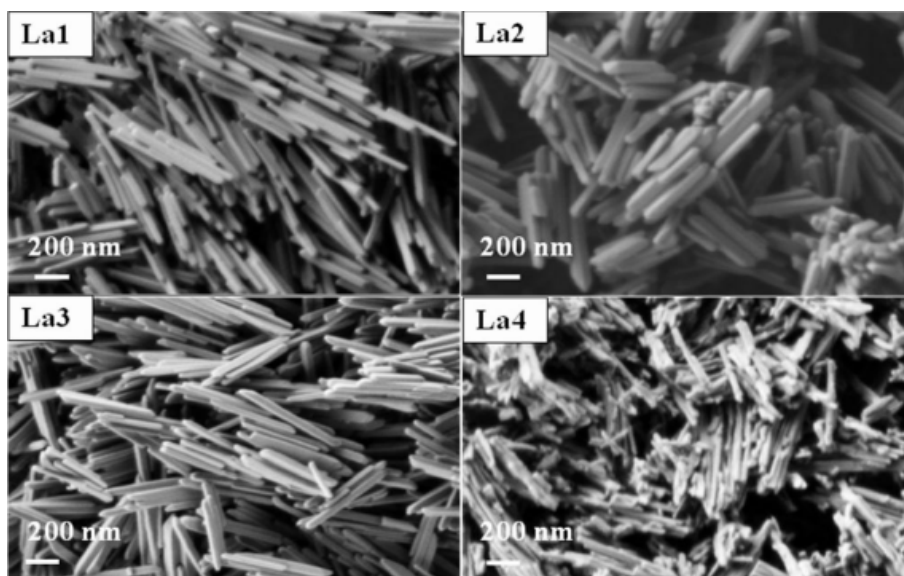


FIG. 3. SEM images of LaPO₄ synthesized at several conditions (°C/ τ , h): 1 – 200/55, 2 – 200/100, 3 – 160/55, 4 – 120/55

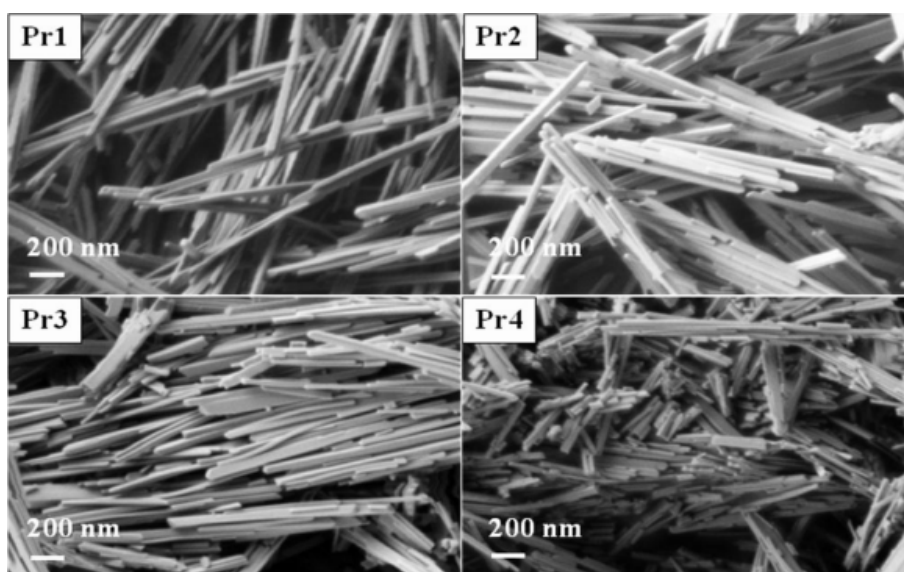


FIG. 4. SEM images of PrPO₄ synthesized at several conditions (°C/ τ , h): 1 – 200/55, 2 – 200/100, 3 – 160/55, 4 – 160/55

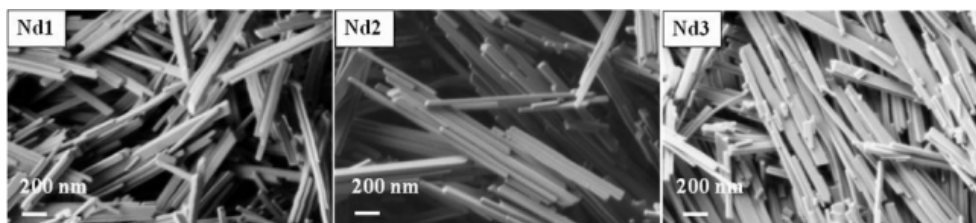


FIG. 5. SEM images of NdPO₄ synthesized at several conditions (°C/ τ , h): 1 – 200/55, 2 – 200/100, 3 – 160/100

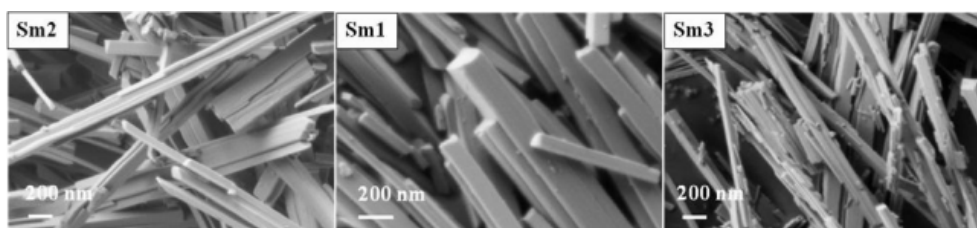


FIG. 6. SEM images of SmPO_4 synthesized at several conditions (°C/ τ , h): 1 – 200/55, 2 – 200/100, 3 – 160/100

4. Conclusions

The hydrothermal synthesis conditions for the preparation of monoclinic LaPO_4 , PrPO_4 , NdPO_4 and SmPO_4 nanowhiskers without any surface and crystal water has been elaborated. The relationship of the size and morphology of the obtained nanoparticles with the treatment time and temperature was revealed.

Acknowledgements

This work was performed using the equipment of the Joint Research Centre of IGIC RAS.

This study was carried out as the part of the State Assignment on fundamental researches of the Kurnakov Institute of General and Inorganic Chemistry and Research program of the Presidium of the Russian academy of sciences “Scientific foundations of new functional materials production”.

References

- [1] Guan H., Zhang Y. Hydrothermal synthesis and characterization of hexagonal and monoclinic neodymium orthophosphate single-crystal nanowires. *J. Solid State Chem.*, 2004, **177**(3), P. 781–785.
- [2] Yan R., Sun X., et al. Crystal structures, anisotropic growth, and optical properties: controlled synthesis of lanthanide orthophosphate one-dimensional nanomaterials. *Chemistry*, 2005, **11**(7), P. 2183–95.
- [3] Yan Z.-G., Zhang Y.-W., et al. General synthesis and characterization of monocrystalline 1D-nanomaterials of hexagonal and orthorhombic lanthanide orthophosphate hydrate. *J. Cryst. Growth*, 2004, **262**(1–4), P. 408–414.
- [4] Yu L., Li D., et al. Dependence of morphology and photoluminescent properties of $\text{GdPO}_4:\text{Eu}^{3+}$ nanostructures on synthesis condition. *Chem. Phys.*, 2006, **326**(2–3), P. 478–482.
- [5] Yu L., Song H., et al. Electronic transition and energy transfer processes in $\text{LaPO}_4\text{-Ce}^{3+}/\text{Tb}^{3+}$ nanowires. *J. Phys. Chem. B*, 2005, **109**(23), P. 114505.
- [6] Lin S., Dong X., Jia R., Yuan Y. Controllable synthesis and luminescence property of LnPO_4 (Ln = La, Gd, Y) nanocrystals. *J. Mater. Sci. Mater. Electron.*, 2010, **21**(1), P. 38–44.
- [7] Mooney R. C. L. X-ray diffraction study of cerous phosphate and related crystals. I. Hexagonal modification. *Acta Crystallogr.*, 1950, **3**(5), P. 337–340.
- [8] Fang Y.-P., Xu A.-W., et al. Systematic synthesis and characterization of single-crystal lanthanide orthophosphate nanowires. *J. Am. Chem. Soc.*, 2003, **125**(51), P. 16025–16034.
- [9] Ni Y., Hughes J.M., et al. Crystal chemistry of the monazite and xenotime structures. *Am. Mineralogist*, 1995, **80**, P. 21–26.
- [10] Bühler G., Feldmann C. Microwave-assisted synthesis of luminescent LaPO_4 : Ce, Tb nanocrystals in ionic liquids. *Angew. Chem. Int. Ed. Engl.*, 2006, **45**(29), P. 48647.
- [11] Brown S.S., Im H.-J., Rondinone A.J., Dai S. Facile, alternative synthesis of lanthanum phosphate nanocrystals by ultrasonication. *J. Colloid Interface Sci.*, 2005, **292**(1), P. 127–132.
- [12] Yu C., Yu M., et al. Facile sonochemical synthesis and photoluminescent properties of lanthanide orthophosphate nanoparticles. *J. Solid State Chem.*, 2009, **182**, P. 339–347.
- [13] Diaz-Guillén J.A., Fuentes A.F., Gallini S., Colomer M.T. A rapid method to obtain nanometric particles of rhabdophane $\text{LaPO}_4\cdot n\text{H}_2\text{O}$ by mechanical milling. *J. Alloys Compd.*, 2007, **427**(1–2), P. 87–93.
- [14] Bregiroux D., Audubert F., et al. Solid-state synthesis of monazite-type compounds LnPO_4 (Ln = La to Gd). *Solid State Sci.*, 2007, **9**(5), P. 432–439.
- [15] Kijkowska R. Preparation of lanthanide orthophosphates. *J. Mater. Sci.*, 2003, **8**(38), P. 229–233.
- [16] Boakye E.E., Mogilevsky P., Hay R.S. Synthesis of Nanosized Spherical Rhabdophane Particles. *J. Am. Ceram. Soc.*, 2005, **88**(10), P. 2740–46.
- [17] Gavrichev K.S., Ryumin M.A., et al. Thermal behavior of $\text{LaPO}_4\cdot n\text{H}_2\text{O}$ and $\text{NdPO}_4\cdot n\text{H}_2\text{O}$ nanopowders. *J. Therm. Anal. Calorim.*, 2010, **102**(2), P. 809–811.
- [18] Li L., Jiang W., et al. Improved Luminescence of Lanthanide(III)-Doped Nanophosphors by Linear Aggregation. *J. Phys. Chem. C*, 2007, **111**, P. 4111–15.
- [19] Ruigang W., Wei P., et al. Synthesis and sintering of LaPO_4 powder and its application. *Mater. Chem. Phys.*, 2003, **79**(1), P. 30–36.
- [20] Chen P., Mah T. Synthesis and characterization of lanthanum phosphate sol for fibre coating. *J. Mater. Sci.*, 1997, **32**(14), P. 3863–67.
- [21] Buissette V., Moreau M., et al. Colloidal Synthesis of Luminescent Rhabdophane $\text{LaPO}_4:\text{Ln}^{3+}\cdot x\text{H}_2\text{O}$ (Ln = Ce, Tb, Eu, $x \approx 0.7$) Nanocrystals. *Chem. Mater.*, 2004, **16**(19), P. 3767–73.

- [22] Kijkowska R. Thermal decomposition of lanthanide orthophosphates synthesized through crystallisation from phosphoric acid solution. *Thermochim. Acta*, 2003, **404**(1–2), P. 81–88.
- [23] Yu M., Lin J., et al. Sol-gel synthesis and photoluminescent properties of $\text{LaPO}_4:A$ ($A = \text{Eu}^{3+}, \text{Ce}^{3+}, \text{Tb}^{3+}$) nanocrystalline thin films. *J. Mater. Chem.*, 2003, **13**(6), P. 1413–19.
- [24] Byrappa K. Preparative methods and growth of rare earth phosphates. *Prog. Cryst. Growth Charact.*, 1986, **13**(3), P. 163–196.
- [25] Bao J.R., Zhu X.W., et al. Hydrothermal Synthesis of Neodymium Orthophosphate with Controlled Structure and Morphology. *Adv. Mater. Res.*, 2012, **399–401**, P. 635–640.
- [26] Onoda H., Nariai H., et al. Formation and catalytic characterization of various rare earth phosphates. *J. Mater. Chem.*, 2002, **12**(6), P. 1754–60.
- [27] Peng Z.A., Peng X. Nearly Monodisperse and Shape-Controlled CdSe Nanocrystals via Alternative Routes: Nucleation and Growth. *J. Am. Chem. Soc.*, 2002, **124**(13), P. 3343–53.
- [28] Zhang Y.-W., Yan Z.-G., et al. General Synthesis and Characterization of Monocrystalline Lanthanide Orthophosphate Nanowires. *Eur. J. Inorg. Chem.*, 2003, **2003**(22), P. 4099–4104.
- [29] Zhang Y., Guan H. The growth of lanthanum phosphate (rhabdophane) nanofibers via the hydrothermal method. *Mater. Res. Bull.*, 2005, **40**(9), P. 1536–43.
- [30] Dong H., Liu Y., et al. Controlled synthesis and characterization of LaPO_4 , $\text{LaPO}_4:\text{Ce}^{3+}$ and $\text{LaPO}_4:\text{Ce}^{3+}, \text{Tb}^{3+}$ by EDTA assisted hydrothermal method. *Solid State Sci.*, 2010, **12**(9), P. 1652–60.
- [31] Wang X., Li Y. Synthesis and characterization of lanthanide hydroxide single-crystal nanowires. *Angew. Chem. Int. Ed. Engl.*, 2002, **41**(24), P. 4790–93.
- [32] Ma J., Wu Q. A novel additive-free oxideshydrothermal approach for monazite-type LaPO_4 nanomaterials with controllable morphologies. *J. Appl. Crystallogr.*, 2010, **43**(5), P. 990–997.
- [33] Byrappa K., Devaraju M.K., et al. Hydrothermal synthesis and characterization of LaPO_4 for bio-imaging phosphors. *J. Mater. Sci.*, 2008, **43**(7), P. 2229–33.
- [34] Yang M., You H., et al. Selective synthesis of hexagonal and monoclinic $\text{LaPO}_4:\text{Eu}^{3+}$ nanorods by a hydrothermal method. *J. Cryst. Growth*, 2009, **311**(23–24), P. 4753–58.
- [35] Thiriet C., Konings R.J.M., Javorský P., Magnani N. The low temperature heat capacity of LaPO_4 and GdPO_4 , the thermodynamic functions of the monazite-type LnPO_4 series. *J. Chem. Thermodyn.*, 2005, **37**(2), P. 131–139.
- [36] Terra O., Clavier N., Dacheux N., Podor R. Preparation and characterization of lanthanum-gadolinium monazites as ceramics for radioactive waste storage. *New J. Chem.*, 2003, **27**(6), P. 957–967.
- [37] Ushakov S., Helean K. Thermochemistry of rare-earth orthophosphates. *J. Mater. Res.*, 2001, **16**(100), P. 2623–33.
- [38] Horchani-Naifer K., Férid M. Crystal structure, energy band and optical characterizations of praseodymium monophosphate PrPO_4 . *Inorganica Chim. Acta*, 2009, **362**(6), P. 1793–96.
- [39] Mullica D.F., Grossie D., Boatner L.A. Structural refinements of praseodymium and neodymium orthophosphate. *J. Solid State Chem.*, 1985, **58**(1), P. 71–77.
- [40] Jardin R., Pavel C.C., et al. The high-temperature behaviour of PuPO_4 monazite and some other related compounds. *J. Nucl. Mater.*, 2008, **378**(2), P. 167–171.
- [41] Mullica D.F., Grossie D., Boatner L.A. Coordination geometry and structural determinations of SmPO_4 , EuPO_4 and GdPO_4 . *Inorganica Chim. Acta*, 1985, **109**(2), P. 105–110.

The characterization of nanosized ZnFe_2O_4 material prepared by coprecipitation

A. T. Nguyen¹, Ph. H. Nh. Phan¹, I. Ya. Mittova², M. V. Knurova², V. O. Mittova³

¹Ho Chi Minh City Pedagogical University, Ho Chi Minh City, Vietnam

²Voronezh State University, Voronezh, Russia

³Voronezh State Medical University named after N.N. Burdenko, Voronezh, Russia

anhtien0601@rambler.ru, pphoainhan@gmail.com, imittova@mail.ru,

cnurova2010@yandex.ru, vmittova@mail.ru

PACS 75.50.Cc, 81.07.Wx

DOI 10.17586/2220-8054-2016-7-3-459-463

The nanosized ZnFe_2O_4 material was synthesized using the coprecipitation method from Zn^{2+} and Fe^{3+} cations in a boiling aqueous medium. The results of TG/DSC, XRD, SEM, TEM and VSM analysis show that the ZnFe_2O_4 material prepared after annealing at 600 °C had tetragonal structure, a size of 20 – 50 nm, $H_c < 70$ Oe, $M_r < 0.5$ emu/g and $M_s \sim 2.5$ emu/g.

Keywords: sol-gel synthesis, nanopowders, zinc ferrite, magnetic properties.

Received: 18 January 2016

1. Introduction

Currently, nanomaterials, especially magnetic materials, have a wide range of relevant application to the manufacture of appliances such as generator transformers, electrical motors, and digital detectors. Among many kinds of magnetic substances, ferrite nanoparticles, spinel AB_2O_4 , have been studied not only because of their high magnetic permeability, but also their appropriate magnetic saturation and resistance for reducing the Foucault current effect, as well as prolonging the life of devices [1–5].

It is worth considering that there are numerous means for synthesizing nanoparticles, for instance, coprecipitation, sol-gel, and coordination. The advantage of these methods is undoubtedly the low crystallization temperature, whereas the traditional ceramic method requires a much higher temperatures to create the desired product. Another advantage is that they can also enhance the homogeneity and purity of target materials [3, 6–11].

According to studies [7–9], some methods, such as sol-gel, gel combustion or coordination, have been used to prepare spinel AB_2O_4 nanoparticles (A is Co, Ni, Zn and B is Fe). However, the single crystallization in these strategies depends on many elements: temperature and time for annealing, pH, molar fraction of gel agents and metallic cations, actual gelling temperature. In addition, there are no scientific reports associated with synthesis of ZnFe_2O_4 nanoparticles by coprecipitation from zinc(II) hydroxide and iron(III) hydroxide because $\text{Zn}(\text{OH})_2$ is completely dissolved in excessive alkaline solution (e.g. NaOH, NH_3).

In this paper, the coprecipitation was utilized through the hydrolysis stage of Zn^{2+} and Fe^{3+} cations in boiling water [9, 10], before the addition of ammonia solution as the precipitating reactant, which helped the target solution attain the proper pH to synthesis and characterization of either crystal morphology or magnetization of ZnFe_2O_4 nanoparticles. The Zn^{2+} and Fe^{3+} cations were hydrolyzed in boiling water, and then the solution was cooled in order to produce stable precipitates and inhibit the agglomeration of nanoparticles [9, 10, 12].

2. Experimental

2.1. Chemicals and equipment

$\text{Fe}(\text{NO}_3)_3 \cdot 9\text{H}_2\text{O}$, $\text{Zn}(\text{NO}_3)_2 \cdot 6\text{H}_2\text{O}$, NH_3 25 % ($d = 0.91$ g·ml⁻¹), deionized water, filtered paper were used in the experiments. $\text{Fe}(\text{NO}_3)_3 \cdot 9\text{H}_2\text{O}$ and $\text{Zn}(\text{NO}_3)_2 \cdot 6\text{H}_2\text{O}$ were mixed in the molar ratio of $\text{Zn}^{2+}:\text{Fe}^{3+} = 1:2$ and they were then dissolved in water prior to precipitation.

Additional equipment included 100 ml, 250 ml, 500 ml flasks, pipette, burette, magnetic stirrer, stir bar, electric stove, furnace, crucible, pH meter.

2.2. Synthesis of ZnFe_2O_4 nanoparticles

The mixture consisting of $\text{Zn}(\text{NO}_3)_2:\text{Fe}(\text{NO}_3)_3 = 1:2$ was carefully added in a dropwise manner to a flask of boiling water (to $> 90\text{ }^\circ\text{C}$). It was stirred until the obtained solution became brown-red and this color remained unchanged when the solution was cooled at room temperature. Next, a 5 % NH_3 solution was carefully added to this system until its pH reached the range of 9.0 – 9.2, followed by a continuous stir of the solid separating from solution for 30 minutes. The precipitate was filtered and washed with water prior to being dried at room temperature for about 3 days. Finally, the precursor was milled and annealed in an aerobic atmosphere at different temperatures with the heating rate of $10\text{ }^\circ\text{C}/\text{minute}$ for the investigation of crystallization and evaluation of phase components.

2.3. Techniques

To determine the desired temperature for single phase ZnFe_2O_4 formation, the sample was analyzed thermally by Labsys Evo (TG-DSC 1600 $^\circ\text{C}$) under a nitrogen atmosphere with a heating rate of $10\text{ }^\circ\text{C}/\text{minute}$, from room temperature to $1100\text{ }^\circ\text{C}$.

XRD patterns were obtained using a D8-ADVANCE (Germany) with CuK_α radiation (wavelength of 0.154056 nm), $2\theta = 10 - 70\text{ }^\circ$, step size of $0.03\text{ }^\circ/\text{min}$. The average size (nm) of crystal was calculated by the Scherrer equation: $D_{hkl} = \frac{k \times \lambda}{\beta_{hkl} \times \cos \theta}$, where β_{hkl} was peak width-full width at half maximum (FWHM-radian), θ was the corresponding diffraction angle (degree), $k = 0.89$.

The microstructure and morphological images were recorded by Scanning Electron Microscopy (SEM) in FESEM S4800 HITACHI (Japan) and Transmission Electron Microscopy (TEM) in JEOL-1400 (Japan).

The magnetic properties of samples were studied at room temperature by a Vibrating Sample Magnetometer (VSM) in MICROSENE EV11 (Japan).

3. Results and discussion

Thermogravimetric analysis (TGA) (Fig. 1) demonstrated a weight loss of 18.51 % during calcination from room temperature to $1100\text{ }^\circ\text{C}$. This was 4.49 % less than the predicted weight loss based on stoichiometry of chemical reaction (23.0 %) due to the steam and CO_2 adsorption of the sample.

These weight losses occurred mainly from $30 - 500\text{ }^\circ\text{C}$, corresponding to the endothermic peaks in the DSC curve, namely at $116.31\text{ }^\circ\text{C}$ and $159.71\text{ }^\circ\text{C}$ because $\text{Zn}(\text{OH})_2$ and $\text{Fe}_2\text{O}_3 \cdot n\text{H}_2\text{O}$ underwent decomposition. From

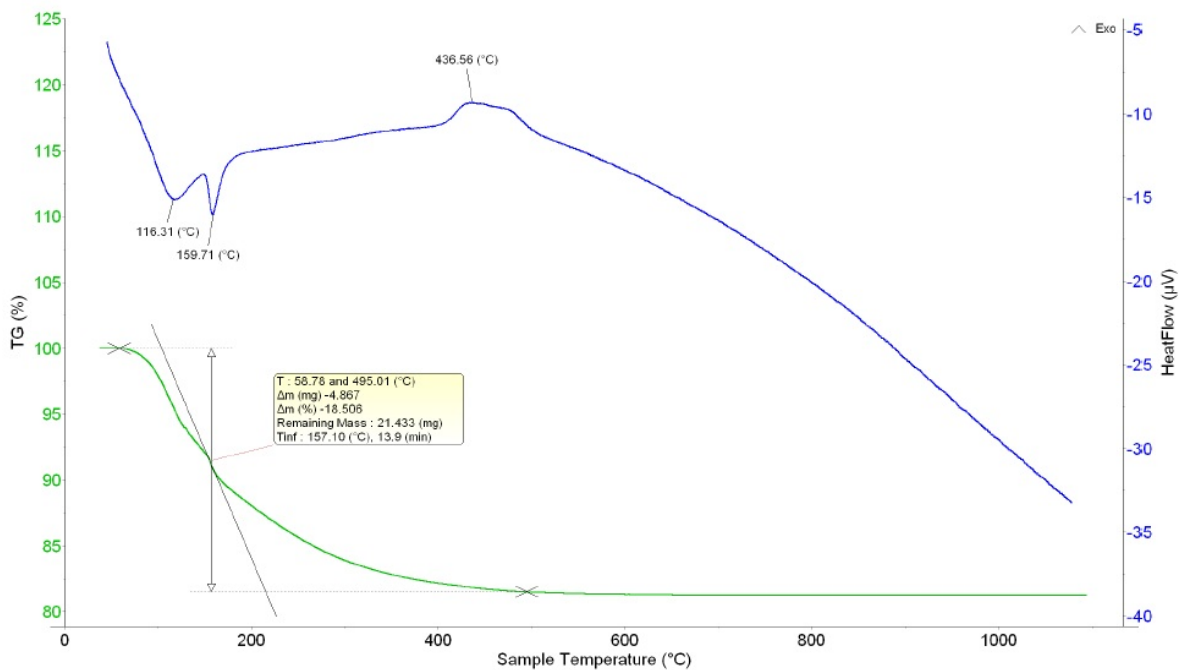


FIG. 1. TG-DSC curves of precursor

300 °C to 600 °C a slight weight loss was recorded and levelled off when the temperature approached 600 °C. Therefore, samples were annealed from 600 °C to investigate the formation of the $ZnFe_2O_4$ phase. The XRD patterns at different temperatures were shown in Figs. 2 and 3.

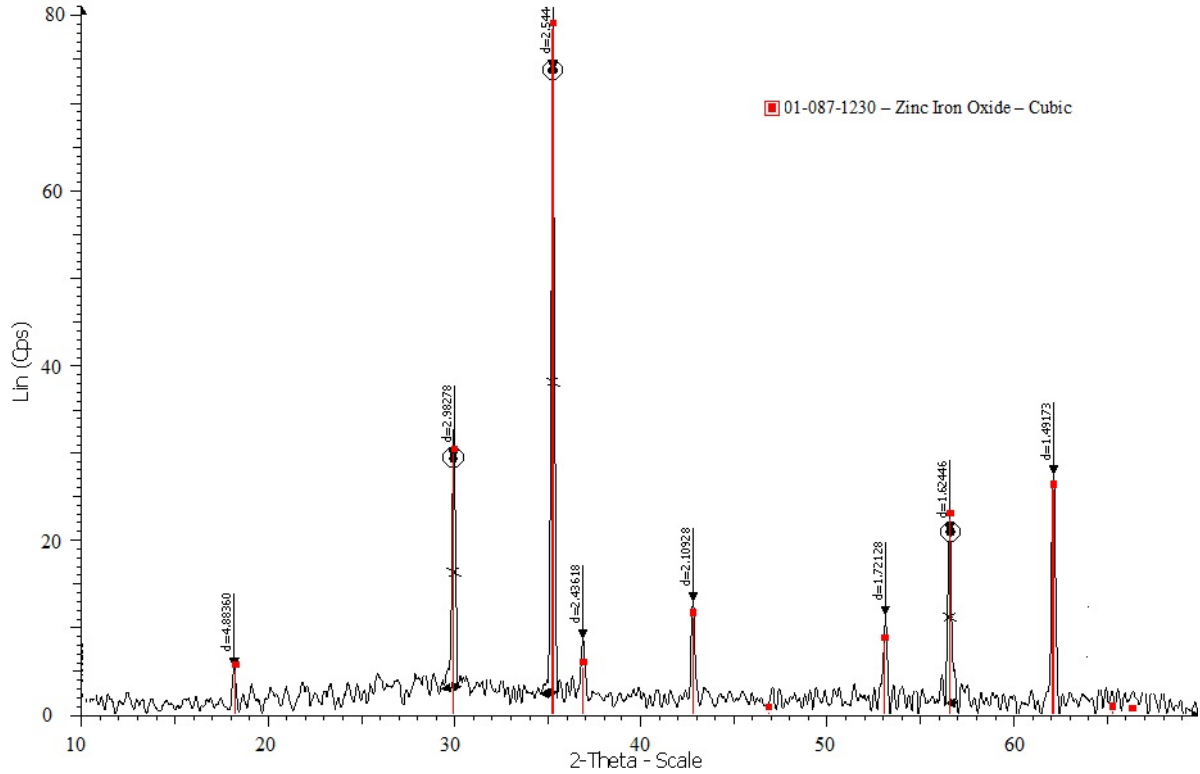


FIG. 2. XRD pattern of $ZnFe_2O_4$ annealed at 800 °C for 2 h in comparison with standard pattern (red bars)

XRD patterns of $ZnFe_2O_4$ annealed at 600 °C, 700 °C and 800 °C for 2 h matched well to standard ones (No. 01-087-1230), which involved the $ZnFe_2O_4$ crystal in cubic structure and led to the conclusion that no other phases existed in the annealed samples. However, the increases in peak intensity as well as the narrowness in the peak width indicated that the crystallization at high temperature was better than the low temperature one. This was confirmed by the growth in the crystal size according to the Scherrer equation (Table 1).

TABLE 1. The magnetic properties of $ZnFe_2O_4$ annealed samples

Annealing temperature, °C	Grain size based on Debye-Scherrer equation, nm	M_r , emu/g	M_s , emu/g	H_c , Oe
600	33.99	0.435	2.507	69.83
700	36.29	0.218	2.306	60.59
800	38.67	0.152	1.617	37.35

SEM and TEM images of sample annealed at 700 °C illustrated that the size of target grains ranged from 30 – 50 nm, which was confirmed by XRD data. Moreover, the agglomeration of particles was observed in these images (Fig. 4).

The magnetic investigation of samples annealed at a variety of temperatures (Fig. 5 and Table 1) showed that residual magnetism M_r values, the saturation magnetization M_s and magnetic coercivity H_c all decreased when the annealing temperature was increased. This means that at higher temperatures, the growth in grain size may decrease the strength of the compound's magnetic properties. For instance, the magnetic coercivity value was calculated by equation [1]:

$$H_c(\text{Oe}) = A/d + D, \quad (1)$$

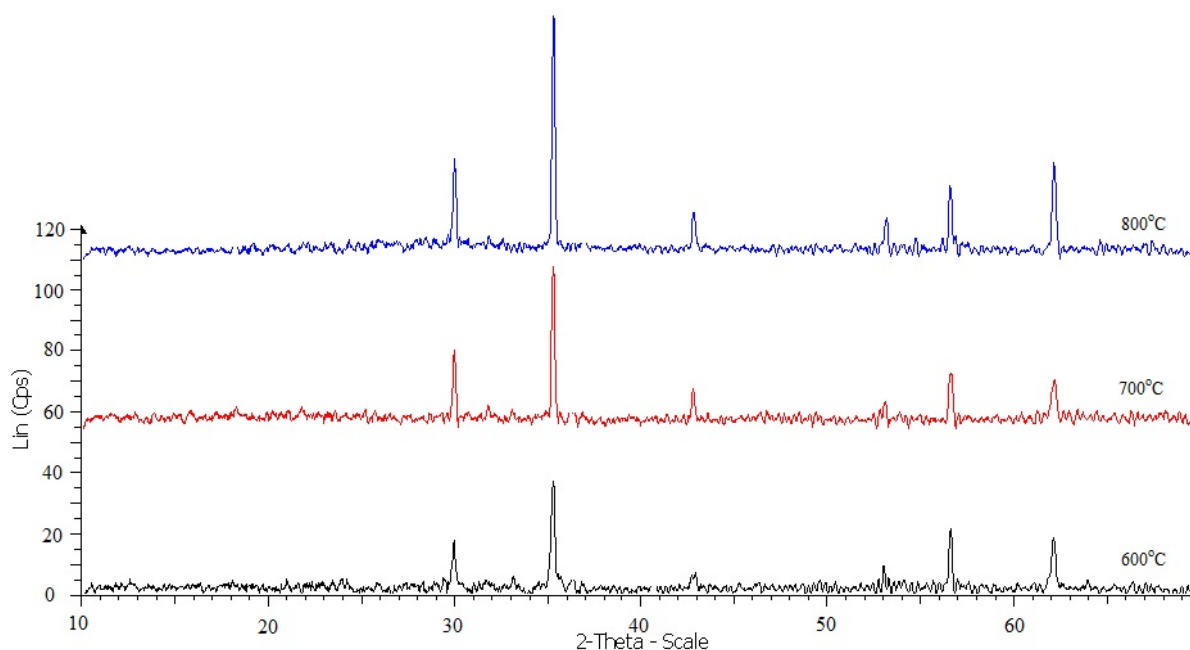


FIG. 3. XRD patterns of ZnFe_2O_4 annealed at 600 °C, 700 °C and 800 °C for 2 h

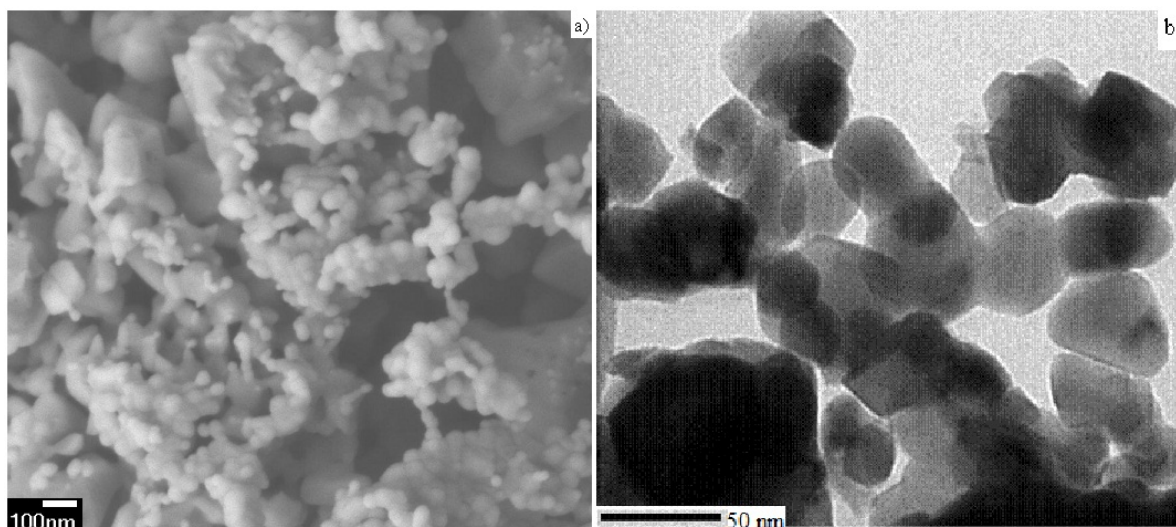


FIG. 4. SEM (a) and TEM (b) images of ZnFe_2O_4 sample annealed at 700 °C ($t = 2$ h)

where A , D were factors depending on concentration of impurities; d was the particle diameter.

ZnFe_2O_4 nanoparticles prepared by coprecipitation had small M_r and H_c at 1500 Oe, and magnetization did not meet the saturation state (narrow hysteresis loop and ongoing curve). This proved not only the soft magnetic properties of the target material, but also the superparamagnetism which can be applied to the manufacture of magnetic cores.

4. Conclusion

ZnFe_2O_4 nanoparticles were prepared by coprecipitation using NH_3 after hydrolyzing cation solution in boiling water. Single phase ZnFe_2O_4 material was produced when the precursor was annealed aerobically from 600 °C. The cubic structure of ZnFe_2O_4 crystal ranged from 30 – 50 nm in size. H_c , M_r , M_s were small and dropped when the grain size increased.

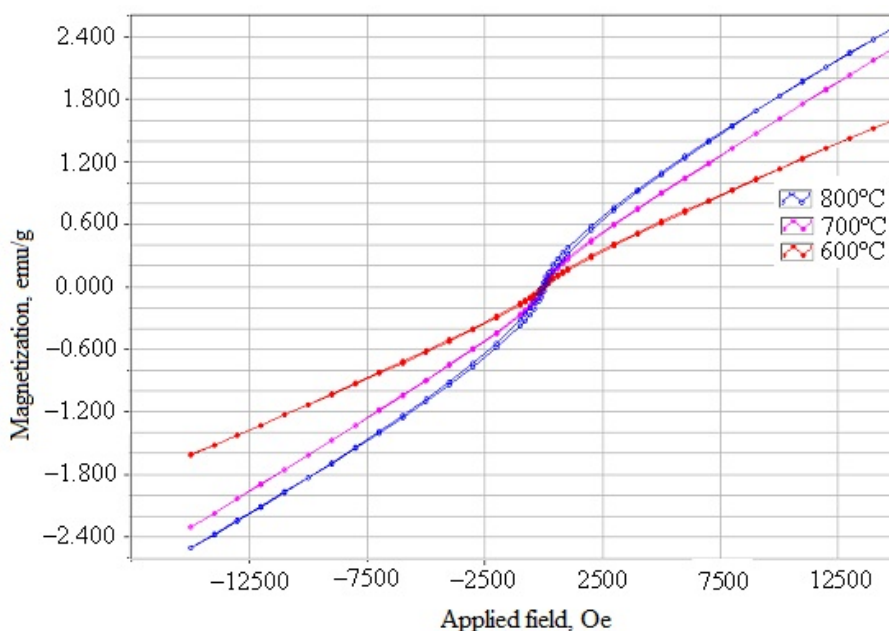


FIG. 5. The magnetic hysteresis curve of ZnFe_2O_4 annealed samples

Acknowledgements

This work was supported by the Ministry of Education and Science of the Russian Federation in line with government order for Higher Education Institutions in the field of science for the years 2014 – 2016 (project No. 225).

References

- [1] Luu T.T. *Magnetic Materials Lecture*. Hanoi National University Publication, 2008, 273 p.
- [2] Brusensov Yu.A., Minaev A.M. *Fundamentals of physics and technology of oxide semiconductors*. Publisher TSTU, Tambov, 2001, 40 p.
- [3] Al Angari Y.M. Magnetic properties of La-substituted NiFe_2O_4 via egg-white precursor route. *Journal of Magnetism and Magnetic Materials*, 2011, **323**, P. 1835–1839.
- [4] Kuznetsova V.A., Almjasheva O.V., Gusarov V.V. Influence of microwave and ultrasonic treatment on the formation of CoFe_2O_4 under hydrothermal conditions. *Glass Physics and Chemistry*, 2009, **35**(2), P. 205–209.
- [5] Komlev A.A., Semenova A.S. Magnetic Characteristics of MgFe_2O_4 -containing nanopowders prepared by the hydrothermal method. *Nanosystems: Physics, Chemistry, Mathematics*, 2012, **3**(6), P. 105–111. (In Russian)
- [6] Komlev A.A., Ilhan S. Formation of iron-magnesium spinel nanoparticles under dehydration of co-precipitated magnesium and iron hydroxides. *Nanosystems: Physics, Chemistry, Mathematics*, 2012, **3**(4), P. 114–121. (In Russian)
- [7] Luu M.D., Nguyen Th.T.L. Synthesis nanosized CoFe_2O_4 by gel combustion. *Vietnam Chemistry Journal*, 2010, **48**(4), P. 404–408.
- [8] Nguyen Th.T.L., Pham Th.H. Synthesis nanosized ZnMn_2O_4 by gel combustion. *Vietnam Chemistry Journal*, 2013, **51**(2), P. 174–179.
- [9] Nguyen A.T., Mittova I.Ya., et al. Influence of the preparation condition on the size and morphology of nanocrystalline lanthanum orthoferrite. *Glass Physics and Chemistry*, 2008, **34**(6), P. 756–761.
- [10] Nguyen A.T., Mittova I.Ya., Almjasheva O.V. Influence of the synthesis conditions on the particle size and morphology of yttrium orthoferrite obtained from aqueous solutions. *Russian Journal of Applied Chemistry*, 2009, **82**(11), P. 1915–1918.
- [11] Nguyen Th.T.L. Synthesis nanosized ZnFe_2O_4 by gel combustion. *Vietnam Chemistry Journal*, 2013, **51**(3), P. 312–316.
- [12] Nazarenko V.A., Antonovich V.P., Nevskaya E.M. *Metal ions hydrolysis in dilute solutions*. Atomizdat, Moscow, 1979, 192 p.

Synthesis and mechanical characterization of nanoparticle-infused polyurethane foams. Statistical analysis of foam morphology

D. V. Pikhurov¹, V. V. Zuev^{1,2}

¹ITMO University, Kronverkskiy pr., 49, 197101 St. Petersburg, Russia

²Institute of Macromolecular Compounds of the Russian Academy of Sciences,
Bolshoi pr., 31, 199004 St. Petersburg, Russia

nefaeron@gmail.com, zuev@hq.macro.ru

PACS 81.07.Lb

DOI 10.17586/2220-8054-2016-7-3-464-471

Nanocomposite polyurethane (PU) foams filled with different loadings (0.1 – 0.7 wt.%) of nanosized silica (average grain size of ~ 7 and 12 nm) and organonano clay were prepared by the prepolymer method, and their mechanical properties were investigated. A statistical analysis of the size distribution for foam cells was successfully applied in order to characterize their morphology. The developed approach was shown to provide a detailed analysis of the morphology development in PU foams, including the primary cell formation and their subsequent break-up and coalescence. The degree of phase separation in nanocomposite polyurethane foams, which is dependent on the nanofiller, was calculated from the IR spectra. The presence of silica nanoparticles and organoclays gives rise to significant differences in the mechanical (stress-strain) properties of the nanocomposite polyurethane foams relative to the pure polymer.

Keywords: polyurethane nanocomposite foams; nanosized silica; organoclay; microphase separation, statistical analysis.

Received: 25 February 2016

Revised: 4 April 2016

1. Introduction

Applications of polyurethane (PU) foams reach into various areas such as: lightweight materials, filtration and separation, biomaterials, electrochemical or catalyst support, heat and sound isolation [1]. These applications require a precise control of the PU foam's morphology to serve different purposes. A thorough description of the morphologies requires data such as cell size, their distribution, cell shape anisotropy, thickness of cell walls, size and shape of struts. One major aim of material science in this field is to improve or create new desirable properties for PU foams. A potential way to solve this problem is the creation of nanocomposites. The benefit of using of nanofillers is that their small amount is sufficient to induce tremendous improvements in desirable properties [2]. The morphology of PU foams synthesized by a phase separation process depends on many parameters, including the composition, type and amount of nanofillers. A quantitative understanding of the evolution of nanocomposite PU foam morphology may permit one to predict and control their properties.

Mathematical description with experimental validation and prediction of PU foam morphology is still scarce in the literature. Kim and Youn [3] and Bikard et al. [4] modelled the formation of PU foams and their characteristics. The mechanism for PU foam formation is complex because it includes phase separation into domains and the formation of gas phase from reacting polymer-monomer mixture. For these reasons, the developed models are phenomenological and allow only qualitative description of the process. The formation of PU foam cells assumes the random growth of cell on randomly-formed nucleates. This process can be described with the aid of kinetic model of reversible aggregation developed by Kilian et al. [5]. The model explains why aggregates of different size are generated across chemical/physical processes in a liquid system. The universality of the model has been shown by its application to statistical ensembles of carbon-black particles [5], spherulites in isotactic poly(methylmethacrylate) [5, 6], microdomains of polyamic acids during their transformation to polyimides [7], defects of metallographic samples under tensile loading [6], bacteria and yeast in the course of their growth [5], and the ordered phase droplets in liquid crystalline systems [8, 9], and in many other systems. A similar approach, we estimate, could successfully be applied to the formation of PU foams reinforced with nanofillers.

In the experimental part of this work, we use a mixture of forpolymer and polyol to create PU foams. We use nanoclay and nanosized silica as nanofillers. The prepared PU foams were investigated by image analysis and mechanical testing.

2. Experimental

2.1. Materials

The isocyanate used in this study was a polymeric aromatic isocyanate based on 4,4'-diisocyanate diphenylmethane (MDI) Wannate PM-200 from Yantai Wanhua (PR China) (molecular weight $M_n = 340$, 30.2 – 32 % NCO, viscosity at 25 °C 150 – 250 cps, specific gravity = 1.25 g/cc). As a rigid chain extender, methylenebis-(2-chloroaniline) (cuamine M) from Ihara Chemical Ind. (Japan) with $MM = 267$ was used. VORANOL 4711 polyether polyol from Dow Chemical (glycerine propoxylated ethoxylated polyol with $M_n = 4711$, OH number 32 – 37, viscosity at 25 °C 790 – 830 cps, specific gravity 1.021 g/cc) was used as the main polyol. As other polyols, VORANOL RA-640 polyether polyol from Dow Chemical (propoxylated ethylenediamine polyol with $M_n = 350$, OH number 640, viscosity at 25 °C 21000 cps, specific gravity 1.00 g/cc) and PDA-800 from Kazan SK (Russia) (polyester of adipic acid and polyethylene glycol with $M_n = 800$, OH number 400, viscosity at 25 °C 11000 cps, specific gravity 1.17 g/cc) were used. DMDEE (2,2'-dimorpholinodiethylether) from Hunstman was used as the cataalyst. As nanoclays, montmorillonite (MMT) clay modified by cation exchange with long-chain (C16 – C18) quaternary ammonium Monamet 1P3 (has a particle size of less than 75 μm , interplate distance 37.5 Å, part of MMT is 80 %, specific gravity 0.45 g/cc) and Monamet 101 (has a particle size of less than 45 μm , interplate distance 41.6 Å, part of MMT is 80 %, specific gravity 0.40 g/cc) [10] from Metaclay (Russia) were used.

Aerosil*200 (has a mean particle size of 12 nm) and Aerosil*300 (has a mean particle size of 7 nm) from Evonik were utilized as the nanosized silica.

2.2. Synthesis of PU foams samples

MDI and polyol were dehydrated under vacuum overnight at room temperature and 60 °C respectively. All samples were prepared using the prepolymer technique [1]. A mixture of 63.9 wt.% of PM 200, 35.1 wt.% of VORANOL 4711 and 1 wt.% of oleic acid was used as the isocyanate prepolymer. A mixture of 58 wt.% of PDA-800, 38 wt.% of Cuamine A and 4 wt.% of VORANOL RA-640 was used as the polyol. The calculated amount of nanofiller was added to polyol and then magnetically stirred for at least 24 h.

The samples in this study were made by box foaming under a fume hood using an 18 × 18 × 12 cm steel box. A mixer with high rotation speed was used. The components in the formulation (13 g of isocyanate prepolymer and 13 g of polyol with nanoadditives) were mixed first for 3 s at 2400 rpm. Then, 0.5 g of 10 wt.% water solution of catalyst was added and immediately mixed for another 5 s at 2400 rpm. The blow off time occurs after the foam reaches maximum height. Once foaming is complete, the foam is further heated at 60 °C for 20 min, and then allowed to cure overnight under the fume hood. Foam sample walls (2.5 cm) are discarded, and the remaining samples are characterized.

2.3. Optical microscopy

A 2.0 cm × 2 cm × 2 mm piece was cut from the bulk with a razor blade. Diamond knife was used for microtomy. An optical microscope Micromed Met 400 (Micromed Met, Russia) with magnification up to 400 was used to analyze the surfaces PU foams.

2.4. Fourier-transform infrared spectroscopy (FT-IR)

Attenuated total reflectance-infrared spectra were acquired using the Vertex Bruker Fourier-transform infrared spectrometer. A spectral resolution of 2 cm^{-1} was maintained, and 32 scans were co-added for acceptable signal-to-noise ratio. Diamond micro-ATR crystal accessory was used. Foam samples were placed between the crystal and a metal tip, and sufficient load was applied to ensure good contact of sample with the ATR crystal.

2.5. Mechanical testing

Mechanical testing was conducted using a TA.XTplus Texture Analyser.

2.6. Thermodynamic model using for statistical analysis

The model of reversible aggregation [5–7] was inspired by application of irreversible thermodynamics. It gives a generalized characterization of microstructure in different liquids. According to the model, a stationary microstructure is developed by linking the energy-equivalent units in metastable clusters called the aggregates. The aggregates are perpetually composed and decomposed under thermal fluctuations; this is a condition of their reversibility.

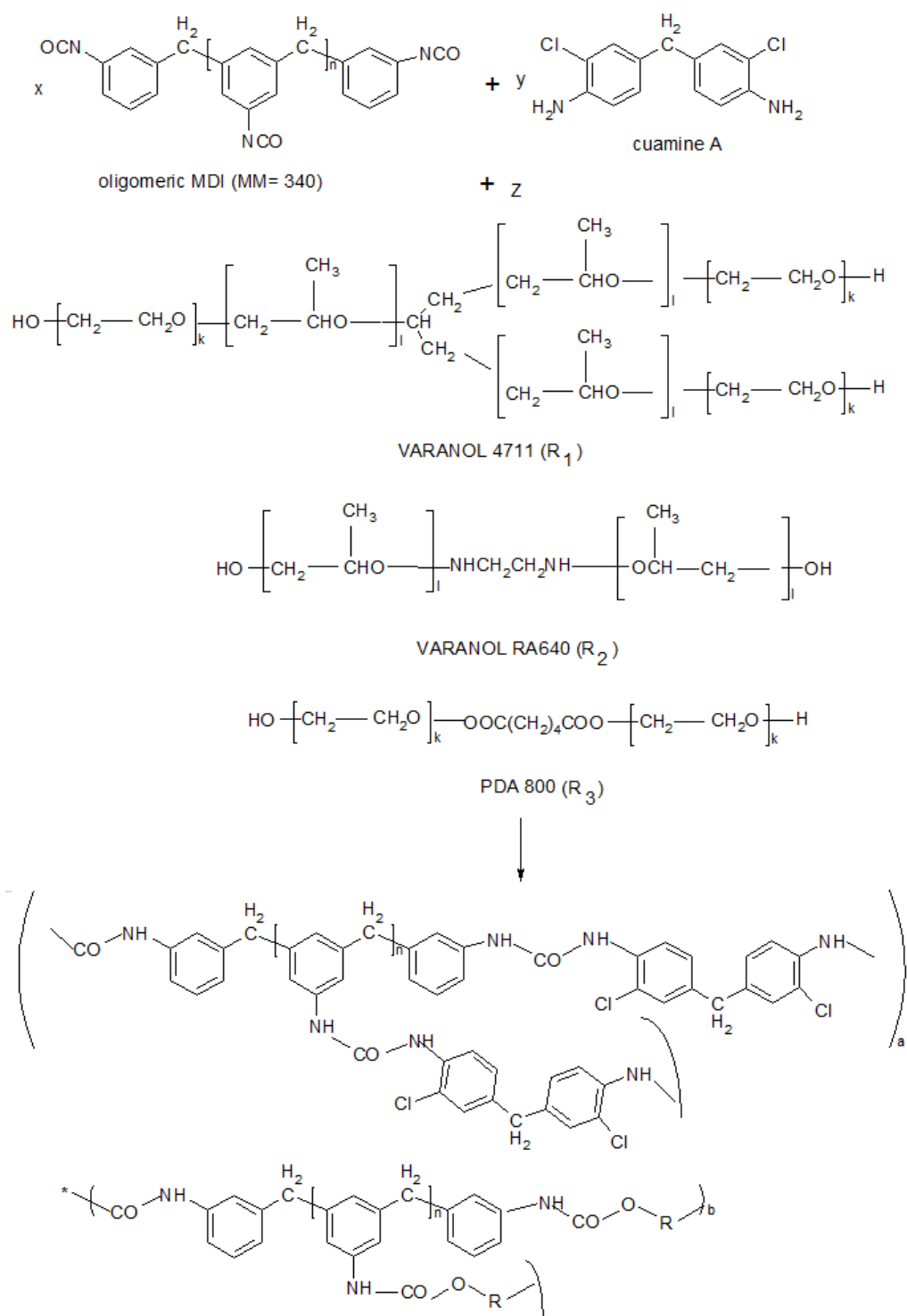


FIG. 1. Synthesis of PU foams samples

According to the model, the stationary statistical distribution $h(s)$ of the projected diameter s of the microstructural entities reads as follows [5–7]:

$$h(s) = as^2 \exp\left(-\frac{s\Delta u_0}{kT}\right), \quad (1)$$

where a is the normalizing factor, Δu_0 is the energy of aggregation, k is the Boltzmann constant, T is the absolute temperature, and k is the energy of thermal fluctuation. In some cases, the aggregates were shown to form not a single but rather multiple statistical ensembles [11]. This may be caused by either consolidation of primary clusters into superstructure (i.e. coalescence) or by the presence of different components in a multi-component system. Following this way, Eq. (1) should be written as [11]:

$$h(s) = \sum_{i=1}^N a_i s_i^2 \exp\left(-\frac{s_i \Delta u_{0i}}{kT}\right), \quad (2)$$

where N accounts for the total number of statistical ensembles of the entities. Eq. (2) allows the determination of the mean entity area $\langle s_i \rangle$ related to the i -th statistical ensemble as a normalized mathematical expectation:

$$\langle s_i \rangle = \frac{\int_{s_{0i}}^{\infty} s_i^3 \exp\left(-\frac{s_i \Delta u_{0i}}{kT}\right) ds_i}{\int_{s_{0i}}^{\infty} s_i^2 \exp\left(-\frac{s_i \Delta u_{0i}}{kT}\right) ds_i} = \frac{3kT}{\Delta u_{0i}}. \quad (3)$$

3. Results and discussion

PU foams were analyzed by optical microscopy in order to determine their morphology relative to the used nanofillers (Fig. 2). The cells basically appear spherical and closed. The purpose of optical microscopy analysis in the present paper is to determine the size of cells and their size distribution which will undoubtedly affect the performance of the resulting PU foams. The optical images obtained were subsequently segmented and subjected to digital analysis using the ImageTool 3.0 software elaborated at the Health Science Center (the University of Texas, San Antonio, USA) to elucidate the statistical size distributions of the dispersed phase droplets. To analyze the resulting histograms, we used the model of reversible aggregation. The area of each cell was then converted into the cell diameter for a circle with the area equivalent to the cell area. Let us note that we analyze a spatially 2D section of a foam sample and the equivalent cell diameters do not represent the real spatially 3D cell size.

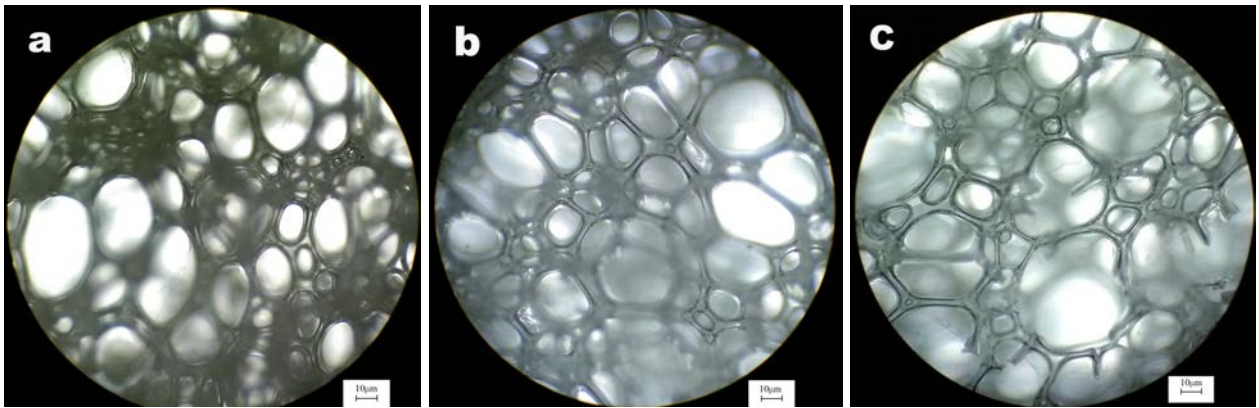


FIG. 2. Optical images of pristine PU foam (a); nanocomposite PU foam loaded with 0.08 wt.% of nanoclay Monamet 101 (b); nanocomposite PU foam loaded with 0.08 wt.% of nanosilica Aerosil*200 (c)

Two opposite processes determine the mean cell size during the PU foam formation process: break-up and coalescence. In order to investigate the evolution of cell size distribution during PU foam synthesis in the presence of different additives, statistical analysis of their diameters was undertaken. Our analysis is based on the model of reversible aggregation proposed by Kilian et al. [6] which has been successfully applied to describe the stationary phase distributions of microstructural entities in various systems. Fig. 3 shows the histograms obtained from the statistical analysis of the optical images of PU foams formed at different nanoparticle loadings (Fig. 2).

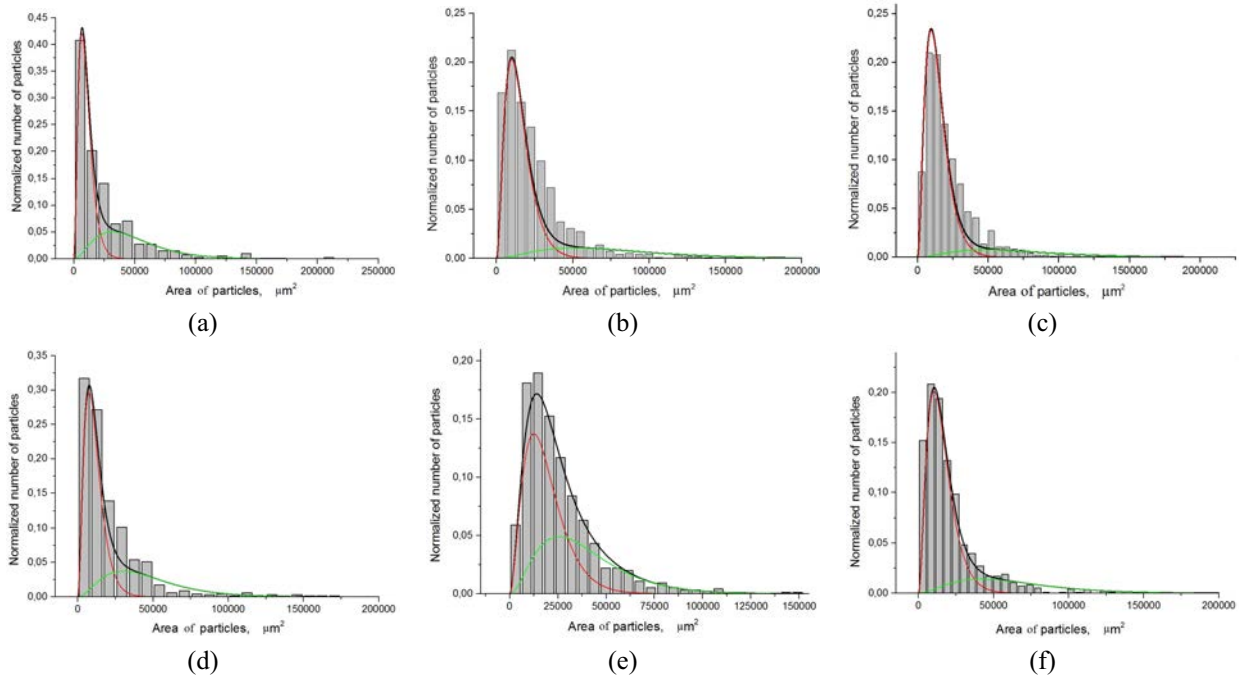


FIG. 3. Statistical distribution of cell area for pristine PU foam (a); nanocomposite PU foam loaded with 0.32 wt.% of nanoclay Monamet 101 (b); nanocomposite PU foam loaded with 0.32 wt.% of nanoclay Monamet 1P3 (c); nanocomposite PU foam loaded with 0.08 wt.% of Aerosil*200 (d); nanocomposite PU foam loaded with 0.63 wt.% of Aerosil*200 (e); nanocomposite PU foam loaded with 0.32 wt.% of Aerosil*300 (f)

Our attempt to describe the statistical ensembles with a unimodal version of the model of reversible aggregation (Eq. (1)) failed. Yet, we succeeded when we applied a bimodal version of the model (Eq. (2), $N = 2$). In Fig. 3, the dashed lines represent the individual distributions, whereas the solid lines represent the sum over two ensembles according to Eq. (2). A successful analytical description indicates that the PU foam cells form two superimposed, thermodynamically optimized, statistical ensembles of primary and coalescence cells all across the phase separation in the filled PU foams studied. We suggest the cells involved in the first statistical ensemble (i.e. small cells) were formed during the primary growth of PU foam synthesis, whereas the cells involved in the second statistical ensemble (big cells) resulted from coalescence.

The mean droplet diameter of each statistical ensemble as a function of the PU foam's compositions is given in Table 1.

As can be seen from Fig. 3, in the pristine PU foam, cells formed two superimposed, thermodynamically optimized, statistical ensembles of primary and coalesced cells. The mean cell size of each statistical ensemble can be assumed as a basic value when the influence of additives on PU foam morphology is analyzed. The first statistical ensemble contains not only primary cells but also droplets after break-up processes. As Fig. 2 and Table 1 show, the insertion of organoclay in the PU does not induce any modification of the cell morphology but led to a significant increase of the mean cell size in both statistical ensembles. For primary cells this, effect can be enhanced by residual water on the organoclay surface, which induces a supplementary CO_2 release. To the contrary, localization of nanoclay plates at the cell walls stimulates coalescence. The most common modeling of the mechanical behavior of cellular materials by the Gibson and Ashby approach [13] predicts that an increase of the cell dimensions should lead to a decrease of the foam's modulus. This view is supported by our measurements (Table 1). However, the mechanical response of these cellular materials also depends on the intrinsic properties of the polymer constituting the cell walls [1]. Morphology is the dominating factor determining the mechanical and many other properties of bulk PUs. PU is a multi-block copolymer that consists of alternating hard and soft segments. A hard segment (HS) consists of diisocyanate and chain extender, and a soft segment (SS) made from polyether or polyester polyol. The HS and SS are thermodynamically incompatible at low temperatures, resulting in the microphase separated structure of PU [14, 15]. The grade of the microphase separation can be determined from IR spectra using the part of free and hydrogen bonded carbonyl groups in urethane and urea bonds [16]. The FTIR spectra of the pristine and nanofilled PU foams and are shown in Fig. 4.

TABLE 1. Effect of loading on the properties of the nanocomposite PU foams

Loading, wt. %	Young's modulus (E), GPa	Tensile strength σ , MPa	Mean cell diameter, μm ; 1 ensemble	Mean cell diameter, μm ; 2 ensemble	Fraction of 1 ensemble	Fraction of hydrogen bonded urethane bond	Fraction of hydrogen bonded urea bond
pristine	4.59±0.02	0.51±0.01	113	246	1.75	0.93	0.37
Monamet 101							
0.08	4.05±0.02	0.50±0.01	145	330	3.2	0.74	0.25
0.16	3.93±0.02	0.48±0.01	141	330	2.7	0.64	0.27
0.32	3.98±0.02	0.49±0.01	138	313	3.7	0.79	0.19
0.63	3.63±0.02	0.41±0.01	150	276	2.5	0.98	0.24
Monamet 1P3							
0.08	4.35±0.02	0.55±0.01	145	301	4.2	0.82	0.43
0.16	4.13±0.02	0.52±0.01	159	301	4.6	0.77	0.55
0.32	3.98±0.02	0.50±0.01	134	301	6.1	0.71	0.56
0.63	3.65±0.02	0.46±0.01	126	340	1.6	0.83	0.41
Aerosil* 200							
0.08	3.96±0.02	0.52±0.01	154	221	1.4	0.78	0.52
0.16	4.67±0.02	0.62±0.01	141	221	1.7	0.81	0.52
0.32	4.60±0.02	0.61±0.01	131	215	1.6	0.75	0.48
0.63	4.12±0.02	0.54±0.01	119	240	1.9	0.76	0.50
Aerosil* 300							
0.08	4.67±0.02	0.62±0.01	126	242	3.2	0.85	0.51
0.32	3.68±0.02	0.49±0.01	140	252	3.5	0.86	0.50
0.63	4.15±0.02	0.55±0.01	134	242	2.5	0.77	0.41

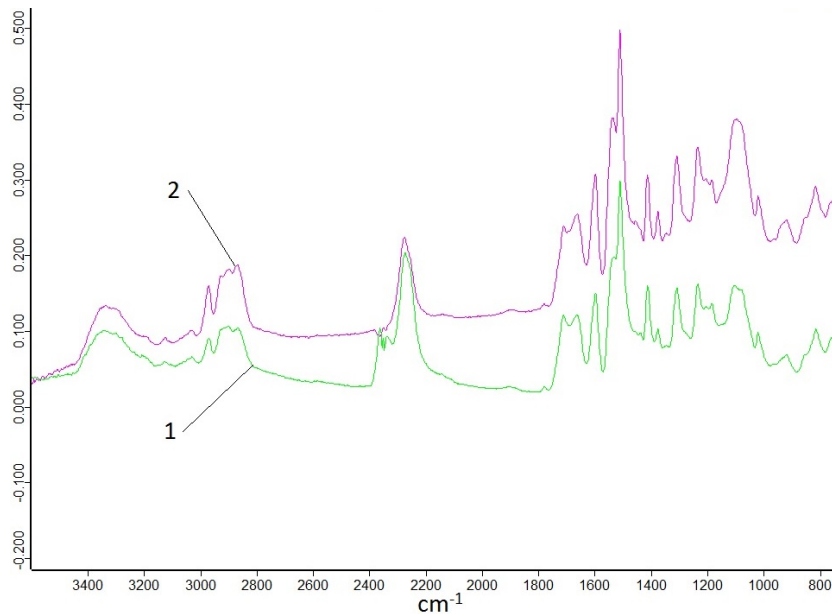


FIG. 4. IR spectra of pristine PU foams (1) and nanocomposite PU foam loaded with 0.32 wt.% of nanoclay Monamet 101 (2)

They are very similar, except in some regions that will be specified below. The positions of the bands characteristic of the functional groups remain the same in all the samples. We are able to derive the peaks of (-N=C=O), (-O-H) and (H-N=C=O). It should be noted that -NCO vibration (2270 – 2280 cm⁻¹), -NH vibration (3360 – 3380 cm⁻¹) and -OH vibration (3530 – 3550 cm⁻¹) are the most important peaks. Other important peaks

are urethane $\text{C}=\text{O}$ vibration ($1740 - 1700 \text{ cm}^{-1}$) and urea $\text{C}=\text{O}$ vibration ($1680 - 1640 \text{ cm}^{-1}$). However, there are significant differences concerning the band intensities in the $\text{C}=\text{O}$ ($1750 - 1600 \text{ cm}^{-1}$) region (Fig. 5).

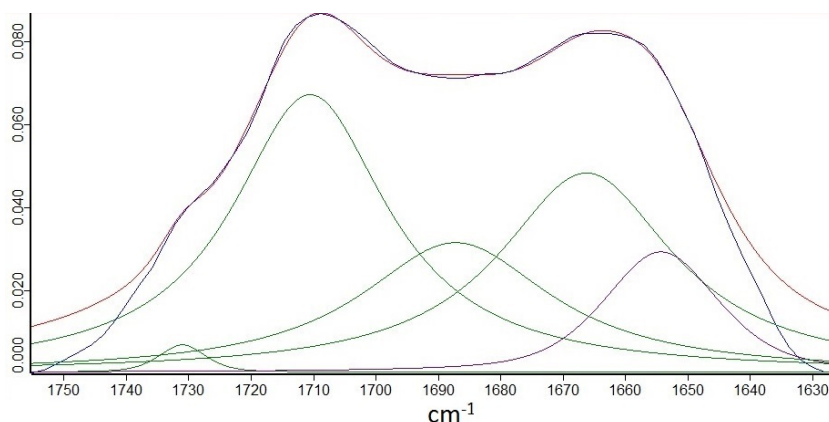


FIG. 5. Deconvolution of bands in IR spectrum of nanocomposite PU foam loaded with 0.32 wt.% of nanoclay Monamet 101 in the region of $\text{C}=\text{O}$ groups stretching

The former region is characteristic of hard segments. The urethane and urea groups take part in the formation of hydrogen bonds. In a pure PU foams, two types of hydrogen bonds can be formed between NH groups and proton accepting oxygen in (i) urethane $\text{C}=\text{O}$ groups, and (ii) urea $\text{C}=\text{O}$ groups. The type and the strength of the hydrogen bonds are usually recognized by the magnitude of the wave number shifts. Traditionally, the $\text{N}-\text{H}\cdots\text{O}=\text{C}$ hydrogen bond between two urea groups has been considered the strongest, with hydrogen bond between two urethane groups being the second strongest. However, recent studies have shown that $\text{N}-\text{H}\cdots\text{O}$ (ether) bond is slightly stronger than $\text{N}-\text{H}\cdots\text{O}=\text{C}$ urethane bond [16]. Conversely, it is known that the primary hydrogen bond acceptor depends on the length the soft segments and the concentration of the hard segments in a chain [17]. FTIR spectra in the carbonyl stretching region are presented in Fig. 5. All the spectra were resolved into five spectral components, the one at 1711 cm^{-1} was assigned to the hydrogen bonding between hard segments and urethane carbonyl groups. The other band at 1734 cm^{-1} corresponds to the stretching vibration of free carbonyl group of urethane bond of hard segments. Similarly, the band at 1644 cm^{-1} was assigned to the hydrogen bonding between hard segments and urea carbonyl groups. The band at 1664 cm^{-1} corresponds to the stretching vibration of free carbonyl group of urea bond of hard segments. The fifth band at 1644 cm^{-1} can be assigned to the allophanate formed as a by-product during the synthesis of PU foams [18].

The microphase separation can be characterized by the degree of phase separation (DPS) that is generally evaluated by the following relation:

$$DPS = \frac{A_b}{A_f + A_b}, \quad (4)$$

where A_b and A_f are the integrated absorbances (ε_b and ε_f are extinction coefficients which are assumed equal, although the actual value of $\varepsilon_b/\varepsilon_f$ is probably between 1.0 and 1.2 [16]) of hydrogen bonded and free molecular group, respectively. In other words, the limiting values of DPS, i.e. 0 and 1, refer to the single phase systems. The $\text{C}=\text{O}$ bands were deconvoluted using Gaussian shape and the obtained values of DPS for PU foam, as well as for their nanocomposites are given in Table 1. The fraction of hydrogen bonded carbonyls equal to DPS is a measure of phase separation, i.e. it relays information on the occurrence and the size of the hard domains. It is known that in pure PU hydrogen bonded components are expected only in hard domains, while the free ones can exist only dispersed in soft domains or in the interphase. Our data for the pristine PU foam supports this model. The DPS for urethane bonds is 0.93 which suggests that their location is in the hard domains. The DPS for urea bonds is 0.37, suggesting that their location is primarily in the interphase. The difference of DPS values for urethane and urea bonds can be explained by the fact that reactivity of cuamine A leads to location of urea groups on the ends of hard segments. The introduction of organoclay in PU foams leads to a decrease in DPS values. The organoclay, which can form hydrogen bonds with urethane and urea bonds, destroys the hard domains and softens the PU cell walls. This, along with increasing the cell diameter in both statistical ensembles, also explains the decrease in the mechanical properties of PU nanocomposite foams filled with organoclay.

A similar situation was observed for PU nanocomposite foams filled with nanosized silica (Table 1). The silica have hydrophilic surface and can forms hydrogen bonds with urethane and urea bonds. As a result, the DPS

for urethane bonds for PU nanocomposite foams filled with nanosized silica are lower than for pristine PU foam. However, the DPS for urea bonds is rather more that can be associated solely with formation of hydrogen bonds with silica.

The PU nanocomposite foam cells filled with nanosized silica also form two statistical ensembles of primary and coalescence cells (Fig. 3). However, the mean cell diameter for second statistical ensemble is practically identical for nanocomposites filled with Aerosil*300 and lower for nanocomposites filled with Aerosil*200 than for pristine PU foam (Table 1). As result, these nanocomposites have mechanical properties similar to pristine PU foam. Thereby, the hydrophilic nanosized filler such silica and organoclay can change supramolecular structure of PU and supervise the cell formation during PU foam synthesis, therefore, allowing one to predetermine the foams' mechanical properties.

4. Conclusions

A statistical analysis of the cell sizes was successfully applied to characterize the morphology of pristine PU foams and nanocomposite PU foams filled with nanosized silica or organoclay. The cells were shown to form two superimposed, thermodynamically optimized, statistical ensembles of primary and coalesced cells all across the phase separation in the foam manufacturing processes studied. The mean cell size of each ensemble was assumed as the basis for analysis of the influence of additives on nanocomposite PU foam morphology. The addition of organoclay led to a significant increase in the mean cell size both statistical ensembles. Hence, the introduction of organoclay decreases the break-up of primary cells and stimulate their coalescence. The addition of nanosized silica, contrary to nanoclay, did not stimulate coalescence but the mean cell size in both statistical ensembles was reduced. The development of phase morphology influences the mechanical properties of PU foams strongly.

The comprehensive IR study showed that in the case when the particles of the nanofiller can form hydrogen bonds with polymer segments, it is necessary to analyze changes due to the hydrogen bonding in foam phase structure. The loading hydrophilic nanofiller in PU foams lead to a decrease in the microphase separation that leads to decreased mechanical strength.

References

- [1] Yang C., Fischer L., Maranda S., Worlitschek J. Rigid polyurethane foams incorporated with phase change materials: A state-of-the-art review and future research pathways. *Energy and Buildings*, 2015, **97**, P. 25–38.
- [2] Mahfuz H., Rangari V.K., Islam M.S., Jeelani S. Fabrication, synthesis and mechanical characterization of nanoparticles infused polyurethane foams. *Composites: Part A*, 2004, **35**, P. 453–460.
- [3] Kim C., Youn J.R. Environmentally friendly processing of polyurethane foam for thermal insulation. *Polym. Plast. Technol. Eng.*, 2000, **39**, P. 163–185.
- [4] Bikard J., Bruchon J., Coupez T., Vergnes B. Numerical prediction of the foam structure of Polymeric materials by direct 3D simulation of their expansion by chemical reaction based on a multidomain method. *J. Mater. Sci.*, 2005, **40**, P. 5875–5881.
- [5] Kilian H.G., Metzler R., Zink B. Aggregate model of liquids. *J. Chem. Phys.*, 1997, **107**, P. 8697–8705.
- [6] Kilian H.G., Köpf M., Vettegren V.I. Model of reversible aggregation: universal features of fluctuating ensembles. *Progr. Colloid Polym. Sci.*, 2001, **117**, P. 172–181.
- [7] Kilian H.G., Bronnikov S., Sukhanova T. Transformation of the micro-domain structure of polyimide films during thermally induced chemical conversion: characterization via thermodynamics of irreversible processes. *J. Phys. Chem. B*, 2003, **107**, P. 13575–13582.
- [8] Zuev V.V., Bronnikov S. Stationary statistical size distribution of nematic droplets in the course of the isotropic liquid-nematic phase transition. *Liq. Cryst.*, 2008, **35**, P. 1293–1298.
- [9] Bronnikov S., Kostromin S., Zuev V.V. Kinetics of the isotropic-nematic phase transition in the melted multi-component liquid crystal mixtures upon cooling. *Phase Trans.*, 2010, **83**, P. 302–308.
- [10] Bachov F.I., Cherkina U.Yu., Shtepa S.V. The method of preparation of gem-organomodified montmorillonite with high thermal stability. Patent 2519174 (2013), Russia.
- [11] Zuev V.V., Steinhoff B., et al. Flow-induced size distribution and anisotropy of the minor phase droplets in a polypropylene/poly (ethylene-octene) copolymer blend: Interplay between break-up and coalescence. *Polymer*, 2012, **53**, P. 755–760.
- [12] Gibson L.J., Ashby M.F. *Cellular solids: Structure & properties*. Pergamon Press, Oxford, 1988, 357 p.
- [13] Chattopadhyay D.K., Raju K.V.S.N. Structural engineering of polyurethane coatings for high performance applications. *Prog. Polym. Sci.*, 2007, **32**, P. 352–418.
- [14] Bandekar J., Klima S. FT-IR spectroscopic studies of polyurethanes Part II. Ab initio quantum chemical studies of the relative strengths of “carbonyl” and ether hydrogen-bonds in polyurethanes. *Spectrochim. Acta A*, 1992, **48**, P. 1363–1370.
- [15] Mokeev M.V., Zuev V.V. Rigid phase domain sizes determination for poly(urethane-urea)s by solid-state NMR spectroscopy. Correlation with mechanical properties. *Eur. Polym. J.*, 2015, **71**, P. 372–379.
- [16] Sun H. Ab initio characterizations of molecular structures, conformation energies, and hydrogen-bonding properties for polyurethane hard segments. *Macromolecules*, 1993, **26**, P. 5924–6.
- [17] Seymour R.W., Estes G.M., Cooper S.L. Infrared studies of segmented polyurethane elastomers. I. Hydrogen bonding. *Macromolecules*, 1970, **3**, P. 579–83.
- [18] Yilgor E., Yilgor I., Yurtsever E. Hydrogen bonding and polyurethane morphology. I. Quantum mechanical calculations of hydrogen bond energies and vibrational spectroscopy of model compounds. *Polymer*, 2002, **43**, P. 6551–9.

Dielectric properties of polyamide 12-chromium (III) oxide nanocompositesE. S. Shapoval¹, V. V. Zuev^{1,2}¹ITMO University, Kronverkskiy pr., 49, 197101 St. Petersburg, Russia²Institute of Macromolecular Compounds of the Russian Academy of Sciences,
Bolshoi pr., 31, 199004 St. Petersburg, Russia

katenka-shapoval@yandex.ru; zuev@hq.macro.ru

PACS 81.07.Lb**DOI 10.17586/2220-8054-2016-7-3-472-478**

Broadband dielectric spectroscopy was employed to study polymer nanocomposites based on PA12 filled with different loading (0.1 – 10 wt.%) of nanosized (average grain size of about 1 – 5 nm) chromium (III) oxide. The experimental dielectric data were analyzed within the formalisms of complex permittivity and electric modulus. Three relaxation processes and Maxwell–Wagner–Sillars (MWS) interfacial polarizations were observed. It was found that all the relaxations were sensitive to filler contents. The presence of nanosized amphoteric chromium (III) oxide was shown to lead to the softening of the polyamide matrix that manifested in decrease of the activation energy of the α - and β -relaxation processes and glass transition temperatures. The softening of polymer matrix is the reason for the decrease in the mechanical properties of the polymer nanocomposites as compared to that of neat PA12.

Keywords: nanocomposites, polyamide 12, chromium (III) oxide, relaxation processes, activation energy dielectric spectroscopy.

Received: 8 February 2016

Revised: 19 March 2016

1. Introduction

Polymer magnetic materials can potentially find a great number of applications in different fields such as data storage, biomedicine, biosensors, drug delivery agent, magnetic resonance imaging devices, and a range of others [1–4]. Theoretical modeling predicts that the mechanical properties of polymer nanocomposites should be superior to those of conventional composites [5,6]. These improved properties are attained at lower filler content in comparison to conventionally filled polymers. However, the introduction of nanosized particles of magnetic oxides into different polymer matrices leads to a decrease in the mechanical properties. This was shown for the introduction of nanosized oxide F_3O_4 into polyurethane [7]. We obtained similar results for the preparation of polymer nanocomposites based on PA12 filled with different loading (0.1 – 10 wt.%) of nanosized (average grain size of about 1 – 5 nm) chromium (III) oxide [8]. It was suggested that the introduction of new fracture mechanisms, rigidity augmentation, and pronounced filler-filler interactions were responsible for the observed behavior instead of filler-polymer interactions [9–12]. The dynamics of polymer matrix changes due to changes in interactions with nanosized filler particles. The polymer dynamics and the glass transition in polymer nanocomposites are more complex than in neat polymer [13]. Here, we use broadband dielectric spectroscopy (BDS) to directly measure the influence of nanoparticles on polymer relaxations corresponding to different lengths and time scales. BDS is one of the most efficient tools for studying the molecular relaxations of polymers. It covers a broad frequency range, allowing measurement of different relaxation processes simultaneously, and even entire chain relaxation processes under favorable circumstances [14]. Relaxation processes in a polymer matrix are clearly connected with its mechanical properties. The β -relaxation is phenomenologically linked to the mechanical properties of polymeric materials [15, 16]. The α -relaxation is connected with the onset of large-scale motions of the chain segments in the vicinity of T_g and determined viscoelastic behavior. The aim of the present work is to provide a description of the relaxation processes for PA12/Cr₂O₃ nanocomposites over a range of temperatures and frequencies. As with any thermoplastic nanocomposites, a description of the relaxation processes parameters is of great interest, and is central for rational approach to thermomechanical processing.

2. Experimental

PA12/Cr₂O₃ nanocomposites were synthesized according [8]. Dielectric measurements were performed using an Alpha Analyzer combined with a Quatro Temperature Control system unit that provides temperature stability of 0.1 °C, both by Novocontrol. Complex dielectric permittivity $\varepsilon^*(f) = \varepsilon'(f) - i\varepsilon''(f)$ was measured isothermally in steps of 5 °C from –150 to +200 °C and over frequencies ranging from 10^{-2} to 10^6 Hz. The nanocomposite

films were placed and melted in a parallel-plate copper capacitor with 20 mm diameter, and a pair of glass fiber with 80 μm diameter was used as the spacers between electrodes.

3. Results and discussion

Plots of the three-dimensional real and imaginary parts, ϵ' and ϵ'' , of the complex dielectric permittivity ϵ^* versus frequency and temperature are presented in Fig. 1 for the sample with 5 wt.% of Cr_2O_3 .

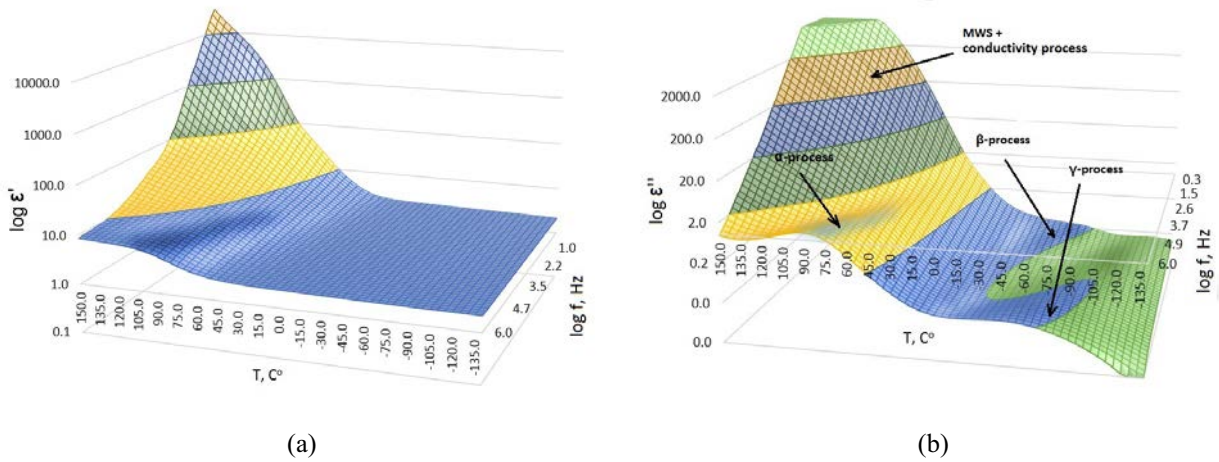


FIG. 1. 3D plot of ϵ' (a) and ϵ'' (b) versus frequency and temperature for nanocomposite with 5 wt.% of nanosized Cr_2O_3

The main relaxation processes identified are the same as those found for pure PA12 [17]: (1) the γ -relaxation appeared between 170 K and 250 K; (2) the β -relaxation appeared between 230 K and 275 K; (3) the segmental α -relaxation occurred between 270 K and 350 K; (4) the MWS/conductivity process visible in the high temperature regime arising from the drift motion of the charges and charge carriers blocked at the interphase between amorphous and crystalline regions and conductivity effects. The four processes are typically for PAs [18] and were observed in all studied samples.

The isochronal graph at 1 kHz, Fig. 2, shows the temperature dependence of ϵ' and ϵ'' for neat PA12 and composites. The differences between samples are noted, especially at higher temperatures, where the MWS/conductivity process is located.

It should be noted that in the ϵ'' (f) plots (Fig. 2b) only an α loss peak was observed. MWS relaxation can be masked by large conduction effects at high temperatures. Moreover, the peak is superimposed by electrode

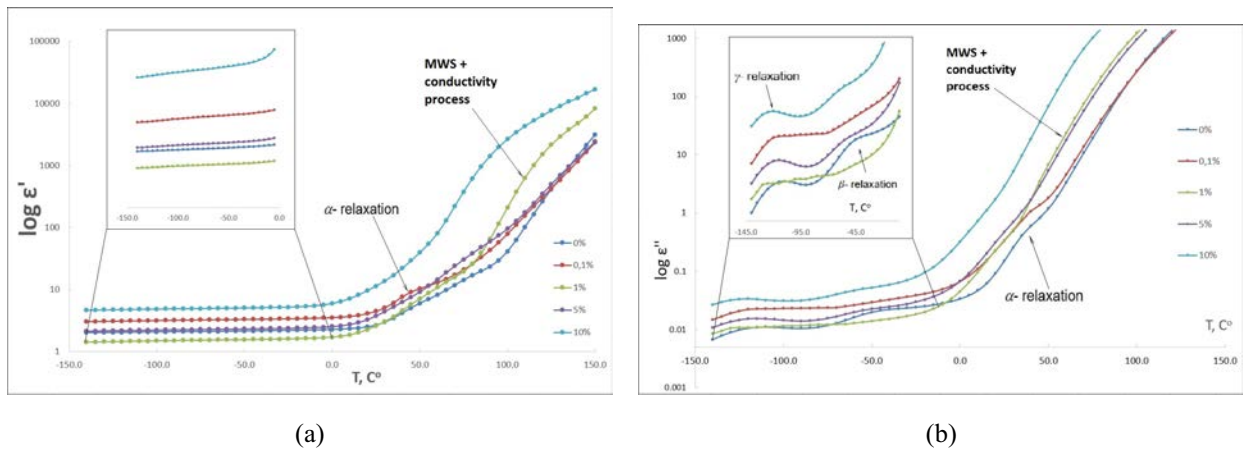


FIG. 2. Temperature dependence of ϵ' (a) and ϵ'' (b) for neat PA12 and all nanocomposites at a frequency of 1 kHz

polarization effects, and therefore not be clearly extracted in the permittivity spectra. Using the complex electric modulus formalism the MWS/conductivity process is visible as a peak in the imaginary part M'' of the complex dielectric modulus M^* . M^* is related to ε^* as follows [19]:

$$M^* = \frac{1}{\varepsilon^*} = M' + iM'',$$

$$M' = \frac{\varepsilon'}{\varepsilon'^2 + \varepsilon''^2} \quad \text{and} \quad M'' = \frac{\varepsilon''}{\varepsilon'^2 + \varepsilon''^2}.$$

A plot of M'' versus frequency and temperature for the sample with 5 wt.% of Cr_2O_3 is shown in Fig. 3.

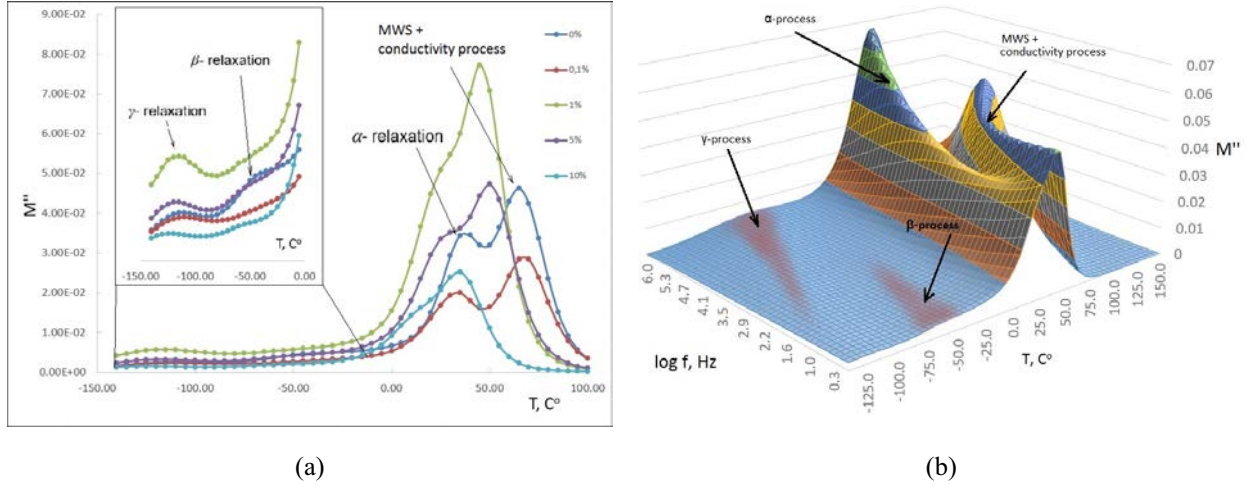


FIG. 3. (a) 3D plot of M'' versus frequency and temperature for nanocomposite with 5 wt.% of nanosized Cr_2O_3 and (b) temperature dependence of M'' for neat PA12 and all nanocomposites at a frequency of 1 kHz

The MWS/conductivity process can now be identified as a peak in the higher frequency regime. In order to evaluate the individual relaxation processes quantitatively, a model function has been fitted to the dielectric data, with the Havriliak-Negami (H-N) phenomenological relation [20]:

$$\varepsilon^*(\omega) = \varepsilon_\infty + \frac{\Delta\varepsilon}{\left(1 + (i\omega\tau_{NH})^{1-\alpha}\right)^\beta}, \quad (1)$$

in its most general form. In this expression, $\varepsilon^* = \varepsilon' - i\varepsilon''$, is the complex dielectric function, $\omega = 2\pi f$, f is the field frequency, $\Delta\varepsilon$ is the intensity of the dielectric process, $\tau_{NH} = 1/2\pi f_{NH}$ and f_{NH} is the position of the relaxation process on the frequency scale, ε_∞ is $\varepsilon'(f)$ for $f \gg f_{NH}$, α and β are shape parameters representing the symmetrical and asymmetrical broadening of the relaxation with respect to the Debye peak. The main characteristic of each relaxation process is the most probable relaxation time, τ_{\max} , determined according to [21] as

$$\tau_{\max} = \tau_{HN} \left(\frac{\sin\left(\frac{\pi\alpha\beta}{2(\beta+1)}\right)}{\sin\left(\frac{\pi\alpha}{2(\beta+1)}\right)} \right)^{1/\alpha}. \quad (2)$$

Figure 4 shows examples of such fits to the composites' relaxation processes at given temperatures for each process in the measured frequency window.

The α -relaxation is associated with the onset of large-scale motions of the chain segments in the vicinity of T_g . At higher temperatures, near the α -relaxation process, heating is accompanied by the creation of carriers due to the ionization of impurities and breaking of chemical bonds (the N-H bonds, etc). Hence, it is necessary to add an additional term related to the conductivity in Eq. (1):

$$\varepsilon^*(\omega) = \varepsilon_\infty + \frac{\Delta\varepsilon}{\left(1 + (i\omega\tau_{NH})^{1-\alpha}\right)^\beta} - i \left(\frac{\sigma_0}{\omega\varepsilon_0} \right). \quad (3)$$

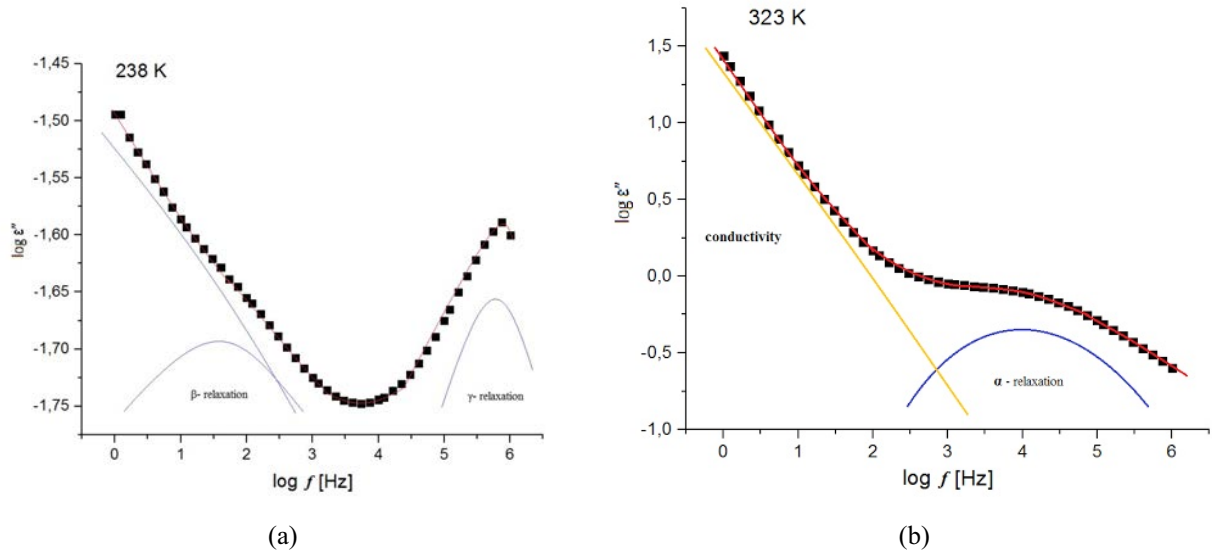


FIG. 4. Isothermal scans (ϵ'' vs frequency) at different fixed temperatures for nanocomposite with 5 wt.% of nanosized Cr_2O_3 . Characteristic temperatures for each process are chosen at which the process is visible in the measured frequency window. (a) γ - and β - relaxation, and (b) α -relaxation. Symbols are the experimental data and full lines represent the total fit

In this equation, σ_0 is the dc conductivity and ϵ_0 is the permittivity of free space (8.854 pF/m). The fitting procedure is complicated very often because of the presence of incomplete peaks, in spite of the frequency window extending over more than 8 orders of magnitude. The quality of the fit is quite good and the characteristic relaxation time for each relaxation process can be extracted. The γ - and β -relaxations are due to relatively shorter chain motions. The dependences of $-\log \tau_{\max}$ on the inverse temperature are linear for all nanocomposites and neat PA12 in the regions of γ and β processes (Fig. 5). As a result, the temperature dependence of these relaxations can be modeled by an Arrhenius type expression (4) [22]:

$$\tau(T)_{\max} = \tau_0 \exp\left(\frac{E_a}{RT}\right). \quad (4)$$

Here, $\tau_0 = \tau_{\max}$ at $T \rightarrow \infty$, E_a is the activation energy. Values of τ_0 and E_a are given in Table 1.

The β -relaxation is phenomenologically linked to the mechanical properties of polymeric materials [15, 16]. From Table 1, one can see that for the composites, both the E_a and Young's modulus decrease. Assignment of molecular motions associated with the β -relaxation is complicated and a number of varying opinions exist in the literature [18, 19]. However, these motions should be associated with the motion of amide groups together with

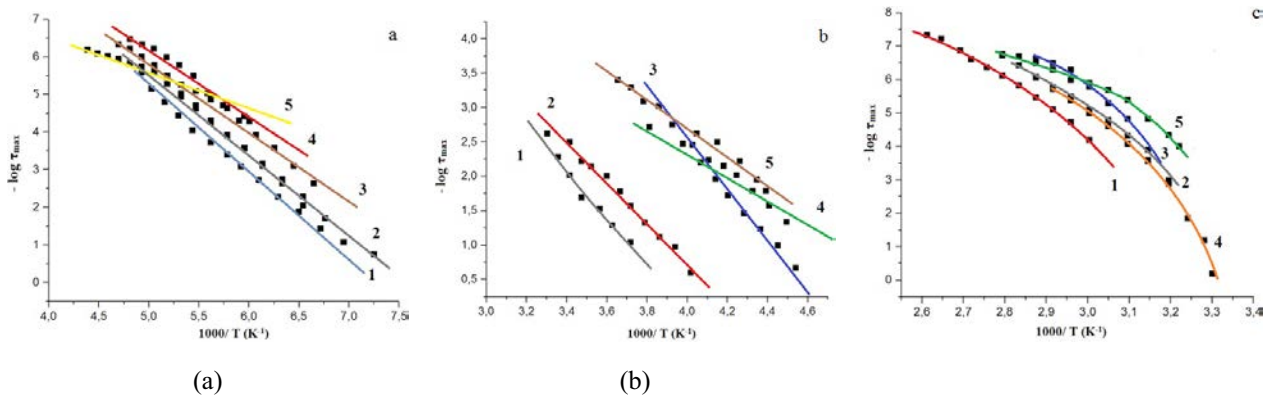


FIG. 5. Dependences of $-\log \tau_{\max}$ on the reciprocal of temperature for neat PA12 (1) and nanocomposites with 0.1 wt.% (2); with 1 wt.% (3); with 5 wt.% (4); and with 10 wt.% (5); (c) α -relaxation; (b) β -relaxation; (a) γ -relaxation

TABLE 1. T_g and parameters of γ , β and α (from VFT fit) relaxation processes of neat PA12 and nanocomposites, where τ_0 is the relaxation time at infinite high temperature, T_0 is so-called Vogel temperature at which the relaxation time goes to infinity, and D is the parameter related to the *fragility* of material

Samples, wt. % Cr ₂ O ₃		E_a , kJ/mol	τ_0 , s	D	T_0 , K	T_g , K	Young's modulus, GPa [8]
0	γ -mode	83.7	3.9×10^{-16}				
	β -mode	59.2	4.4×10^{-13}				
	α -mode	292.4	1.4×10^{-7}	3.32	280	332	0.97
0.1	γ -mode	62.7	3.9×10^{-16}				
	β -mode	48.3	3.9×10^{-13}				
	α -mode	266.6	4.0×10^{-10}	4.25	253	329	0.66
1	γ -mode	80.0	3.1×10^{-16}				
	β -mode	60.25	3.6×10^{-13}				
	α -mode	270.2	1.0×10^{-10}	2.95	267	318	0.49
5	γ -mode	71.4	4.3×10^{-16}				
	β -mode	59.4	2.3×10^{-13}				
	α -mode	279.0	2.3×10^{-10}	3.10	265	315	0.47
10	γ -mode	67.0	3.8×10^{-16}				
	β -mode	52.6	4.9×10^{-13}				
	α -mode	225.0	2.0×10^{-9}	2.47	256	303	0.36

neighboring methylene groups. Cr₂O₃ is an amphoteric oxide which can undergo bonding with the amide group, therefore disrupting the H-bonding network between adjacent polymer chains. This leads to decrease in the E_a of the β -relaxation and, hence, lowering in the Young's modulus. The decrease in the activation energy of the β -relaxation process indicates that the mobility of polymer matrix is a pre-condition for this mechanism to be effective.

The low temperature γ -relaxation involves the motion of short sequences of CH₂ groups connected with an amide group which provides the dielectric activity. As a result, the dependence of E_a of the γ -relaxation on the amount of nanofillers is quite.

The α -relaxation is associated with onset of large-scale motions of the chain segments in the vicinity of T_g . The temperature dependence of the characteristic relaxation times can then be described using the Vogel-Fulcher-Tammann equation [22]:

$$\tau = \tau_0 \exp\left(\frac{DT_0}{T - T_0}\right), \quad (5)$$

where τ_0 is the relaxation time at infinite high temperature, T_0 is so-called Vogel temperature at which the relaxation time goes to infinity, and D is the parameter related to the *fragility* of material [23]. A smaller D value implies a steeper temperature dependence for the relaxation time or a more "fragile" behavior. The D data are given in Table 1. According to Plazek et al. [24, 25] the activation energy of α -relaxation process can be calculated using the following expression:

$$\frac{E_a}{R} = \frac{DT_0}{\left(1 - \frac{T_0}{T_g}\right)^2}, \quad (6)$$

where E_a is the activation energy, R is the gas constant and T_g the glass transition temperature. The values of D and T_0 parameters were extracted from the best fit to equation (3). The values of activation energies for α -relaxation as well as the VFT parameters T_0 , D and T_g are gathered in Table 1. As can see, T_g values of for

the composites decrease in comparison to neat PA12, so the decrease in the moduli upon the introduction of the nanoparticles can be due to a plasticizing effect that the Cr_2O_3 nanoparticles could have exerted on the polymer matrix. However, T_g of the composite with 0.1 wt.% of Cr_2O_3 is very similar (if not identical) to the T_g of the pure polymer, but their Young's modulus is similar to moduli for other composites and is much smaller than that of pure PA12 [8], so the decrease in the moduli upon the introduction of the nanoparticles are not only due to a plasticizing effect. The softening of polymer matrix associated with local mobility (β -relaxation) is probably more important. This effect is opposite to the typical result of nanofiller addition, and is manifested as the well-documented "antiplasticizing phenomenon" [26]. Because of their small size, nanofillers have a high surface-to-volume ratio and provide high-energy surfaces. A desired consequence of embedding nanosized fillers into a polymer matrix is the enhanced bonding between the matrix and additives. The composite theory predicts that improved bonding between polymer matrix and reinforcing phase leads to hindering of polymer chain motions [27]. Despite these predictions, however, BDS investigations of nanocomposites have provided mixed results [28]. We believe that this is caused by the presence of specific intermolecular interactions (e.g., H-bonding), within polymer matrix like PAs which can be influenced by nanoparticles. The nature of these interactions can depend upon both the polymer's and nanoparticles' chemical properties.

At temperatures above α -relaxation, a MWS polarization [29] (Fig. 4) is observed. Moreover, at these temperatures, conductivity effects also play a role, and therefore, both the MWS process and conductivity phenomenon contribute to the high temperature dielectric response. To separate these processes is impossible, therefore they are not considered for further discussion.

4. Conclusions

In the present work, the molecular dynamics of nanocomposites based on PA12 filled with different loadings (0.1 – 10 wt.%) of nanosized (average grain size of about 1 – 5 nm) chromium (III) oxide was investigated by means of dielectric spectroscopy. For all polymer nanocomposites samples, two local relaxation modes, the γ - and β -relaxation, and a segmental α -relaxation was observed. These relaxation modes were evaluated for further analysis. In addition, a high temperature response due to a MWS process combined with conductivity effects was noted.

The E_a of the β -relaxation was shown to decrease for nanocomposites in comparison to neat PA12. The β -relaxation is phenomenologically linked to the mechanical properties of polymeric materials, hence, this observation can explain the Young's modulus decreases for these composites after nanofiller loading. The molecular reason for polymer matrix softening could be related to the disruption of amide H-bonds between neighboring polymer chains after complexation with nanosized chromium (III) oxide. The softening of the polymer matrix associated with local mobility (β -relaxation) is supported by decreases in the glass transition temperatures related to the α -relaxation for all nanocomposites. The E_a of the α -relaxation also decreases, therefore, a plasticizing effect was observed upon the introduction of nanosized chromium (III) oxide into the polyamide matrix.

References

- [1] Yan F., Li J., et al. Preparation of Fe_3O_4 /polystyrene composite particles from monolayer oleic acid modified Fe_3O_4 nanoparticles via miniemulsion polymerization. *J. Nanopart. Res.*, 2009, **11**, P. 289–296.
- [2] Balakrishnan S., Bonder M.J., Hadjipanayis G.C. Particle size effect on phase and magnetic properties of polymer-coated magnetic nanoparticles. *J. Magn. Mater.*, 2009, **321**, P. 117–122.
- [3] Giri S.K., Pradhan G.C., Das N. Thermal, electrical and tensile properties of synthesized magnetite/polyurethane nanocomposites using magnetite nanoparticles derived from waste iron ore tailing. *J. Polym. Res.*, 2014, **21**, 446.
- [4] Kalia S., Kango S., et al. Magnetic polymer nanocomposites for environmental and biomedical applications. *Colloid. Polym. Sci.*, 2014, **292**, P. 2025–2052.
- [5] Vollenberg P.H.T., Heikens D. Particle size dependence of the Young's modulus of filled polymers: 1. Preliminary experiments. *Polymer*, 1989, **30**, P. 1656–1662.
- [6] Gersappe D. Molecular Mechanisms of Failure in Polymer Nanocomposites. *Phys. Rev. Lett.*, 2002, **89**, 058301(1–4).
- [7] Dos Santos L.R., Ligabue R., et al. New magnetic nanocomposites: Polyurethane/ Fe_3O_4 -synthetic talc. *Eur. Polym. J.*, 2015, **69**, P. 38–49.
- [8] Shapoval E.S., Zuev V.V. Novel polyamide 12/ chromium (III) oxide nanoparticles composites: melting behaviour and complex isothermal crystallization kinetics. *Polymer Composites*, 2015, **36** (6), P. 999–1005.
- [9] Jordan J., Jacob K.I., et al. Experimental trends in polymer nanocomposites? a review. *Mater. Sci. Eng. A*, 2005, **393**, P. 1–11.
- [10] Zhu L., Narh K.A. Numerical simulation of the tensile modulus of nanoclay-filled polymer Composites. *J. Polym. Sci. Part B. Polym. Phys.*, 2004, **42**, P. 2391–2406.
- [11] Ciprari D., Jakob K., Tannenbaum R. Characterization of polymer nanocomposites interphase and its impact on the mechanical properties. *Macromolecules*, 2006, **39**, P. 6565–6573.
- [12] Kango S., Kalia S., et al. Surface modification of inorganic nanoparticles for development of organic/inorganic nanocomposites? A review. *Prog. Polym. Sci.*, 2013, **38**, P. 1232–1261.

- [13] Allegra G., Raos G., Vacatello M. Theories and simulations of polymer based nanocomposites: from chain statistics to reinforcement. *Prog. Polym. Sci.*, 2008, **33**, P. 683–731.
- [14] Adachi K., Kotaka T. Dielectric normal mode relaxation. *Progr. Polym. Sci.*, 1993, **18**, P. 585–622.
- [15] Boyer R.F. Dependence of mechanical properties on molecular motion in polymers. *Polym. Eng. Sci.*, 1968, **8**, P. 161–185.
- [16] Liu H., Brinson L.C. Reinforcing efficiency of nanoparticles: a simple comparison for nanocomposites. *Compos. Sci. Tech.*, 2008, **68**, P. 1502–1512.
- [17] Rathmanathan K., Cavaille J.Y., Johari J.P. The dielectric properties of dry and water- Saturated nylon 12. *J. Polym. Sci. Part B. Polym. Phys.*, 1992, **30**, P. 341–348.
- [18] Laredo E., Hernandez M.C. Moisture effect on the low- and high-temperature dielectric relaxations in nylon-6. *J. Polym. Sci. Part B. Polym. Phys.*, 1997, **35**, P. 2879–2888.
- [19] Starkweather Jr.H.W., Avakian P. Conductivity and the electric modulus in polymers. *J. Polym. Sci. Part B. Polym. Phys.*, 1992, **30**, P. 637–641.
- [20] Havriliak S., Negami S., A complex plane analysis of α -dispersions in some polymer systems. *J. Polym. Sci. Part C*, 1966, **14**, P. 99–117.
- [21] Havriliak S., Negami S., A complex plane representation of dielectric and mechanical relaxation processes in some polymers. *Polymer*, 1967, **8**, P. 161–210.
- [22] Kremer F., Schonhals A. *Broadband dielectric spectroscopy*. Springer, New York, 2003.
- [23] Angell C.A., Ngai K.L., et al. Relaxation in glassforming liquids and amorphous solids. *J. Appl. Phys.*, 2000, **88**, 3113.
- [24] Plazek D.J., Magil J.H. Physical properties of aromatic hydrocarbons I. *J. Chem. Phys.*, 1998, **35**, P. 3038–3050.
- [25] Bureau E., Cabot C., Marais S., Saiter J.M. Study of the γ -relaxation of PVC, EVA and 50/50 EVA70/PVC blend. *Eur. Polym. J.*, 2005, **41**, P. 1152–1158.
- [26] Treacy M.M.J., Ebesen T.W., Gibson J.M. Nanoparticles as reinforced agents. *Nature (London)*, 1996, **381**, P. 678–680.
- [27] Schaefer D.W., Justice R.S. How nano are nanocomposites. *Macromolecules*, 2007, **40**, P. 8501–8517.
- [28] Sinitin A.N., Zuev V.V. Dielectric relaxation of fulleroid materials filled PA6 composites and the study of its mechanical performance. *Nanosystems: physics, chemistry, mathematics*, 2015, **6**, P. 570–582.
- [29] Baird M.E., Goldworthy G., Creasey C.J. Low frequency dielectric behavior of polyamides. *Polymer*, 1971, **12**, P. 159–175.

Magnetic field dependent resonant light scattering by magnetic spheres in a magnetizable medium

Hem Bhatt

Shantilal Shah Engineering College, Sidsar, Bhavnagar. 364060, India
drhembhatt@gmail.com

PACS 47.65.Cb, 42.25.Fx, 42.68.Ay, 41.20.Jb

DOI 10.17586/2220-8054-2016-7-3-479-481

The anisotropy factor is a parameter from which one can determine preferential forward and backward light scattering. In the present study, we have calculated anisotropy factor $\langle \cos \theta \rangle$ as a function of magnetic field for magnetic spheres in a magnetic medium. We have noticed resonances in $\langle \cos \theta \rangle$ which indicate preferential enhanced scattering in forward and backward directions. Anisotropy factor is analyzed for various size parameters. The study clearly indicates that scattering can be modulated by means of size parameter of magnetic spheres as well as magnetic field. We have further confirmed the result by studying forward and backward intensity as a function of magnetic field. Resonances noticed in the intensity are in good agreement with the previous argument. This observation can be useful for the magnetic field dependent directional scattering and novel magneto-photonics devices.

Keywords: mie resonances, scattering, magnetic colloids, magneto-photonics.

Received: 23 January 2016. Revised: 8 March 2016

1. Introduction

In the recent past, the high energy and working efficiency of photonic devices have attracted researchers to design and study materials in which light transport can be tuned by controlling some external parameters. Recently, a new frontier has also emerged with a goal of controlling light transport by means of interference in artificially engineered optical materials and metamaterials [1–6]. Remarkable progress has been noted in the fabrication of nanophotonic structures with many novel properties [7]. The disorder present and the magnetic tenability have made magnetically polarizable fluids preferable for many applications like optical switches, modulators, filters and gratings, etc. [8,9]. Light transport and optical study of resonant behavior have been studied in disordered magnetic media along with coherent backscattering and light localization [10–13]. But very few have used magnetic tuning of magnetic spheres to predict theoretical and experimental photonic effects [14–16]. Several groups are working on single and multiple scattering by magnetic scatterers in non-magnetic medium [17–19]. Our recent studies have shown some unusual light transport in ferrocolloids in presence of external magnetic field [20]. This study reflects effect of magnetic field Mie resonance by magnetic spheres dispersed in magnetic nanofluids and its impact on light transport in magnetic colloids.

2. Theory

We consider a magnetizable sphere of arbitrary size parameter $\alpha (= 2\pi r\lambda)$ with ‘ r ’ being the radius of the particle and λ is free space wavelength of incident light and refractive index m_s surrounded by a magnetizable medium like a ferrofluid. According to Mie theory, scattered intensities for the two orthogonalized linearly polarized states are given by $i_1 = |S_1(m_s, \alpha, \theta)|^2$ and $i_2 = |S_2(m_s, \alpha, \theta)|^2$, i_1 and i_2 correspond to the scattered field components, perpendicular and parallel to the scattering plane (i.e. plane formed by the direction of applied field and the propagation direction). The scattering coefficients $S_1(m_s, \alpha, \theta)$ and $S_2(m_s, \alpha, \theta)$ are defined by:

$$S_1(m_s, \alpha, \theta) = \sum_{n=1}^{\infty} \frac{2n+1}{n(n+1)} [\alpha_n \pi_n(\cos \theta) + b_n \tau_n(\cos \theta)],$$

$$S_2(m_s, \alpha, \theta) = \sum_{n=1}^{\infty} \frac{2n+1}{n(n+1)} [\alpha_n \tau_n(\cos \theta) + b_n \pi_n(\cos \theta)],$$

where Mie coefficients a_n and b_n for magnetic sphere are defined by [20]:

$$a_n = \frac{\mu \Psi'_n(\beta) \Psi'_n(\alpha) - m \Psi'_n(\beta) \Psi'_n(\alpha)}{\mu \Psi'_n(\beta) \zeta'_n(\alpha) - m \Psi'_n(\beta) \zeta'_n(\alpha)},$$

$$b_n = \frac{m \Psi_n(\beta) \Psi'_n(\alpha) - \mu \Psi'_n(\beta) \Psi_n(\alpha)}{m \Psi'_n(\beta) \zeta'_n(\alpha) - \mu \Psi'_n(\beta) \zeta'_n(\alpha)},$$

and $\pi_n(\cos \theta)$ and $\tau_n(\cos \theta)$ are the partial derivative of the Legendre polynomials and angle θ is the angle between the forward and scattering directions. μ_s and m_s are respectively magnetic permeability and refractive index of the scatterers with respect to the surrounding medium. ψ_n and ζ_n are respectively Riccati Bessel and Hankel functions. Prime denote derivative with respect to arguments. The arguments of Riccati-Bessel and Hankel functions are given by $\alpha = 2\pi r/\lambda$ and $\beta = (m_s\alpha)$.

In the present case however, the medium is magnetically active and both μ_m and m_s may depend on the applied magnetic field. Ferrofluids usually contain nanomagnetic particles of magnetic oxides like Fe_2O_3 or Fe_3O_4 hence we shall assume that at optical frequencies $\mu_m \sim 1$. The refractive index of the ferrofluid may be expressed as $m_f = m_\infty L(\xi) + m_0$, where m_0 is the refractive index at zero field and m_∞ is the saturation value of the field dependent refractive index and the Langevin function $L(\xi) = \coth(\xi) - \frac{1}{\xi}$, with $\xi = \frac{\mu H}{kT}$ where μ is the magnetic moment of the monodomain nanomagnetic particles of ferrofluid, H is the applied field; k and T are respectively the Boltzmann constant and absolute temperature of the medium [21]. Considering the ferrofluid as a magnetizable medium, the relative refractive index of the MMS will be given by $m_{MMS} = m_{scat}/m_f$. Since m_f depends on $\xi = \frac{\mu H}{kT}$; m_{MMS} will also depend on H . This will lead to the field dependence of the scattering parameters a_n , b_n , $S_1(m_s, \alpha, \theta)$, $S_2(m_s, \alpha, \theta)$ and i_1 and i_2 .

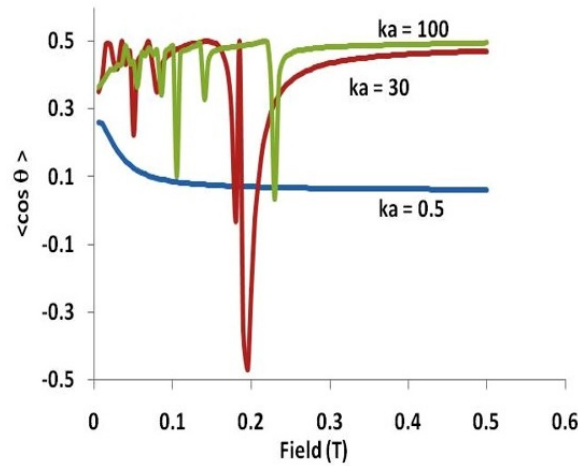


FIG. 1. It shows the $\langle \cos \theta \rangle$ as a function of magnetic field for different values of size parameter ka . For $ka = 30$ large resonance is observed. The negative value suggests preferential backscattered intensity

3. Result and discussion

It is known that for micron sized dielectric spheres the incident light excites localized electromagnetic modes at the surface of spheres. Such modes may trap light near the surface of the sphere by repeated total internal reflections. Resonances in such systems are a consequence of the refractive index mismatch, or shape or size, and are called morphology-dependent resonance (MDR) [22].

In Fig. 1, the anisotropy factor $\langle \cos \theta \rangle$ is plotted as a function of the applied magnetic field for different size parameter ka . It is noted that for $ka = 0.5$ no resonance is observed, it suggests that the system behaves as a Rayleigh scatterer. For $ka = 30$ maximum resonant behavior is observed, but for $ka = 100$ the resonance is not so strong. This suggests that for critical size parameter, the resonance is pronounced. The fact that $\langle \cos \theta \rangle$ can assume negative values indicates a predominant backward scattering. This is quite unusual in the case of scattering by non-magnetic spheres. The reason for the appearance of a preferential backscattering configuration in the small particle limit is the significant contribution given by magnetic dipolar radiation in magnetic scattering. These resonances may produce a standing wave configuration within the spheres that can cause the delay in light transport in magnetic colloids, which can be tunable by external magnetic field.

Figure 2 (A and B) shows the resonance produced in the light transport for $\sim 3 \mu\text{m}$ size magnetic spheres suspended in magnetic nanofluids (for forward and backscattered light) as a function of magnetic field. It should be noted here that at certain magnetic field values, the transmitted intensity becomes zero and generates magnetically induced stop band of light.

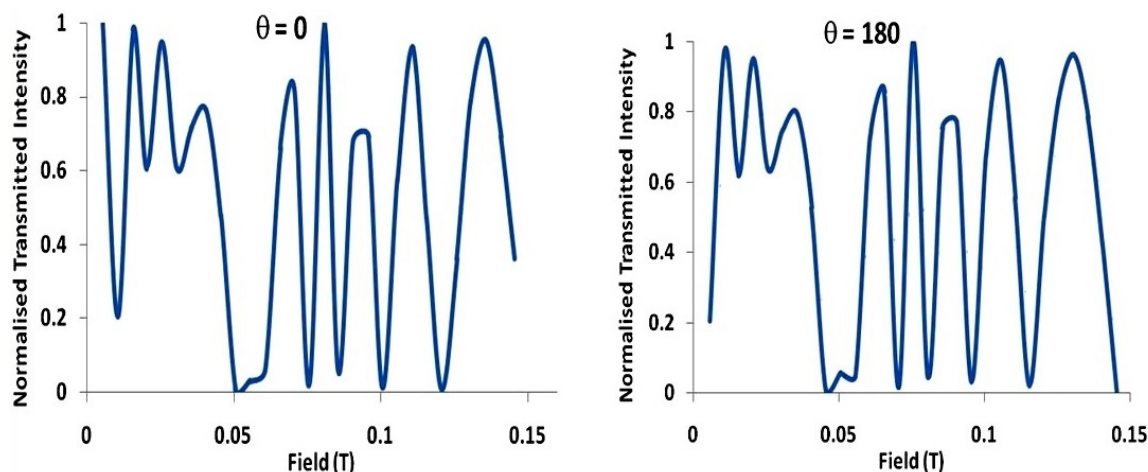


FIG. 2. Variation of forward and backward scattering intensity as functions of magnetic field for a magnetizable micronsized sphere (MMS) having diameter $3 \mu\text{m}$ suspended in magnetic nanofluids. Transmitted intensity exhibits magnetic field dependent resonant behavior

4. Conclusion

The present study has shown that an externally applied magnetic field induced morphological dependent resonance in a magnetizable sphere surrounded by magnetic nanofluids. This system exhibits resonance in forward as well as in backward direction. $\langle \cos \theta \rangle$ as a function of magnetic field shows preferential backward scattering. Such resonance produces standing wave within the magnetic spheres and can cause delay in light transport. These properties of such a system are useful for the development of novel magneto-photonics devices.

References

- [1] Yablonovitch E. Inhibited Spontaneous Emission in Solid-State Physics and Electronics. *Phys. Rev. Lett.*, 1987, **58**, P. 2059–2062.
- [2] John S. Strong localization of photons in certain disordered dielectric superlattices. *Phys. Rev. Lett.*, 1987, **58**, P. 2486.
- [3] Anderson P.W. The question of classical localization A theory of white paint? *Philos. Mag. B.*, 1985, **52**, P. 505–509.
- [4] Kuga Y., Ishimaru A. Retroreflectance from a dense distribution of spherical particles. *J. Opt. Soc. Am. A.*, 1984, **8**, P. 831–835.
- [5] Van Albada M.P., Lagendijk A. Observation of Weak Localization of Light in a Random Medium. *Phys. Rev. Lett.*, 1985, **55**, P. 2692–2695.
- [6] Sebbah P., Hu B., et al. Spatial-Field Correlation: The Building Block of Mesoscopic Fluctuations. *Phys. Rev. Lett.*, 2002, **88**, P. 123901-04.
- [7] Sheng P. *Introduction to Wave Scattering, Localization and Mesoscopic Phenomena*. Academic, San Diego, 1995.
- [8] Liu T., Chen X., et al. Tunable magneto-optical wavelength filter of long-period fiber grating with magnetic fluids. *Appl. Phys. Lett.*, 2007, **91**, P. 121116.
- [9] Chieh J.J., Yang S.Y., et al. Magnetic-fluid optical-fiber modulators via magnetic modulation. *Appl. Phys. Lett.*, 2007, **90**, P. 133505.
- [10] Pinheiro F.A., Martinez A.S., Sampaio L. Vanishing of energy of transport velocity and diffusion constant of electromagnetic waves in disordered magnetic media. *Phys. Rev. Lett.*, 2000, **85**, P. 5563.
- [11] Pinheiro F.A., Martinez A.S., Sampaio L. New Effects in Light Scattering in Disordered Media and Coherent Backscattering Cone: Systems of Magnetic Particles. *Phys. Rev. Lett.*, 2000, **84**, P. 1435–1438.
- [12] Garcia P.D., Sapienza R., et al. Resonant light transport through Mie modes in photonic glasses. *Phys. Rev. A.*, 2008, **78**, P. 023823.
- [13] Hau L.V., Harris S.E., Dutton Z., Behroozi C.H. Light speed reduction to 17 metres per second in an ultracold atomic gas. *Nature*, 1999, **397**, P. 594.
- [14] Kim H., Ge J., et al. Structural colour printing using a magnetically tunable and lithographically fixable photonic crystal. *Nat. Photon.*, 2009, **3**, P. 534–540.
- [15] Pu S., Liu M. Tunable photonic crystals based on MnFe_2O_4 magnetic fluids by magnetic fields. *J. Alloys and Comp.*, 2009, **481**, P. 851–854.
- [16] Ge J., Hu Y., Yin Y. Highly Tunable Superparamagnetic Colloidal Photonic Crystals. *Angew. Chem. Int. Ed.*, 2007, **46**, P. 7428.
- [17] Kerker M., Wang D.S., Giles C.L. Electromagnetic scattering by magnetic spheres. *J. Opt. Soc. Am.*, 1983, **73**(6), P. 765.
- [18] García-Cámara B., Moreno F., et al. Light scattering resonances in small particles with electric and magnetic properties. *J. Opt. Soc. Am.*, 2008, **25**, P. 327–334.
- [19] Tarento R.J. Mie Scattering of Magnetic Spheres. *Phys. Rev. E*, 2004, **69**, P. 026606-1.
- [20] Lacoste D., van Tigglen B.A. Coherent backscattering of light in a magnetic field. *Phys. Rev. E*, 2000, **61**, P. 4556–4565.
- [21] Chan Y.F., Yang S.Y., et al. Thermal effect on the field-dependent refractive index of the magnetic fluid film. *Appl. Phys. Lett.*, 2003, **82**, P. 3481–3484.
- [22] Bhatt H., Patel R., Mehta R.V. Magnetically induced Mie resonance in a magnetic sphere suspended in a ferrofluid. *J. Opt. Soc. Am. A*, 2010, **27**, P. 873.

Effect of precipitating agent NaOH on the preparation of copper oxide nanostructures for electrochemical applications

M. Balasubramaniam, S. Balakumar

National Centre for Nanoscience and Nanotechnology, University of Madras,
Guindy campus, Chennai – 600 025, India

balasuga@yahoo.com

PACS 82.47.Uv

DOI 10.17586/2220-8054-2016-7-3-482-487

Copper oxide (CuO) nanostructures with different concentrations of sodium hydroxide for electrochemical applications such as supercapacitors have been synthesized using a simple and low-cost precipitation method. X-ray diffraction pattern confirmed the formation of CuO nanostructures without any impurities and further confirmed its highly crystalline, single phase, monoclinic nature. UV-diffuse reflectance spectral (UV-DRS) studies provided the absorption edge of the material and the estimated band gap value for the nanostructures were calculated using Kubelka-Munk (KM) absorbance plot that are determined to be around 4.74 – 4.84 eV. Field emission scanning electron microscopy (FESEM) investigations revealed the morphology of the copper oxide nanocrystals and showed the increment of diameter of the CuO nanostructures. The electrochemical behavior of the CuO nanostructures were investigated using electrochemical impedance spectroscopy (EIS) and cyclic voltammetry (CV) techniques which showed the stability, reversibility, symmetric and capacitive nature of the nanostructures.

Keywords: copper oxide nanostructures, sodium hydroxide, electrochemical behavior, capacitive nature, stability.

Received: 23 January 2016. Revised: 18 April 2016

1. Introduction

In recent years, considerable research has been done to develop nanostructured materials for supercapacitors by virtue of their exclusive properties such as high specific surface area, shorter ion diffusion, and electrochemical activity [1–5]. Ruthenium Oxide (RuO₂) and Iridium Oxide (IrO₂) of noble metal oxide materials were used as pseudocapacitive electrode materials with extraordinary performance [6, 7]. However, the high cost of hydrous RuO₂ and IrO₂ hindered their wide application. Consequently, increasing interest has been generated for the use of cheap transition metal oxides, such as nickel oxide (NiO) [8], cobalt oxide (Co₃O₄) [9], vanadium oxide (V₂O₅) [10], manganese oxide (MnO₂) [11], and copper oxide (CuO) [12]. Of these, CuO has attracted much research interest due to its unique properties, such as high catalytic activity, easy synthesis route, environmentally friendly nature and variable morphologies at the nanoscale. It has found potential applications in electrochemistry as an electrode material for lithium-ion batteries and electrochemical capacitors, solar energy systems, heterogeneous catalysts and selective gas sensors [13, 14]. CuO is a metal oxide with encouraging redox properties, and thus thin CuO films fabricated by different techniques such as electrodeposition [15] and chemical bath deposition [16] can find certain use in supercapacitors. However, the highest specific capacitances obtained in those studies are only 37 and 43 F·g⁻¹, respectively [15, 16]. The low capacitances may be due to the film morphology with a poorly-accessible surface area. It is also difficult for the ions and electrons to diffuse through a submicron-thick film. To overcome the above-mentioned drawbacks, it is necessary to prepare different CuO nanostructures in order to create well-dispersed and an increased number of active sites that can interact with ions and the electrolyte. Furthermore, the different morphologies of CuO have been shown to have effects on the optical, semiconducting, and piezoelectric properties. In this study, we report the preparation of various CuO nanostructures using different molar concentrations of precipitating agent, sodium hydroxide by simple precipitation method. The obtained CuO nanostructures were characterized using XRD, FESEM, and UV-DRS techniques. Also, the electrochemical behaviors of CuO nanostructures for supercapacitors were investigated using EIS and CV studies.

2. Materials and Methods

Copper acetate monohydrate (Cu(CH₃COO)₂·H₂O, Merck), sodium hydroxide (NaOH, Merck) and double distilled water were used in the preparation. All the chemicals were of analytical grade. A calculated amount of copper acetate monohydrate was added in 20 ml of double distilled water, after complete dissolving of the precursor material in the solvent, precipitating agent sodium hydroxide (NaOH) solution at various concentrations such as 1.5 M, 3.0 M, 4.5 M and 5.0 M were added dropwise and the mixture was stirred for 2 h. After 2 h, the color of the solution changed from blue to black with precipitates under the supernatant solution. The precipitates

were filtered, washed with distilled water for several times and dried in a hot air oven at 100 °C for 6 h. The X-ray diffraction (XRD) technique (Model D8 Advance, Rigaku X-ray Diffractometer) was used for structural analysis. Field emission scanning electron microscopy (FE-SEM) (Hitachi SU-6600) was used for the imaging of the morphologies. The optical reflectance and band gap properties were studied using a UV-DRS technique (Perkin Elmer Lambda 650 Spectrophotometer). The electrochemical behaviors of the CuO nanostructures were studied using cyclic voltammetry (CV) and electrochemical impedance spectroscopy (EIS) studies (Bio-logic-science instruments). Cyclic voltammetric and EIS measurements were performed with an electrochemical analyzer in a conventional three electrode cell with glassy carbon electrode (GCE) as a working electrode, on which the CuO sample was coated, Ag/AgCl as the reference electrode and a Pt wire as the counter electrode. All potentials were reported with respect to the Ag/AgCl electrode. KOH (1M) solution was used as an electrolyte.

3. Results and discussion

3.1. XRD analysis

Figure 1 displays the XRD profiles of the CuO nanostructures synthesized using different concentrations of NaOH. All of the Bragg's reflections can be indexed to the monoclinic-phase [17–19] of CuO (space group C2/c), which is very close to the reported data (JCPDS 48-1548) whereas no characteristic peaks of any other impurities such as Cu(OH)₂, Cu₂O, or precursors used were observed. In all cases, peak broadening was observed, which depicts the nanostructural crystalline domains in CuO. The average crystallite size was determined using Debye-Scherrer's relation which is represented in Table 1. From the β values, it is evident that the crystallographic growth was suppressed at 5.0 M NaOH, which is the maximum crystal growth concentration.

TABLE 1. Average crystallite size and FWHM of CuO nanostructures

Concentration of NaOH	FWHM (β)	Crystallite size (nm)
1.5 M	0.9194	~20
3.0 M	0.90133	~20.5
4.5 M	0.64512	~29
5.0 M	0.9200	~20

3.2. Optical analysis

Figure 2(a) displays the reflectance spectra of CuO nanostructures prepared at different concentrations of sodium hydroxide. In all the cases, the spectra were recorded with the onset of an absorption edge at 350 nm and it extended toward the UV region of the spectra. The band gap values were estimated using the Kubelka-Munk (K-M) absorption plot shown in Fig. 2(b). The optical band gap values were determined and found to be 4.84, 4.81, 4.76 and 4.74 eV [20] for ultrathin CuO nanorods, thin CuO nanorods, CuO nanorods and CuO nanotubes respectively, which also illustrated that the addition of NaOH on the CuO nanostructures shows remarkable changes in the optical properties. As the diameter of the crystal (ultrathin nanorods) is smaller for the case of 1.5 M NaOH, the band gap value is high (4.84 eV) compared to other nanostructures such as, thin nanorods (4.81 eV), nanorods (4.76 eV) and nanotubes (4.74 eV). The blue shift in optical band gap energy satisfies the quantum confinement effect.

3.3. Morphological analysis

NaOH is a strong electrolyte that may neutralize the surface charges of the CuO, thereby preventing them from possible crystalline aggregation. Finally, the use of high concentration NaOH may create diffusion layers on certain surfaces of CuO, which may in turn create an additional growth anisotropy, allowing only energetically favorable crystallographic planes to grow. Fig. 3 shows the FESEM micrographs of CuO nanostructures prepared at 1.5, 3.0, 4.5 and 5.0 M concentrations of NaOH that were imaged at an operating voltage of 15 kV. At 1.5 M NaOH, CuO nanostructures were formed with bundles of ultrathin nanorod morphology with diameters in the range of 7 – 33 nm and rod lengths of 92 – 172 nm. At 3.0 M NaOH, bundles of thin nanorod morphology with diameters in the range of 9 – 35 nm and rod lengths of 88 – 159 nm were observed. At 4.5 M NaOH, bundles of nanorod morphology with diameters in the range of 19.5 – 36 nm and rod lengths of 85 – 151 nm were observed. At 5.0 M NaOH, bundles of nanotube morphology with diameters ranging from 42 – 598 nm and tube lengths of 159 nm to several microns were observed. From the figures, it is evident that the addition of a greater number of OH⁻ ions on the CuO makes the crystal grow along the diameter. In all four nanostructures, quantum confinement exists in

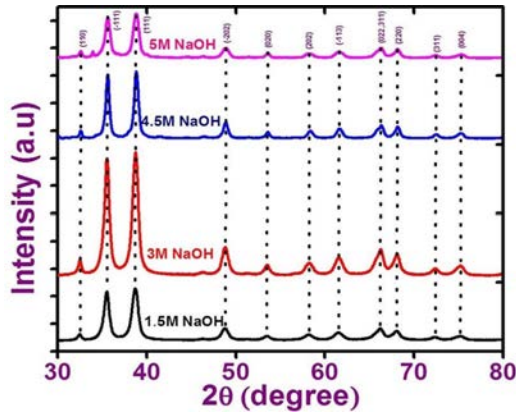


FIG. 1. XRD pattern of CuO nanostructures prepared using different concentrations of NaOH (1.5 M, 3.0 M, 4.5 M and 5.0 M)

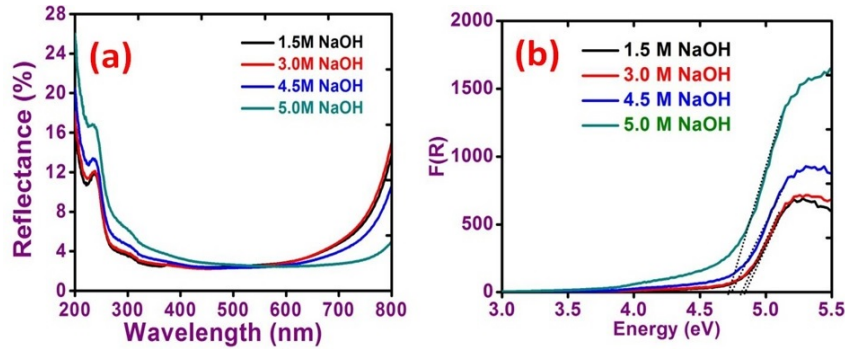
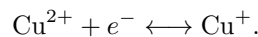


FIG. 2. (a) UV-diffuse reflectance spectra and (b) Kubelka-Munk (K-M) absorbance plot of CuO nanostructures prepared using different concentrations of NaOH (1.5 M, 3.0 M, 4.5 M and 5.0 M)

the diameter axis which is found to be in nanoscale regime and this could be the crucial factor for better capacitor characteristics.

3.4. Electrochemical analysis

To investigate the electrochemical behavior of the CuO nanostructures for energy storage devices such as supercapacitors, cyclic voltammetry studies were performed on all four types of CuO nanostructures. Fig. 4(a) exhibits the CV curves of all the CuO nanostructures, electrochemical redox peaks are observed at potentials ranging from 0.1 to 0.4 V. As observed, the CV current response of sample increases gradually with increasing scan rate, indicating reversible redox reaction taking place at the electrode material interface: all CV curves show typical pseudocapacitance behavior. These results also show two main peaks: a broad cathodic peak, and sharp-edged anodic peaks that are corresponding to redox reaction of Cu^{2+}/Cu [21]. Storage mechanism in CuO has been proposed as follows. It is based on the intercalation/extraction of protons in the electrode that is oxidation/reduction of the electrode (surface adsorption and desorption of protons) [21]. When the CuO electrode is swept towards a negative potential, cathodic current flows according to $\text{Cu}^{2+} \leftrightarrow \text{Cu}^+$ reduction process whereas during a positive potential sweep, anodic current flows due to $\text{Cu}^+ \leftrightarrow \text{Cu}^{2+}$ oxidation process [21]. The net redox reaction can be represented by the equation.



Thus, the CV curves indicated that the nanomaterial has reversibility, is symmetric and has capacitive behavior. Even though all the samples are prepared at different concentrations of NaOH, all the CV curves exhibit similar pattern in shape that evidently confirmed the electrochemical stability of the nanostructure at different NaOH concentrations. In addition, the specific capacitance value was calculated for all the four samples by using the relation (1) and the values are tabulated in Table 2:

$$C_s = \frac{1}{mS} \times \text{area of integration.} \quad (1)$$

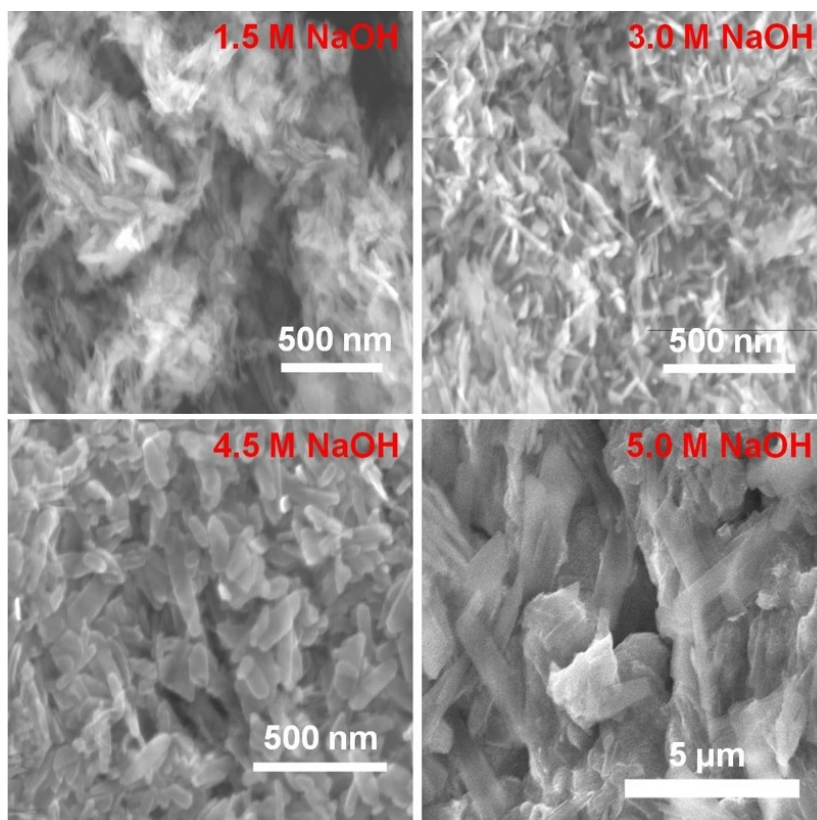


FIG. 3. FESEM micrographs of CuO nanostructures prepared using different concentrations of NaOH (1.5 M, 3.0 M, 4.5 M and 5.0 M)

TABLE 2. Specific capacitance of CuO nanostructures at different scan rates

Samples	Scan rate (mV/s)	Specific Capacitance (F/g)
1.5 M	20	753.34
	50	426.34
	100	338.26
3.0 M	20	759.51
	50	450.48
	100	322.70
4.5 M	20	640.32
	50	297.28
	100	300.0
5.0 M	20	667.82
	50	385.97
	100	305.06

The electrochemical studies evidently confirms that the CuO nanostructures prepared by using simple precipitation method shows better capacitive performance with high specific capacitance values, which may be due to two major reasons: (1) high specific surface area and (2) the diameter in all four nanostructures is found to be in the nanoscale regime and the aggregation effects are also minimal, so the electrolyte ions can migrate or diffuse easily between the structures and access the active sites in CuO nanostructures and also the smaller particles have better accessibility and mobility towards OH⁻ ions from the electrolyte thereby resulting in a higher capacitance value.

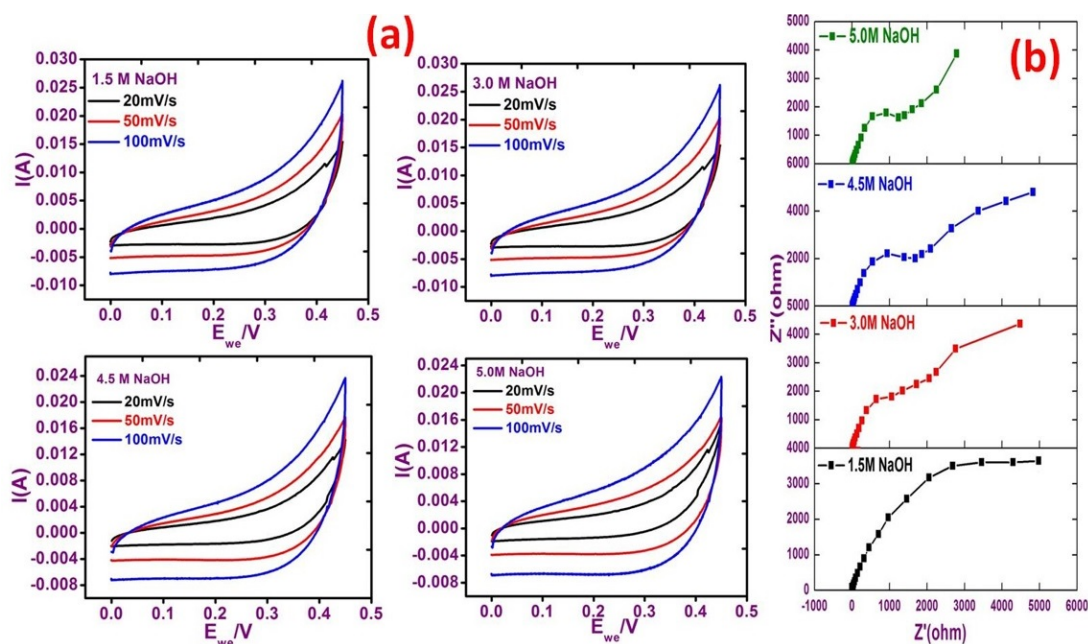


FIG. 4. (a) Typical cyclic voltammograms and (b) Nyquist plots of CuO nanostructures prepared using different concentrations of NaOH (1.5 M, 3.0 M, 4.5 M and 5.0 M) at different scan rates (20, 50 and 100 mV/s) in 1 M KOH solution

The specific capacitance was found to be significantly higher than the reported values [21]. Hence, the CuO nanostructures prepared by this simple approach would contribute as a cheap and efficient metal oxide supercapacitor electrode material.

Also, to better determine the nanostructure among the four different nanostructures for electrochemical capacitor applications, EIS studies were carried out. EIS is an excellent tool used to explore the electrochemical characteristics of electrode/electrolyte interface using a Nyquist plot. The main purpose of the EIS experiments is to study the effect of NaOH on the interfacial properties of CuO electrodes (capacitance and electron charge transfer resistance). The Nyquist plot of the four prepared electrodes is shown in Fig. 4(b). In all four samples, a partial semicircle in the high-frequency region corresponding to the electron charge transfer resistance due to the Faradaic redox process at the electrode/electrolyte interface was observed. This resistance is associated with two resistances: electrolyte resistance and the material (oxide) resistance which arises from the non-uniform continuity in the charge transfer process at the electrode/electrolyte interface because of the conductivity differences between the oxide (CuO) and the electrolyte [22]. A line is observed in the low frequency region corresponding to electron-transfer diffusion process. It is worth stating that for ideal electrochemical capacitors, the plot should be a line perpendicular to the real axis at low frequency region. A comparison of the low frequency region in all four samples reveals that the 5.0 M NaOH made CuO nanostructure that shows the best electron diffusion process in comparison to the other three nanostructures. Thus, we conclude that the CuO nanotubes (5.0 M NaOH) are a better nanostructure for electrochemical applications.

4. Conclusion

In summary, CuO nanostructures were synthesized by varying the concentration of NaOH for electrochemical capacitor applications using a facile precipitation method. The XRD pattern confirmed the formation of CuO nanostructures without any impurities and further confirmed the highly crystalline, single phase, monoclinic nature of the CuO nanostructures. UV-DRS spectra confirmed the absorption edge of the material and the band gap values were estimated using Kubelka-Munk absorbance plot and were in the range of 4.74 to 4.84 eV. The FESEM investigations revealed that the addition of OH^- ions increased the diameter of the CuO crystals. The electrochemical behavior was studied using CV and EIS techniques that exhibited the stability, reversibility, symmetric and capacitive nature of the nanostructures. Among the CuO nanostructures, the nanotubes were found to have good electron diffusion activity than the other nanostructures that was evident from the EIS curves. The study finally concluded that the CuO nanostructures can be used as a potential electrode material for supercapacitor applications.

Acknowledgement

The authors acknowledge DST-INSPIRE, India for providing the fund to do our research work.

References

- [1] Rakhi R.B., Chen W., Cha D., Alshareef H.N. Substrate dependent self-organization of mesoporous cobalt oxide nanowires with remarkable pseudocapacitance. *Nano Letters*, 2012, **12**, P. 2559–2567.
- [2] Wang H., Holt C. et al. Graphene-nickel cobaltite nanocomposite asymmetrical supercapacitor with commercial level mass loading. *Nano Research*, 2012, **5**, P. 605–617.
- [3] He X., Li R., et al. Synthesis of mesoporous carbons for supercapacitors from coal tar pitch by coupling microwave-assisted KOH activation with a MgO template. *Carbon*, 2012, **50**, P. 4911–4921.
- [4] Chen C.Y., Shih Z.Y., Yang Z., Chang H.T. Carbon nanotubes/cobalt sulfide composites as potential high-rate and high-efficiency supercapacitors. *Journal of Power Sources*, 2012, **215**, P. 43–47.
- [5] Song M.K., Cheng S., et al. Correction to Anomalous Pseudocapacitive Behavior of a Nanostructured, Mixed-Valent Manganese Oxide Film for Electrical Energy Storage. *Nano Letters*, 2012, **12**, P. 3483–3490.
- [6] Terasawa N., Mukai K., Asaka K. Superior performance of a vapor grown carbon fiber polymer actuator containing ruthenium oxide over a single-walled carbon nanotube. *Journal of Materials Chemistry*, 2012, **22**, P. 15104–15109.
- [7] Murakami Y., Nakamura T., Zhang X.G., Takasu Y. Preparation of highly porous iridium oxide electrodes by pore initiation with rare earth ions. *Journal of Alloys and Compounds*, 1997, **259**, P. 196–199.
- [8] Zhang Y.Q., Xia X.H., et al. Self-assembled synthesis of hierarchically porous NiO film and its application for electrochemical capacitors. *Journal of Power Sources*, 2012, **199**, P. 413–417.
- [9] Zhang F., Yuan C., et al. Facile growth of mesoporous Co₃O₄ nanowire arrays on Ni foam for high performance electrochemical capacitors. *Journal of Power Sources*, 2012, **203**, P. 250–256.
- [10] Ghosh A., Ra E.J., et al. High Pseudocapacitance from Ultrathin V₂O₅ Films Electrodeposited on Self-Standing Carbon-Nanofiber Paper. *Advanced Functional Materials*, 2011, **21**, P. 2541–2547.
- [11] Dong M., Zhang Y.X., et al. Self-assembled spongy-like MnO₂ electrode materials for supercapacitors. *Physica E*, 2012, **45**, P. 103–108.
- [12] Sun G., Li K., et al. Physical and electrochemical characterization of CuO-doped activated carbon in ionic liquid. *Electrochimica Acta*, 2010, **55**, P. 2667–2672.
- [13] Shaikh J.S., Pawar R.C., et al. CuO-PAA hybrid films: Chemical synthesis and supercapacitor behavior. *Applied Surface Science*, 2011, **257**, P. 4389–4397.
- [14] Xiang J.Y., Tu J.P., et al. Self-assembled synthesis of hierarchical nanostructured CuO with various morphologies and their application as anodes for lithium ion batteries. *Journal of Power Sources*, 2010, **195**, P. 313–319.
- [15] Patake V.D., Joshi S.S., Lokhande C.D., Joo O.S. Electrodeposited porous and amorphous copper oxide film for application in supercapacitor. *Materials Chemistry and Physics*, 2009, **114**, P. 6–9.
- [16] Dubal D.P., Dhawale D.S., et al. Fabrication of copper oxide multilayer nanosheets for supercapacitor application. *Journal of Alloys Compounds*, 2010, **492**, P. 26–30.
- [17] Aixia Gu, Guangfeng Wang, Xiaojun Zhang, Bin Fang. Synthesis of CuO nanoflower and its application as a H₂O₂ sensor. *Bulletin of Materials Science*, 2010, **33**, P. 17–20.
- [18] Anita Sagadevan Ethiraj, Dae Joon Kang. Synthesis and characterization of CuO nanowires by a simple wet chemical method. *Nanoscale Research Letters*, 2012, **7**, P. 70.
- [19] Volanti D.P., Keyson D., et al. Synthesis and characterization of CuO flower-nanostructure processing by a domestic hydrothermal microwave. *Journal of Alloys and Compounds*, 2008, **459**, P. 537–542.
- [20] Han Ho Choi, Joodong Park, Singh R.K. Nanosized CuO Encapsulated Silica Particles Using an Electrochemical Deposition Coating. *Electrochemical and Solid-state Letters*, 2004, **7**, P. C10–C12.
- [21] Bello A., Dodoo-Arhin D., et al. Surfactant Assisted Synthesis of Copper Oxide (CuO) Leaf-like Nanostructures for Electrochemical Applications. *American Journal of Materials Science*, 2014, **4**, P. 64–73.
- [22] Meher S.K., Justin P., Rao G.R. Microwave-Mediated Synthesis for Improved Morphology and Pseudocapacitance Performance of Nickel Oxide. *ACS Applied Materials & Interfaces*, 2011, **3**, P. 2063–2073.

Magnetic silica nanoparticles for the removal of Pb⁺² from water

N. Shukla^{1,2}, A. Saxena^{1,*}, V. Gupta¹, A. S. Rawat¹, V. Kumar¹,
S. Shrivastava², C. Rajagopal¹, P. K. Rai^{1,*}

¹Centre for Fire, Explosive and Environment Safety, Timarpur, Delhi-110054, India

²Department of Chemistry, Institute of Excellence in Higher Education, Bhopal-462016, India

*pramrai@rediffmail.com, *amsa888@rediffmail.com

PACS 81.16.Be

DOI 10.17586/2220-8054-2016-7-3-488-491

Zero valent iron impregnated silica nanoparticles (Fe⁰/n-SiO₂) were synthesized using sol-gel process followed by supercritical drying, wet impregnation and hydrogen reduction. The synthesized nanoparticles were characterized by nitrogen Brunauer–Emmett–Teller (N₂-BET), Scanning Electron Microscopy, Transmission Electron Microscopy, Scanning Electron Microscopy with Energy-Dispersive X-ray spectroscopy, Vibrating Sample Magnetometer and X-ray diffraction techniques. Prepared samples were found to be magnetic with ultra-low density (0.048 g/mL) and high surface area (422 m²/g). Prepared samples were evaluated for adsorptive removal of Pb⁺² (5, 10, 25 and 50 ppm) from contaminated water. Results indicated that the adsorption of Pb⁺² was faster at lower concentrations (5 and 10 ppm) as > 80 % of Pb⁺² was removed within 480 minutes. At higher concentrations, the adsorption was slower, and the removal efficiency of 51.24 and 21.78 % were observed for 25 and 50 ppm Pb⁺² respectively, whereas for bare SiO₂ nanoparticles, it was 39.64 and 14.04 %.

Keywords: Fe⁰/n-SiO₂, Pb⁺², removal capacity, removal percentage, pH enhancement.

Received: 23 January 2016

Revised: 22 April 2016

1. Introduction

Lead (Pb⁺²) is one of the most common and hazardous inorganic water pollutants. A huge amount of Pb⁺² is introduced daily in water streams in the form of wastewater from industries such as battery and paint manufacturers. Lead-containing pipes used in water supply systems are also responsible for the water contamination [1]. It has been proved that Pb⁺² is non-biodegradable and produces poisonous effects on living beings. In the human body, it can accumulate in kidneys, bones, muscles and may cause of anaemia, irritability, dizziness, renal weakness and cancer [2]. The World Health Organization (WHO) has set permissible limit for Pb⁺² as 0.010 mg/L in potable water. To reduce the threats of Pb⁺² poisoning, many water treatment techniques have been developed for the removal of Pb⁺² from water. Common treatment methods for Pb⁺² removal from water are chemical precipitation, ion exchange, electro-flotation, membrane filtration and reverse osmosis [3]. All of these methods have some commercial and operational limitations, therefore, it is essential to develop new technologies having low cost and high Pb⁺² removal efficiencies. There has been intense interest in the utilization of nanoparticles for the purification of Pb⁺²-contaminated water. Due to their small size and high specific surface area, nanoparticles possess a wide range of reactive sites to adsorb environmental contaminants [4]. Various nanoparticles have been previously reported for the removal of Pb⁺² from water. Nano zero valent iron (Fe⁰) has been found as one of the most successful nano-adsorbent for the removal of Pb⁺² from contaminated water [5]. Although Fe⁰ has been proved to be an efficient adsorbent of Pb⁺², it also has some drawbacks. It is highly unstable and is readily oxidized with atmospheric oxygen and water. Furthermore, Fe⁰ nanoparticles also aggregate with time and due to these drawbacks the available binding sites and reactivity of these nanoparticles become reduced. To overcome or minimize these drawbacks, Fe⁰ nanoparticles have been loaded or impregnated on solid supports. Various composites of Fe⁰ nanoparticles supported/ impregnated clays, zeolites, etc. have been previously reported for the removal of Pb⁺² from contaminated water [6]. Silica based solid supports (zeolites, MCM-41 and SBA-15) have been found most suitable matrices among all supporting materials for the impregnation of Fe⁰ nanoparticles [7]. Previous attempts to disperse Fe⁰ nanoparticles over silica were limited to SBA-15 and MCM-41. In the present work, we report the synthesis of high surface area and low density Fe⁰ impregnated silica nanoparticles (Fe⁰/n-SiO₂) and their application for the removal of Pb⁺² from contaminated water.

2. Preparation and characterization of $Fe^0/n-SiO_2$

The synthesis of $Fe^0/n-SiO_2$ was carried out by a two-step procedure, in the first step, SiO_2 nanoparticles ($n-SiO_2$) were synthesized by the sol-gel procedure followed by supercritical drying of liquid gel to aerogel at 265 °C [8]. In the second step, the synthesized SiO_2 particles were impregnated with solution of $FeCl_3$ in methanol containing 8.0 % w/w of Fe. The material was dried and subjected to reduction under H_2 gas at 600 °C for 3 – 4 h. This resulted in magnetic silica nanoparticles having 7.2 % Fe^0 (determined by Atomic Absorption Spectrophotometer).

Detailed characterization of $n-SiO_2$ has been reported in our previous communications [8, 9], herein the characterization of impregnated system, i.e., $Fe^0/n-SiO_2$ has been discussed. Nitrogen adsorption-desorption isotherm of $Fe^0/n-SiO_2$ showed type IV pattern, which indicated that all particles have mesoporous characteristics. The appearance of H3 hysteresis loop also signified the presence of slit shaped pores in nanoparticles and wide pore size distributions [10]. $Fe^0/n-SiO_2$ showed BET surface area as 422 m^2/g . The BJH pore size distribution curve of $Fe^0/n-SiO_2$ indicated pore maxima for micropores and mesopores at 18 and 200 Å respectively. $Fe^0/n-SiO_2$ was found to possess low density (0.048 g/mL) and low moisture content (0.56 %). The X-ray diffraction (XRD) pattern of $Fe^0/n-SiO_2$ (Fig. 1) was matched from reported literature. It displayed the characteristic peak at 44.83 °, which indicated the presence of iron predominantly in the zero valency state, diffraction peaks at 44.83 ° (110), 64.99 ° (200) and 82.45 ° (211) confirmed that the Fe^0 is in bcc (body-centered cubic) phase (JCPDS 00-006-0696). Moreover broad hump at 21.56 ° indicated the presence of amorphous hydrated silica [11].

Scanning Electron Microscope (SEM) image of $Fe^0/n-SiO_2$ (Fig. 2) displayed its dendritic texture in which all nanoparticles aggregated and depicted huge porosity. Scanning Electron Microscope with Energy-Dispersive X-ray spectroscopy (SEM-EDX) data of $Fe^0/n-SiO_2$ indicated around 7.2 % loading of Fe^0 with uniform distribution on the silica nanoparticles (Fig. 3). Transmission Electron Microscope (TEM) image of $Fe^0/n-SiO_2$ indicated the spherical shape of prepared nanoparticles (Fig. 2-inset). The particle diameter $Fe^0/n-SiO_2$ was observed in between 7 to 32 nm (maximum particles were of 17 nm). The magnetic properties of $Fe^0/n-SiO_2$ were examined using Vibrating Sample Magnetometer (VSM) analysis. The appearance of hysteresis loop indicated the value of saturation magnetization (M_s) ~ 4.409 emu/g with a high coercivity (H_c) of 121.7 Oe. The sample showed higher coercivity and lower saturation magnetization in comparison to bulk iron ($H_c=0.9$ Oe, $M_s=220$ emu/g), which is indicative of iron particles in nanometer size range [12], furthermore, these impregnated nanoparticles also showed magnetic attraction. Characterization data of $Fe^0/n-SiO_2$ supported the formation of low density magnetic zero-valent iron loaded SiO_2 nanoparticles. Characterization data also suggested that the surface area, bulk density and moisture content of bare $n-SiO_2$ were decreased, whereas particle size of $n-SiO_2$ increased after impregnation with Fe^0 (Table 1).

TABLE 1. Characteristics of bare $n-SiO_2$ and Fe^0 impregnated $n-SiO_2$

Adsorbent	Bulk density (g/ml)	Moisture content (%)	Surface area (m^2/g)	Particle size range (nm)	Particle shape
$n-SiO_2$	0.035	0.80	628	3 – 25	Spherical
$Fe^0/n-SiO_2$	0.048	0.56	422	7 – 32	Spherical

3. Absorptive removal of Pb^{+2} using prepared nanoparticles

Prepared nanoparticles of $n-SiO_2$ and $Fe^0/n-SiO_2$ were examined to remove Pb^{+2} from water. The experiments were carried out at four different Pb^{+2} concentrations, viz, 5, 10, 25 and 50 ppm. Adsorptive removal studies were performed at a dose level of 1 mg/mL (nanomaterial/ Pb^{+2} solution). 100 mg of $Fe^0/n-SiO_2$ was taken separately in 100 mL Pb^{+2} solutions of different concentrations. All samples were shaken continuously in rotatory shaker at the speed of 200 rpm. After shaking for fixed time periods, 2 mL sample was taken out, centrifuged and separated. Additionally, the Pb^{+2} concentrations were determined using an Atomic Absorption Spectrophotometer. Results indicated > 80 % removal of Pb^{+2} by both the adsorbents within 360 min for 5 ppm Pb^{+2} . As the concentration of Pb^{+2} varied from 5 to 50 ppm the adsorption potential of $n-SiO_2$ and $Fe^0/n-SiO_2$ decreased from 100 to 14.04 % and 100 to 21.78 % respectively within 2880 min (Fig. 4 and 5).

The change in pH during the kinetics experiments was also measured because of its importance in controlling the removal of Pb^{+2} .

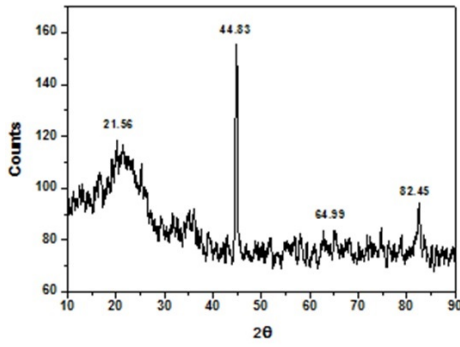


FIG. 1. XRD pattern of $Fe^0/n-SiO_2$

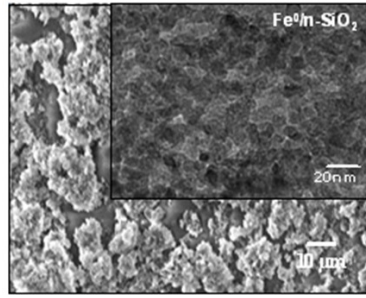


FIG. 2. SEM & TEM (inset) images

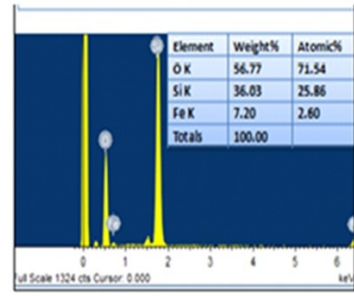


FIG. 3. SEM-EDX of $Fe^0/n-SiO_2$

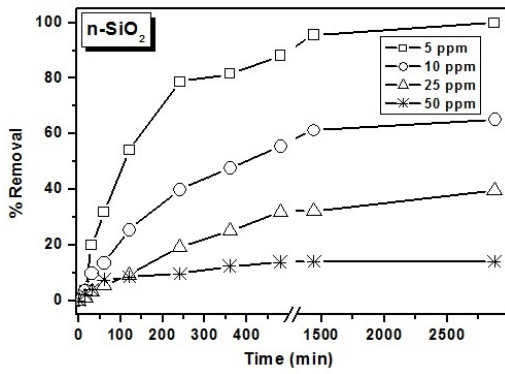


FIG. 4. Removal of Pb^{2+} by $n-SiO_2$

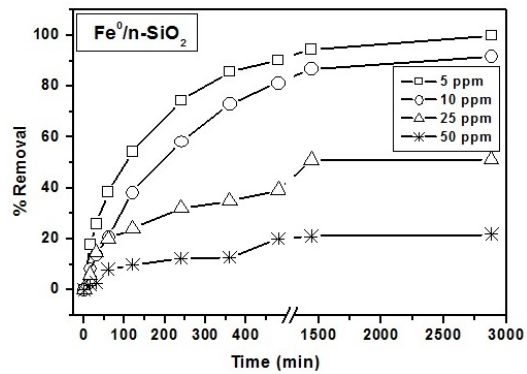


FIG. 5. Removal of Pb^{2+} by $Fe^0/n-SiO_2$

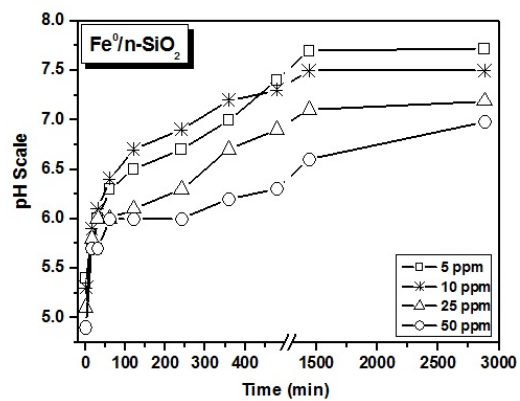
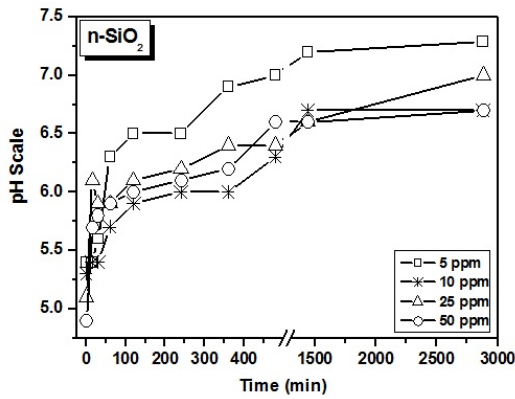


FIG. 6. Change in pH by the both adsorbents during Pb^{2+} removal

Considerable change in pH for n-SiO₂ and Fe⁰/n-SiO₂ was observed during the Pb⁺² removal studies (Fig. 6). The maximum hike in pH for n-SiO₂ and Fe⁰/n-SiO₂ was measured as 7.29 and 7.72 respectively (initial pH was 5.4). The increase in pH of medium by zero valent iron impregnated nano adsorbents was due to the formation of iron oxide/hydroxides on oxidation in aqueous medium. The removal kinetics also affected at higher pH as Pb⁺² got precipitated to Pb⁰, PbO, Pb(OH)₂, etc. [9] at this pH. Here, it was also noticeable that the removal of Pb⁺² increased with gradual increase of the medium's pH, which may be due to the protonation/deprotonation of the hydroxyl species on the surface of the nanoparticles. Overall studies indicated Fe⁰/n-SiO₂ system as a promising material for the removal of Pb⁺² from contaminated water.

4. Conclusion

Magnetic nanoparticles of Fe⁰/n-SiO₂ with high surface area and low density were prepared using the sol-gel method followed by wet impregnation technique and hydrogen reduction. The synthesized nano-composite and bare SiO₂ nanoparticles were evaluated for adsorptive removal of Pb⁺² from contaminated water. Although the surface area of n-SiO₂ was higher than Fe⁰/n-SiO₂, yet it showed lower Pb⁺² removal percentage. The pH enhancement (up to 7.72) by both adsorbents was also recorded during the removal studies. The results suggested that the removal of Pb⁺² by both the adsorbents may be due to high surface area and also by the protonation/deprotonation of the hydroxyl species created on the surface of nanoparticles after reaction with water. Further work is going on to establish the specific mechanism for Pb⁺² removal.

Acknowledgements

We are thankful to Dr. Chitra Rajagopal, OS & Director CFEES, Delhi for providing lab facilities to carry out and publish this work.

References

- [1] Chen J.Z., Tao X.C., Xu J., Zhang T., Liu Z.L. Biosorption of lead, cadmium and mercury by immobilized microcystis aeruginosa in a column. *Process Biochemistry*, 2005, **40**(12), P. 3675–3679.
- [2] Naeem A., Saddique M.T., Mustafa S., Kim Y., Dilara, B. Cation exchange removal of Pb from aqueous solution by sorption onto NiO. *Journal of Hazardous Materials*, 2009, **168**(1), P. 364–368.
- [3] Brooks R., Bahadory M., Tovia F., Rostami H. Removal of lead from contaminated water. *International Journal of Soil, Sediment and Water*, 2010, **3**(2), Article 14, P. 1–13.
- [4] Ali I. New generation adsorbents for water treatment. *Chemical Reviews*, 2012, **112**, P. 5073–5091.
- [5] Li X.Q., Elliott D.W., Zhang W.X. Zero-valent iron nanoparticles for abatement of environmental pollutants. *Critical Reviews in Solid State and Material Science*, 2006, **31**, P. 111–122.
- [6] Crane R., Scott T.B. Nanoscale zero valent iron: future prospectus for an emerging water treatment technology. *Journal of Hazardous Materials*, 2011, **211-212**, P. 112–125.
- [7] Petala E., Dimos K., Douvalis A., Bakas T., Tucek J., Zbořil R., Karakassides M.A. Nanoscale zero-valent iron supported on mesoporous silica: Characterization and reactivity for Cr(VI) removal from aqueous solution. *Journal of Hazardous Materials*, 2013, **26**, P. 295–306.
- [8] Saxena A., Srivastava A.K., Singh B., Kinetics of adsorption of 2-CEES and HD on impregnated silica nanoparticles under static conditions. *American Institute of Chemical Engineers Journal*, 2009, **55**(5), P. 1236–1245.
- [9] Shukla N., Saxena A., Gupta V., Rawat A.S., Kumar V., Rai P.K., Shrivastava S. Removal of lead from water by using low density metal oxide nanoparticles. *Advance Science Engineering and Medicine*, 2015, **7**(5), P. 298–405.
- [10] Chang S.S., Clair B., Ruelle J., Beauche J., Renzo F.D., Quignard F., Zhao G.J., Yamamoto H., Gril J. Mesoporosity as a new parameter for understanding tension stress generation in trees. *Journal of Experimental Botany*, 2009, **60**(11), P. 3023–3030.
- [11] Xu Y.M., Qi J., He D.M., Wang D.M., Chen H.Y., Guan J., Zhang Q.M. Preparation of amorphous silica from oil shale residue and surface modification by silane coupling agent. *Oil Shale*, 2010, **27**(1), P. 37–46.
- [12] Pelecky D.L.L., Rieke R.D. Magnetic properties of nanostructured materials. *Chemistry of Materials*, 1996, **8**, P. 1770–1783.

Chemically treated multi-walled carbon nanotubes for sensor applications

Khurshed A. Shah

Nanomaterials Research Laboratory, Department of Physics, Govt. Degree College for Women,
Anantnag (J&K), India
drkhursheda@gmail.com

PACS 81.07.De, 81.16.Be, 87.64.kp

DOI 10.17586/2220-8054-2016-7-3-492-493

In this study, Multi-Walled Carbon Nanotubes (MWCNTs) were chemically treated in order to investigate the structural and chemical changes in them and to use them for sensor applications. Raman spectroscopic analysis reveals that the chemically treated MWCNTs are useful for chemical and gas sensor applications.

Keywords: Carbon nanotubes, chemical treatment, Raman spectroscopy, sensor applications.

Received: 23 January 2016

1. Introduction

The last decade has witnessed vigorous research activity in the field of Carbon nanotubes (CNTs) due to their extraordinary properties. There are various structures of carbon nanotubes (CNTs) depending on how the tube is rolled up and it is defined by the chiral index (n, m) and its quantum properties depend on the diameter and chirality [1, 2]. It exists both in single and multi-walled form. Isolated single-wall carbon nanotubes do not normally occur. Mostly, group of SWNTs led to formation of bundles of tubes, so-called nanoropes containing between 20 to hundred individual tubes [3, 4]. There are various applications of CNTs which includes sensors as well [5, 6].

The CNTs as produced by the various synthesis techniques contain various impurities [7] and for many applications, these impurities have to be separated from the carbon nanotubes before they can be used for sensor applications. Purification techniques include air oxidation, acid treatment, annealing, micro filtration, sonication, ferromagnetic separation, functionalization, and chromatography techniques have been devised in order to improve the quality and yield of carbon nanotubes [8]. Among these methods in this study the chemical method has been chosen in order to attach functional groups to CNTs. The Raman spectra analysis shows that carboxylic groups have been successfully attached to the carbon nanotubes after chemical treatment. These carboxylic groups are very useful for chemical and gas sensing applications.

2. Experimental details

As-produced multiwall carbon nanotubes (MWCNTs) were treated in a mixture of H_2SO_4 , HNO_3 under a refluxing condenser with magnetic stir for 5 hr. After refluxing, the mixture was cooled to room temperature, diluted with methanol and filtered through Whatman filter paper. The dried sample was then analyzed by a Raman Spectrometer.

2.1. Results and discussion

Figure 1 shows Raman spectra of treated CNTs excited with the 532.8 nm laser line.

In the case of CNTs, defect induced band (D band) and graphitic band (G band) are usually found in the range of $1332 - 1365 \text{ cm}^{-1}$ and $1516 - 1585 \text{ cm}^{-1}$ respectively. From Fig. 1, it is seen that the two peaks were observed at 1356 cm^{-1} (D band) and at 1577 cm^{-1} (G band) showing the characteristics of CNTs, when the acid treatment of CNTs was conducted. Furthermore it is seen that the peak position does not change, indicating that the acid treatment does not destroy the structure of CNTs [9], although the spectra is not shown in the Fig. 1. The intensity ratio of D-to G-mode (I_D/I_G) values of chemically treated and as-grown MWCNTs increases. As observed from Raman spectra, the ratio between the intensity of the D band and the G band is 0.68. The ratio between the intensity of G' band to G band is 0.43. These results are generally attributed to the presence of more structural defects [10]. The adsorption of functional groups increases the number of defects in the structure of nanotubes, increasing the ratio I_D/I_G and providing for early decomposition of CNTs. These results indicate certain insertion of defects and/or break on the structure of nanotubes and attach some functional groups which are useful for chemical and gas sensor application as many researchers have studied [11].

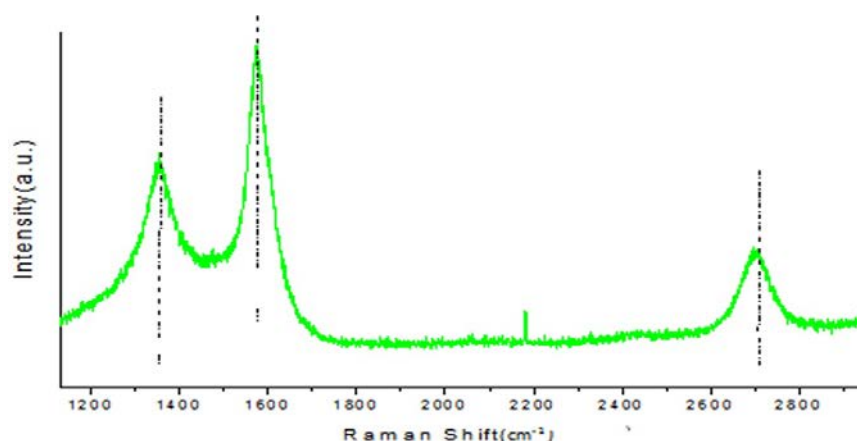


FIG. 1. Raman spectra of chemically treated carbon nanotube sample with excitation wavelength 532.8 nm

3. Conclusion

The as-produced MWCNT sample was characterized by Raman spectroscopy after chemical functionalization. The analysis of Raman spectra indicated there was modification of the CNTs structure after chemical treatment resulting in an increase in the number of defect sites. Some carboxylic groups are attached with these defect sites which are very useful for chemical and gas sensing applications.

Acknowledgement

This work has been financially supported by the Department of Science and Technology, Science and Engineering Research Board (DST-SERB), Govt. of India (Project grant No.SB/S2/CMP-36/2013).

References

- [1] Ebbesen T.W. *Carbon Nanotubes: Preparation and Properties*. CRC Press, Boca Raton, Florida, 1997.
- [2] Rao A.M., Richter E., Bandow S., Chase B., Eklund P.C., Williams K.A., Fang S., Subbaswamy K.R., Menon M., Thess A., Smalley R.E., Dresselhaus G., Dresselhaus M.S. Diameter-Selective Raman Scattering from Vibrational Modes in Carbon Nanotubes. *Science*, 1997, **275**, P. 187–191.
- [3] Iijima S., Ichihashi T. Single-Shell Carbon Nanotubes of 1-nm Diameter. *Nature*, 1993, **363**, P. 603–605.
- [4] Journet C., Bernier P. Production of Carbon Nanotubes. *Appl. Phys. A*, 1998, **67**, P. 1–9.
- [5] Liu J.H., Liu J.Y., Yang L.B., Chen X., Zhang M.Y., Meng F.L., Luo T., Li M.Q. Nanomaterial-Assisted Signal Enhancement of Hybridization for DNA Biosensors: A Review. *Sensors*, 2009, **9**, P. 7343–7346.
- [6] Balasubramanian K., Burghard M. Biosensors Based on Carbon Nanotubes. *Anal. Bioanal. Chem.*, 2006, **385**, P. 452–468.
- [7] Koshio A., Shiraiishi M., Kobayashi Y., Ishihara M., Koga Y., Bandow S., Iijima S., Kokai F. Modification of Carbon Nanotubes by Laser Ablation of Copper. *Chemical Physics Letters*, 2004, **396**, P. 410–414.
- [8] Agboola A.E. et al. *Conceptual Design of Carbon Nanotube Processes*. Springer-Verlag, 2007, **9**, P. 289–311.
- [9] Osorio A.G., Silveira I.C.L., Bueno V. L., Bergmann C.P. H₂SO₄/HNO₃/HCl-Functionalization and Its Effect on Dispersion of Carbon Nanotubes in Aqueous Media. *Applied Surface Science*, 2008, **255**, P. 2485–2489.
- [10] Tian Z.Q., Jiang S.P., Liang Y.M., Shen P.K. Synthesis and Characterization of Platinum Catalysts on Multiwalled Carbon Nanotubes by Intermittent Microwave Irradiation for Fuel Cell Applications. *J. Phys. Chem. B*, 2006, **110**, P. 5343–5350.
- [11] Bekyarova E., Davis M., Burch T., Itkis M.E., Zhao B., Sunshine S., Haddon R.C. Chemically Functionalized Single Walled Carbon Nanotubes as Ammonia Sensors. *J. Phys. Chem. B*, 2004, **108**, P. 19717–19720.

Investigation on structural and photoluminescence properties of (Co, Al) Co-doped SnO₂ nanoparticles

P. Venkateswara Reddy¹, S. Venkatramana Reddy^{1*}, B. Sankara Reddy², R. P. Vijayalakshmi¹

¹Department of Physics, Sri Venkateswara University, Tirupati-517 502, A.P., India

²Visweswaraiah Institutes of Science and Technology, Angallu, Madana Palli, A.P., India

drsvreddy123@gmail.com

PACS 81.07.Bc, 81.07.Nb

DOI 10.17586/2220-8054-2016-7-3-494-498

Pure and (Co, Al) co-doped (Co=1, 3, 5 mol %, and Al = 5 mol % as constant) SnO₂ nanoparticles were synthesized in aqueous solution by the chemical co-precipitation method using polyethylene glycol (PEG) as a stabilizer. The effects of structural and photoluminescence of (Co, Al) co-doped SnO₂ nanoparticles are investigated. The XRD pattern reveals that the samples are in a single phase rutile type tetragonal crystalline structure of SnO₂. The peak positions with Co concentration are slightly shifted to lower 2θ values and size of particles from XRD calculations are in between 20–30 nm. The Raman studies of the samples reveal that the Raman peaks are shifted towards lower wave numbers, when compared to those of pure SnO₂ at 150 cm⁻¹, 303 cm⁻¹, 476 cm⁻¹, 630 cm⁻¹, and 765 cm⁻¹ respectively. Photoluminescence studies show that pure SnO₂ has an emission peak at 444 nm and (Co, Al) co-doped samples show emission peaks at 417 nm, 433 nm and 485 nm with exciting wave length 320 nm. The PL intensity increases and broadening of peaks for co-doped samples with increase of Co concentration indicates the decrease of size of the crystallinity. The UV absorption spectrum exhibits absorption at 310 nm, and is in agreement with the emission spectra.

Keywords: EDAX, co-precipitation method, PL, UV-Absorption.

Received: 23 January 2016

1. Introduction

The importance for the synthesis of nanoparticles with desirable size and surface morphology has increased because of their potential applications in various fields in material sciences [1], electronics [2], and optics [3,4]. Tin oxide (SnO₂) is an n-type metal oxide semiconductor with a wide band gap (3.6 eV) [5–7]. As such, SnO₂ offers wide range of applications in solar cells [8,9], catalytic support materials [10], transparent electrodes [11,12] and solid state chemical sensors [13–17]. Many efforts have been made to synthesize the SnO₂ nanoparticles by sol-gel, chemical vapor deposition (CVD), thermal decomposition [18], co-precipitation [19], microwave assisted solution [20], and gas phase condensation [21] methods. Preparation of SnO₂ nanoparticles at low cost on an industrial scale is a challenge in material production, and co-precipitation is a simple technique under suitable conditions of synthesis. High surface area with agglomeration and irregular particle morphology of SnO₂ nano powders have been reported [22–24]. The preparation of desirable size of metal oxide nanoparticles using chemical co-precipitation method and their characterization are still challenging. Optical techniques, such as photoluminescence (PL), are very useful to determine the structure, defects and impurities in the nano crystals. Previous investigations have generated many reports on the luminescence of SnO₂ nanocrystals [22–26]. The luminescence has been observed to range from 350–550 nm (UV and visible regions), which may be due to defects such as oxygen vacancies and tin interstitials or dangling bonds [27–31]. The generation of defects in nanocrystals varies with shape of nanocrystals, which would influence the emission properties. Feng Gu et. al. [32] have proposed a model for blue emission from SnO₂ nanocrystals. The room temperature photoluminescence of blue emission with weak intensity has recently been reported by Zhijie Li [33]. Particle size plays a significant role in the optical properties the valence band. In order to overcome the stronger luminescence property with peak shift and to prepare SnO₂ nanocrystalline powders with the desired size, the chemical co-precipitation method was chosen. In the present paper, a systematic study was undertaken to characterize the structure of nanocrystalline pure and (Co, Al) co-doped nanoparticles prepared by the chemical co-precipitation method. The photoluminescence properties and the results are also discussed.

2. Synthesis

SnCl₂·2H₂O, Co (CHOOH)₆H₂O and AlCl₃ are AR grade for the synthesis of Sn_{1-x}Co_xAl_yO₂ series. The required amount of SnCl₂·2H₂O is dissolved in de-ionized water, and aqueous ammonia is added drop wise to the above solution to maintain $pH = 9$ under constant stirring. Then, under constant stirring, co-doped ions are added

to the above solution. A light brown precipitate was obtained, and then 2 ml of polyethylene glycol was added to stabilize the particle size. Finally, the obtained precipitate was washed with de-ionized water and filtered out separately. Thereafter, the precipitate was dried at 80 °C. The dried powders were subsequently annealed at 600 °C for 4 hours, affording (Co, Al) co-doped SnO₂ nanoparticles.

2.1. Characterizations

The prepared powders were carefully subjected to the following characterization studies. Powder XRD pattern was recorded on Bruker diffractometer within the 2θ range of 20 to 80° using CuK_α as X-ray source (λ = 1.53906 Å). The structure of pure and co-doped SnO₂ were analyzed by Micro Raman Spectroscopy (LAB-RAM HR, HORIBA JOBIN-YVON Spectrophotometer). The optical properties were analyzed by UV-VIS diffusion reflectance Spectroscopy using CARY 5E UV-VIS-NIR Spectrophotometer in the wavelength range 200–2500 nm. The room temperature photoluminescence (PL) studies were carried out with a PL Spectrometer.

3. Results and Discussion

3.1. X-RAY Diffraction studies

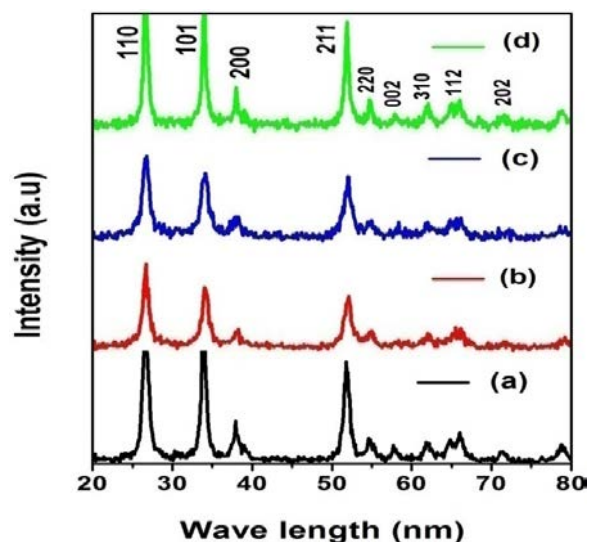


FIG. 1. XRD Spectra of (a) pure (b) 1 mol % Co (c) 3 mol % Co (d) 5 mol % Co with 5 mol % Al co-doped SnO₂ nanoparticles

Figure 1 shows the XRD pattern of pure and co-doped (Co = 1, 3, 5 mol % with 5 mol % Al as constant) SnO₂ nanoparticles. The diffraction peaks of the samples corresponded to the rutile phase of SnO₂, and peak positions are in good agreement with the standard pattern [JCPDS CARD No: 41-1445]. The absence of extra peaks showed that no impurity phases were present in samples within the detection limit of the instrument. However, it was found that the diffraction peaks of all co-doped samples were slightly shifted to lower positions when compared to the pure SnO₂ nanoparticles. The crystallite size (*d*) is calculated using Scherer formula:

$$d = \frac{0.91\lambda}{\beta \cos \theta}$$

The calculated particle size for pure and Co (1, 3, 5 mol %) with 5 mol % of Al co-doped SnO₂ nanoparticles were in between 20–30 nm. The diffraction calculations showed that the size of pure SnO₂ particles was small and the size increased with the doping of Co with 5 mol % of Al doped SnO₂.

3.2. Raman studies

Figure 2 shows the Raman spectrum of synthesized nano crystals. In the present investigation, for pure SnO₂, exhibit peaks were observed at 476 cm⁻¹, 630 cm⁻¹ and 776 cm⁻¹ which corresponded to E_g, A_{1g} and B_{2g} respectively. The Raman peaks of Co (1, 3, 5 mol %) with 5 mol % of Al to SnO₂ nanoparticles at 150 cm⁻¹, 303 cm⁻¹, 476 cm⁻¹, 630 cm⁻¹, 692 cm⁻¹, and 765 cm⁻¹ and. They correspond to B_{1g}, E_u, E_g, A_{1g}, A_{2u} LO (LO: mode of longitudinal optical phonons), and B_{2g} respectively. The peak at 856 nm is might be laser peak.

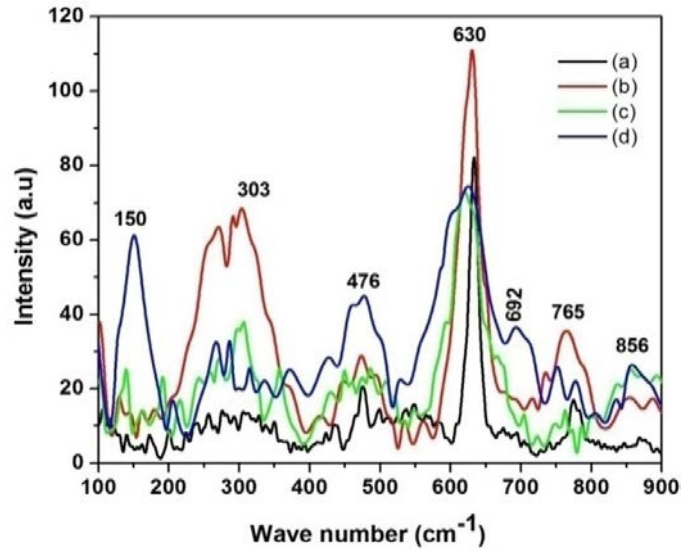


FIG. 2. Raman Spectra of (a) pure (b) 1 mol % Co (c) 3 mol % Co (d) 5 mol % Co, with 5 mol % of Al co-doped SnO₂ nanoparticles

The co-doped peaks are broad and slightly shifted to lower wave numbers as compared to bulk rutile SnO₂. The sharp band located between 550 – 650 cm⁻¹ is attributed to the surface vibration modes [34]. The origin of peaks at 303 cm⁻¹ may be due to E_u mode and peak at 476 cm⁻¹ represents the Raman active E_g doubly degenerate mode. The A_{1g} and B_{2g} are non-degenerate modes at 630 cm⁻¹ and 765 cm⁻¹ respectively.

3.3. Photoluminescence analysis

The PL emission peaks for pure SnO₂ nanoparticles were at 417 nm and 456 nm and for co-doped samples the peaks were at 417 nm, 433 nm, and 485 nm when the excitation wavelength was 320 nm. The spectrum was characteristic of the UV emissions at 417 nm, and 433 nm. The peak at 485 nm indicates blue emission, which was due to the reduced nanocrystal sizes and intrinsic defects in lattice of SnO₂. With an increase in the Co concentration, the oxygen vacancies increased, which resulted in the broadening of the peaks along with increased peak intensity. This might be due to the electron transitions mediated by defect levels in the band gap and also due to the non-uniformity of the particle size [35].

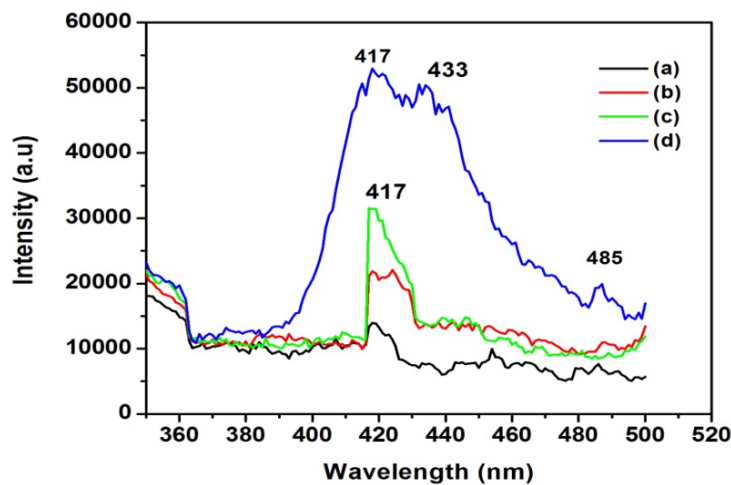


FIG. 3. PL spectra of (a) pure (b) 1 mol % Co, (c) 3 mol % Co (d) 5 mol % Co with 5 mol % Al co-doped SnO₂ nanoparticles

3.4. UV-VIS Absorption

Absorption spectroscopy is a powerful non destructive technique used to investigate the optical properties of semiconducting nanoparticles. The optical absorption spectra of (Co, Al) co-doped SnO₂ nanoparticles are shown in Fig. 4. The absorption spectra showed an absorption edge at ~ 310 nm, and for different samples the value is almost identical. It is interesting to note that (Mn, Al) doped samples do not show a sharp absorption edge due to Mn d states extending in to the band gap region resulting from the overlapping of orbitals by Mandal et al [36]. The changes in local disorder result from the varying crystalline size and annealing temperature of the samples.

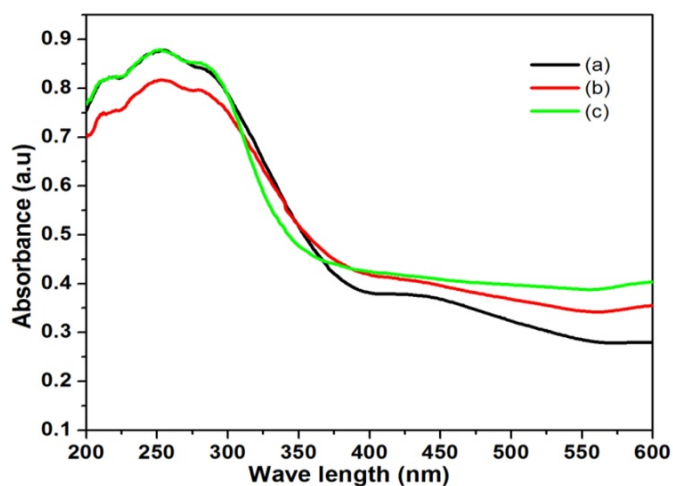


FIG. 4. UV-Absorption Spectra of (a) 1 mol % Co (b) 3 mol % Co (c) 5 mol % Co co-doped with 5 % Al into SnO₂ nanoparticles

4. Summary and conclusion

In summary, tin oxide (SnO₂) nanocrystalline powders were successfully synthesized by a simple precipitation method obtained at 600°C by a reaction of SnCl₂ and NH₃ derived from aqueous ammonia. The XRD patterns confirm that SnO₂ nanocrystalline powders possess a tetragonal rutile structure. The average crystallite size of the nanopowders is in the nanometer range; the crystallite size of the SnO₂ was found to increase from 20 to 30 nm. The heating effect has influence on the size of the crystallites in the nanocrystalline powders. When samples were heated, the lattice parameters and dislocation density decreased, and thus, a smaller number of unit cells started to grow. The Photoluminescence emission exhibited peaks at 417 nm, 433 nm and 485 nm. The peak at 417 nm is related to the recombination of electrons in singly occupied oxygen vacancies with photo-excited holes in the valence band. The heating temperature also affects the luminescence process, the emission resulting in the decrease in the oxygen vacancies, as revealed by the decrease in luminescence at 485 nm. This is in agreement with the absorption edge at 310 nm.

Acknowledgement

The authors wish to express their gratitude to Prof. Y. Prabhakara Reddy (Retd.), Department of Physics, S. V. University, Tirupati for his critical discussions during the course of investigation.

References

- [1] Gudiksen M.S., Lauhon L.J., Wang J., Smith D., Lieber C.M. *Nature*, 2002, **415**, P. 617.
- [2] Wang Z.L., Song J.H. *Science*, 2006, **312**, P. 242.
- [3] Sun X.M., Li Y.D. *Angew. Chem., Int. Ed.*, 2004, **43**, P. 3827.
- [4] Tang Z.Y., Wang Y., Shanbhag S., Giersig M., Kotov N.A. *J. Am. Chem. Soc.*, 2006, **128**, P. 6730.
- [5] Kar A., Patra A. *J. Phys. Chem C*, 2009, **113**, P. 4375.
- [6] Xu X., Zhuang J., Wang X. *J. Am. Chem. Soc.*, 2008, **130**, P. 12527.
- [7] Lu E.J.H., Ribeiro C., Giraldo T.R., Longo E., Leite E.R., Varela J.A. *Appl. Phys. Lett.*, 2004, **84**, P. 1745.
- [8] Harrison P.G., Willet M.J. *Nature*, 1988, **332**, P. 337.
- [9] Ferrere S., Zaban A., Gregg B.A. *J. Phys. Chem B*, 1997, **101**, P. 4490.
- [10] Wang W.W., Zhu Y.J., Yang L.X. *Adv. Funct. Mater.*, 2007, **17**, P. 50.
- [11] Zhu J., Lu Z., Aruna S. T., Aurbach D., Gedanken A. *Chem. Mater.*, 2000, **12**, P. 2557.

- [12] He Y.S., Campbell J.C., Murphy R.C., Arendt M.F., Swinnea J.S. *J. Mater. Res.*, 1993, **8**, P. 3131.
- [13] Wang Y., Jiang X., Xia Y. *J. Am. Chem. Soc.*, 2003, **125**, P. 16176.
- [14] Xi G., Ye J. *Inorg. Chem.*, 2010, **49**, P. 2302.
- [15] Chen Y.J., Xue X.Y., Wang Y.G., Wang T.H. *Appl. Phys. Lett.*, 2005, **87**, P. 233503.
- [16] Liu Z., Zhang D., Han S., Li C., Tang T., Jin W., Liu X., *C. Adv. Mater.*, 2003, **15**, P. 1754.
- [17] Kolmakov A., Klenov D.O., Lilach Y., Stemmer S., Moskouits M. *Nano Lett.*, 2005, **5**, P. 667.
- [18] Liu Y., Dong J., Liu M. *Adv. Mater.*, 2004, **16**, P. 353.
- [19] Ki Chang Song, Yong Kang, *Materials Letters*, 2000, **42**, P. 283.
- [20] H. Hallila, P. Méninia, H. Auberta. *Procedia Chemistry*, 2009, **1**, P. 935.
- [21] Zhang J., Gao L. *Chem. Lett.*, 2003, **32**, P. 458.
- [22] Gu F., Wang S.F., Lu^o M.K., Zhou G.J., Xu D., Yuan D.R. *J. Phys. Chem B*, 2004, **108**, P. 8119.
- [23] Chowdhury P.S., Saha S., Patra A. *Solid State Commun.*, 2004, **131**, P. 785.
- [24] Faglia G., Baratto C., Sberveglieri G., Zha M., Zappeltini A. *Appl. Phys. Lett.*, 2005, **86**, P. 011923.
- [25] Maestre D., Cremades A., Piqueras J. *J. Appl. Phys.*, 2005, **97**, P. 044316.
- [26] Gu F., Wang S.F., Song C.F., Lu^o M.K., Qi Y.X., Zhou G.J., Xu D., Yuan D.R. *Chem. Phys. Lett.*, 2003, **372**, P. 451.
- [27] Munnix S., Schmeits M. *Phys. Rev. B*, 1983, **27**, P. 7624.
- [28] Chiodini N., Paleari A., Dimartino D., Spinolo G. *Appl. Phys. Lett.*, 2002, **81**, P. 1702.
- [29] Vanheusden K., Warren W.L., Seager C.H., Tallant D.R., Voigt J.A., Gnade B.E. *J. Appl. Phys.*, 1996, **79**, P. 7983.
- [30] Liu Y.X., Yang Q.B., Xu C.F. *J. Appl. Phys.*, 2008, **104**, P. 064701.
- [31] Godinho K.G., Walsh A., Watson G.W. *J. Phys. Chem. C*, 2009, **113**, P. 439.
- [32] Gu F., Wang S.F., Lu^o M.K., Zhou G.J., Xu D., Yuan D.R. *J. Phys. Chem B*, 2004, **108**, P. 8119.
- [33] Zhijie Li, Wenzhong Shen, Xue Zhang, Limei Fang, Xiaotao Zu. *Colloids and surfaces A: Physicochem. Eng. Aspects*, 2008, **327**, P. 17.
- [34] Abello L., Bochu B., Gaskov A., Koudryavtseva S., Lucazeau G., and Rumyantseva, M. Structural characterization of nanocrystalline SnO₂ by X-Ray and Raman Spectroscopy. *J. Solid State Chem.*, 1998, **135**, P. 78–85.
- [35] Fang L.M., Zu X.T., Li Z.J., Zhu S., Liu C.M., Wang L.M., Gao F., Microstructure and luminescence properties of Co-doped SnO₂ nanoparticles synthesized by hydrothermal method. *J. Mater. Sci.: Mater. Electron*, 2008, **19**, P. 868–874.
- [36] Mandal S.K., Nath T.K., Das A. *J. Appl. Phys.*, 2007, **101**, P. 123920.

Synthesis and characterization of highly ordered nanosized PbS thin films: modified silar

Kishorkumar V. Khot^{1,*}, Vishvanth B. Ghanwat¹, Pallavi B. Patil¹, Chaitali S. Bagade¹, Rahul M. Mane¹, Dadaso B. Shinde¹, Sandip K. Jagadale¹, Ji-hyung Jang², P. N. Bhosale^{1,**}

¹Materials Research Laboratory, Department of Chemistry, Shivaji University, Kolhapur, India

²Nanocrystal Laboratory, School of Energy and Chemical engineering, Ulsan National Institute of Science and Technology (UNIST), South Korea

*khotkishor7575@gmail.com, **p_n.bhosale@rediffmail.com

PACS 81

DOI 10.17586/2220-8054-2016-7-3-499-501

In the current status, we have successfully synthesized lead sulfide (PbS) thin films using a modified successive ionic layer absorption and reaction (SILAR) method. The synthesized film was characterized using UV-Vis-NIR spectrophotometer, X-ray diffraction (XRD) and field emission scanning electron microscopy (FESEM) techniques for optical, structural and morphological properties. Opto-structural study demonstrates that synthesized thin film has a pure crystal structure. The surface morphology study indicates a nanospherical surface morphology without pinhole on the substrate surfaces. Overall study clearly demonstrates that the synthesized PbS thin film by SILAR method have great potential for sensitization of oxide microstructure.

Keywords: nanomaterials, thin films, SILAR method, XRD, SEM.

Received: 23 January 2016

Revised: 11 April 2016

1. Introduction

Lead sulfide (PbS) belongs to the IV^A-VI^A group of semiconductor materials. PbS is a black semiconductor with a band gap of 0.4 eV (at 300 K). It has great potential for fabrication of thin film solar cell due to its efficient light absorbing capacity from the visible to near infrared region of the solar spectrum, relatively long excitonic life time and the large excitation Bohr radius (18 nm), etc. Also, the band gap of PbS can be tuned from 0.41 eV to 2.3 eV by quantum size effect [1–4].

PbS thin films have potential utility in different applications, such as light emitting diodes, nonlinear optics, high speed switching, IR detectors, display devices, and solar cells. So far, both physical and chemical methods have been used to prepare PbS thin films. While, PbS thin films were synthesized by various methods, including vacuum evaporation, hot-wall epitaxy, molecular-beam epitaxy, pulsed laser deposition. These methods require sophisticated instrumentation and high cost, materials, etc. However, chemical methods mainly include spray pyrolysis, chemical bath deposition (CBD), successive ionic layer adsorption and reaction (SILAR), electrochemical deposition and hydrothermal method, etc [5].

In the present investigation, our main aim is to synthesize nanocrystalline PbS thin film, especially for the sensitization to hierarchically nanostructured metal oxide thin films such as, zinc oxide (ZnO) or titanium oxide (TiO₂) in order to improve the overall conversion efficiency. So considering this, we have selected SILAR technique, because compared to other techniques used, SILAR is best suited for development of sensitized solar cells. As well as, among these thin film synthesis techniques, SILAR has many superior properties such as simple application, low cost, low temperature synthesis and can be used to deposit the materials on a variety of substrates such as insulators, semiconductors, and metals. Therefore, we have synthesized PbS thin film on a soda lime glass substrate by using SILAR technique. Furthermore, the synthesized PbS thin film was characterized by using different techniques such as, UV-Vis-NIR spectrophotometer, X-ray diffraction (XRD) and field emission scanning electron microscopy (FESEM) for optical, structural and morphological studies respectively.

2. Experimental details

All chemicals in the experiment were purchased from Sigma Aldrich and without further purification. Lead nitrate (Pb(NO₃)₂, Sigma Aldrich), sodium sulfide (Na₂S, Sigma Aldrich), methanol (CH₃OH, Sigma Aldrich) were used for the synthesis of PbS thin film. In the PbS thin film synthesis, soda lime glass substrates were immersed in 0.1 M Pb(NO₃)₂ methanolic solution for 30s to allow the absorption of Pb²⁺ ions and rinsed with a pure methanol solution for 1 min to remove loosely bound and excess Pb²⁺ ions. Then, substrates were dipped

in 0.1 M Na₂S methanolic solution for 30 sec., where deposited Pb²⁺ ions react with S²⁻ ions to form a thin layer of PbS and rinsed with a pure methanol solution for 1 min. These dipping procedures are called as “One SILAR cycle”. In the present investigation, we have studied different properties of PbS thin film synthesized by 15 SILAR cycles. The synthesized PbS thin film is abbreviated as PbS.

The film thickness was measured by using a surface profilometer (AMBIOS XP-1). An optical absorption study was carried out by using UV-Vis-NIR spectrophotometer (Shimadzu, UV-1800). The crystal structure of thin film was analyzed from X-ray diffraction study (XRD, D/MAX, Ultima III, Rigako Japan). The surface morphology was recorded from field emission scanning electron microscopy (FESEM, Hitachi, S4700).

3. Results and discussions

Thickness of synthesized PbS thin film is 70 nm. The optical absorption spectrum of PbS thin film was recorded in the 400 – 2000 nm wavelength range and absorption plot is shown in Fig. 1(a). The optical absorption plot of the synthesized PbS thin film shows the linear nature of absorption.

Fig. 1(b) shows a direct band energy plot and the PbS thin film shows 1.40 eV band gap energy value, which is in good accordance with other reported values in literature [6, 7]. The crystal structure of the synthesized thin film was confirmed by using XRD study.

The Fig. 2 shows XRD pattern. PbS thin film shows diffraction peaks for (111), (200) and (220) planes at 25.70, 29.94 and 42.79 ° respectively for cubic crystal structure (JCPDS Card No. 78-1058).

Figure 3 shows FESEM images of the PbS thin film deposited by SILAR method. The low resolution FESEM image indicates the formation of compactly arranged surface morphology with pinhole free nature (Fig. 3(a)). Further high resolution FESEM image of Fig. 3(b) clearly indicates that interconnected smaller nanospheres are grown on the substrate surface having an average grain size of about 30 – 40 nm.

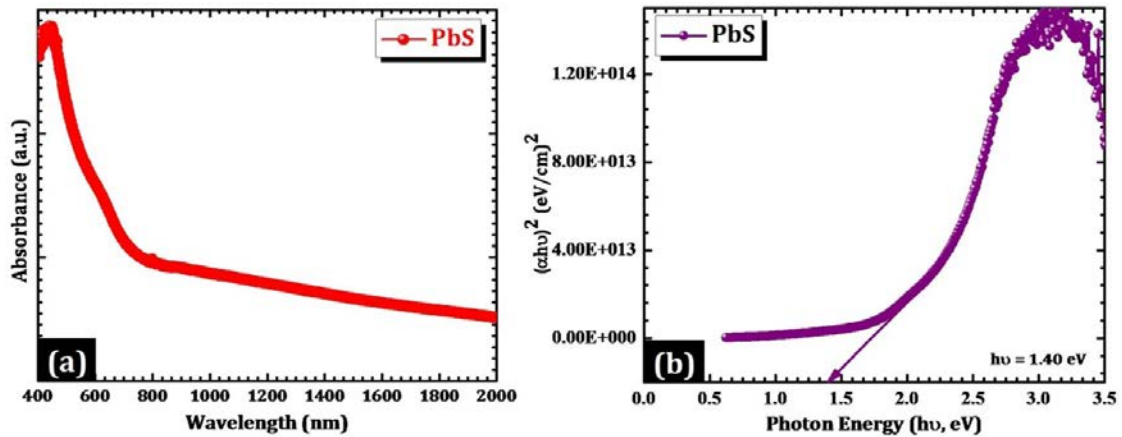


FIG. 1. (a) Optical absorption plot, (b) Plot of $(\alpha h\nu)^2$ (eV/cm)² vs. photon energy ($h\nu$, eV)

4. Conclusions

In the present article, we have successfully synthesized a PbS thin film by using the modified SILAR method. The synthesized thin film shows directly allowed transition and a band gap energy of 1.40 eV. XRD pattern confirms the formation of cubic crystal structure. FESEM images demonstrated that interconnected smaller nanospheres are formed on the overall substrate surface with pinhole-free nature. The obtained results indicate that synthesized material is highly favorable for solar cell application.

Acknowledgement

One of the authors, Dr. Kishorkumar V. Khot is very much thankful to Department of Science and Technology (DST), New Delhi for awarding “DST-INSPIRE fellowship” for financial support (Registration No. IF130751).

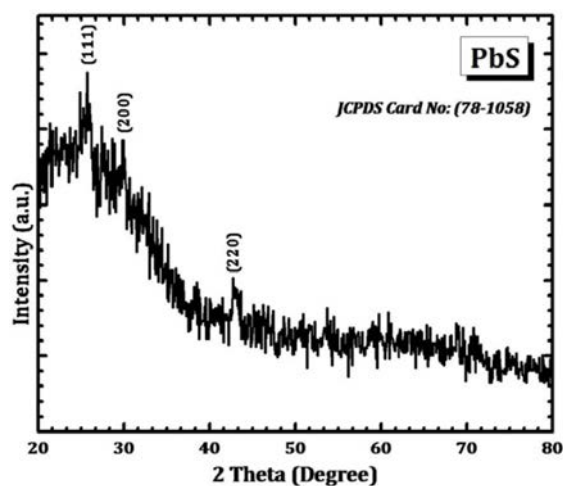


FIG. 2. XRD pattern of PbS thin film

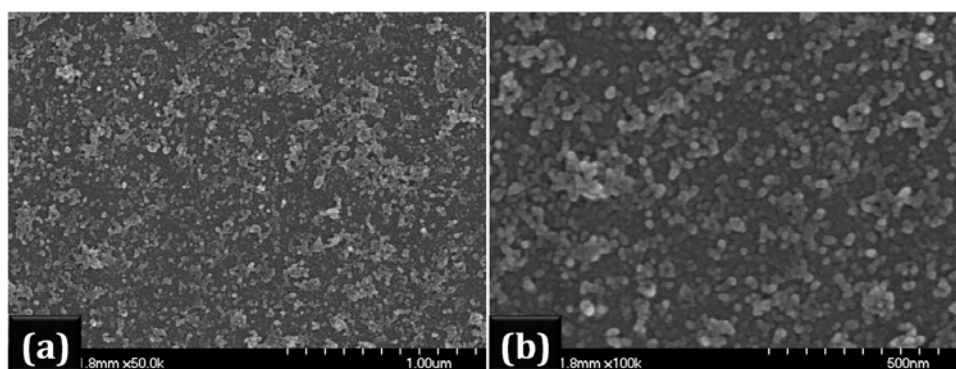


FIG. 3. (a,b) FESEM images of PbS thin film

References

- [1] Mondal A., Mukherjee N. Cubic PbS thin films on TCO glass substrate by galvanic technique. *Mater. Lett.*, 2006, **60**, P. 2672–2674.
- [2] Jauregui J.J.V., Bon R.R., Galvan A.M., Lerma M.S. Optical properties of PbS thin films chemically deposited at different temperatures. *Thin Solid Films*, 2003, **441**, P. 104–110.
- [3] Khot K.V., Mali S.S., Mane R.M., Patil P.S., Hong C.K., Kim J.H., Heo J., Bhosale P.N. Synthesis, characterization and photoelectrochemical properties of PbS sensitized vertically aligned ZnO nanorods: Modified aqueous route. *J Mater Sci: Mater Electron*, 2015, **26**, P. 6897–6906.
- [4] Saikia D., Phukan P. Fabrication and evaluation of CdS/PbS thin film solar cell by chemical bath deposition technique. *Thin Solid Films*, 2014, **562**, P. 239.
- [5] Khot K.V., Mali S.S., Ghanwat V.B., Kharade S.D., Mane R.M., Hong C.K., Bhosale P.N. Photocurrent enhancement in a $\text{Cu}_2\text{Cd}(\text{SSe})_2$ photoanode synthesized via an arrested precipitation route. *New. J. Chem.*, 2016, **40**, P. 3277.
- [6] Tohidi T., Ghaleh K.J., Namdar A., Ghaleh R.A. Comparative studies on the structural, morphological, optical, and electrical properties of nanocrystalline PbS thin films grown by chemical bath deposition using two different bath compositions. *Mater. Sci.: Semicond. Process*, 2014, **25**, P. 197–206.
- [7] Khot K.V., Mali S.S., Pawar N.B., Mane R.M., Kondalkar V.V., Ghanwat V.B., Patil P.S., Hong C.K., Kim J.H., He J.o, Bhosale P.N. Novel synthesis of interconnected nanocubic PbS thin films by facile aqueous chemical route. *J. Mater. Sci.: Mater. Electron*, 2014, **25**, P. 3762–3770.

Exploring the properties of lead oxide and tungsten oxide based graphene mixed nanocomposite films

A. Deepak, P. Shankar

Saveetha School of Engineering, Saveetha University, Chennai–602105, India

deepak.nanozone@gmail.com, principal.sse@saveetha.com

DOI 10.17586/2220-8054-2016-7-3-502-505

This work reports the possibility of mixing metal oxides along with graphene and polymer to form Metal Oxide-Graphene-Polymer films. The metal oxides used in this work were lead Oxide (PbO) and tungsten oxide (WO_3). Polyvinylidene fluoride (PVDF) is the polymer, which is used as matrix in preparation of these metal oxide and graphene mixed nanocomposite films. Metal Oxide-Graphene-PVDF films were developed using a chemical technique called solvent casting. The prepared films were characterized using techniques like FE-SEM, XRD and FT-IR to understand its morphological, crystalline and functional properties. I-V characteristics were analyzed using four-probe techniques. The developed Metal Oxide-Graphene-PVDF films have potential applications in a wide range of fields and particularly for electronic applications. The ability of these films to be used as electronic components in devices was explored.

Keywords: graphene, polymer, metal oxide.

Received: 28 January 2016

1. Introduction

Graphene is a single layer of carbon atoms peeled from graphite as flakes. Graphene has numerous extraordinary properties which make it exceptionally valuable for different applications [1]. Graphene is preferred compared to carbon Nano tubes, carbon Nano fibers and other carbon materials due to its aspect ratio, high surface area, high tensile strength, good thermal conductivity, good electrical conductivity, transparency and flexibility [2,3]. Graphene is capable of being blended with a wide range of polymer matrices including, epoxy, polystyrene, polyaniline, nafion, poly (vinyl alcohol), polyurethane, polyvinylidene fluoride, poly (3,4-ethyldioxythiophene), polyethylene terephthalate and polycarbonate [4]. Such composites were also shown to exhibit superior properties compared to base polymer materials, as a result of graphene's novel properties. In this present work, graphene along with metal oxides like lead oxide and tungsten oxide were mixed separately with PVDF polymer matrix in order to explore the conductivity behavior of graphene based nanocomposite films before and after mixing with various metal oxides, as previously mentioned.

2. Materials and methods

Functionalized graphene were purchased from Ad Nano Technologies with 99 % purity. Lead Oxide and tungsten Oxide were purchased from Sigma Aldrich with 99.4 % purity. Polyvinylidene Fluoride (PVDF) was purchased from Sigma Aldrich with 99 % purity. Dimethylformamide (DMF) of laboratory grade with 98 % purity was purchased from Sigma Aldrich.

FESEM and EDX images were examined using F E I Quanta FEG 200 – High Resolution Scanning Electron Microscope with EDX system. The prepared samples were examined at 50 μm range with 1000–2000 x magnification at low vacuum. XRD measurements are carried out using X'pert Pro Powder X-Ray Diffractometer system. The system used the high speed solid-state X'celerator as a detector type at the range of 0 – 100 °. FTIR pattern is measured using ALPHA-T FT-IR Spectrometer. The spectral range used for analyzing is 400 to 1000 cm^{-1} range. The spectral resolution used is better than 2 cm^{-1} .

3. Preparation protocol of nanocomposite films

3.1. Preparation of 2wt% of graphene-PVDF nanocomposite

Graphene (0.04 mg) and PVDF (1.96 mg) is mixed with DMF solution and sonicated for 1 hour to get proper mixing in the solution. Obtained graphene-PVDF solution is magnetically stirred for 1 hour by maintaining the temperature between 45 to 65 ° C to get homogenous dispersion in the solution [5]. Finally the solution is kept in hot air oven for 6 hours by keeping constant temperature at 60 °C.

3.2. Preparation of 2wt% of graphene-PVDF-PbO nanocomposite

Graphene (0.04 mg), lead Oxide (0.04 mg) and PVDF (1.92 mg) is mixed with a DMF solution and sonicated for 1 hour to get homogenous mixing in the solution. The obtained graphene-PVDF-PbO solution is magnetically stirred for 1 hour by maintaining the temperature between 45 to 65 °C to get proper dispersion in the solution. Finally, the solution is kept in hot air oven for 6 hours by keeping constant temperature at 60 °C.

3.3. Preparation of 2wt% of graphene-PVDF-WO₃ nanocomposite

The procedure used is similar to that of graphene-PVDF-PbO nanocomposites. Here lead Oxide is replaced with tungsten Oxide.

4. Results and discussions

Figure 1 shows FESEM images of (a) graphene-PVDF, (b) graphene-PVDF-PbO and (c) graphene-PVDF-WO₃ respectively. Superior bonding is noticed which shows the homogenous mixing in the prepared nanocomposites whereas the EDX pattern shows the presence of chemical compounds present in the nanocomposite. EDX images in Fig. 1(d) shows the presence of Carbon and Fluorine in the graphene-PVDF film, in Fig. 1(e) shows the presence of Carbon, Fluorine and Lead in the graphene-PVDF-PbO film and in Fig. 1(f) shows the presence of Carbon, Fluorine and Tungsten in the graphene-PVDF-WO₃.

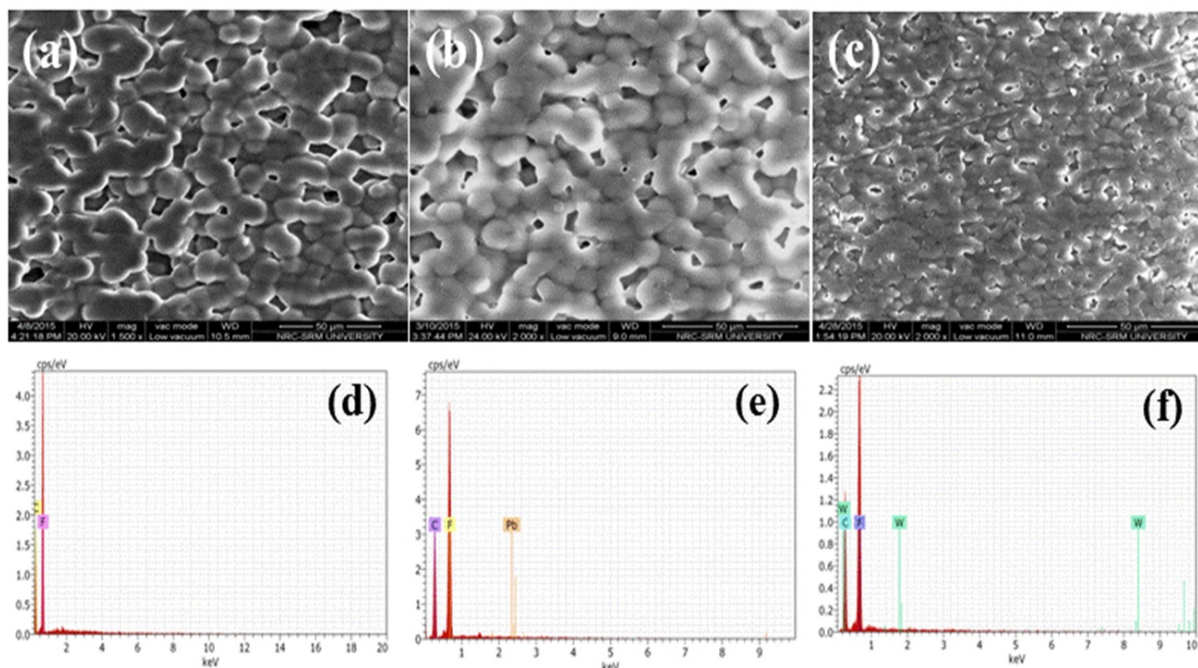


FIG. 1. FESEM images of (a) graphene-PVDF, (b) graphene-PVDF-PbO & (c) graphene-PVDF-WO₃ and EDX images of (d) graphene-PVDF, (e) graphene-PVDF-PbO & (f) graphene-PVDF-WO₃

Figure 2 shows the XRD pattern of (a) graphene-PVDF, (b) graphene-PVDF-PbO and (c) graphene-PVDF-WO₃ respectively. Fig. 2(a) shows the 2θ peaks at 20 ° (110) and 40 ° (002), which confirms the presence of PVDF and at 26 ° (021) as graphene (JCPDS Card No. 00-41-1487). Fig. 2(b) shows the 2θ peaks at 20 ° (110) and 40 ° (002) which confirms the presence of PVDF, at 26 ° (021) as graphene and at 31 ° (111) and 48 ° (220) as lead (JCPDS Card No. 00-38-1477) [6]. Fig. 2(c) shows the 2θ peaks at 20 ° (110) and 40 ° (002), which confirms the presence of PVDF, at 26 ° (021) as graphene and at 18 ° (100), 37.5 ° (021), 45 ° (020) and 48 ° (124) as Tungsten (JCPDS Card No. 00-43-1035) peak [7]. Fig. 3(a) shows the peaks of graphene-PVDF at 440 cm⁻¹, 485 cm⁻¹ and 510 cm⁻¹. Fig. 3 (b) shows the peaks of graphene-PVDF-PbO at 430 cm⁻¹, 470 cm⁻¹, 500 cm⁻¹ and 865 cm⁻¹. Fig. 3(c) shows the peaks of graphene-PVDF-WO₃ at 427 cm⁻¹, 465 cm⁻¹ and 860 cm⁻¹. These peaks show the presence of aromatic C-C bonds between (400 – 600 cm⁻¹), C-O bonds between (700 – 1000 cm⁻¹) and C-H bonds between (400 – 650 cm⁻¹), which is due to the presence of carbon fillers.

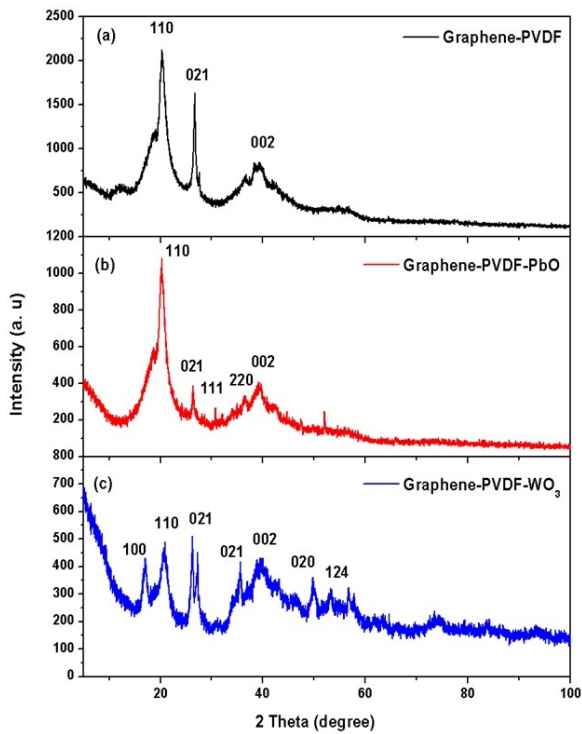


FIG. 2. XRD Pattern of (a) graphene-PVDF, (b) graphene-PVDF-PbO and (c) graphene-PVDF-WO₃

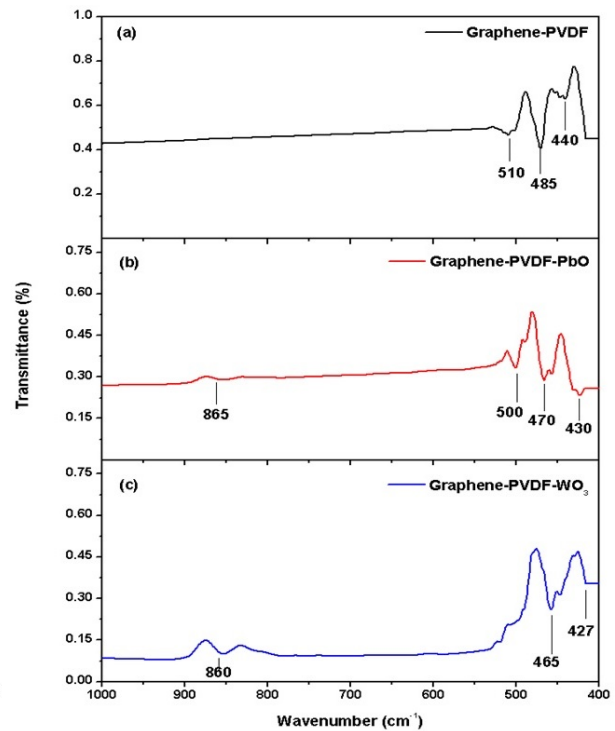


FIG. 3. FTIR Pattern of (a) graphene-PVDF, (b) graphene-PVDF-PbO and (c) graphene-PVDF-WO₃

Figure 4 shows the I-V Characteristics of (a) graphene-PVDF, (b) graphene-PVDF-PbO and (c) graphene-PVDF-WO₃ were obtained using four probe techniques. Temperature is kept as constant at room temperature and voltage is varied between 0 V to 1.4 V. Current measurements are carried out across all the three types of nanocomposite films, as shown in Fig. 4. Graphene-PVDF-WO₃ shows better conductivity when compared to graphene-PVDF-PbO and graphene-PVDF nanocomposite. This indicates metal oxide graphene based nanocomposite shows better conductivity due to incorporation of metal oxides in graphene based nanocomposites.

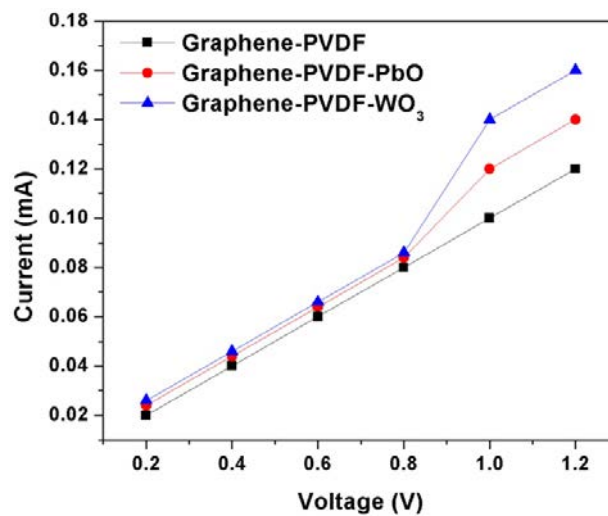


FIG. 4. I-V Characteristics of (a) graphene-PVDF, (b) graphene-PVDF-PbO and (c) graphene-PVDF-WO₃

5. Conclusions

Three different nanocomposite films, namely graphene-PVDF, graphene-PVDF-PbO and graphene-PVDF-WO₃ were prepared. SEM shows the morphological variations in all types of films. EDX shows the presence of elemental compositions such as carbon, fluorine, lead and tungsten of each film individually. XRD spectra shows the peaks of PVDF at 20 ° & 40 °, graphene at 26 °, lead at 31 ° & 48 ° and tungsten at 18 °, 37.5 °, 45 ° & 48 °. FT-IR spectra show the presence of various functional groups like aromatic C–C bonds, C–O bonds and C–H bonds. Developed nanocomposite films will have utility in flexible electronics in the near future.

References

- [1] Novoselov K.S., Geim A.K., Morozov S.V., Jiang D., Zhang Y., Dubonos S.V., Grigorieva I.V., Firsov A.A. Electric Field Effect in Atomically Thin Carbon Films. *Science*, 2004, **306**, P. 666–669.
- [2] Bae S., Kahya O., Sharma B.K., Kwon J., Cho H.C., Ozyilmaz B., Ahn J. Graphene-P(VDF-TrFE) Multilayer Film for Flexible Applications. *ACS Nano*, 2013, **7**, P. 3130–3138.
- [3] Shin Keun-Young., Hong Jin-Yong., Jang J. Flexible and transparent grapheme films as acoustic actuator electrodes using inkjet printing. *Chemical Communication*, 2011, **47**, P. 8527–8529.
- [4] Mukhopadhyay P., Gupta R.K. Trends and Frontiers in Graphene-Based Polymer. *Plastics Engineering*, 2011, P. 32–43.
- [5] Deepak A., Ganesan V., Karthik V., Shankar P. Nanomaterial Based Non- Destructive Evaluation Sensor for Defect Detection and Strain Measurement. *Journal of Nanostructured Polymers and Nanocomposites*, 2014, **10**, P. 5–12.
- [6] Arafat H.M. Economically viable route for synthesis of lead oxide (α -PbO) nanoparticles with an aim to reduce the manufacturing cost of lead acid batteries. *World Journal of Pharmaceutical Sciences*, 2014, **2**(12), P. 1947–1952.
- [7] Hsieh Y-T., Chang L-W., Chang C-C., Wei B-J., Shih H.C. Novel Synthetic Route for Tungsten Oxide Nanobundles with Controllable Morphologies. *Recent Trend in Electrochemical Science and Technology*, 2012, P. 249–260.

Effect of substrate temperature on microstructural, vibrational and electrical properties of ZnO nanostructured thin films

A. K. Prasad, S. Dhara

Nanomaterials and Sensors Section, Surface and Nanoscience Division, Materials Science Group,
Indira Gandhi Centre for Atomic Research, Kalpakkam, 603102, India
akp@igcar.gov.in

PACS 81.07.-b, 81.15.Rs

DOI 10.17586/2220-8054-2016-7-3-506-508

ZnO nanostructured thin films are synthesized by a simple spray pyrolysis technique using zinc acetyl acetonate precursor on Si substrates. The morphology control is achieved by varying the substrate temperature during deposition between 350 and 450 °C. The microstructural changes accompanying the changes in growth conditions are observed under the transmission electron microscopy. The vibrational properties of these films are studied using Raman spectroscopy and the differences in crystallinity are explained. The electrical properties are determined from I-V measurements.

Keywords: spray pyrolysis, ZnO nanostructured thin films, substrate effect, Raman.

Received: 31 January 2016

1. Introduction

Zinc oxide is a well-known semiconductor material with excellent optical and electronic properties. It has a wide direct band gap of 3.37 eV, a large exciton binding energy of 60 meV and a high melting temperature of 2248 K [1]. It crystallizes in hexagonal wurtzite structure and the presence of structural defects from growth process play an important role in varied applications such as solar cells, gas sensors, ultrasonic oscillators and transducers. Though ZnO has been synthesized in various shapes by different thin film deposition techniques, spray pyrolysis offers a simple yet versatile approach in controlling the properties through changes in processing parameters. ZnO has been synthesized by spray pyrolysis as early as 1995 as demonstrated by Krunks et al. [1] More recently, it has been shown to be a popular technique to synthesize nanostructures with various morphologies [2–5]. It is well known that *c*-axis orientation of the ZnO films increases as the deposition temperature or the annealing temperature is increased [6,7]. The effect of substrate temperature on crystal structure, morphology and gas sensing of ZnO thin films grown by economic spray pyrolysis process has been previously reported [6]. In this paper, we discuss the effect of substrate temperature on grain size, vibrational and electrical properties of ZnO thin films grown by spray pyrolysis.

2. Experimental

Thin films of ZnO were grown on Si substrates by an ultrasonic spray pyrolysis technique. A solution of zinc acetate was prepared by dissolution in 3:1 ratio of ethanol and water. Acetic acid was added to keep the pH around 5.5. A static ultrasonic nebulizer with 1.7 MHz resonator was employed to generate aerosols having a fairly uniform size distribution in the range 1 – 3 μm. Films were synthesized at three different deposition temperatures 350 °C, 400 °C and 450 °C. The nozzle-substrate distance was maintained at 10 mm. Spraying time was optimized depending on the substrate temperature to obtain films of uniform thicknesses of around 400 ~ 450 nm. The crystallite orientation, grain sizes and structure are confirmed using Zeiss Libra 200 FE high resolution transmission electron microscopy (HRTEM) operated at 200 kV assisted with selected area electron diffraction (SAED) studies. The vibrational properties are obtained from micro-Raman scattering studies using a inVia Renishaw spectrometer with 514.5 nm line of Ar⁺ laser excitation (< 1 mm laser spot at the sample surface) using 3000 gr mm⁻¹ grating. Electrical properties were measured from I-V plots performed in 2-probe method.

3. Results and Discussion

The microstructure of the ZnO thin films are characterized using TEM. The morphology of the films deposited at 350 and 400 °C consisted mainly of nanoparticles which appeared similar. For the sake representation, the microstructure from deposited at 400 °C alone is shown. From Fig. 1a, it is observed that the size of ZnO nanoparticles are in the range of 6 – 10 nm. The SAED pattern shown in inset of Fig. 1a depicting fine rings is signature of the films nanocrystalline nature. These rings are indexed to wurtzite ZnO with the presence of

characteristic (110) and (102) planes corresponding to the d spacing of 0.164 and 0.191 nm, respectively (JCPDS# 00-036-1451). Fig. 1b shows rod-like morphology for the films deposited at 450 °C. These nanorods are around 40 nm in diameter and several hundreds of nanometers in length. On closer observation, serrated features are observed on the nanorods which indicates the growth pattern in these structures. The appearance of discrete spots indicates the formation of larger grains at higher temperatures, as shown in the inset of Fig. 1b with [010] zone axis. These nanorods formed a part of the largely particle morphology as reported in our earlier studies [6]. The rod-like structures indicate the onset of preferred oriented growth.

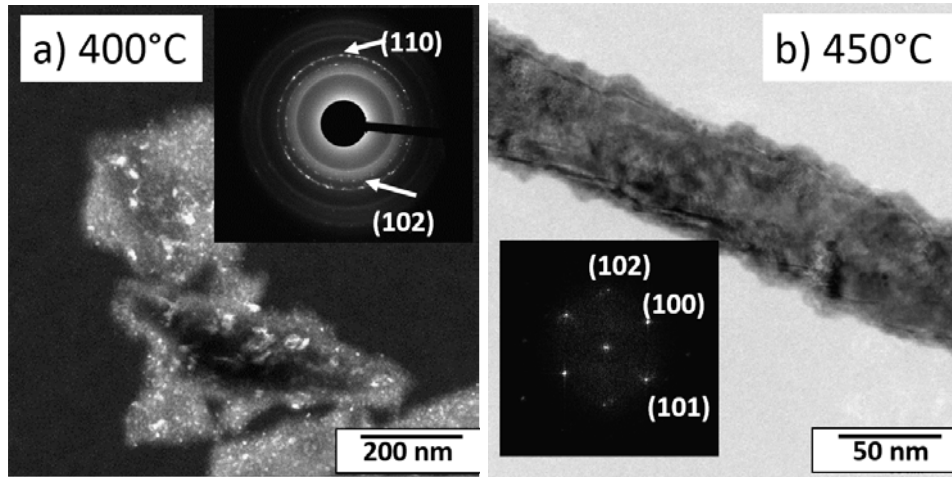


FIG. 1. a) Dark field TEM image showing nanocrystalline particles deposited at 400 °C Inset: SAED showing ring pattern; b) Bright field TEM image showing nano-rod like structures deposited at 450 °C Inset: SAED pattern showing spot pattern

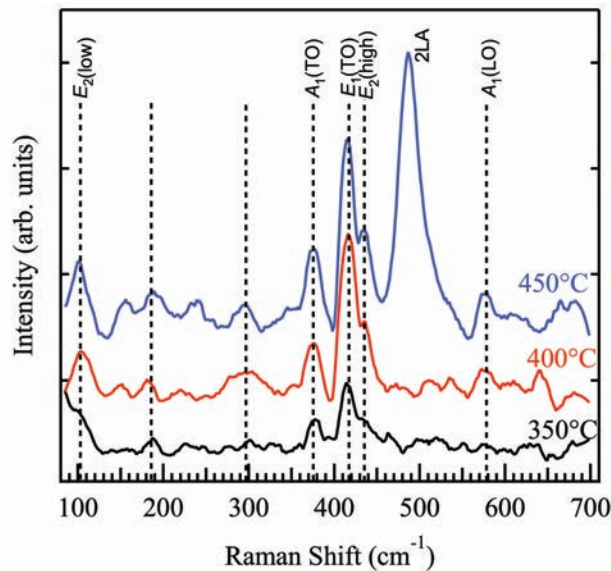


FIG. 2. Raman spectra of ZnO grown at different temperatures

The wurtzite-type lattice structure of ZnO shows 3 acoustic modes ($1 \times LA$, $2 \times TA$) and 9 optical phonons ($3 \times LO$, $6 \times TO$). At the zone-center (Γ -point of the Brillouin zone), the optical phonons have the irreducible representation $\Gamma_{opt} = A_1 + 2B_1 + E_1 + 2E_2$ [8], whereas the E modes are doubly degenerate. The B_1 modes are silent, i.e. IR and Raman inactive, and the E_2 branches are Raman-active only.

The vibrational spectra of ZnO thin films deposited at three different temperatures is shown in Fig. 2. The presence of triplet $A_1(TO)$, $E_1(TO)$ and E_2 (high) at 378, 410 and 438 cm^{-1} respectively confirms the presence

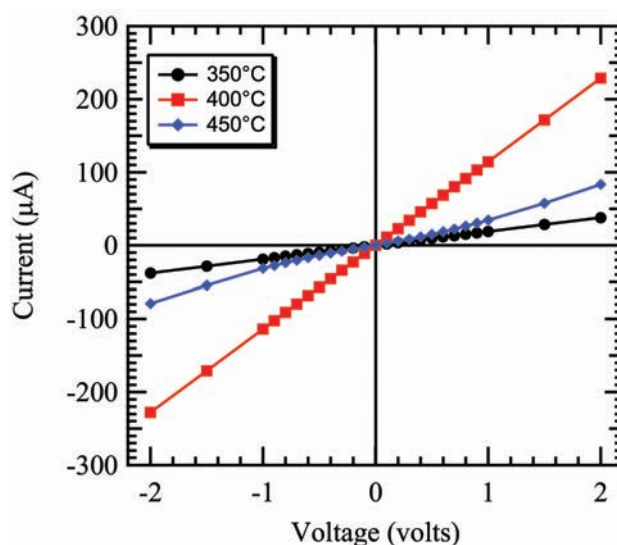


FIG. 3. $I - V$ Characteristics of ZnO grown at different temperatures

of wurtzite ZnO. This is more prominent at higher temperatures than at 350 °C. The presence of peak at 487 cm^{-1} for the thin film annealed at 450 °C is attributed to LA overtone (2LA) along $M - K$ Brillouin zone, belonging to A_1 symmetry as reported for high crystalline quality ZnO sample [9]. At the zone boundary, phonon dispersion is nearly flat and hence the phonon density of states is very high, showing a very strong intensity for the 2LA mode. Higher degree of crystallinity is observed for films grown at higher temperatures.

The electrical properties of the films shown in Fig. 3 reveals that the current increases linearly from -2 V to $+2\text{ V}$, which is indicative good ohmic behavior. Higher current is obtained for films deposited at 400 °C for a given applied voltage. This is due to lower dislocation densities in these films, as compared to other films as observed from earlier studies [6]. Hence, 400 °C is the optimum substrate temperature for better electrical applications.

4. Conclusion

ZnO thin films are grown on Si substrate using a simple yet versatile spray pyrolysis technique. By varying the substrate temperature during growth, films with varying grain sizes are obtained. Morphology is found to vary from nanocrystalline particles to nano-rod like particles as the temperature is increased. Raman study reveals differences arising due to phonon interactions in these films. Electrical charge carriers are also affected by this change in processing parameters.

Acknowledgements

AKP thanks Dr. Tom Mathews for help with synthesis and Dr. A. K. Tyagi for encouragement.

References

- [1] Krunks M., Mellikov E. Zinc oxide thin films by the spray pyrolysis method. *Thin Solid Films*, 1995, **270** (1–2), P. 33–36.
- [2] Alver U., Kilinç T., Bacaksız E., Nezir S. Temperature dependence of ZnO rods produced by ultrasonic spray pyrolysis method. *Materials Chemistry and Physics*, 2007, **106**, P. 227–230.
- [3] Dedova T., Krunks M., et al. A novel deposition method to grow ZnO nanorods: Spray pyrolysis. *Superlattices and Microstructures*, 2007, **42** (1–6), P. 444–450.
- [4] Mohammad M.T., Hashim A.A., Al-Maamory M.H. Highly conductive and transparent ZnO thin films prepared by spray pyrolysis technique. *Materials Chemistry and Physics*, 2006., **99** (2–3), P. 382–387.
- [5] Vimalkumar T.V., Poornima N., Sudha Kartha C., Vijayakumar K.P. On tuning the orientation of grains of spray pyrolysed ZnO thin films. *Applied Surface Science*, 2010, **256** (20), P. 6025–6028.
- [6] Prasad A.K., Shwathy R, et al. Microstructure dependent ammonia sensing properties of nanostructured zinc oxide thin films using in-house designed gas exposure facility. *IEEE Xplore Conference Proceedings of the "International Conference on Nanoscience, Engineering and Technology (ICONSET)"*, 2011, Chennai, India, P. 73–77.
- [7] Yang P.F., Wen H.C., et al. Characteristics of ZnO thin films prepared by radio frequency magnetron sputtering. *Microelectronic Reliability*, 2008, **48**, P. 389–394.
- [8] Chakraborty S., Dhara S., et al. Resonant exciton-phonon coupling in ZnO nanorods at room temperature. *AIP Advances*, 2011, **1**, 03213.
- [9] R. Cuscó, E. Alarcón-Lladó, et al. Temperature dependence of Raman scattering in ZnO. *Physical Review B*, 2007, **75**, 165202.

Effect of excess selenium in the formation of $\text{Cu}_2\text{Zn}_{1.5}\text{Sn}_{1.2}(\text{S}_{0.9}+\text{Se}_{0.1})_4$ alloys for solar cell applications

Chinnaiyah Sripan¹, Annamraju Kasi Viswanath¹, Ganesan R.²

¹Centre for Nanoscience and Technology, Pondicherry University, Pondicherry, India

²Department of Physics, Indian Institute of Science, Bangalore, Karnataka, India

Srimannano2007@gmail.com, v_kasi@hotmail.com, rajamanickam.ganesan@gmail.com

PACS 81.05.Bx, 88.05.Ec, 81.05.Hd

DOI 10.17586/2220-8054-2016-7-3-509-512

Copper zinc tin sulfide/selenide $\text{Cu}_2\text{ZnSn}(\text{S}, \text{Se})_4$ (CZTSSe) is an alternative promising material for solar cell applications. It exhibits a high optical absorbance and tunable band gap. We have investigated the effect of excess selenium on the formation of CZTSSe phase which was prepared by the thermal melt method. The CZTSSe alloys were characterized by X-ray diffraction (XRD), Raman spectroscopy and UV-VIS spectroscopy. The crystallographic structure and phase were confirmed by X-ray diffraction and Raman spectroscopic techniques. In Raman spectroscopy, we found that the phase shifts from 327 cm^{-1} to 338 cm^{-1} when the selenium content excess is 5 %. In optical studies, a band gap for the CZTSSe alloys of about 1.43 eV to 1.44 eV was observed.

Keywords: $\text{Cu}_2\text{ZnSn}(\text{S}, \text{Se})_4$, raman spectroscopy, solar cell.

Received: 2 February 2016

Revised: 18 April 2016

1. Introduction

The development of clean energy resources as an alternative to fossil fuels has become one of the most important tasks assigned to current researchers. Recently, photovoltaic devices based on several semiconductor nanocrystal (NCs), including CdTe, Cu(In,Ga)Se₂ and Cu(In,Ga)S₂ have been realized. Through this research, technologies have reached commercial module production with power conversion efficiencies of up to 9 %, however, their potential is restricted by the limited supply of In and Ga as well as by restrictions on the safe usage of Cd. $\text{Cu}_2\text{ZnSnS}_4$ (CZTS) and $\text{Cu}_2\text{ZnSnSe}_4$ (CZTSe) are two promising materials for Photovoltaic applications. Copper-Indium-Gallium-Selenide/Sulfide (CIGS) solar cells have achieved about 20 % conversion efficiency at the laboratory scale, which is one of the highest efficiency among various thin film solar cells. However, CIGS solar cells adopt rare earth elements. In this point of view $\text{Cu}_2\text{ZnSn}(\text{S},\text{Se})_4$ (CZTSSe) is a very promising absorber material [1–4]. It includes earth abundant elements Sn, Zn, moreover less toxic S and Se. In addition, the CZTSSe exhibits excellent optical properties such as a direct band gap of 1.1 to 1.5 eV and a large absorption coefficient of 10^4 cm^{-1} in visible spectrum range. CZTS thin film has been prepared by various methods such as vacuum based synthesis and solution based synthesis. Band gap of CZTSSe thin film can be tuned by controlling the stoichiometry of the reactants. In this material, the theoretically predicted power conversion is 32.2 %, but in experiments they have achieved 6.77 % efficiency by vacuum-based process [5] and 12.6 % by another solution process. However the device performance was greatly improved, basic research on CZTSSe material itself are insufficient, for example fabrication of compositionally-uniform CZTSSe film is still hard task due to the loss of Sn during the annealing process [7]. Considering that high efficiency solar cell can be realized just with Cu poor and Zn rich CZTS [8], careful and precise adjustment of chemical compositions of CZTS is prerequisite. Based on this research, we adjusted the stoichiometry of $\text{Cu}/(\text{Zn}+\text{Sn})=0.77$ and $\text{Zn}/\text{Sn}=1.25$ for much-improved grain size. Hence, the systematic sulfurization and experiments under controlled temperature and surrounding atmosphere came to be significant.

2. Experimental methods

Polycrystalline alloys $\text{Cu}_2\text{Zn}_{1.5}\text{Sn}_{1.2}(\text{S}_{0.9}+\text{Se}_{0.1})_4$, (without excess selenium) $\text{Cu}_2\text{Zn}_{1.5}\text{Sn}_{1.2}(\text{S}_{0.9}+\text{Se}_{0.105})_4$ – 5 % of excess Se, $\text{Cu}_2\text{Zn}_{1.5}\text{Sn}_{1.2}(\text{S}_{0.9}+\text{Se}_{0.110})_4$ – 10 % of excess Se and $\text{Cu}_2\text{Zn}_{1.5}\text{Sn}_{1.2}(\text{S}_{0.9}+\text{Se}_{0.115})_4$ – 15 % of excess Se were prepared by a thermal melt technique using separate single source materials. The single source materials were prepared by taking elements in stoichiometry ratio of 2.0:1.5:1.2:4. Pure elements of Cu, Zn, Sn, S and Se (99.999 % Alfa Aesar) were weighed in atomic stoichiometry ratio and transferred to meticulously-cleaned quartz ampoule. The ampoules were sealed at 1×10^{-5} mbar vacuum and this ampoule was placed in electric furnace and slowly heated at $500 \text{ }^\circ\text{C}$ ($5 \text{ }^\circ\text{C}/\text{min}$) and kept at that temperature for one hour. The temperature was

then increased to 950 °C. To ensure the homogeneity of the molten materials, the ampoules were rotated for 24 hrs at this temperature and gradually cooled to room temperature.

2.1. Material characterizations

The structural analysis of the base material powder was done by XRD using Cu-K α source (wavelength=1.5405 Å) with a diffraction angle from 10 ° to 80 ° degree (BRUKER D8-ADVANCE). The investigation of the phase formation of CZTSe bulk materials were characterized by Raman spectroscopy using the excitation wavelength of 532 nm (HORIBA Jobin YVON Lab RAM HR800 spectrometer). The UV-Visible spectra of CZTSe alloy materials were recorded by Perkin Elmer UV/Visible spectrometer Lambda 35 from 400 – 1100 nm.

3. Results and discussion

The structures of the as-synthesized alloys were characterized by XRD, as show in Fig. 1a and 1b. The diffraction peaks of as-prepared CZTSSe alloys can be indexed to pure phase of kesterite structure (CZTSSe) (ICSD No-184475). The major diffraction peak appeared at 2θ 28.23 °, 32.3 °, 47.27 ° and 55.8 ° attributed to (112), (200), (220) and (312) hkl planes, can be seen clearly. The lattice parameters $a = b = 5.62$ Å, $c = 11.22$ Å of the typical sample were similar to that described in the literature [8,9]. Also, the secondary peaks SnSe and ZnS presented all excess selenium presented alloys. But in excess selenium content 5 % the intensity of SnSe and ZnS was much less compared to the 0 % and 10 % excess selenium.

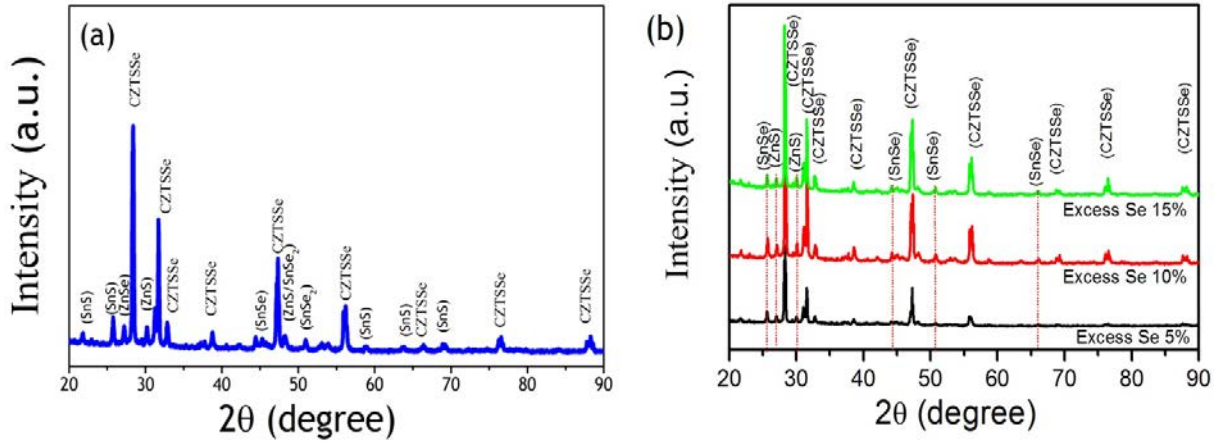


FIG. 1. X-ray diffraction (XRD) pattern of synthesized CZTSSe alloys. (a) $\text{Cu}_2\text{Zn}_{1.5}\text{Sn}_{1.2}(\text{S}_{0.9}+\text{Se}_{0.1})_4$ alloy, (b) 5, 10 and 15 % of excess selenium alloys

Also, we have noted the differentiation of (112) diffraction peaks shift for alloys of no excess selenium alloy and 5 % excess selenium. Fig. 2 shows that the diffraction peak shifted from smaller 2θ values to higher 2θ values as the selenium content increases, indicating the replacement of sulfur with selenium [10]. The Raman spectra of $\text{Cu}_2\text{Zn}_{1.5}\text{Sn}_{1.2}(\text{S}_{0.9}+\text{Se}_{0.1})_4$ and $\text{Cu}_2\text{Zn}_{1.5}\text{Sn}_{1.2}(\text{S}_{0.9}+\text{Se}_{0.105})_4$ (5 % excess selenium) bulk materials are shown in Fig. 3. In bulk materials, the primary vibration of $\text{Cu}_2\text{Zn}_{1.5}\text{Sn}_{1.2}(\text{S}_{0.9}+\text{Se}_{0.1})_4$ was detected at 327 cm^{-1} and 197 cm^{-1} due to selenium-selenium vibration, but could not detected secondary phases, which might be due to the difference in sensitivity or the minute presence of CZTSSe alloys. In $\text{Cu}_2\text{Zn}_{1.5}\text{Sn}_{1.2}(\text{S}_{0.9}+\text{Se}_{0.105})_4$ (5 % excess selenium) alloy the primary peaks were detected at 337 cm^{-1} , 287 cm^{-1} and 367 cm^{-1} for CZTS and 197 cm^{-1} and 239 cm^{-1} for CZTSe. The peak shifted from lower wave number to higher wave numbers [10].

The optical band gap (E_g) for $\text{Cu}_2\text{Zn}_{1.5}\text{Sn}_{1.2}(\text{S}_{0.9}+\text{Se}_{0.1})_4$ and $\text{Cu}_2\text{Zn}_{1.5}\text{Sn}_{1.2}(\text{S}_{0.9}+\text{Se}_{0.105})_4$ (5 % excess selenium) alloys were calculated where the absorbance co-efficient value was $> 10^4\text{ cm}^{-1}$. The optical band gap of material was determined by the Tauc and the Davis and Mott models [11]. This is shown in Fig. 4:

$$(\alpha h\nu) = B(h\nu - E_g)^n,$$

where B is constant (Tauc parameter), h is Planck's constant, ν is frequency, E_g is optical band gap and n is a number which related mechanism of transition process, the value of n is taken to be $1/2$ for direct transition. In an alloy without excess selenium, a band gap of 1.44 eV was obtained experimentally. For $\text{Cu}_2\text{Zn}_{1.5}\text{Sn}_{1.2}(\text{S}_{0.9}+\text{Se}_{0.105})_4$ (5 % excess selenium) alloy, the band gap decreased to 1.43 eV. The reduction in the number of unsaturated defects, which decreases the density of localized states in the band structure and consequently decreases the optical band gap, may be attributable to an excess of selenium present.

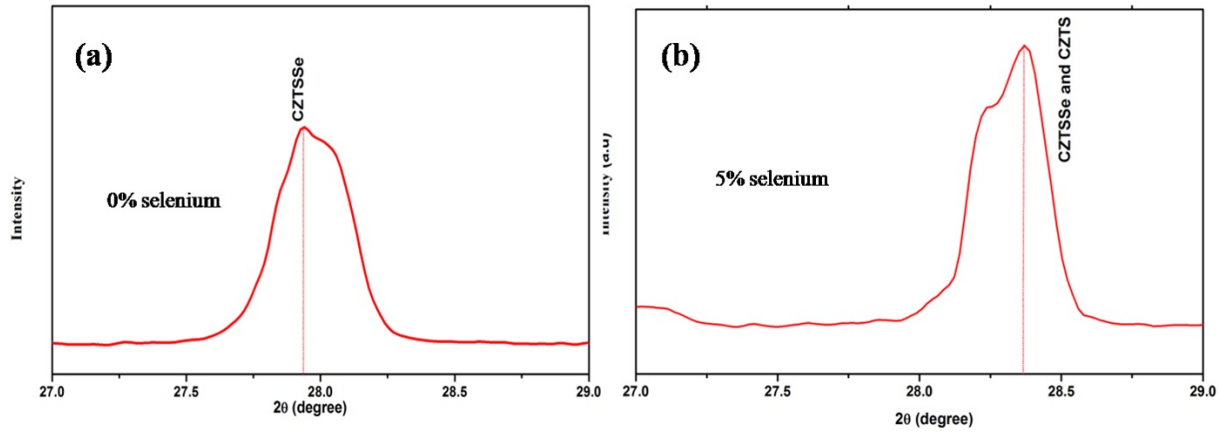


FIG. 2. X-ray diffraction (XRD) pattern- differentiates the peak shift of $\text{Cu}_2\text{Zn}_{1.5}\text{Sn}_{1.2}(\text{S}_{0.9}+\text{Se}_{0.1})_4$ and $\text{Cu}_2\text{Zn}_{1.5}\text{Sn}_{1.2}(\text{S}_{0.9}+\text{Se}_{0.105})_4$ alloys

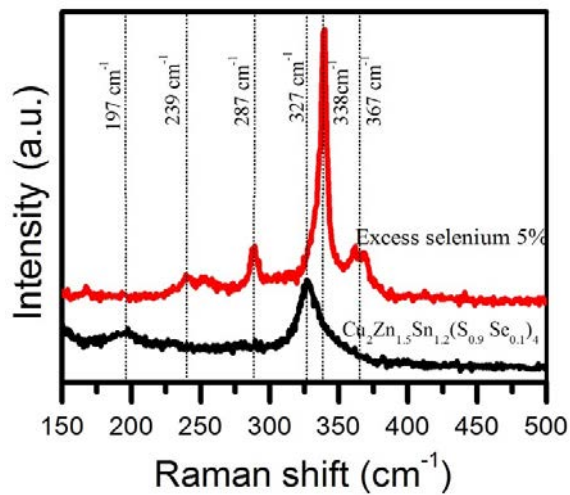


FIG. 3. Raman spectroscopy of CZTSSe alloys in different excess selenium

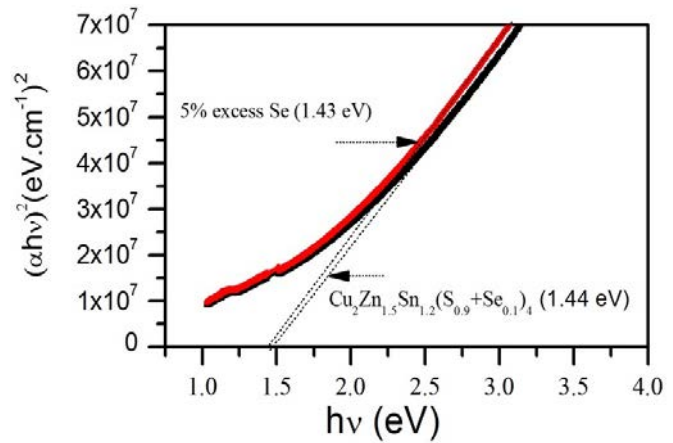


FIG. 4. Optical band gap of CZTSSe alloys in different excess selenium

4. Conclusion

We have investigated the effect of excess selenium on the formation of CZTSSe phase prepared via the thermal melt method. The crystallographic structures of CZTSSe alloys phase were confirmed by X-ray diffraction and Raman spectroscopic techniques. In Raman spectroscopic analyses, we found that the phase shifts from 327 cm^{-1} to 338 cm^{-1} when the selenium content is 5 % in excess. In optical studies, we have found the band gap for CZTSSe alloys to be about 1.43 – 1.44 eV.

Acknowledgement

The authors thank Inorganic and Physical Chemistry (IPC-IISc, Bangalore) and Department of Physics (IISc, Bangalore) for XRD and UV-Visible characterizations.

References

- [1] Ito K., Nakazawa T. Direct Liquid Coating of Chalcopyrite Light-Absorbing Layers for Photovoltaic Devices. *Jpn. J. Appl. Phys.*, 1988, **27**(1), P. 2094–2097.
- [2] Katagiri H., Saitoh K., et al. Miyajima Development of thin film solar cell based on $\text{Cu}_2\text{ZnSnS}_4$ thin films. *Sol. Energy Mater. Sol. Cells*, 2001, **65**(1), P. 141–148.
- [3] Seol J.S., Lee S.Y., et al. Electrical and optical properties of $\text{Cu}_2\text{ZnSnS}_4$ thin films prepared by rf magnetron sputtering process. *Sol. Energy Mater. Sol. Cells*, 2003, **75**(1), P. 155–162.

- [4] Katagiri H., Jimbo K., et al. Development of CZTS-based thin film solar cells. *Thin Solid Films*, 2009, **517**(7), P. 2455–2460.
- [5] Katagiri H., Jimbo K., et al. Enhanced Conversion Efficiencies of $\text{Cu}_2\text{ZnSnS}_4$ -Based Thin Film Solar Cells by Using Preferential Etching Technique. *Appl. Phys. Express*, 2008, **1**(4), P. 041201.
- [6] Todorov T.K., Reuter K.B., Mitzi D.B. Photovoltaic Devices: High-Efficiency Solar Cell with Earth-Abundant Liquid-Processed Absorber. *Adv. Mater* 2010, **22**(20), P. E156-9.
- [7] Weber A., Mainz R., Schock H.W. On the Sn loss from thin films of the material system Cu–Zn–Sn–S in high vacuum. *J. Appl. Phys*, 2010, **107**(1), P. 013516.
- [8] Mitzi D.B., Gunawan O.i., et al. The path towards a high-performance solution-processed kesterite solar cell. *Sol. Energy Mater. Sol. Cells*, 2011, **95**(6), P. 1421–1436.
- [9] Jiang C., Lee J.-S., Talapin D.V. Soluble Precursors for CuInSe_2 , $\text{CuIn}_{1-x}\text{Ga}_x\text{Se}_2$, and $\text{Cu}_2\text{ZnSn}(\text{S},\text{Se})_4$ Based on Colloidal Nanocrystals and Molecular Metal Chalcogenide Surface Ligands. *J. Am. Chem. Soc.*, 2012, **134**(11), P. 5010–5013.
- [10] Yang W., Duan H.-S., et al. Novel Solution Processing of High-Efficiency Earth-Abundant $\text{Cu}_2\text{ZnSn}(\text{S},\text{Se})_4$ Solar Cells. *Adv. Mater* 2012, **24**(47), P. 6323–6329.
- [11] Fischereder A., Rath T., et al. Investigation of $\text{Cu}_2\text{ZnSnS}_4$ Formation from Metal Salts and Thioacetamide. *Chem. Mater*, 2010, **22**(11), P. 3399–3406.

Titanium dioxide supported ruthenium nanoparticles for carbon sequestration reaction

Praveenkumar Ramprakash Upadhyay, Vivek Srivastava*

NIIT University, NH-8 Jaipur/Delhi Highway, Neemrana (Rajasthan), 301705, India

*vivek.shrivastava@niituniversity.in

DOI 10.17586/2220-8054-2016-7-3-513-517

Ru metal doped TiO₂ nanoparticles were synthesized using a sol gel method with and without ionic liquid. Ru metal is well dispersed while utilizing ionic liquid as reaction medium for catalyst synthesis with respect to Ru–TiO₂ catalyst. A TEM image for Ru–TiO₂–IL catalyst reveals, stable, well dispersed and agglomeration free Ru metal doped TiO₂ nanoparticles. CO₂ Hydrogenation reaction on task specific ionic liquid medium, offered the formic acid in high TON/TOF value with added advantage of 5 times catalyst recycling.

Keywords: ruthenium metal, titanium dioxide, nanoparticles, hydrogenation, carbon sequestration, formic acid.

Received: 2 February 2016

Revised: 15 April 2016

1. Introduction

Various physiochemical methods have been reported for the fixation of CO₂ gas, such as carbonates, geological or ocean storage or afforestation [1–4]. However, these approaches have severe drawbacks in terms of economic factors, safety, efficiency, and reliability of their immediate application. It is also known that functionalized ionic liquid mediated Ru (II) compounds can promote the partial hydrogenation of CO₂ to formic acid where the ionic liquid not only captures the formed formic acid but also shifts the equilibrium of the hydrogenation reaction. The pre-organized structure of imidazolium based ionic liquids (ILs) provides structural directionality through their hydrogen bonding, as opposed to classical salts in which the aggregates display charge-ordering structures [4]. The structural organization of ILs provides a special “entropic drivers” for natural, precise, and prolonged assembling of nanoscale assemblies [5,6]. We successfully applied imidazolium ionic liquids as a template, additive, and solvent for the synthesis of an excess of transition-metal nanoparticles [7]. The catalytic properties (activity and selectivity) of these soluble metal nanoparticles direct that they possess a pronounced surface like (multi-site) rather than single-site-like catalytic properties [8–10]. The main goal of this proposed work is to develop supported functionalized ionic liquid ruthenium nanoparticles [11] in TiO₂ (nanoparticles and nanotubes) for the hydrogenation of CO₂.

2. Experimental

Reagent Plus[®] grade ruthenium (III) chloride hydrate and titanium tetraisopropoxide were purchased from Aldrich. Other ReagentPlus[®] and extra pure grade chemicals were purchased from Spectrochem. Nuclear Magnetic Resonance (NMR) spectra were recorded on a standard Bruker 300WB spectrometer with an Avance console at 400 and 100 MHz for ¹H NMR. All the hydrogenation reactions were carried out in a 100 mL stainless steel autoclave (Amar Equipment, India). The catalyst material was characterized by TEM (Hitachi S-3700N) and Energy-dispersive X-ray spectroscopy (EDX) (Perkin Elmer, PHI 1600 spectrometer). FTIR data for all the samples were studied with Bruker Tensor-27. 1-Butyl-3-methylimidazolium Chloride, 1,3-*di*(*NN*-dimethylaminoethyl)-2-methylimidazolium trifluoromethanesulfonate ([DAMI][TfO]), 1,3-*di*(*NN*-dimethylaminoethyl)-2-methylimidazolium *bis* (trifluoromethylsulfonyl) imide ([DAMI][NTf₂]) and 1-butyl-3-methylimidazolium chloride ionic liquids were synthesized as per reported procedures [12,13]. FTIR data for all the samples were studied with Bruker Tensor-27. The morphology of catalysts was investigated by transmission electron microscopy (TEM) using a Philips CM12 instrument. XRD was performed on Philips X-Pert diffractometer. The normalized X-ray absorption near stretcher (XANES) spectra was recorded on BL01C1.

3. Result and discussion

We synthesized two different ruthenium metal doped TiO₂ nanoparticles with and without ionic liquids, Ru–TiO₂–IL and Ru–TiO₂ respectively, using the sol-gel method and followed by calcination at 250 °C for 5 hours. The XRD pattern of TiO₂ was compared with that of Ru–TiO₂–IL and Ru–TiO₂ (Fig. 1) [14] from the wide angle XRD pattern. The titania samples were found only in anatase phase with characteristic diffraction peaks of 2 degree values near 42 – 44 °, being assigned to metallic ruthenium (PDF No. 06-0633) observed for the Ru–TiO₂

catalyst. However, there were no characteristic peaks of Ru⁰ observed for the Ru-TiO₂-IL catalyst, indicating a high dispersion of Ru on the TiO₂ support.

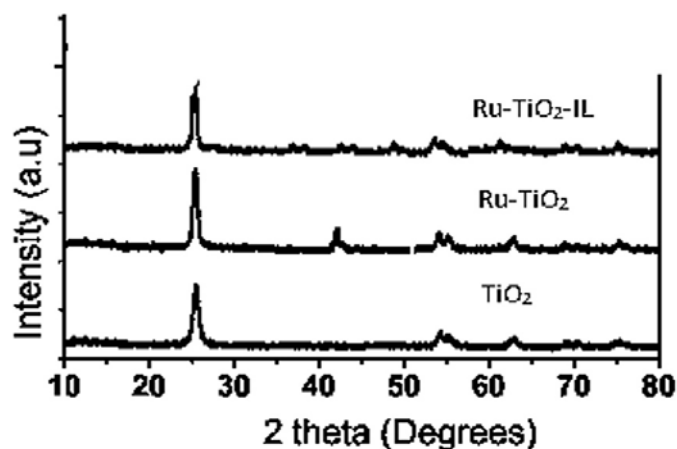


FIG. 1. XRD data for ruthenium metal doped titanium dioxide nanoparticles

The FTIR analysis of TiO₂ with respect to Ru-TiO₂-IL and Ru-TiO₂ catalysts was carried out from 400 – 4000 cm⁻¹ (Fig. 2). In Ru loaded TiO₂, clear bands for the O-Ti-O bonding were found near 445 and 708 cm⁻¹. The representing band for δ -H₂O bending appeared near to 1605 cm⁻¹. A broad absorption band showing the O and O-Ti-O flexion vibration band found between 400 cm⁻¹ and 800 cm⁻¹.

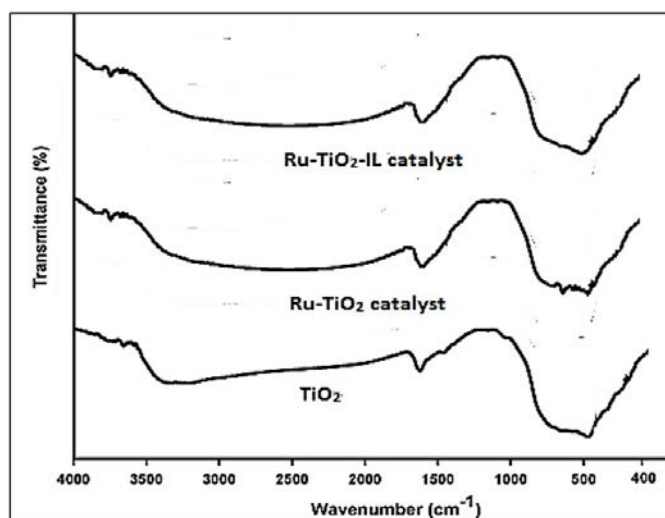


FIG. 2. Infrared data for Ru-TiO₂ nanoparticles

TEM micrographs of TiO₂, Ru-TiO₂-IL and Ru-TiO₂ are shown in Fig. 3. Electron microscopy reveals the morphology of the TiO₂, Ru-TiO₂-IL and Ru-TiO₂. It was clearly observed that for Ru-TiO₂ catalyst, many severely strained ruthenium nanoparticles larger than 25 ± 5 nm were found on the surface of TiO₂ while in Ru-TiO₂-IL catalysts, ultrafine Ru nanoparticles with uniform particle size were dispersed on the surface of TiO₂. It is worth noting here that no particles larger than 20 nm, were observed despite our careful attention. More intuitively, the average particle size for the Ru-TiO₂ catalyst was found to be 25 ± 5 nm. However, it was only 15 ± 5 nm with narrower particle size spreading for the Ru-TiO₂-IL catalyst. These observations indicated that the reaction medium type could remarkably affect the dispersion of Ru on the TiO₂ surface and the ionic liquid was a more efficient reaction medium than conventional solvents to stabilize the smaller nano-sized particles of Ru.

Theoretical (cation exchange capacity) and an experimental (ICP-AES) method was used to calculate the amount of Ru species in TiO₂. Both theoretical and experimental values were found to be in good agreement, and 2.5 wt% Ru was found in the Ru-TiO₂-IL catalyst while in Ru-TiO₂ catalyst, there was 2.1 wt% Ru metal.

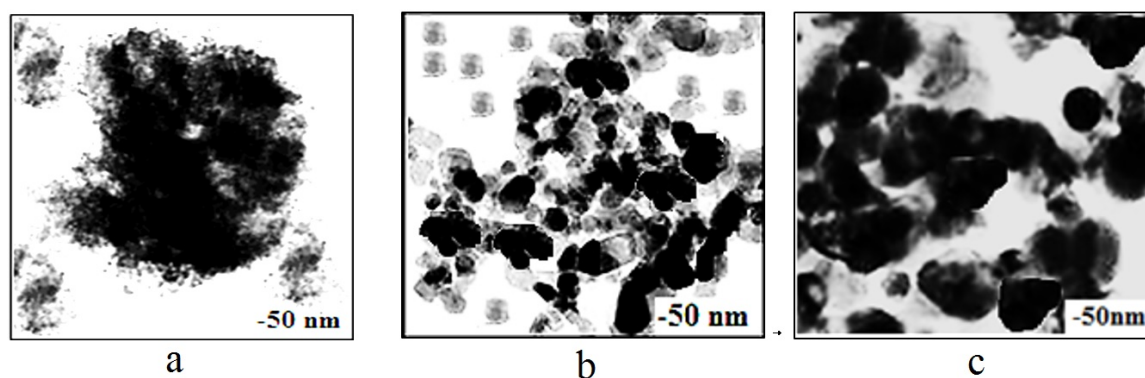


FIG. 3. TEM data for Ruthenium Metal Doped Titanium Dioxide Nanoparticles. (a) Ru-TiO₂ catalyst, (b) Ru-TiO₂-IL catalyst (Before catalysis), (c) Ru-TiO₂-IL catalyst (After catalysis)

This protocol also minimizes the loss of Ru nanoparticles during the process. Hydrogenation of CO₂ was carried out using H₂ gas in the presence of both the catalysts (without any pretreatment) with functionalized ionic liquids separately at 80 °C under high pressure. After the reaction, formic acid was isolated from the reaction mass followed by the nitrogen flow at 125 – 130 °C. The results obtained while optimizing the reaction conditions with respect to TON/TOF values for formic acid were summarized in Table 1, entry 1 – 17. Acid-base titration using phenolphthalein indicator and ¹H NMR analysis was used to calculate the quantity of formic acid formed [12, 13].

Initially, both catalysts were tested under the same reaction conditions for CO₂ hydrogenation and high TON/TOF values were obtained with [DAMI][NTf₂] immobilized Ru-TiO₂-IL (Table 1, Entry 1 & 2). All the other important reaction parameters and technical variables were investigated using [DAMI][NTf₂] immobilized Ru-TiO₂-IL (Table 1, Entry 3 – 17). We obtained good TON/TOF value at 100 °C when, the total H₂/CO₂ gas pressure was 40 MPa (Table 1, Entry 3). The effect of water was also studied on the reaction kinetics of CO₂ hydrogenation reaction only, with 2 ml of water with a high TON/TOF value (Table 1, entry 12). CO₂ may react with water and an amine group of ionic liquid to give off bicarbonates which may act as a perfect substrate for the hydrogenation reaction. RuCl₃ was also evaluated for the hydrogenation reaction, but formic acid was obtained with a low TON/TOF value compared to [DAMI][NTf₂] immobilized Ru-TiO₂-IL (Table 1), Entry 17). After the reaction, formic acid was isolated with the aid of N₂ gas and the [DAMI][NTf₂] ionic liquid immobilized Ru-TiO₂-IL went for a recycling test after washing with diethyl ether. [DAMI][NTf₂] ionic liquid immobilized Ru-TiO₂-IL were recycled up to 5 times with slight loss of their catalytic action mainly because of agglomeration of Ru NPs which was also confirmed by TEM analysis of the Ru NPs (Fig. 4).

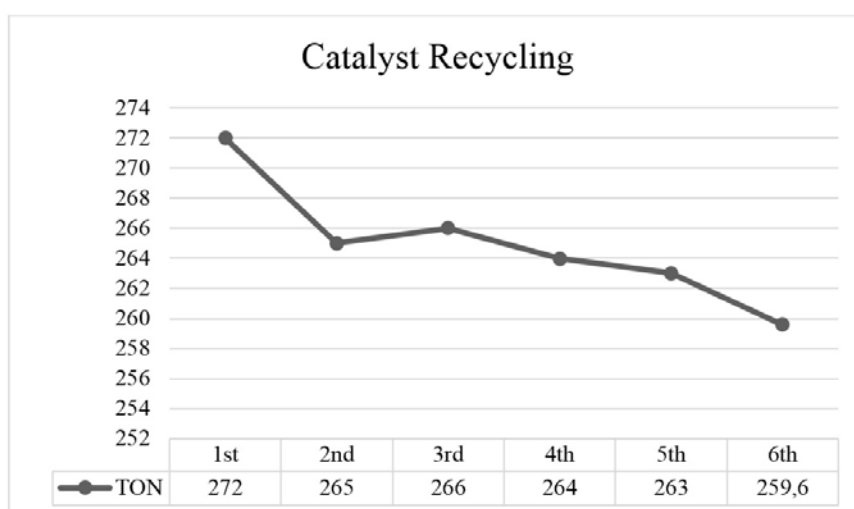


FIG. 4. Catalyst recycling experiment

TABLE 1. Hydrogenation of CO₂ to Formic acid using ionic liquid immobilized TiO₂ dropped Ru metal¹

Entry	Catalytic system	P(H ₂) P _{total} (MPa) ²	Temperature(°C)	Time (h)	TON ³
1.	Ru-TiO ₂ -IL / [DAMI][TfO]	20 (40)	80	1	252
2.	Ru-TiO ₂ /[DAMI][TfO]	20 (40)	80	1	222
3.	Ru-TiO ₂ -IL / [DAMI] [NTf ₂]	20 (40)	80	1	246
4.	Ru-TiO ₂ -IL / [DAMI][TfO]	20 (40)	100	1	253
5.	Ru-TiO ₂ -IL / [DAMI][TfO]	20 (40)	120	1	253
6.	Ru-TiO ₂ -IL / [DAMI][TfO]	20 (40)	50	1	195
7.	Ru-TiO ₂ -IL / [DAMI][TfO]	20 (40)	100	1.5	152
8.	Ru-TiO ₂ -IL / [DAMI][TfO]	20 (40)	100	0.3	85
9.	Ru-TiO ₂ -IL / [DAMI][TfO]	10 (20)	100	1	195
10.	Ru-TiO ₂ -IL / [DAMI][TfO]	30 (60)	100	1	252
11.	Ru-TiO ₂ -IL / [DAMI][TfO]+ H ₂ O (1 mL)	20 (40)	100	1	258
12.	Ru-TiO ₂ -IL / [DAMI][TfO]+H ₂ O (2 mL)	20 (40)	100	1	270
13.	Ru-TiO ₂ -IL / [DAMI][TfO]+H ₂ O (3 mL)	20 (40)	100	1	272
14.	Ru-TiO ₂ -IL / [DAMI] [TfO] (0.100g)+ H ₂ O (2 mL)	20 (40)	100	1	272
15.	Ru-TiO ₂ -IL / [DAMI] [TfO] (0.500g)+ H ₂ O (2 mL)	20 (40)	100	1	272
16.	Ru-TiO ₂ -IL / [DAMI][NTf ₂]+ H ₂ O (2 mL)	20 (40)	100	1	260
17.	RuCl ₃ (0.07g) ⁴ + [DAMI][NTf ₂](0.250g)	20 (40)	100	1	224

1. Reaction conditions: 0.250 g catalytic system; 2. The total pressure of the system is indicated in parentheses; 3. Turn over number = n (formic acid) n (Ru)⁻¹ in one reaction cycle; 4. Turnover frequency = n (formic acid) n (Ru)⁻¹h⁻¹; 5. RuCl₃ · xH₂O (50 % Ru metal).

4. Conclusion

Here, we reported the synthesis of air/moisture stable, TiO₂ supported Ru nanoparticles with a narrow particle size distribution. The [DAMI] [NTf₂] ionic liquid immobilized Ru-TiO₂-IL catalyst was found to be highly active in terms of TON/TOF value for the production of formic acid over conventional and Ru-TiO₂ catalyst. Effect of water was also studied during the CO₂ hydrogenation reaction. The presence of functionalized ionic liquid as well as water was promising. Five times catalyst recycling, low catalyst loading and selectivity were the major advantages for this proposed protocol.

Acknowledgement

This work is financially supported by DST Fast Track (SB/FT/CS-124/2012).

References

- [1] Sakakura T., Choi J.C., Yasuda H. Transformation of Carbon Dioxide *Chem. Rev.*, 2007, **107** (6), P. 2365–2387.
- [2] Thampi K.R., Kiwi J., Gratzel M. Methanation and photo-methanation of carbon dioxide at room temperature and atmospheric pressure. *Nature*, 1987, **327** (6122), P. 506–508.
- [3] Zhang Z.F., Xie E., Li W.J., Hu S.Q., Song J.L., Jiang T., Han B.X. Hydrogenation of Carbon Dioxide is Promoted by a Task-Specific Ionic Liquid. *Angew. Chem. Int. Edit.*, 2008, **47** (6), P. 1127–1129.
- [4] Dupont J. On the solid, liquid and solution structural organization of imidazolium ionic liquids. *J. Braz. Chem. Soc.*, 2004, **15** (3), P. 341–350.
- [5] Migowski P., Dupont J. Catalytic Applications of Metal Nanoparticles in Imidazolium Ionic Liquids. *Chem. Eur. J.*, 2007, **13** (1), P. 32–39.
- [6] Antonietti M., Kuang D.B., Smarsly B., Yong Z. Ionic Liquids for the Convenient Synthesis of Functional Nanoparticles and Other Inorganic Nanostructures. *Angew. Chem. Int. Edit.*, 2004, **43** (38) P. 4988–4992.

- [7] Dupont J., Fonseca G.S., Umpierre A.P., Fichtner P.F.P., Teixeira S.R. Transition-Metal Nanoparticles in Imidazolium Ionic Liquids: Recyclable Catalysts for Biphasic Hydrogenation Reactions. *J. Am. Chem. Soc.*, 2002, **124** (16), P. 4228–4229.
- [8] Scheeren C.W., Machado G., Dupont J., Fichtner P.F.P., Teixeira S.R. Nanoscale Pt(0) Particles Prepared in Imidazolium Room Temperature Ionic Liquids: Synthesis from an Organometallic Precursor, Characterization, and Catalytic Properties in Hydrogenation Reactions. *Inorg. Chem.*, 2003, **42** (15), P. 4738–4742.
- [9] Scheeren C.W., Machado G., Teixeira S.R., Morais J., Domingos J.B., Dupont J. Synthesis and Characterization of Pt(0) Nanoparticles in Imidazolium Ionic Liquids. *J. Phys. Chem. B*, 2006, **110** (26), P. 13011–13020.
- [10] Cassol C.C., Umpierre A.P., Machado G., Wolke S.I., Dupont J. The Role of Pd Nanoparticles in Ionic Liquid in the Heck Reaction. *J. Am. Chem. Soc.*, 2005, **127** (10), P. 3298–3299.
- [11] Silveira E.T., Umpierre A.P., Rossi L.M., Machado G., Morais J., Soares G.V., Baumvol I.L.R., Teixeira S.R., Fichtner P.F.P., Dupont J. The Partial Hydrogenation of Benzene to Cyclohexene by Nanoscale Ruthenium Catalysts in Imidazolium Ionic Liquids. *Chem. Eur. J.*, 2004, **10** (15) P. 3734–3740.
- [12] Srivastava V. In Situ Generation of Ru Nanoparticles to Catalyze CO₂ Hydrogenation to Formic Acid. *Catalysis letters*, 2014, **144** (10), P. 1745–1750.
- [13] Srivastava V. Ru-exchanged MMT Clay with Functionalized Ionic Liquid for Selective Hydrogenation of CO₂ to Formic acid. *Catalysis letters*, 2014, **144** (12) P. 2221–2226.
- [14] Wang Y., Zhang R., Li J., Li L., Lin S. First-principles study on transition metal-doped anatase TiO₂. *Nanoscale Research Letters*, 2014, **9** (1), P. 46.
- [15] Bagheri S., Chekin F., Hamid S.B.A. Cobalt Doped Titanium Dioxide Nanoparticles: Synthesis, Characterization and Electrocatalytic Study. *J. Chin. Chem. Soc.*, 2014, **61** (6), P. 702–706.

Mathematical modeling for the evaluation of various parameters of 5-methyl salicylaldehyde aniline nano composite using fuzzy evidence theory

R. Irene Hepzibah^{1,4}, G. Geethalakshmi², R. Ida Malarselvi^{3,4}

¹ Department of Mathematics, AVC College of Engineering, Mayiladuthurai- 609305, Tamil Nadu, India

² Department of Mathematics, K.S.K College of Engineering and Technology, Kumbakonam, Tamil Nadu, India

³ Centre for Advanced Material Research, Government Arts College, Kumbakonam, Tamil Nadu, India

⁴ Research and Development Centre, Bharathiar University, Coimbatore – 641046, Tamil Nadu, India
ireneraj74@gmail.com, geethavish294@gmail.com, idamalaiselvi@gmail.com

PACS 02.10Ab, 02.50Cw, 02.50.Le, 07.05.Mh

DOI 10.17586/2220-8054-2016-7-3-518-522

Densities, viscosities, surface tension and Ultrasonic speeds of nano composite 5- Methyl Salicylaldehyde (5MS) with Aniline (A) were measured over the entire composition range at temperature 303 K. The adiabatic compressibility (β), free length (L_f), free volume (V_f) and viscous relaxation time (T) have been calculated from the experimental data. The experimental results have been correlated using Fuzzy Evidence Theory and the results are interpreted on the basis of possible hydrogen bonding between unlike molecules and changes in molecular association equilibria as well as structural effects for these systems. A good agreement among experimental data and the values estimated by theoretical procedure was obtained.

Keywords: 5-MS-A composite material, hydrogen bonding, acoustical and physical parameters, Fuzzy Evidence Theory.

1. Introduction

Organic liquid state is a fascinating area of current research. The term composites are now well-established in the understanding of such organic liquids. In many industrial applications, liquid mixtures are used in processing and product formulations. Studies on viscosity and acoustic properties of liquid composites consisting of 5 MS with aniline are of interest because of their use as dye carrier formulations in textile processing and pharmaceutical industry. These properties are of considerable interest in understanding the intermolecular interactions in liquid mixtures. Yet, a unified understanding of the mixing behavior of liquids is still controversial. In this respect, it is of interest to further carry out the systematic investigations of these properties for a better knowledge of the molecular interactions. A very large number and variety of intermolecular interactions have been used in composites. Most notable among such interactions are hydrogen bonding which arises from the non-polar regions of aromatic molecules and very effective design element in composite materials. Much research has compared the experimental values of interaction parameters with theoretically calculated values for composites using different models. G. M. Badger and A. G. Moritz [1] examined the C–H stretching of methyl groups attached to polycyclic aromatic hydrocarbons. V. C. Farmer and R. H. Thomson [2] studied the inter- and intramolecular hydrogen bonding in anilines. Infrared studies on the self-association of chloroform were given by Edwin D. Becker [3] in 1950. J. C. Evans [4] proposed the vibrational assignments and configuration of aniline, aniline NHD and ND₂. In spite of technological importance of 5MS-A no such studies on spectral and acoustical properties for 5MS-A systems are available in literature. We report here the above said studies of 5MS-A with CCl₄ at 303 K over the entire composition range. In the present work, an attempt has been made to employ fuzzy evidence theory for optimizing the key influencing parameters in the formation of 5MS-A composite.

2. Experimental

2.1. Materials and measurements

Analytical grade reagents were used without any further purification. The infrared spectrum of the title mixture was recorded using PERKIN ELMER spectrum RX FT-IR system. The ¹H-NMR spectrum of title mixture was performed in CDCl₃ by using BRUKER AC 400 (400 MHz) Spectrometer. The sound speed was measured using a Single crystal Ultrasonic Interferometer at an operating frequency of 2 MHz. The viscosity was measured using an Oswald's Viscometer calibrated with double distilled water. The density was measured by a 10 ml specific gravity bottle calibrated with double distilled water and acetone. Refractive indices were measured with an Abbe refractometer (Erma A 302A) and the values were obtained for Na–D light with an error less than ± 0.0002 units. Surface Tension was measured using the pendent drop method.

2.2. Synthesis of 5MS with aniline in CCl₄ solvent

Materials having moderate to high solubility at temperature ranging from room temperature to 303 K at atmospheric pressure form complexes when their samples were carefully mixed. In the present systems, the various concentrations of the ternary liquid mixtures were prepared in terms of mole fractions, out of which, the mole fractions for the first component 5-MS varied from 0.01 to 0.05 ml and the second component aniline were varied from ml. The required solute concentrations of the above-title mixture were prepared in 5 ml CCl₄. The formation of the complex was noticed by its pale color and also the absence of solid precipitates.

3. Results and discussion

3.1. Spectroscopic characterization

FT-IR spectra of newly synthesized composite material were recorded from (400 – 4000 cm⁻¹). All the above spectral data confirm the formation of the composite due to intermolecular hydrogen bonding. The relevant work was done by Ramachandra Raja. C et.al. [5] in 2013 and Maneesh Sharma et.al. [6] in 2012. The 300 MHz proton NMR spectrum of the synthesized composite 5MS-A was measured in CDCL₃ using Bruker instrument. The signals observed in the NMR spectra were in good agreement with reported values in the literature. The relevant work was done by Ida Malarselvi R. et.al. [7] in 2014.

3.2. Molecular acoustical and physico-chemical behavioural studies

In the composite, the ultrasonic velocity increases with the increasing concentration of 5MS-A. The variation of sound speed in a solution depends upon the increase or decrease of intermolecular free length (Lf) after mixing the compounds. A reduction in adiabatic compressibility is an indication that component molecules are held closely to each other. The internal pressure of the new material in the present study, which increases with increased concentration of 5-MS, can be attributed to there being definite interaction present between the different components of the mixture. The acoustic impedance (Z) of a material is the opposition exerted by the medium particles to sound energy. In the present system, the cohesive energy (CE) increases and the relaxation time decreases, which shows that the intermolecular energy is so high in the new composite material. The viscosity increases as the molar concentration of the solute mixture increases up to 100 mole% and further increase of the mole fraction of the solute mixture it still increases, which shows the strong solute-solvent interactions in the title mixture. The density is ever increasing and the refractive index decreases due to the formation of strong hydrogen bonding and the molecular association of the new material. Xinghua Su et.al. [8] in 2012 pointed out the same relative work. Due to the strong intermolecular interactions, the surface tension decreases with the increased mole fraction value. The intermolecular forces are attractive in nature. The molecules of the 5MS-A composite are strongly attracted by the liquid molecules. Concentration at the surface layer of the liquid results, in a decrease in the surface electrons and brings about a decrease in surface tension. Similar results were reported by K. Prasad et.al. [9] in 2006 and M. V. Rathnam et.al. [10] in 2012. See also [11–15].

TABLE 1. Mole Fractions of 5MS (X_1), Mole Fractions of Aniline (X_2), Values of Velocity (C), Density (P), Viscosity (N), Refractive Index (D), Surface Tension (T) and BPA

X_1	X_2	$C \text{ ms}^{-1}$	$i\rho \text{ kgm}^{-3}$	$\eta \times 10^3 \text{ Nsm}^2$	D	$T \times N/m$
0.04	0.0273	641	1.5852	0.00116	5.9877	0.0134668
0.08	0.0547	724	1.5920	0.00127	2.9021	0.0162094
0.12	0.0820	772	1.6183	0.00151	1.7048	0.0151904
0.16	0.1094	906	1.6239	0.00173	1.2424	0.0162238
0.20	0.1368	1047	1.6415	0.00186	0.9045	0.0162652
0.24	0.1436	1065	1.6521	0.00192	0.9028	0.0162785
0.28	0.1572	1079	1.6635	0.00205	0.9006	0.0162964
0.32	0.1625	1104	1.6743	0.00214	0.8924	0.0170562

4. Dempster-Shafer theory (DST) of evidence

Dempster-Shafer Theory (DST) is a mathematical theory of evidence. In a finite discrete space, Dempster-Shafer theory can be interpreted as a generalization of probability theory where probabilities are assigned to sets as opposed to mutually exclusive singletons. In traditional probability theory, evidence is associated with only one possible event. In Dempster-Shafer Theory, evidence can be associated with multiple possible events.

A frame of discernment, (or simply a frame), is usually denoted as a set of mutually exclusive and exhaustive propositional hypotheses, of which, one and only one is true [8]. Evidence theory is based on two dual non-additive measures, namely Belief measure and Plausibility measure. There is one important function is Dempster-Shafer theory to define Belief measure and plausible measure which is known as Basic Probability Assignments.

TABLE 2. Mole Fraction of 5MS (X_1), Mole Fraction of Aniline (X_2), Values of Adiabatic Compressibility (β), Internal Pressure (π_1), Cohesive Energy(CE), Acoustic Impedance (Z), Free Length (L_f) and Relaxation Time (T)

X_1	X_2	$i\beta \times 10^{-10}$ M^2n^{-1}	$\pi_i \times 10^6$ nm^{-2}	CE $kJ mol^{-1}$	$Z \times 10^6$ $Kgm^{-2}s^{-1}$	$L_f \times 10^{-10}$ m	$\tau \times 10^{-12}$ s
0.04	0.0273	7.0092	3.8124	19.1440	1.0161	46.3507	0.2020
0.08	0.0547	6.9793	3.6564	36.7160	1.1526	47.0367	0.1851
0.12	0.0820	6.8691	3.6375	53.8885	1.2493	47.4595	0.1587
0.16	0.1094	6.8422	3.4015	66.9709	1.4712	48.0739	0.1388
0.20	0.1368	6.7688	3.2329	78.7204	1.7186	48.5914	0.1307
0.24	0.1436	6.6790	3.1100	89.3542	1.9321	49.0433	0.1295
0.28	0.1572	6.5430	3.0125	98.0032	2.1096	49.6024	0.1254
0.32	0.1625	6.4852	2.8955	107.9962	2.3061	50.1278	0.1195

A function $m : 2^\Theta \rightarrow [0, 1]$ is called Basic Probability Assignments (BPA) on the set Θ if it satisfies the following conditions:

$$m(\phi) = 0, \quad (1)$$

$$\sum_{A \subseteq \Theta} m(A) = 1, \quad (2)$$

where ϕ is an empty set and A is any subset there of.

The Basic Probability Assignment function (or mass function) is a primitive function. Given a frame, Θ , for each source of evidence, a mass function assigns a mass to every subset of Θ , which represents the degree of belief that one of the hypotheses in the subset is true, given the source of evidence. A subset A of a frame Θ is called the focal elements of m , if $m(A) > 0$.

The lower bound, Belief for a set A is defined as the sum of all the basic probability assignments of the proper subsets (B) of the set of interest $c(A)(B \subseteq A)$. The upper bound, Plausibility is the sum of all the basic probability assignments of set (B) that intersect the set of interest (A)($B \cap A \neq \phi$). Formally for all sets A that are elements of the power set $A \in P(X)$, [16], $Bel(A) = \sum_{B/B \subseteq A} m(B)$ and $Pl(A) = \sum_{B/B \cap A \neq \phi} m(B)$.

The two measures, Belief and Plausibility are non-additive. This can be interpreted to mean that it is not required for the sum of all the Belief measures to be one, and similarly for the sum of all the Plausibility measures. Hence, interval $[Bel(A), Pl(A)]$ is the range of belief A .

4.1. The dempster rule of combination

The Dempster rule of combination is critical to the original conception of the Dempster-Shafer theory. The measure of Belief and Plausibility are derived from the combined basic assignments. Dempster's rule combines multiple belief functions through their basic probability assignments (m). These belief functions are defined on the same frame of discernment, but are based on independent assignments or bodies of evidence. The Dempster rule of combination is purely a conjunctive operation (AND). The combination rule results in a belief function based on conjunctive pooled evidence [17].

Let m_1 and m_2 be two mass functions defined on the same frame of discernment, and then a combined BPA can be obtained by using Dempster's combination rule, the combined BPA $m = m_1 \oplus m_2$ is defined as follows

$$m = \begin{cases} \frac{\sum_{B \cap C = A} m_1(B)m_2(C)}{1 - \sum_{B \cap C = \phi} m_1(B)m_2(C)}, & \forall \phi \subseteq \Theta; \\ 0, & \text{otherwise.} \end{cases}$$

5. Application of evidence theory to the experimental data

Evidence theory can handle both aleatory and epistemic uncertainty. Three important functions in evidence theory, the basic probability assignment function (bpa), Belief function (Bel) and Plausibility function (Pl) are used to quantify the given variable. As already stated in this paper interval focal elements and their Basic Probability Assignments of two variables are combined by Modified Interval Arithmetical operations. To determine the quantitative formation characteristics of the composite, fuzzy evidence theory was employed to identify the level of importance in interaction parameters on their performance characteristics. The effect of these parameters on interaction has been investigated using Basic Probability Assignments of two variables X_1 and X_2 and the variation of this interaction parameter with the mole fraction of composite has been discussed in terms of molecular interaction. The validity of the observed values developed and the results were discussed below in Table 3. In this study, the sum of Basic Probability Assignments (BPA) is equal to one. The effectiveness of the model has been checked by the validation with experimental values and the molecular interactions and the complex formation evolved through Basic Probability Assignments can successfully predict the complex formation for any combination of the experimental results. The experimental results have been validated by asserting that the predicted values are very close to each other and hence the developed models are suitable.

TABLE 3. BPA

X_1	X_2	BPA
0.04	0.0273	0.10
0.08	0.0547	0.10
0.12	0.0820	0.25
0.16	0.1094	0.20
0.20	0.1368	0.15
0.24	0.1436	0.05
0.28	0.1572	0.10
0.32	0.1625	0.05

6. Conclusion

The newly synthesized potential 5MS-A composite with optimum physical and acoustical properties are expected to find a special position in the biomedical field like antibiotic and Anti-elementic agent. 5MS based on 5MS-A were expected to possess a higher co-efficient of viscosity, density and hence may be used in the synthesis of dyes. Dempster's rule combines multiple belief functions through their basic probability assignments and the model can be successfully related with the above process parameters by the molecular interactions and the complex formation.

Acknowledgements

This work was financially supported by University Grants Commission, Govt of India, New Delhi, within the Minor Research Project scheme under the approval cum sanction No.F MRP-5150/14 (SERO/UGC). All the spectral data were obtained from SAIF, Indian Institute of Technology, Chennai.

References

- [1] G.M. Badger and A.G. Moritz. *Spectrachimica Acta*. Pergamon Press Ltd, 1959, **9**, P. 672–678.
- [2] J.C. Evans. *Spectrachimica Acta*, Pergamon Press Ltd, 1960, **16**, P. 428–443.
- [3] Edwin D. Becker. *Spectrachimica Acta*, Pergamon Press Ltd, 1950, **9**, P. 743–746.
- [4] V.C. Farmer and R.H. Thomson. *Spectrachimica Acta*, Pergamon Press Ltd, 1960, **16**, P. 559–562.
- [5] Maneesh Sharma, Anant A Naik, P.Raghunathan and S.V.Eswaran. *J.Chem.Sci.*, 2012, **124**(2), P. 395–401.
- [6] C. Ramachandra Raja and R.Ida Malarselvi. *International J. Science and Research (IJSR)*, **2**(1), P. 2319–7064.
- [7] Xinghua Su and Chengwen Qiang, *Bull. Mater.Sci.*, 2012, **35**(2), P. 183–189.
- [8] R.Ida Malarselvi, C.Ramachandra Raja and Priscilla. R. *International J. Science and Research (IJSR)*, **4**(1), P. 2319–7064.
- [9] K. Prasad, K. Siva Kumar, G. Prabhakar, P. Venkateswarlu. *Journal of Molecular Liquids*, 2006, **123**, P. 51–58.
- [10] M.V. Rathnam, Reema T.Sayed, Kavita R. Bhanushali, M.S.S.Kumar. *Journal of Molecular Liquids*, 2012, **166**, P. 9–16.
- [11] Philbin P, Gordon S. Recent research on the machining of wood- based composite materials. *International Journal of Machining and Machinability of Materials1*, 2006, **2**, P. 186–201.
- [12] Gokay Nemli, IsmailbAydin, Emir Zekovic. Evaluation of some of the properties of particle board as function of manufacturing parameters. *Journal of Materials and Design*, 2007, **28**, P. 1169–1176.
- [13] Cochran WG, Cox GM. *Experimental designs*. Wiley, New York, 1992.
- [14] Montgomery C., *Design and Analysis of experiments*, 4-th edition, Wiley Newyork, 1997.
- [15] Zhiming Zhang. Interval Valued Intuitionistic Hesitant Fuzzy Aggregation operators and their applications in Group Decision Making. *Journal of Applied Mathematics*, 2013, **3**, Article ID 670285, 33 pages, <http://dx.doi.org/10.1155/2013/670285>.
- [16] George J. Klir, Z. Wang. *Generalized Measure Theory*. Springer, 1998.
- [17] G. Shafer. *A Mathematical Theory of Evidence*. N.J Princeton University press, 1976.

Chemosynthesis, characterization and PEC performance of CdZn(SSe)₂ thin films by arrested precipitation technique (APT)

S. K. Jagadale, D. B. Shinde, R. M. Mane, K. V. Khot, V. B. Ghanwat, P. N. Bhosale*, R. K. Mane**

Materials Research Laboratory, Department of Chemistry, Shivaji University, Kolhapur-416004, India

*p_n_bhosale@rediffmail.com, **rmane.1970@gmail.com

DOI 10.17586/2220-8054-2016-7-3-523-527

In the present work, we have used simple, cost effective arrested precipitation technique (APT) to deposit CdZn(SSe)₂ thin films. Preparative conditions were optimized during the initial stage of experimentation to obtain good quality CdZn(SSe)₂ thin films. The as-deposited film was studied for its structural, morphological, optical, and compositional analysis by XRD, SEM, UV-Vis-NIR spectrophotometer and EDS analysis techniques respectively. XRD analysis revealed that the film was polycrystalline in nature and exhibit hexagonal crystal structure. The SEM micrograph shows the formation of spherical surface morphology. EDS results confirm the presence of Cd, Zn, S and Se elements in the synthesized thin film. The band gap value of thin film was calculated from the absorption spectra which is found to be 1.8 eV. From J-V measurements, photo-conversion efficiency is found to be 0.07%.

Keywords: arrested precipitation technique, thin films, XRD, photoconversion efficiency.

Received: 4 February 2016

Revised: 10 April 2016

1. Introduction

The II-VI compounds are becoming interesting and important because of their major applications in solar cells [1] and opto-electronic devices [2]. A variety of techniques presently used for the synthesis of cadmium and zinc chalcogenide semiconductor thin films [3–8]. In all these methods, APT is self organized, cost effective, suitable for large area deposition [9] and is presently used by us to prepare CdZn(SSe)₂ thin films. In the present investigation, we propose the synthesis, growth mechanism, optostructural, morphological, compositional and photoelectrical properties of quaternary CdZn(SSe)₂ thin films by arrested precipitation technique (APT).

2. Experimental details

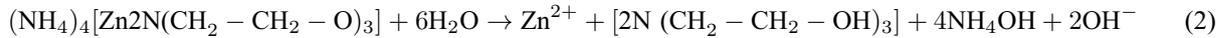
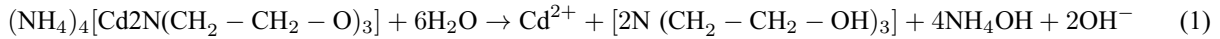
All the chemicals used in the present investigation are of AR grade and used as received without further purification. The cadmium sulfate hydrate (CdSO₄·3H₂O), zinc sulfate hydrate (ZnSO₄·7H₂O), thiourea (NH₂–CS–NH₂), and sodium selenosulfite (Na₂SeSO₃), were used as precursors for Cd²⁺, Zn²⁺, S²⁻, Se²⁻-ions. Ammonia is used to maintain pH of reaction bath and triethanolamine (TEA) was used as a complexing agent. For measuring the PEC performance, sulfide/polysulfide redox electrolyte is used. The solution of sodium selenosulfite was prepared by refluxing selenium metal powder with Na₂SO₃ at 90 °C for 9 h. Commercial glass slides and FTO were used as the substrate for thin film deposition. In the APT method, metal ions of the precursors are arrested using a stable organic complexing agent (in this case triethanolamine) in alkaline medium. All the preparative parameters such as pH of reaction bath, precursor concentration and temperature are optimized initially to 10.8 ± 0.2, 0.1 M and 55 ± 2 °C respectively, to obtain good quality thin films.

The optical absorbance was measured using UV-Visible NIR-spectrophotometer (Hitachi model 330, Japan) in the wavelength range 300 – 1100 nm. The structural analysis is done by X-ray diffraction (XRD) analysis [Bruker AXS Analytical Instruments. Model D2 PHASER] with Cu K α target for the 2 θ ranging from 10 ° to 100 °. The compositional analysis of deposited thin film was determined by energy dispersive X-ray analysis (EDS) attached to scanning electron microscope (SEM). (JEOL-JSM-6360A). J–V measurements (PEC) were recorded on semiconductor characterization instrument (SCS-4200 Keithley, Germany) using a two electrode configuration.

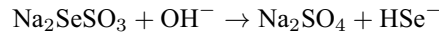
3. Results and discussion

3.1. Reaction mechanism for thin film formation

In the present investigation, we have successfully deposited CdZn(SSe)₂ thin films by arrested precipitation technique. APT is based on Ostwald ripening law [9]. The mechanism is given below. In an alkaline medium, Cd-TEA and Zn-TEA complexes slowly release Cd²⁺ and Zn²⁺-ions at pH 10.8 ± 0.2.



Na_2SeSO_3 and thiourea dissociates in an alkaline medium to produce Se^{2-} and S^{2-} ions respectively



The overall reaction is . . .



3.2. Optical study

The optical absorption was measured at room temperature for the $\text{CdZn}(\text{SSe})_2$ thin films at wavelengths ranging from 300 – 1100 nm. The linear nature of the optical absorption plot confirms the direct allowed transition and is obtained by using formula given in [9].

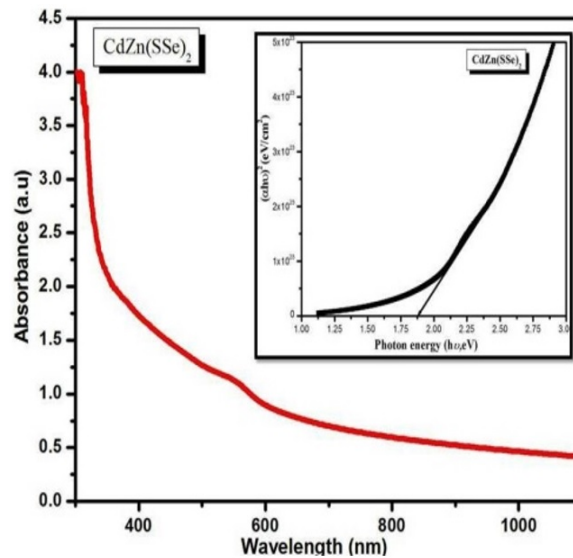


FIG. 1. Optical absorption plot and **Inset:** band gap energy plot of synthesized thin film

3.3. X-ray diffraction study

Figure 2 shows X-ray diffraction pattern of $\text{CdZn}(\text{SSe})_2$ thin film. Four peaks observed at diffraction angle of 2θ of 24.92 (100), 26.20 (100), 41.92 (110), and 71.87 (105) corresponding to 3.568, 3.396, 2.149 and 1.312 'd' values respectively. These values are matched with standard JCPDS data (card No. 80-006, 35-1469 and 77-2307). XRD data demonstrate a polycrystalline phase and a hexagonal crystal structure of $\text{CdZn}(\text{SSe})_2$ thin film. The crystallite size, calculated by using the Debye Scherer formula, was found to be 20 nm.

3.4. SEM /EDAX studies

Figure 3 shows SEM micrograph of surface morphology of $\text{CdZn}(\text{SSe})_2$ thin film which exhibits well adherent, smooth and uniform distribution of nanosphere, which cover the entire substrate surface. The average grain size is calculated by standard scale bar method, and was found to be ~120 nm. The EDS spectrum for $\text{CdZn}(\text{SSe})_2$ film is shown in Fig. 4. The EDS spectrum indicates the present peaks for the Cd, Zn, S and Se elements in the synthesized thin film. The spectrum also shows peak for platinum, which is used for coating the sample during analysis.

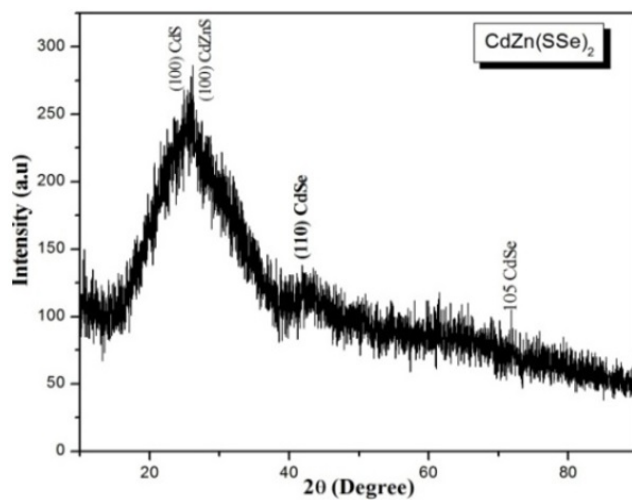


FIG. 2. X-ray diffraction pattern of CdZn(SSe)₂ thin film

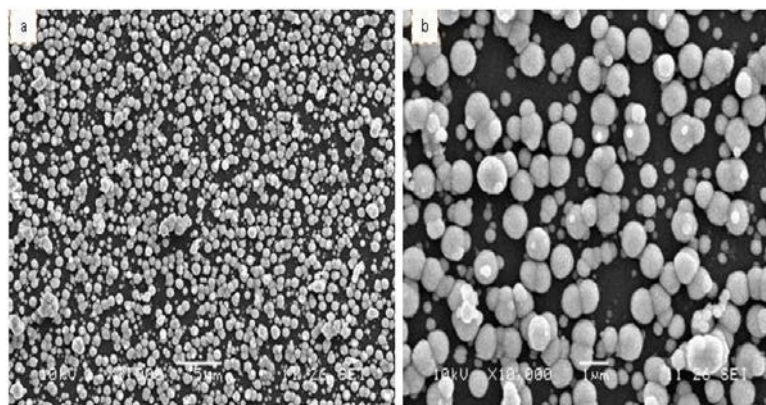


FIG. 3. SEM micrographs of CdZn(SSe)₂ thin film

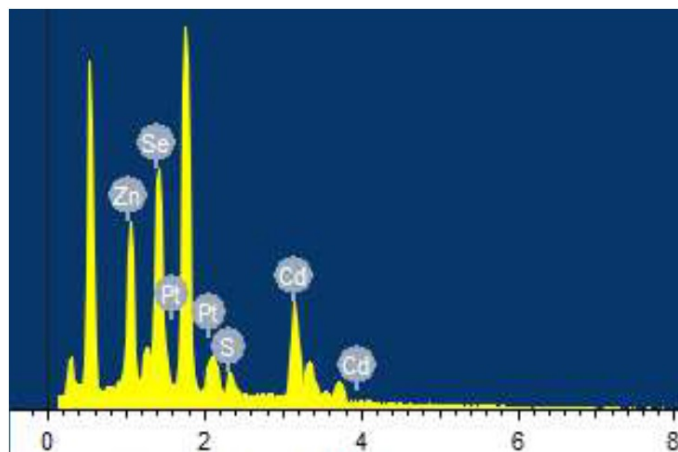


FIG. 4. EDS spectrum of CdZn(SSe)₂ thin film

3.5. Photoelectrochemical performance

The PEC performance of deposited CdZn(SSe)₂ thin film was verified using the standard two electrode configuration, both in dark and under light illumination of a 500 W tungsten filament lamp having a light intensity of 30 mW cm⁻², in sulphide/polysulphide redox electrolyte. The current density–voltage (J–V) characteristics of glass/FTO/CdZn(SSe)₂/electrolyte/graphite were measured. J–V characteristic curve of CdZn(SSe)₂ thin film in dark display diode-like rectifying characteristics. Upon illumination, the magnitude of the open circuit voltage (V_{oc}) increases with negative polarity towards the CdZn(SSe)₂ electrode, indicating cathodic behavior and which confirms that CdZn(SSe)₂ thin film is p-type. The output parameters of the PEC solar cell, i.e. light conversion efficiency (η%) and fill factor (FF), were calculated from eqn (6) and (7), respectively:

$$FF = \left(\frac{J_{max} X V_{max}}{J_{sc} X V_{oc}} \right) \quad (6)$$

$$\eta\% = \left(\frac{J_{sc} X V_{oc}}{P_{in}} X FF X 100 \right), \quad (7)$$

where J_{sc} is the short-circuit current density and V_{oc} is the open circuit voltage. J_{max} and V_{max} are the maximum current density and the maximum voltage, and P_{in} is the input light intensity (30 mW cm⁻²). From the J–V measurements, the obtained values for J_{sc} , V_{oc} and FF for the sample are 0.1917 mA cm⁻², 457.2 mV and 0.27 respectively. The resultant conversion efficiency for the synthesized thin film is 0.07 %.

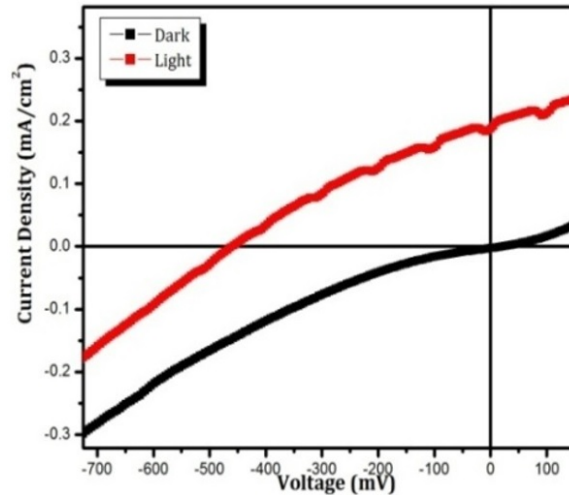


FIG. 5. J–V measurement curve of CdZn(SSe)₂ thin films

4. Conclusions

The arrested precipitation technique is found to be the most convenient method for the deposition of metal chalcogenide thin films. Optical band gap energy value was found to be 1.87 eV. The XRD study revealed the polycrystalline nature with pure hexagonal crystal structure of the CdZn(SSe)₂ thin film. The SEM micrograph shows that the spherical grain structure of the surface without any pinholes. EDS results confirm the presence of Cd, Zn, S and Se elements in the synthesized thin film. The J–V measurement curve showed the efficiency of CdZn(SSe)₂ film to be 0.07 %. This revealed that CdZn(SSe)₂ thin films deposited by APT technique, showed potential as candidates for solar cell applications.

References

- [1] Chavan S., Sharma R., New trends to grow the n-CdZn(S_{1-x}Se_x)₂/p-CuIn(S_{1-x}Se_x)₂ heterojunction thin films for solar cell applications. *Sol. Energ. Mat. Sol. Cells*, 2006, **90**(9), P. 1241–1253.
- [2] Sharma M., Kumar S., Sharma L. M., Sharma T. P., Husain M., CdS sintered films: growth and characteristics. *Physica B: Condensed Matter*, 2004, **348**, P. 15–20.
- [3] Chandramohan R., Mahalingam T., Chu J.P., Sebastian P.J., Preparation and characterization of semiconducting Zn_{1-x}Cd_xSe thin films. *Sol. Energ. Mat. Sol. Cells*, 2004, **81**, P. 371–378.
- [4] Chavhan S.D., Senthilarasu S., Lee S.H., Annealing effect on the structural and optical properties of a Cd_{1-x}Zn_xS thin film for photovoltaic application. *App. Surf. Sci.*, 2008, **254**, P. 45439–45445.

- [5] Ilican S., Zor M., Caglar, Y., Caglar M., Optical characterization of the CdZn(S_{1-x}Se_x)₂ thin films deposited by spray pyrolysis method. *Optica Applicata*, 2006, **36** (1)
- [6] Pathan H.M., Lokhande C.D., Deposition of metal chalcogenide thin films by successive ionic layer desorption and reaction (SILAR) method. *Bull. Mater. Sci.*, 2004, **27**, P. 85–111.
- [7] Subbaiah Venkata Y.P., Pratap P., Reddy Ramkrishna K.T., Miles R.W., Yi J., Studies on ZnS_{0.5}Se_{0.5} buffer based thin film solar cells. *Thin solid films*, 2008, **516**, P. 7060–7064.
- [8] Bagade C.S., Mali S.S., Ghanwat V.B., Khot K.V., Patil P.B., Kharade S. D., Mane R.M., Desai N.D., Hong C.K., Patil P.S., Bhosale P.N. A facile and low cost strategy to synthesize Cd_{1-x}Zn_xSe thin films for photo electro chemical performance: effect of zinc content. *RSC Adv*, 2015, **5**, P. 55658–55668.
- [9] Khot K.V., Mali S.S., Pawar N.B., Kharade R.R., Mane R.M., Kondalkar V.V., Patil P.B., Patil P.S., Hong C.K., Kim J.H., Heo J., Bhosale P.N. Development of nanocoral-like Cd(SSe) thin films using an arrested precipitation technique and their application. *New J.Chem*, 2014, **38**, P. 5964–5974.

Experimental investigation of quenching behavior of heated zircaloy rod in accidental condition of nuclear reactor with water and water based nanofluids

A. S. Chinchole, P. P. Kulkarni, A. K. Nayak

Reactor Engineering Division, Bhabha Atomic Research Centre, Trombay Mumbai 400085, India

chinchole@barc.gov.in, parimalk@barc.gov.in, arunths@barc.gov.in

PACS 87.85.Rs

DOI 10.17586/2220-8054-2016-7-3-528-533

The physical phenomena of rewetting and quenching are of prime importance in nuclear reactor safety in the event of Loss of Coolant Accident (LOCA). In such a case, the fuel pins become dry hot. Under this condition, cold water is injected from emergency core cooling system (ECCS). The quenching behavior of such heated rod bundle (re-flood heat transfer behavior) is quite complex. It is well known that Nanofluids have better heat removal capability and a high heat transfer coefficient owing to their enhanced thermal properties. Recent investigations have shown that the addition of the Al_2O_3 nanoparticles result in better cooling capabilities as compared to the traditionally used quenching media. In this context, the authors have carried out experiments on quenching behavior of hot zircalloy tube with water and nanofluids as stated above. Quenching of the tube was observed to occur within few seconds in both the cases in the presence of decay heat. It was also observed that the nanofluids showed slightly reduced quenching time as compared to water.

Keywords: Rewetting, quenching, Al_2O_3 nano-fluids, zircaloy tube.

Received: 4 February 2016

Revised: 10 April 2016

1. Introduction

Quenching still remains one of the most widely used industrial heat treatment processes. This means the rapid cooling of high temperature materials mainly in demineralised (DM) water, oil and molten salt or polymer solution baths, which is frequently encountered in various engineering applications, such as heat treatments of steel, safety of nuclear reactors, and the rapid solidification processing. Thus, an acceleration of the transition from film boiling to nucleate boiling is often desirable, as it results in a much higher heat transfer rate. A new type of quenching media has recently been developed and today world's leading scientific institutions are conducting research to find out more about this medium called nanofluid. Nanofluids are colloidal suspensions of stably dispersed nanoparticles in base fluids. The term was first introduced by Das et al. [1] in 1995. Nanoparticles dispersed in base fluid can be metal oxides, such as CuO , Al_2O_3 and TiO_2 [2–5] and for base fluid, most commonly deionized or fresh water is used. Today there is no exact confirmed theoretical background available that would explain all nanofluid properties. Nevertheless, the use of nanofluids as a heat transfer medium has gained a lot of momentum. Nanofluids are of interest to a variety of industry branches due to a wide range of possible applications such as heat transfer applications, automotive, electronics and biomedical applications. At MIT [3] quenching of steel and zircaloy spheres in nanofluids with 0.1 % Al_2O_3 was studied. They reported that the main reason for quenching acceleration is the surface roughness increase and the wettability enhancement due to nanoparticle deposition. They observed a thin layer of nanoparticles on sphere surface. Therefore, the deposition of nanoparticles prevented the formation of vapor film and resulted in quick quenching of the hot sphere.

Buongiorno and Hu [5] studied the boiling behavior of nanofluids, prominently CHF limit and quenching phenomena. The nanoparticle deposition layer was found to increase the surface roughness and wettability, both of which could be linked to CHF enhancement and quenching acceleration. Kim et al. [3] observed that nanoparticles dispersed in the fluid at low concentration (< 0.1 %) did not change the quenching process. Nanoparticles deposited on the rodlet surface are responsible for accelerated quenching. The quenching acceleration strongly depends on the material used for nanoparticle. Ciloglu and Bolukbasi [6] investigated the quenching behavior of aqueous nanofluids containing various volume fractions of Al_2O_3 , SiO_2 , TiO_2 and CuO nanoparticles around high temperature brass rod experimentally. They observed that after the repetition tests in nanofluids, a nanoparticle porous layer occurs on the quenched surface and thus the film boiling vanishes. The results show that contact angle decreases and surface roughness increases. They concluded that the primary reason of CHF enhancement is the change of the surface characteristics due to the porous layer. Application of nanofluids as quenching media in quenching process was also tested experimentally in 2004 by Das et al. [7]. High temperature copper spheres were quenched in alumina nanofluids in order to investigate the effect suspended nanoparticles on film boiling heat

transfer characteristic. Even though high particle concentrations were used, from 5 to 20 vol.%, nanofluids showed lower boiling heat transfer rate than pure DM water. More important, the experiments conducted on a previously quenched sphere resulted in a much more rapid process compared to quenching of a clean sphere.

Whereas most of the work has been cited on spheres, much less work has been carried out on rods, that too generating decay heat which is of a concern from nuclear safety. In this work, the authors have carried out experiments on the quenching behavior of hot zircalloy tube with DM water and metal oxide nanofluids as above. Tube quenching was observed within a few seconds, even with the presence of decay heat.

1.1. Quenching process

In the quenching process, the hot components are cooled down to room temperature by immersion into a liquid, spraying with a liquid or by pouring over a liquid (i.e. quench media). The quenching medium can be DM water, oils and aqueous polymer solutions, nanofluids etc. Before a component is quenched, it is heated to a uniform temperature and then is rapidly cooled by the cooling medium. During this process, thermal stresses are developed due to a high temperature gradient in the material. Residual stresses remaining in the material are undesirable because they may cause unpredictable distortions and have a deleterious effect on fracture and corrosion performance.

The quenching process is a complex thermodynamic and fluid dynamic problem consisting of several different phases. If the quenching media is vaporizable liquid, four modes of cooling can be observed: i) shock film boiling, ii) full film boiling, iii) nucleate boiling and iv) convection cooling mode (Fig. 1). Each of these modes is characterized by different surface heat transfer coefficients (HTC) and cooling rates.

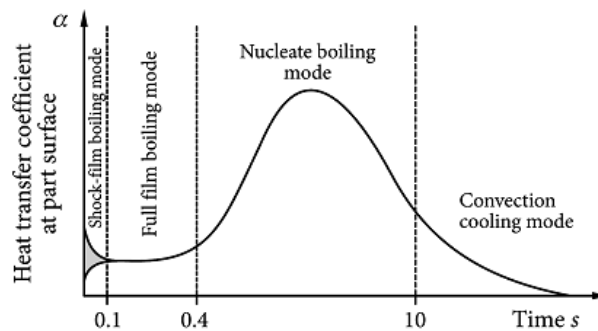


FIG. 1. Different types of cooling at quenching process

1.2. Experiment on quenching with hot zircalloy rod

This system is designed to study the clad performance during Emergency Core Cooling System (ECCS) activation in a nuclear reactor during Loss of Coolant Accident (LOCA) scenario when cold DM water is injected over hot clad surface. During ECCS injection, DM water is sprayed onto the hot rod in the form of a jet only from front direction. The objectives of these experiments are to determine the extent of quenching with presence of decay heat, study the radial temperature variation in the tube and study the extent of enhancement on quenching by use of nanofluids.

2. Experiments conducted

2.1. Experimental setup

The experimental setup is as shown in Fig. 2. Two concentric stainless steel pipes 50 NB (Sch. 30) and 40 NB (Sch. 30) form the vessel. The inner pipe has been perforated, with 1.5 mm diameter holes along the length having 10 mm linear pitch and 450 angular pitch, to allow DM water and nanofluids to inject over the tube surface. The hollow zircalloy tube (16 OD, 0.5 mm thick) is placed at the center of the vessel. The gap between inner perforated pipe and zircalloy tube is 12.9 mm. A small uniform gap of 2.86 mm has been maintained in the annular space so that DM water and nanofluids jets attain sufficient velocity to reach hot zircalloy tube surface. Both pipes are welded to two 150 lbs blind flange at either ends. Two nickel plugs are used to connect the zircalloy tube to power supply for direct resistance heating. Two central 'through' hole have been provided on the Nickel plug to vent out air from the Zircalloy tube which expands due to heating. Vent holes of 5 mm diameter (4 Nos.) are provided on the top flange to release steam along with hydrogen generated (if any) and air during the experiment.

DM water and nanofluids will be supplied from radial direction with four inlet pipes (10 NB) on the outer pipe in to the annular space at a location near top of the set up and the same will be collected in to the drain at the bottom after impinging over hot zircalloy tube surface. The whole setup will be supported at a distance of 45 mm from the ground. The tube was equipped with K type SS sheathed thermocouple of 1.5 mm diameter brazed at different axial and locations along the length at uniform spacing of 30 mm. Thermocouples are also brazed on the diagonally opposite location on the surface behind the spray nozzle location. Tube Surface temperature was measured over the total heated length. All these measurements will be recorded by a portable recorder at a span of 125 ms.

Figure 3 shows the location of thermocouple position on the zircalloy tube in the experimental setup. Each thermocouple was situated within a specific location on surface of the zircalloy tube.

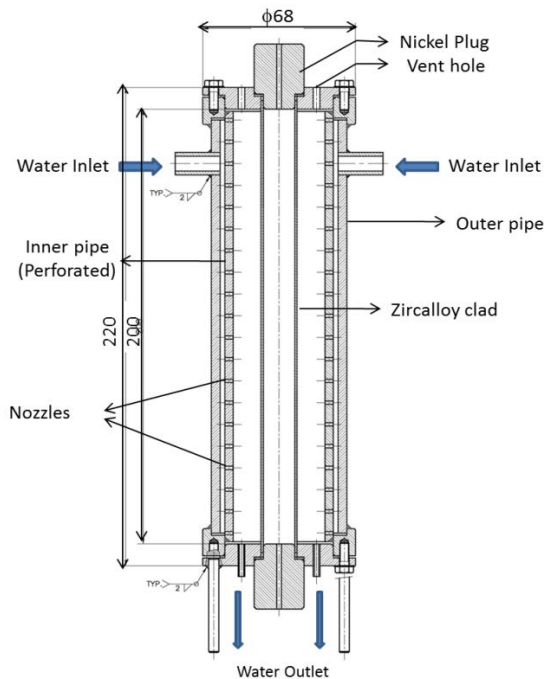


FIG. 2. Experimental setup

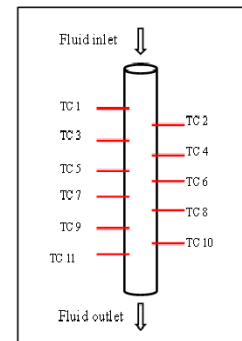


FIG. 3. Thermocouple position on zircalloy tube

2.2. Experimental procedure for nanofluids

In the present experiment, the zircalloy tube was heated gradually in a stepwise manner from ambient temperature to a maximum temperature of 650 °C. The tube was maintained at the required temperature for 3 minutes and then DM water was injected through a flexible inlet pipe using a pump with a constant flow rate of 10 lpm. Initially, the experiment was carried out with DM water. The experiment was repeated with Al₂O₃ nanofluid of different concentrations to check the quenching phenomena for zircalloy tube with Al₂O₃ nanofluids.

2.3. Preparation and characterization of nanofluids

An aqueous solution of nanofluids was prepared by adding desired concentration (by weight) of Al₂O₃ (Alumina) nanopowder of particle size 10 – 100 nanometer and 99.7 % purity to the DM water. The reason for using Al₂O₃ nanoparticle is the fact that the thermo-physical characteristics of the base fluid (DM water) is most widely known and the thermal properties of DM water – Al₂O₃ nanofluids for different particle concentration have already been studied [7]. To prevent the particles from agglomerating and settling, the suspension was sonicated in an ultrasonic bath. The dispersion of the particles was first done by mixing the required volume of powder in a chemical measuring flask with DM water and then using ultrasonication with frequency 50 Hz and power of 120 W. After making a proper mixture, the flask was kept again under ultrasonic treatment for about 4 h, which is a sufficient time to ensure stable particle dispersion in DM water without agglomeration [8]. The size of nanoparticles in powder form was characterized by transmission electron microscope (TEM). After preparing the

nanofluid, it was poured in the storage tank of the apparatus and the experiment was repeated for nanofluids with different concentrations.

The nano fluid is used immediately after its preparation so as to avoid any issue regarding its stability. Since the wt. % of nanoparticle used in the preparation of nanofluids is very small, the agglomeration begins only after 24 hours of its preparation.

3. Results and discussion

The following are the Transmission Electron Microscopic images of Al₂O₃ nanoparticles before and after the quenching process.

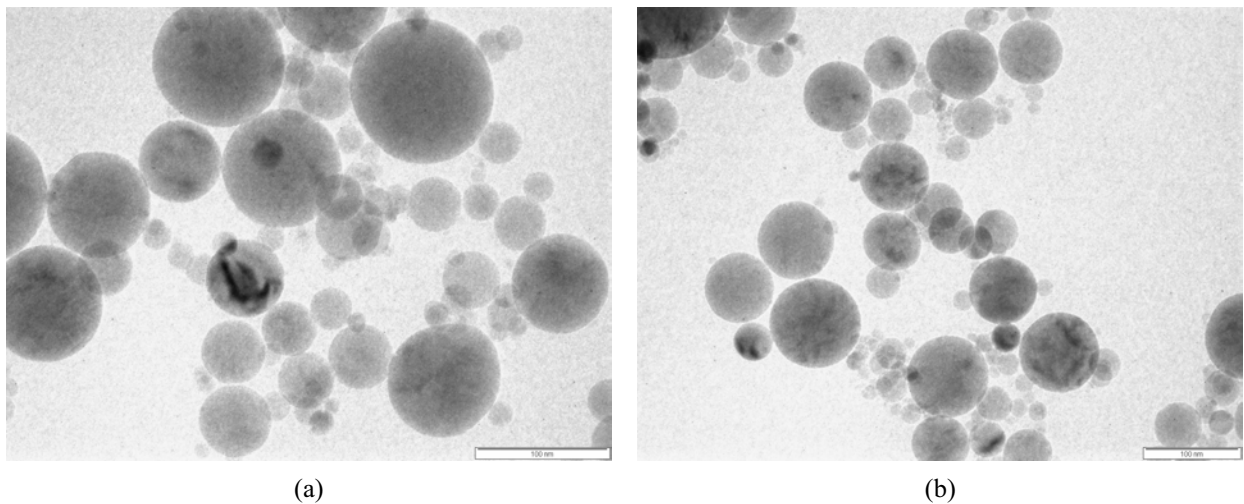


FIG. 4. TEM images of Al₂O₃ Nanofluids (a) before Injection, (b) after injection

Figure 4 shows that TEM images, having resolution of 100 nm, reveal that there is no change in the size of Al₂O₃ nano particles before and after their injection in the test apparatus for the quenching experiment.

Figure 5 shows the quenching data with DM water. All thermocouples showed rapid quenching from about 650 °C to DM water ambient temperature within 15 s period. There is slight delay in onset of quenching of thermocouples TC7 and TC11. This is due to the fact that, they are located diametrically opposite on the tube from the entry of DM water. However, complete quenching is eventually observed.

Figure 6 shows the quenching data with 0.01 wt.% Al₂O₃ nanofluids. All thermocouples showed rapid quenching from about 650 °C to DM water ambient temperature within a 15 s period. There is slight delay in

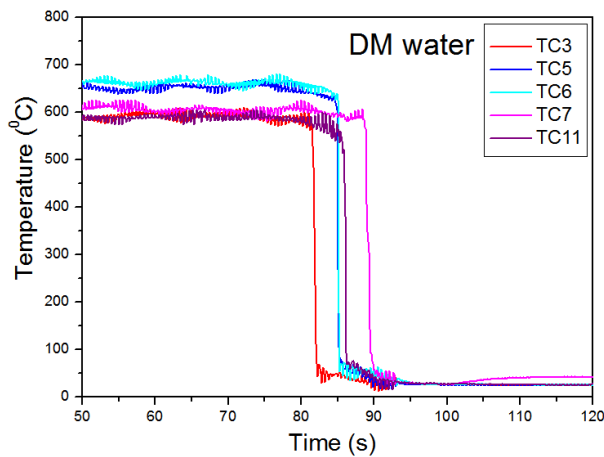


FIG. 5. Quenching time for DM DM water

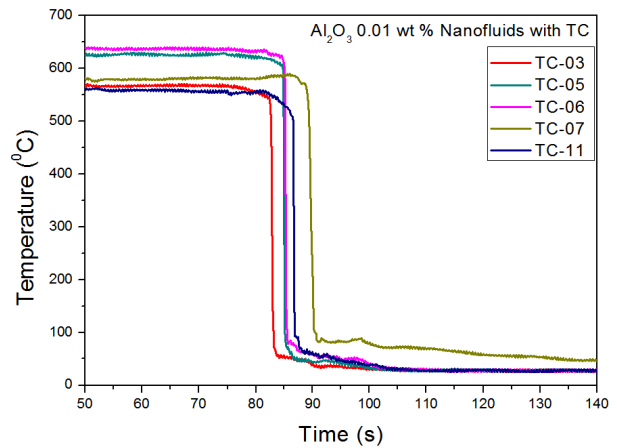


FIG. 6. Quenching time for 0.01 wt.% Al₂O₃ Nanofluids on all TC

onset for the quenching of thermocouples TC7 and TC11. This is due to the fact that, they are located diametrically opposite on the tube from the entry of DM water. However, complete quenching is eventually observed.

Figure 7 shows the quenching data with DM water & Al_2O_3 nanofluids with different concentrations at location TC-1. Since TC-1 is near the top surface, there is heat loss which reduces the maximum temperature to about 650 °C. It is seen that rapid quenching from about 650 °C to water ambient temperature within 15 s period. Complete quenching was observed for different concentrations of nanofluids. Different concentrations of nanofluids showed different rates of quenching, based on the particles' concentration as compared to DM water. Figure shows that the zircaloy tube became quenched slightly faster by using nanofluids as compared to the DM water. All the temperature profiles depended upon the thermocouple position of the zircaloy tube.

Figure 8 shows the temperatures on the tube at axially different positions. TC 11, which is at the bottom, was shown to be quenched very quickly due to the fact that the DM water is accumulated at the bottom first. TC 7, which is opposite in the middle of the tube, takes almost an additional 10 s for quenching which is the delay that caused the slight rise in temperature. Nevertheless, there is no increase in temperature and complete quenching is observed.

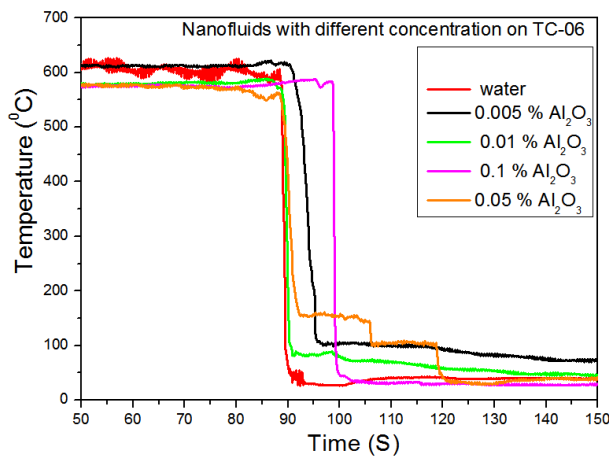


FIG. 7. Quenching time for Al_2O_3 nanofluids with different concentration on TC 6

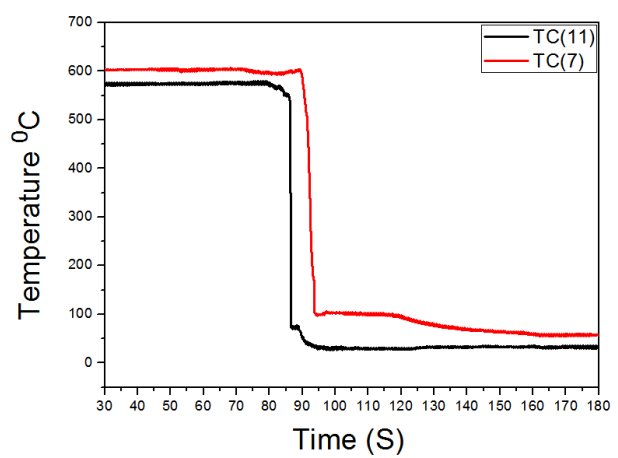


FIG. 8. Comparison between front & backside thermocouple

Figure 9 shows the difference in onset of quenching because of location. The thermocouple located at the diametrically opposite position shows quenching after delay of about 30 s. This is due to the fact that, when the DM water is sprayed from front, the thermocouple located there shows immediate quenching. However, the backside thermocouple quenches only when the sprayed DM water falls down and fills the entire cavity which introduces certain delay. But nevertheless, there is complete quenching of the tube.

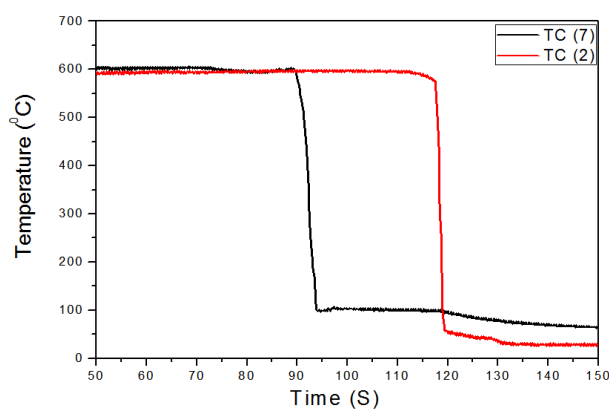


FIG. 9. Frontside & backside thermocouple in experimental facility

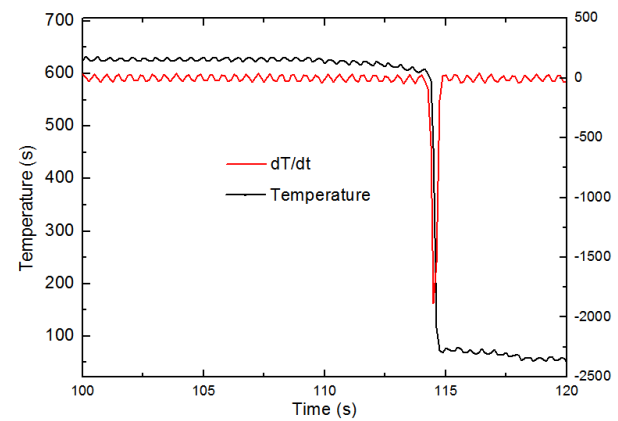


FIG. 10. Quenching time for Al_2O_3 nanofluid

In order to measure the exact quenching time, the rate of change of temperature was plotted as shown in Fig. 10. There, a sharp change in the slope can be seen for the temperature at the onset and completion of quenching. The difference between these two readings gives an accurate measure of quenching time.

Quenching times varied from 0.6 s to 0.9 s for all the fluids, as shown in Fig. 11. The quenching times for nanofluids were shown to be marginally reduced. It is seen that at lower concentrations, the quenching times are less, however at higher concentrations, there is a slight increase in the quenching time. The reason can be attributed to formation of a nanolayer on the rod. A similar process occurs during boiling in nanofluid [9]. At lower concentrations, there is a fine layer formation, which assists the wetting of the rod and thus reduces the quenching time. At higher concentrations, there is a thick nanolayer formation, which changes the wetting characteristics of the rod which in turn delays the quenching. Nevertheless, the thick nanolayer has better wetting characteristics than the bare rod.

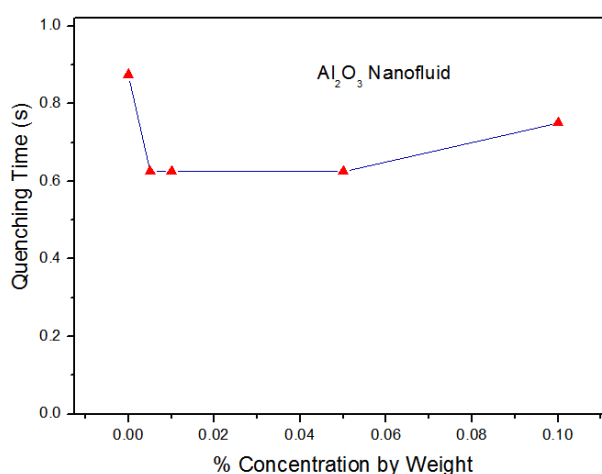


FIG. 11. Quenching time for Al₂O₃ nanofluid

4. Conclusions

In this work, quenching behavior of hot zircalloy tube was studied. It was observed that, even with the presence of decay heat, the tube was quenched within a short period of time. Quenching behavior was shown to be more or less similar for all the fluids, however, nanofluids did exhibit slightly reduced quenching times.

References

- [1] Das S.K., Choi S.U.S., Yu W., Pradeep T. *Nanofluids: Science and Technology*. John Wiley & Sons, Inc., Hoboken, New Jersey, 2008.
- [2] Kim H., Kim J., Kim M. Experimental study on CHF characteristics of DM water-TiO₂ nano-fluids. *Nuclear engineering and technology*, 2006, **38** (1), P. 61–68.
- [3] Kim H., DeWitt G., et al. On the quenching of steel and zircaloy spheres in DM water-based nanofluids with alumina, silica and diamond nanoparticles. *International Journal of Multiphase Flow*, 2009, **35**, P. 427–438.
- [4] Kim H., Buongiorno J., Hu L., McKrell T. Nanoparticle deposition effects on the minimum heat flux point and quench front speed during quenching in DM water-based alumina nanofluids. *International Journal of Heat and Mass Transfer*, 2010, **53**, P. 1542–1553.
- [5] Buongiorno J. et al. A benchmark study on the thermal conductivity of nanofluids. *Journal of Applied Physics*, 2009, **106**, P. 094312 (14 p.).
- [6] Ciloglu D., Bolukbasi A., Comakli K. Effect of Nanofluids on the Saturated Pool Film Boiling. *World Academy of Science, Engineering and Technology*, 2012, **6**, P. 7–29.
- [7] Park H.S., Shiferaw D., et al. Film boiling heat transfer on a high temperature sphere in nanofluid. *Proceedings of 2004 ASME Heat Transfer/Fluids Engineering Summer Conference*, 2004, P. 1–8NC.
- [8] Das S.K., Putra N., Thiesen P., Roetzel W. Temperature dependence of thermal conductivity enhancement for nanofluids. *Journal of Heat Transfer – Transactions of the ASME*, 2003, **125**, P. 567–574.
- [9] Nayak A.K., Kulkarni P.P., Chinchole A.S. Experimental Investigation on Pool Boiling Critical Heat Flux with Nanofluids. *Journal of Nanofluids*, 2015, **4**, P. 140–146.

Effect of surfactant concentration and solvent used for washing in the preparation of Yb:Y₂O₃ transparent ceramics

Pratik Deshmukh*, S. Satapathy**, M. K. Singh, P. K. Gupta

Nano Functional Materials Laboratory, Laser Materials Development & Devices Division,
Raja Ramanna Centre for Advanced Technology, Indore 452013, India

*ppdeshmukh@rrcat.gov.in, **srinu73@rrcat.gov.in

PACS 81.20.Ev; 78.67.Bf; 42.70.Hj

DOI 10.17586/2220-8054-2016-7-3-534-537

Nanoparticles of Yb:Y₂O₃ have been synthesized by co-precipitation synthesis routes. The (NH₄)₂SO₄ surfactant was added to Y(OH)₃ precipitate during synthesis to control the size, morphology, agglomeration and phase of nanoparticles. The dried precipitates were calcined at 900 °C to obtain the desired cubic phase Yb:Y₂O₃ nano particles. In the present study we reported the effects of surfactant concentration on size, morphology, agglomeration and phase of Yb:Y₂O₃ nanoparticles. However the addition of surfactant is not enough to get non-agglomerated nanoparticles. The extracted precipitate should be washed in proper solvent to avoid formation of hard agglomerate during drying. Hence the effects of washing solvent (i.e. water and methanol) on agglomeration and transparency were also reported. The transparency of the sintered pellets, prepared by varying the surfactant concentration and washing solvent, was evaluated. A transparency of ~ 80 % at 1500 nm was achieved in 1 mm thick Yb:Y₂O₃ ceramic pellet by optimization of the surfactant and washing solvent.

Keywords: transparent ceramics, Yb:Y₂O₃, surfactant.

Received: 4 February 2016

1. Introduction

Nanotechnology and sintering techniques can be utilized in combination for the fabrication of rare earth-doped yttria transparent ceramics because the high surface area of the nanoparticles facilitates sintering, permitting one to reach full density more rapidly at temperatures far below the melting point of the material [1,2]. The fabrication of Yb doped Y₂O₃ transparent ceramic involves the synthesis of non-agglomerated nanoparticles of Yb doped Y₂O₃ and sintering of pressed pellets (prepared using a nanopowder) at high temperatures under low pressure [3]. Of the different methods adopted for the preparation of non-agglomerated nanoparticles, the co-precipitation method has been widely used for nanopowder synthesis because the particle size and morphology can be efficiently controlled [4].

However, in case for the synthesis of Yb:Y₂O₃ nanopowders using co-precipitation method, the Y(OH)₃ precipitate underwent severe agglomeration during drying. This agglomeration led to poor sinterability for the Yb:Y₂O₃ nanopowder obtained after calcination. Thus, special measures were adopted during precipitation, such as addition of surfactant to create non-agglomerated nanoparticles. It is reported that the surfactant (NH₄)₂SO₄, which adsorbs on the surface of the Y(OH)₃, hinders the bonding between particles [5,6]. It has also been shown that the morphology of precursors was affected by the [(NH₄)₂SO₄]/[Nd:Y₂O₃] ratio (measured by weight) [7]. However, the effect of surfactant concentration on the crystallographic phase of the prepared nanopowder has not been investigated yet. Similarly, the solvent used to wash the precipitate plays a crucial role in the agglomeration of nanoparticles. Some solvents remove the surfactant from the particle surface and cause hard agglomeration during drying of precipitate [8]. The chemical nature of the washing solvent may be different for dissimilar oxide nano particles.

Thus, the aim of this work is to study the effect of surfactant concentration on the size, morphology, agglomeration and phase of Yb:Y₂O₃ nanoparticles obtained using the co-precipitation method as well as its influence on the transparency of sintered pellets incorporating these nanoparticles. The effect of the solvent used for washing the precipitate on the transparency of the pellet is also evaluated.

2. Experimental

A 0.2 M mother solution of Yb doped (1 mol%) Y₂O₃ (using Yb₂O₃ and Y₂O₃ powders of purity 99.99 %; make: Alfa Aesar) was prepared by dissolution with dilute nitric acid. The mother solution was titrated with 1 M aq. ammonia by normal striking. A white jelly like basic Yb:Y(OH)₃ precipitate was formed during the titration which was controlled by measuring online pH. After aging, the hydroxide precipitate was divided into five equal parts. In order to investigate the effects of surfactant concentration on the transparency of sintered Yb:Y₂O₃ pellets, (NH₄)₂SO₄ surfactant having 5, 10, 15, 20 and 30 wt% concentration was added to each part of the precipitate separately i.e. 5 wt% of (NH₄)₂SO₄ solution were added into first part of hydroxide precipitate and so

on. Then, the samples were washed using methanol and dried in an oven. Calcination was performed at 900 °C for 4 h in air. Then, the calcined powders were pressed under a pressure of 150 MPa using a uniaxial press. To show only the effect of morphology and particle size distribution on pellet's transparency, a cold isostatic press (CIP) was not used for pellet pressing. The pellets were sintered at 1750 °C for 5 h using a high temperature high vacuum furnace with a tungsten mesh heating element (Hind High Vacuum High Temperature Furnace, Hind High Vac. Co (P). Ltd., Bangalore). Finally, the pellets were polished using 300 nm alumina powders. Phase identifications of the Yb (1 mol%):Y₂O₃ nanopowders prepared using different surfactant concentrations were performed using X-ray diffractometry (XRD) (Cu-K α , Rigaku) and morphology was observed by field emission scanning electron microscope (FESEM, Zeiss).

3. Results and discussion

X-ray diffraction (XRD) patterns of Yb(1 mol%):Y₂O₃ powders prepared using different surfactant concentrations are shown Fig. 1. The XRD patterns of these powders are in good agreement with that of Y₂O₃ (Standard JCPDS, Card no. 41-1105) crystal [9, 10]. The results revealed that the precursor transformed to cubic phase of Y₂O₃ crystals after calcination at 900 °C for 5 wt% and 10 wt% of surfactant concentration but for 15 wt% and above surfactant concentrations, it transforms to a mixed phase i.e. combination of cubic and monoclinic phase Y₂O₃ crystal. The reflection from the monoclinic phase (space group C2/m) (Y₂O₃: PDF 44-0399) appeared in the diffraction patterns for 15, 20 and 30 wt% surfactant concentration as shown in Fig. 1 [10].

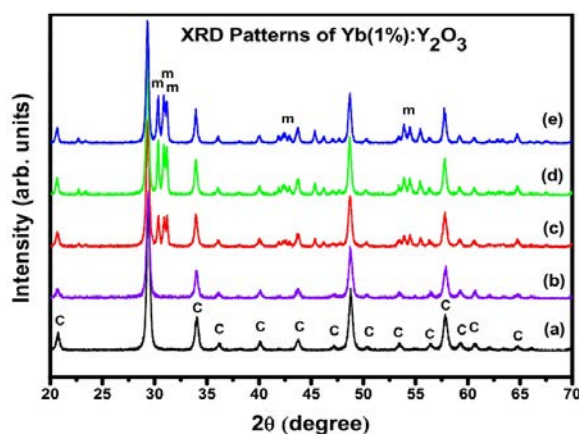


FIG. 1. X-ray diffraction patterns of Yb (1 mol%):Y₂O₃ nanopowders prepared using different surfactant concentrations: (a) 5 wt%, (b) 10 wt%, (c) 15 wt%, (d) 20 wt % and (e) 30 wt%

Scanning electron micrographs of Yb (1 mol%):Y₂O₃ powder prepared using different surfactant concentrations are shown in Fig. 2. The morphologies of the Yb (1 mol%):Y₂O₃ nanoparticles are nearly spherical and are unchanged with variation in surfactant concentration. The existence of SO₄²⁻ on the surface of yttrium hydroxide precursors at comparatively high temperature inhibits volume diffusion and/or grain boundary diffusion, and then particle growth proceeds by surface diffusion or evaporation-condensation, which results in collapse of agglomerates into well-dispersed nanopowders [12].

Photographs of sintered pellets of Yb (1 mol%):Y₂O₃ prepared using different surfactant concentrations i.e. (a) 5 wt%, (b) 10 wt%, (c) 15 wt%, (d) 20 wt% and (e) 30 wt% are shown in Fig. 3. As is clearly visible, the transparency of the sample (a) and (b) is so good, as to allow the easy reading of the underlying print, however, the transparency does seem to be decreased at higher surfactant concentrations. This may be due the transformation of the phase from cubic to a mixed one (as evident from Fig. 1).

Figure 4 shows the photograph of sintered pellet of Yb (1 mol%):Y₂O₃ prepared by using 5 wt% concentration of surfactant and water as the washing solvent. The simple change in washing solvent from methanol to water during synthesis would appear to lead to a drastic decrease in the transparency of the sintered Yb (1 mol%):Y₂O₃ pellet. This is due to the formation of high strength agglomerates after washing with the liquid having higher surface tension like water (greater than methanol) [13].

Using the above experimental conditions, we have successfully fabricated highly transparent Yb (1 mol%):Y₂O₃ ceramics pellets (transparency ~ 80 % in visible-IR region without considering Fresnel's reflection).

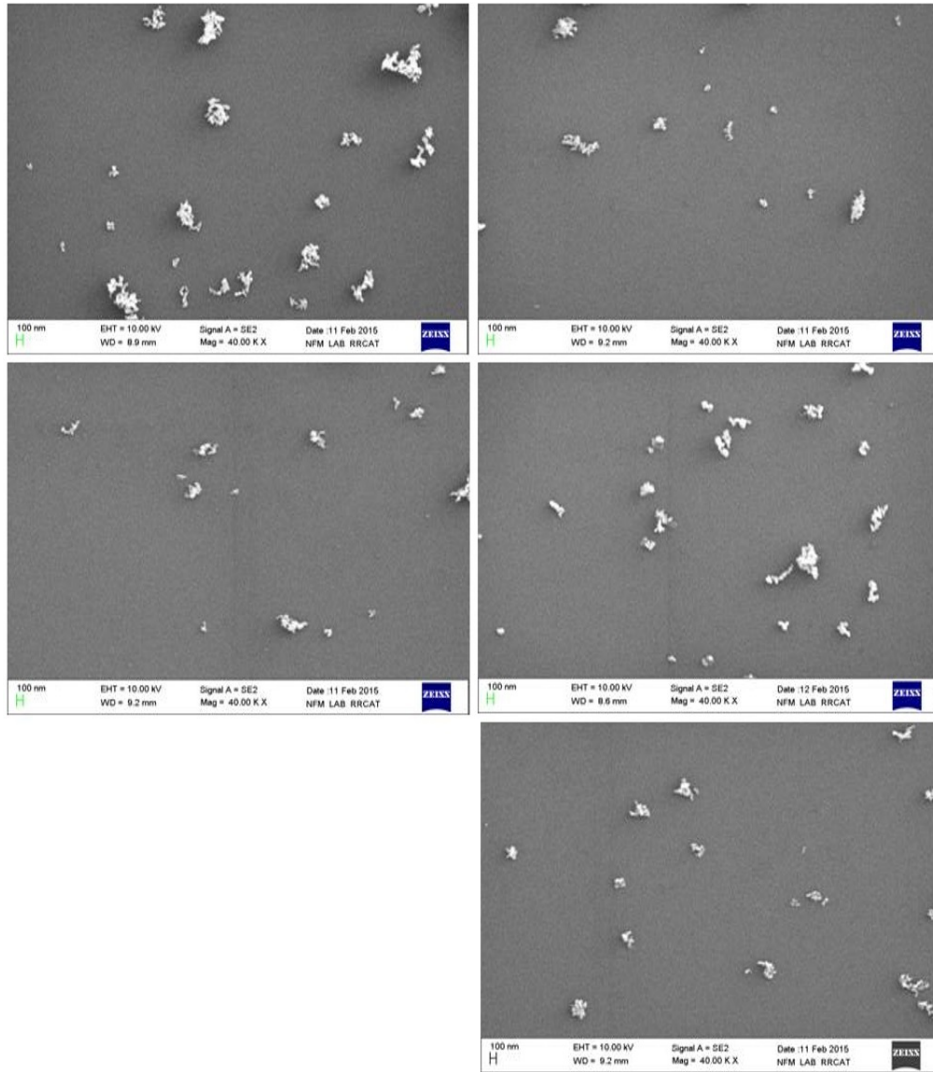


FIG. 2. FESEM images of Yb (1 mol%): Y_2O_3 nano powders prepared using different surfactant concentrations: (a) 5 wt%, (b) 10 wt%, (c) 15 wt%, (d) 20 wt% and (e) 30 wt%



FIG. 3. Photograph of sintered pellets of Yb(1 mol%): Y_2O_3 prepared using different surfactant concentrations: (a) 5 wt%, (b) 10 wt%, (c) 15 wt%, (d) 20 wt% and (e) 30 wt%



FIG. 4. Photograph of sintered pellet of Yb(1 mol%): Y_2O_3 prepared using 5 wt% of surfactant concentration and water as the washing solvent

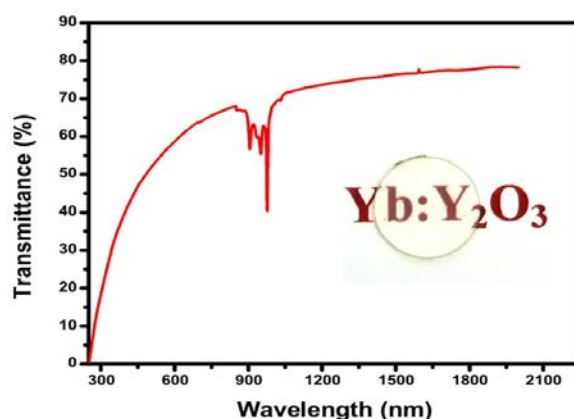


FIG. 5. Optical transmittance spectrum of a sintered pellet of Yb (1 mol%): Y_2O_3 and inset shows the photograph of transparent ceramic

4. Conclusion

The use of surfactant $(NH_4)_2SO_4$ during the synthesis of nanoparticles is helpful to control particle size and agglomeration. The excess concentration of it does not affect the particle morphology. Hence, the sinterability (which mainly depends on the size, agglomeration and morphology of the particles) of the all samples (prepared using different $(NH_4)_2SO_4$ concentrations) would remained same. Thus, the observed difference in transparency of Yb (1 mol%): Y_2O_3 sintered pellets is due to transformation of the phase from cubic to mixed (i.e. combination of cubic and monoclinic phase). Additionally, the surface tension of washing solvent affects the agglomeration during drying of the precipitate. The optimized synthesis parameters for Yb: Y_2O_3 nanoparticles i.e. 5 wt% surfactant concentration and methanol as washing solvent have been used to successfully fabricate highly transparent Yb (1 mol%): Y_2O_3 ceramics pellets.

References

- [1] Lu J., Lu J., et al. Nd^{3+} : Y_2O_3 ceramic laser. *Japanese Journal of Applied Physics*, **40**(2001), P. L1277–L1279.
- [2] Shirakawa A., Akaichi K., et al. First mode-locked ceramic laser: femtosecond Yb^{3+} : Y_2O_3 ceramic laser. *Laser Physics*, 2004, **14**(11), P. 1375–1381.
- [3] Ikegami T., Mori T., et al. Fabrication of Transparent Yttria Ceramics through the Synthesis of Yttrium Hydroxide at Low Temperature and Doping by Sulfate Ions. *J. Ceram. Soc. Jpn.*, Int. Ed., 1999, **107**(3), P. 297.
- [4] Ji-Guang Li, Takayasu Ikegami, et al. Co-precipitation synthesis and sintering of yttrium aluminum garnet (YAG) powders: the effect of precipitant. *Journal of the European Ceramic Society*, 2000, **20**, P. 2395–2405.
- [5] Saito N., Matsuda S-I., Ikegami T. Fabrication of transparent yttria ceramics at low temperature using carbonate-derived powder. *J. Am. Ceram. Soc.*, 1998, **81**(8), P. 2023–2028.
- [6] Lu J., Ueda K.I., et al. Neodymium doped yttrium aluminum garnet ($Y_3Al_5O_{12}$) nanocrystalline ceramics—a new generation of solid state laser and optical materials. *J. Alloys Comp.*, 2002, **341**, P. 220–225.
- [7] Wang H.Z., Gao L., Niihara K. Synthesis of nanoscaled yttrium aluminum garnet powder by the co-precipitation method. *Mater. Sci. Eng.*, 2000, **A288**, P. 1.
- [8] Gao L., Qiao H.C., Qiu H.B., Yan D.S. Preparation of Ultrafine Zirconia Powder by Emulsion Method. *J. Eur. Ceram. Soc.*, 1996, **16**, P. 437.
- [9] Wen L., Sun X., et al. Synthesis of yttria nanopowders for transparent yttria ceramics. *Opt. Mater.*, 2006, **29**, P. 239.
- [10] Gajovic A., Tomasic N., et al. Influence of mechanochemical processing to luminescence properties in Y_2O_3 powder. *J. Alloys and Compd.*, 2008, **456**, P. 313–319.
- [11] JCPDS International Centre for Diffraction DATA, Swarthmore, PA, 1996.
- [12] Takayasu I., Li J.G., Sakaguchi I., Hirota K. Morphology change of undoped and sulfate-ion-doped yttria powders during firing. *J. Am. Ceram. Soc.*, 2004, **87**(3), P. 517–519.
- [13] Mouzon J., Oden M., Tillement O., Jorand Y. Effect of drying and dewatering on yttria precursors with transient morphology. *J. Am. Ceram. Soc.*, 2006, **89**(10), P. 3094–3100.

Sitting posture health monitoring for scoliosis patients using capacitive micro accelerometer

P. Naveen¹, K. Gomathi¹, A. Senthilkumar², S. Thangavel¹

¹Department of Mechatronics Engineering, Kongu Engineering College, Erode, India

²Department of Electrical and Electronics Engineering, Dr. MCET, Pollachi, Tamilnadu, India
shairnav@gmail.com, gomu.k@yahoo.com, ask_rect@yahoo.com, thangavel.kks@hotmail.com

PACS 85.85.+j

DOI 10.17586/2220-8054-2016-7-3-538-541

Recently, the accelerometer has taken on a vital role in health monitoring system. The monitoring of patients disease has been aided by the use of different diagnostics. These devices exist at the macro level and also in micro level for condition monitoring. Capacitive Micro-accelerometer is a wearable sensor for monitoring of scoliosis disease in patients by analyzing their sitting posture, asymmetrical balance of patients. A new approach for accelerometer, using an *L-shaped cantilever parallel plate MEMS accelerometer* design is proposed. This micro accelerometer is designed using INTELLISUITE 8.6. Static analysis is done using Thermo Electro Mechanical module to examine the performance. Proposed design is compared with the existing design. In the future, this can also be applied in NANO level applications with respect to its design and fabrication.

Keywords: health monitoring, scoliosis disease, sitting posture, micro-accelerometer.

Received: 4 February 2016

1. Introduction

MEMS accelerometers are widely fabricated on batch-fabricated silicon [1]. MEMS based accelerometers have been making a bigger impact over the last few years [2]. Different accelerometers are available, such as capacitive [3], piezoresistive and piezoelectric. The L-shaped cantilever type capacitive accelerometer is widely used for many applications in different areas, like health monitoring in the medical field [4, 5], automobile, communication., etc which gives better sensitivity [6]. Scoliosis is a medical condition in which a person spinal axis has a three dimensional deviation, deals with problems like uneven musculature on one side of the spine, uneven hips or arms or leg lengths. Health monitoring of patients with this disease is essential, in such situations, the accelerometer is used as a health monitoring agent. Analysis will go by good and bad sitting posture. Good posture provides normal biomechanical functions of the musculoskeletal system. On the other hand, bad posture results in muscle imbalance and structural problems in the spine. Although many devices are invented for the health monitoring, accelerometers are the practical device to perform the function of health monitoring effectively by focusing on the human imbalance and posture control in real life. Good posture data are compared with the bad posture in improvising the data quality.

2. Design of accelerometer

The accelerometer design involves multiple steps like designing mask, fabrication, 3-D builder simulation, analysis etc.. These processes are carried out with help of the INTELLISUITE software. It possess intellifab for fabrication, intellimask for mask design. Mask specification is taken from *L-shaped cantilever parallel plate mems accelerometer design* [7]. By extracting the heart of the design and implementing in this work, the mask design specification is as follows:

$$\begin{aligned}\text{Proof mass size} &= 463 \times 463 \times 2 \mu\text{m}^3; \\ \text{Length of beam } (L_1) &= 457 \mu\text{m}; \\ \text{Length of beam } (L_2) &= 90 \mu\text{m}; \\ \text{Beam width } (W_1) &= 2 \mu\text{m}; \\ \text{Beam width } (W_2) &= 4 \mu\text{m}; \\ \text{Proof mass thickness} &= 2 \mu\text{m}.\end{aligned}$$

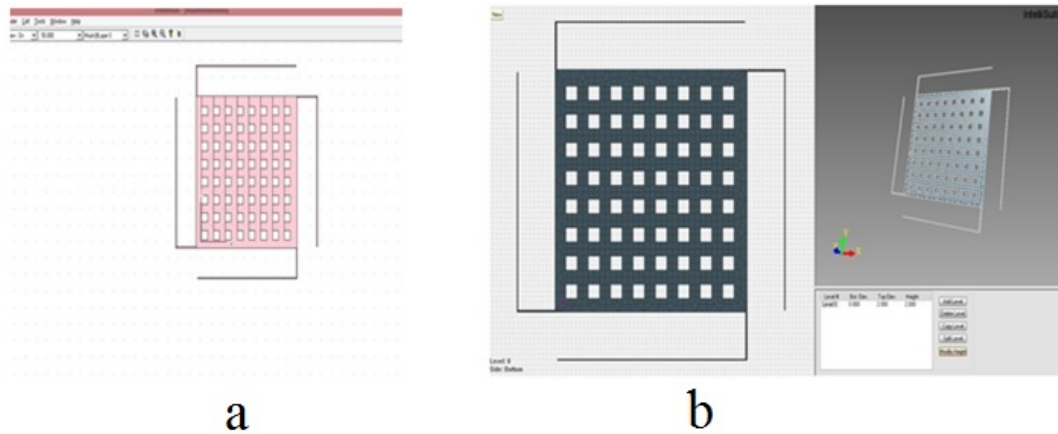


FIG. 1. (a) Design mask, (b) 3-D builder simulation

2.1. Mask design & simulation using 3-d builder

Fig. 1(a,b) shows the design mask created using intellimask and 3-D builder simulation. The L-shaped cantilever beams, created by calculating the x, y co-ordinates appropriate to the proof mass. Holes in the proof mass are created by using the array portion in the manner of matrix (8×8) . A single layer mask (mask@layer0) is created. For simulation using 3-D builder, the mask has to be exported from the intellimask. In mesh type, non-Manhattan isotropic is enabled and the mesh size $30 \mu\text{m}$ is given. The height of the mask can be magnified by using modify height.

2.2. Design analysis

Thermo Electro Mechanical (TEM) analysis done in the Intellisuite, the following properties are used for the analysis.

TABLE 1. Material properties

Material property	Silicon	Pyrex glass
σ_y (yield strength) 10^9 N/m^2	7	0.5 – 0.7
E (Young’s modulus) 10^{11} N/m^2	1.69	400
ν (Poisson’s ratio)	0.28	0.17
α (thermal expansion coefficient) $10^{-6} \text{ mt/mt } ^\circ\text{C}$	2.5	0.5
ρ (density) g/cm^3	2.3	2.225

Using material properties, the design has been analyzed for various pressure values.

Figure 2 shows the static analysis of micro accelerometer for various pressure values. Load is applied in the form of pressure, applied to the face of the design is 0.0001 MPa to 0.001 MPa. The boundary condition is fixed at all ends of the 4 beams and the static analysis mode is given. As a result, the change in displacement of $0.096 \mu\text{m}$ to $0.96 \mu\text{m}$ (x -direction) and deformed shape due to the load pressure is acquired. The changes in shape can be represented in a pictorial format as shown above. A pressure value of 0.002 MPa shows a breakage ($1.92 \mu\text{m}$) in accelerometer due to overload pressure.

Deflection can be well read through the graphical representation as shown below. Fig. 3 graph shows linearity in deflection with respect to the given pressure.

3. Conclusion

This paper concludes that the *L-shaped cantilever parallel plate MEMS accelerometer* is used to monitor the scoliosis disease in patients by analyzing their posture when seated, asymmetrical balance of patients. The static analysis shows the deformation in accelerometer. For the load conditions, 0.0001 MPa to 0.001 MPa, the

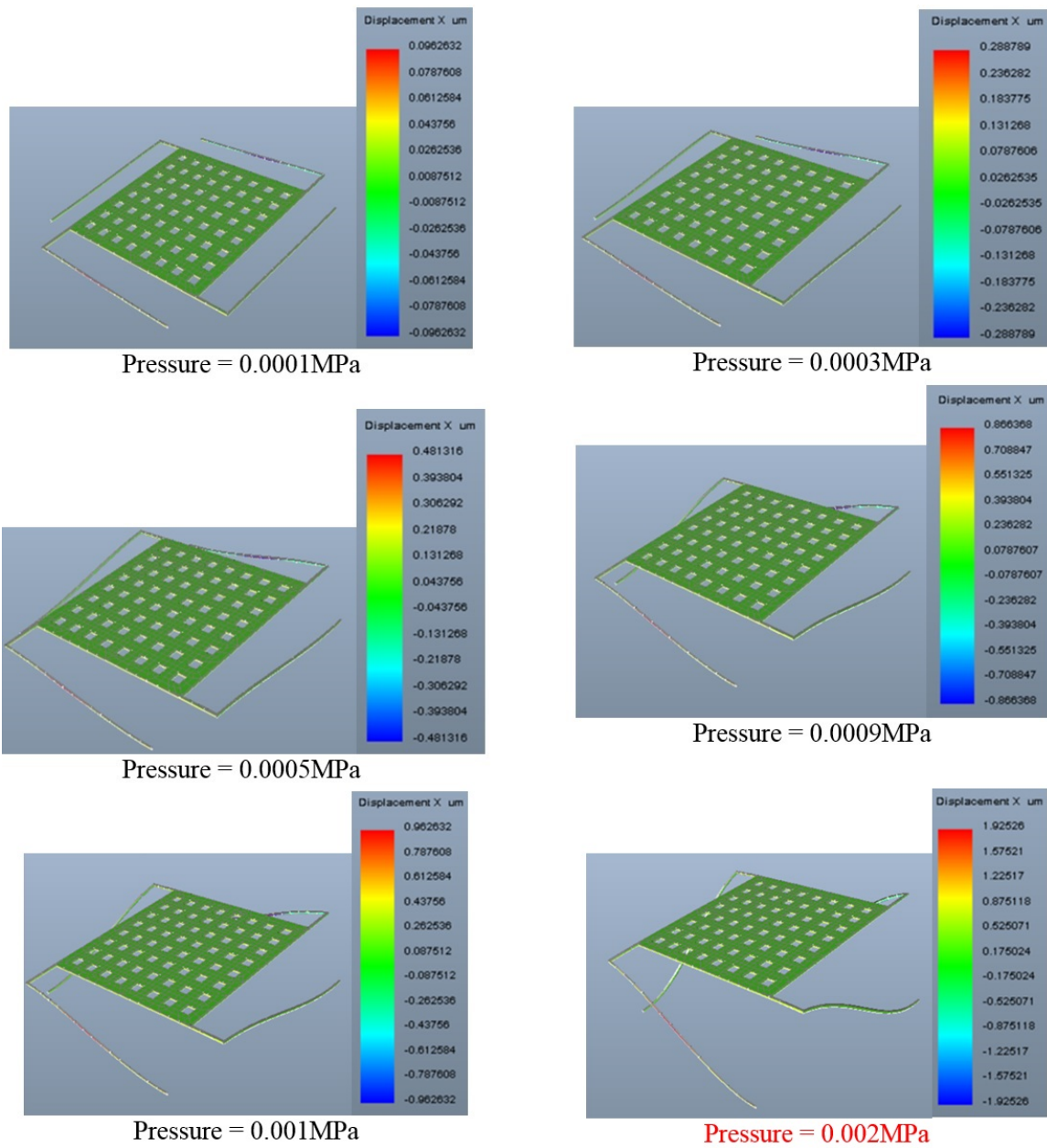


FIG. 2. Static analysis of micro accelerometer for various pressure values

displacement varies from $0.096 \mu\text{m}$ to $0.96 \mu\text{m}$ in x -direction respectively. Based upon the results obtained, the design has the limit pressure up to 0.001MPa , thus it is capable of monitoring for scoliosis patients. This design and simulation belongs to the micro level category devices, further work can be done to create nano level devices. The same design can be applied for the nano level with changes in design specifications.

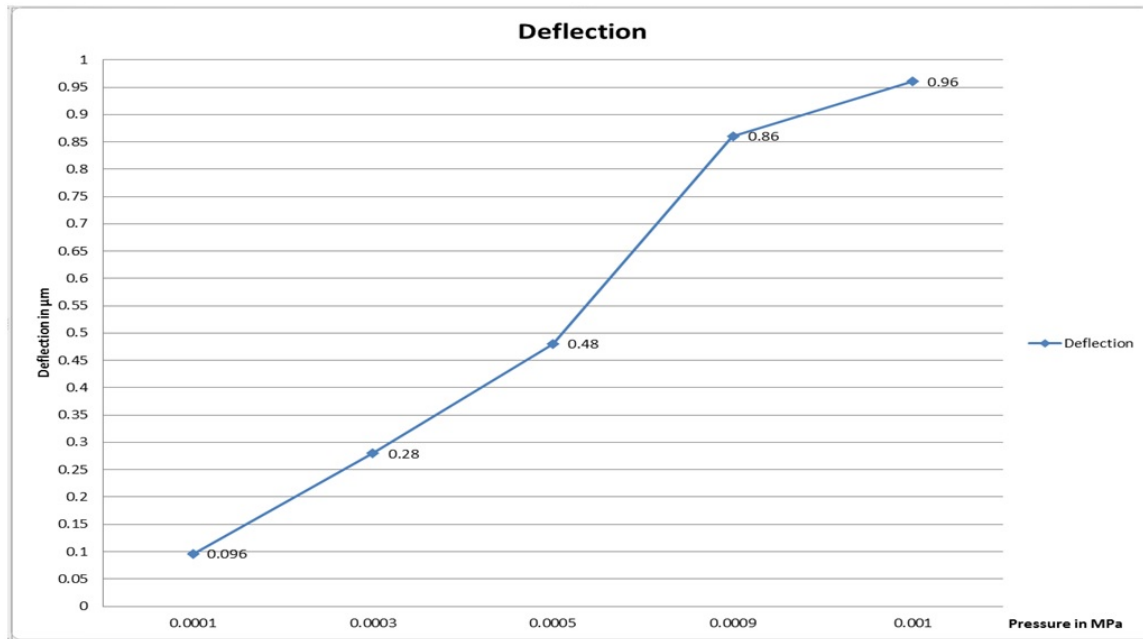


FIG. 3. Pressure vs deflection

References

- [1] L.M. Roylance and J.B. Angell. A Batch-Fabricated Silicon Accelerometer. *IEEE Trans. Elec. Dev.*, 1979, **ED-26**, P. 1911.
- [2] Trolier Mckinstry and P. Muralt. Thin film piezoelectrics for MEMS. *J. Electroceramics*, 2004, **12**(1-2), P. 7–17.
- [3] T. Berther, G.H. Gautschi, J. Kubler. Capacitive accelerometers for static and low-frequency measurements. *Sound and Vibration*, 1996, **30**(6), P. 28–30.
- [4] Vincas Benevicius et al. Identification of Capacitive MEMS Accelerometer Structure Parameters for Human Body Dynamics Measurements. *Sensors*, 2013, **13**, P. 11184–11195. doi:10.3390/s130911184.
- [5] D. Ozevin et al. Resonant capacitive MEMS acoustic emission transducers. *Smart Mater. Struct.*, 2006, **15**, P. 1863–1871. doi:10.1088/0964-1726/15/6/041.
- [6] Yoshida K., Matsumoto Y., Ishida M., Okada K. High-Sensitive Three Axis SOI Capacitive Accelerometer Using Dicing Method. *Proceedings of Technical Digest of the 16-th Sensor Symposium*, Toyohashi, Japan, 2–3 June 1998, P. 25–28.
- [7] Oukil, Souad, et al. L-shaped cantilever parallel-plate mems accelerometer design parameters using a gravitational search algorithm. *International Journal on Smart Sensing & Intelligent Systems*, 2015, **8**, P. 1.

A graphene-organic composite as a fluorescent chemosensor for Ag⁺

N. Bhuvanesh¹, K. Velmurugan¹, S. Suresh¹, T. Sakthivel², R. Nandhakumar^{1,*},

¹Department of Chemistry, Karunya University, Karunya Nagar, Coimbatore, TamilNadu, 641114 India

²Department of Nanoscience and Technology, Karunya University, Karunya Nagar, Coimbatore, TamilNadu, 641114 India

nandhakumar@karunya.edu

PACS 81.05.ue

DOI 10.17586/2220-8054-2016-7-3-542-546

A novel reduced graphene oxide (rGO) decorated organic binol based receptor ((S)-1) has been designed and synthesized. The resulting nanocomposite (rGO-(S)-1) material was then utilized as a selective fluorescent chemosensor for Ag⁺ ion in aqueous media at physiological pH. In addition, the nanocomposite showed no cross-reaction with any of the potential interfering metal ions. The reduced graphene oxide-organic nanocomposite was characterized using various spectroscopic, microscopic and analytical studies.

Keywords: rGO, Binol, nanocomposite, Fluorescence, Silver, off-on probe.

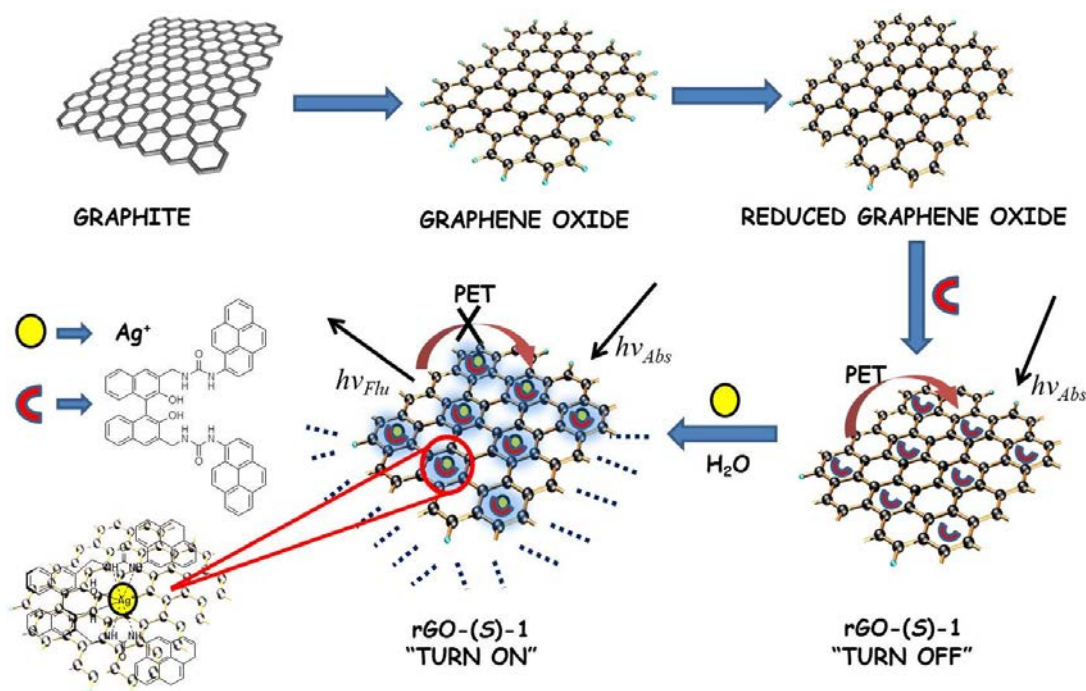
Received: 4 February 2016

1. Introduction

Graphene, possessing unique planar structure, remarkable mechanical properties, fascinating electron transfer and exceptional optical properties, has attracted considerable attention in recent years [1]. As a “rising star” in materials science and nanotechnology, it holds great promise for potential applications in many fields, such as nanocomposites [2], chemical sensors [3], energy storage [4], electronics [5], photonics [6], and catalysis [7]. Graphene oxide (GO), a two-dimensional nanosheet produced by the oxidation of graphene, has attracted great interest because of its unique characteristics, such as good dispersibility and facile surface functionality [8,9]. For a long time it has been well known that silver ions have the ability to kill harmful bacteria [10–12]. Silver has always been regarded as a precious metal. Silver ions, however, can cause severe damage to both the environment and to humans [13,14]. As one of the most toxic heavy metals, surpassed only by mercury, silver ion has been assigned to the highest toxicity class [15]. Silver ions may damage bacteria, and inhibit their growth, thereby affecting their reproduction [16]. Excessive intake of silver ions can also lead to long term insoluble substances formed in eye and skin cells [17]. Ag⁺ is widely used in the electrical industry, photography/imaging industry, and pharmaceutical industry [18,19], because of the high toxicity of Ag⁺ in aquatic organisms, monitoring of Ag⁺ levels has become an important issue. Indeed, almost all the reported sensors for Ag⁺ still suffer from serious drawbacks, such as poor water solubility, poor sensitivity, and poor selectivity. Traditional analytical methods used for the trace determination of Ag⁺ ion are generally based on different instrumental techniques. Especially in recent years, with the recent development of nanoscience, various silver nanoparticle products, such as nano-Ag catalyzer and antimicrobial reagents, have been widely used in research and in clinics. After being discharged into the environment, some of the silver nanoparticles are oxidized to silver ions and dissolve in environmental water and some are deposited in mud. Thus, they may cause more serious pollution to the environment and damage to human health. Therefore, it is of great significance to develop a rapid, selective, sensitive and simple detection method for silver ion in environmental samples and human fluids. We herein designed and synthesized an rGO-(S)-1 nanocomposite as shown in Fig. 1. The composite material is then utilized as a selective fluorescent chemosensor for Ag⁺ ion in aqueous media at a neutral pH. The synthesis, characterization and the selectivity studies with different metal ions are reported here.

2. Experimental section

All solvents were purchased commercially with reagent grade quality. rGO and compound (S) – 1 were prepared using a reported procedure [20,21]. Scanning Electron Microscope (SEM) studies were carried out on JEOL model JSM-6390. Absorption spectra were recorded on a Shimadzu UV-240 spectrophotometer. Fluorescence measurements were taken using a Jasco FP-8200 spectrofluorimeter equipped with quartz cuvettes of 1 cm path length. IR Studies were performed on a Shimadzu Prestige 20 IR spectrometer. All absorption and emission spectra were recorded at 24 ± 1 °C. Stock solutions for analyses were prepared (2 × 10⁻³ M) for rGO-(S)-1 (H₂O, HEPES=50 mM, pH=7.0) immediately before the experiments. The solutions of metal ions were prepared from the

FIG. 1. Synthesis and sensing of **rGO-(S)-1**

nitrate salts of Al^{3+} , Pb^{2+} , Ce^{3+} , Cd^{2+} , La^{3+} , Mg^{2+} , Zn^{2+} , Ba^{2+} , Hg^{2+} , Ag^+ , Fe^{3+} , Fe^{2+} , Ni^{2+} , Cr^{3+} , Ca^{2+} , Mn^{2+} , Na^+ , K^+ , Cu^{2+} and Co^{2+} .

2.1. Synthesis of **rGO-(S)-1** nanocomposite

The graphene-organic nanocomposite was prepared by the hydrothermal method [22]. Briefly, 2 mg of reduced graphene oxide was sonicated to make to a clear solution in distilled water (pH=7.0) and then 4 mg of **(S)-1** added to it. The resulting solution was transferred to an autoclave and kept in a hot air oven at 180 °C for 24 h. After the completion of the reaction, the autoclave was allowed to cool to room temperature. The formed precipitate was washed with a copious amount of water and ethanol and filtered. The final product **rGO-(S)-1** was obtained after drying the precipitate at 50 °C overnight.

3. Results and discussion

We have designed and synthesized a novel **rGO-(S)-1** nanocomposite through hydrothermal method as a selective and sensitive chemosensor for Ag^+ . The chemosensor **rGO-(S)-1** was confirmed by IR, SEM, UV and fluorescence studies. The UV and fluorescence spectra for **rGO**, **(S)-1** and the nanocomposite **rGO-(S)-1** are very distinct, and for the nanocomposite, the fluorescence is quenched. The IR spectrum of **(S)-1** shows a characteristic absorption bands at 1658 and 3441 cm^{-1} , which were assigned to the uryl C=O and the binol -OH groups, and the **rGO** characteristic absorption band appeared at 1573 and 1224 cm^{-1} [23]. In the case of the **rGO-(S)-1** nanocomposite, the 1658 cm^{-1} band was downshifted to 1637 cm^{-1} and the 3441 cm^{-1} band disappeared followed by the appearance of a new one at 2356 cm^{-1} . Conversely, in **rGO**, the bands at 1573 cm^{-1} were shifted to 1523 cm^{-1} after nanocomposite formation, as shown in Fig. 2. These shifts in the absorption bands are due to the $\pi - \pi$ stacking between the aromatic rings and the non-covalent interactions between **(S)-1** and the **rGO** composite.

The newly-prepared composite material and its precursor were analyzed by scanning electron microscopy. Accordingly, the SEM images of the **(S)-1** and **rGO-(S)-1** were recorded. The organic molecules **(S)-1** had rod like structure. However, in the case of nanocomposite material, the organic molecules were uniformly distributed over the surface of the 2D graphene sheet as a result of hydrothermal treatment. This composite formation between graphene and organic compound enhances the sensing properties of metal ions due to the high electron conductivity (Fig. 3).

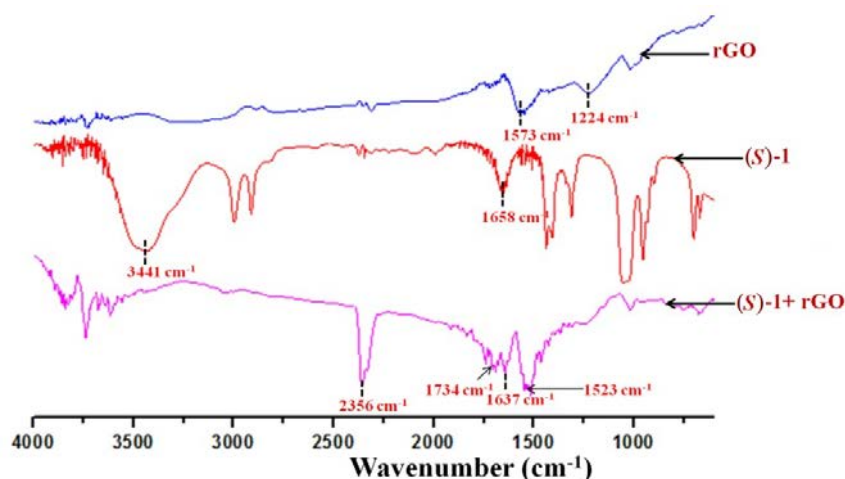


FIG. 2. IR Spectrum of rGO, (S)-1 and rGO-(S)-1

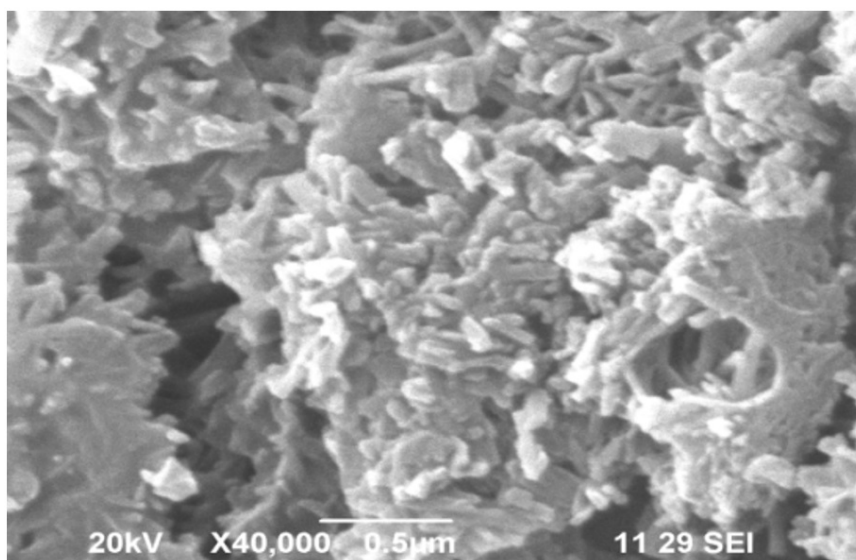


FIG. 3. SEM image of rGO-(S)-1

4. Metal selectivity studies of rGO-(S)-1 nanocomposite

The preliminary screening of the metal ion binding ability of rGO-(S)-1 nanocomposite in aqueous media at a neutral pH was performed by using the fluorescence technique. Receptor rGO-(S)-1 nanocomposite, exhibits very weak fluorescence. However, upon the addition of 100 equiv. of Ag^+ to the solution, significant enhancement of fluorescence with an emission maximum at 354 nm was observed. Interestingly, at the same concentration, other metal ions (Na^+ , K^+ , Pb^{2+} , Cu^{2+} , Cd^{2+} , Hg^{2+} , La^{3+} , Zn^{2+} , Co^{2+} , Ni^{2+} , Ca^{2+} , Mn^{2+} , Cr^{3+} , Ba^{2+} , Ce^{3+} , Mg^{2+} , Fe^{2+} , Fe^{3+} and Al^{3+}) when added to the rGO-(S)-1 nanocomposite did not produce any significant fluorescence changes. Therefore, these observations indicated that the sensor rGO-(S)-1 has an excellent selectivity towards Ag^+ in aqueous media at a neutral pH as a fluorescence “off-on” probe (Fig. 4).

For practical applicability, and to check the anti-jamming ability (i.e. the possible interferences by other metal ions), competitive complexation experiments were conducted. The fluorescence spectral changes of rGO-(S)-1 was measured by the treatment of Ag^+ ions (100 equiv.) in the presence of other metal ions at the same concentration, including Na^+ , K^+ , Pb^{2+} , Cu^{2+} , Cd^{2+} , Hg^{2+} , La^{3+} , Zn^{2+} , Co^{2+} , Ni^{2+} , Ca^{2+} , Mn^{2+} , Cr^{3+} , Ba^{2+} , Ce^{3+} , Mg^{2+} , Fe^{2+} , Fe^{3+} and Al^{3+} . All of the tested interfering metal ions showed no observable interference with the detection of Ag^+ ion. These results suggested that the receptor could be used for the selective detection of Ag^+ -ion in environmental and biological samples (Fig. 5).

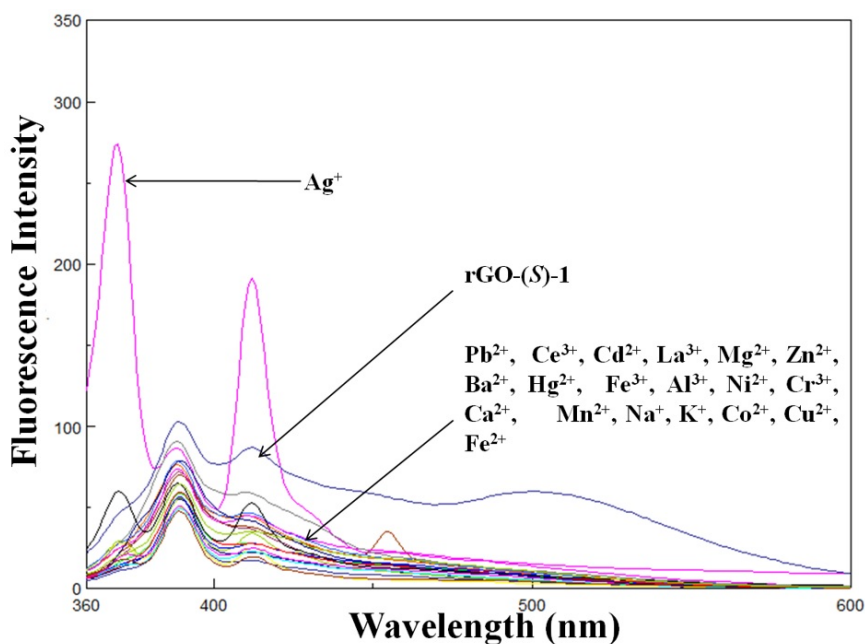


FIG. 4. Fluorescence changes of rGO-(S)-1 (4×10^{-6} M) solution (H_2O , $\text{pH}=7.0$) in the presence of various metal ions (100 equiv. of each, excited at 344 nm)

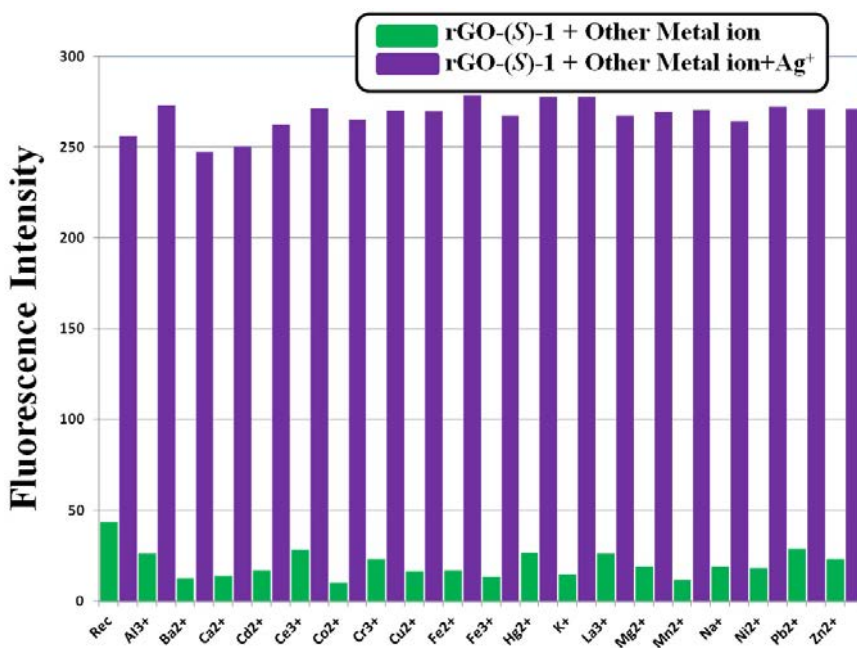


FIG. 5. Fluorescence changes of rGO-(S)-1 (4×10^{-6} M) solution (H_2O , $\text{pH}=7.0$) in the presence of various metal ions (100 equiv. of each, excited at 344 nm)

5. Conclusion

In conclusion, we have designed and synthesized a novel **rGO-(S)-1** nanocomposite through hydrothermal method and confirmed by usual spectroscopic, microscopy and analytical studies. The **rGO-(S)-1** nanocomposite exhibited high selectivity toward Ag^+ in comparison to other commonly-interfering metal ions in aqueous media at room temperature. This paves a pathway for further studies, such as chiral molecule sensing, anion sensing etc., which are currently underway in our laboratory. Moreover, we expect that this sensor will have tremendous potential application in biological fields, environmental monitoring works, and other relevant areas.

References

- [1] Luo J., Jang H.D., Huang J. Effect of Sheet Morphology on the Scalability of Graphene-Based Ultracapacitors. *ACS Nano*, 2013, **7**(2), P. 1464–1471.
- [2] Mao L., Zhang K., Chan H.S.O., Wu J. Surfactant-stabilized graphene/polyaniline nanofiber composites for high performance supercapacitor electrode. *J. Mater. Chem.*, 2012, **22**, P. 80–85.
- [3] Cui Y., Cheng Q.Y., Wu H., Wei Z., Han B.H. Graphene oxide-based benzimidazole-crosslinked networks for high-performance supercapacitors. *Nanoscale*, 2013, **5**, P. 8367–8374.
- [4] Xiang H. F., Li, Z. D., Xie.K., Jiang J.Z., Chen J.J., Lian P.C., Wu J.S., Yu Y., Wang H.H. Graphene sheets as anode materials for Li-ion batteries: preparation, structure, electrochemical properties and mechanism for lithium storage. *RSC Adv.*, 2012, **2**, P. 6792–6799.
- [5] Wu Z.S., Pei S., Ren W., Tang D., Gao L., Liu B., Li F., Liu C., Cheng H.M. Field emission of single-layer graphene films prepared by electrophoretic deposition. *M. Adv. Mater.*, 2009, **21**, P. 1756–1760.
- [6] Yoo E., Okata T., Akita T., Kohyama M., Nakamura J., Honma I. Enhanced Electrocatalytic Activity of Pt Subnanoclusters on Graphene Nanosheet Surface. *Nano Lett.*, 2009, **9**(6), P. 2255-9.
- [7] Seger B., Kamat. Thickness-Controlled Graphene Hybrid Interface for Highly. *J. Phys. Chem. C*, 2000, **113**, P. 7990–7995.
- [8] Liu Z., Tabakman S., Welsher K., Dai H. Carbon nanotubes in biology and medicine: in vitro and in vivo detection, imaging and drug delivery. *J. Am. Chem. Soc.*, 2008, **130**, P. 10876–10877.
- [9] Mohanty N., Berry V., A graphene-based fluorescent nanoprobe for silver (I) ions detection by using graphene oxide and a silver-specific oligonucleotide. *Nano Lett.*, 2008, **8**, P. 4469–4476.
- [10] Jun Jeon H., Chul Yi S., Geun Oh S. Preparation and antibacterial effects of Ag–SiO₂ thin films by sol–gel method. *Biomed. Mater.*, 2000, **52**, P. 662.
- [11] Lansdown A.B.G. Silver dressings. *J. Wound Care*, 2002, **11**, P. 125–130.
- [12] Chatterjee A., Santra M., Won N., Kim S., Kim J.K., Kim S.B., Ahn K.A. Selective fluorogenic and chromogenic probe for detection of silver ions and silver nanoparticles in aqueous media. *J. Am. Chem. Soc.*, 2009, **131**(6), P. 2040–2041.
- [13] Purcell T.W., Peters J.J. Sources of silver in the environment. *Environ. Toxicol. Chem.*, 1998, **17**, P. 539.
- [14] Park K.S., Lee J.Y., Park H.G. Mismatched pyrrolo-dC-modified duplex DNA as a novel probe for sensitive detection of silver ions. *Chem. Commun.*, 2012, **48**, P. 4549–4551.
- [15] Hook S.E., Fisher N.S. Sublethal effects of silver in zooplankton: importance of exposure pathways and implications for toxicity testing. *Environ.Toxicol. Chem.*, 2001, **20**(3), P. 568–574.
- [16] He X., Qing Z., Wang K., Zou Z., Shi H., Huang J. Engineering a unimolecular multifunctional DNA probe for analysis of Hg²⁺ and Ag⁺. *Anal.Methods*, 2012, **4**, P. 345–347.
- [17] Liao S.Y., Read D.C., Pugh W.H., Furr J.R., Russell A.D. Interaction of silver nitrate with readily identifiable groups: relationship to the antibacterial. *Lett. Appl. Microbiol.*, 2003, **25**, P. 279–283.
- [18] Barriada, J. L., Tappin A.D., Evans E.H., Acterberg E.P. Dissolved silver measurements in seawater. *Trends Anal. Chem.*, 2007, **26**, P. 809–817.
- [19] Kim J., Kim S., Lee S. Differentiation of the toxicities of silver nanoparticles and silver ions to the Japanese medaka (*Oryzias latipes*) and the cladoceran *Daphnia magna*. *Nanotoxicology*, 2011, **5**, P. 208–214.
- [20] Cao N., Yuan Z. Study of Reduced Graphene Oxide Preparation by Hummers' Method and Related Characterization. *Nanomaterials*, 2015, DOI 10.1155/2015/168125.
- [21] Wang F., Nandhakumar R., Hu Y., Kim D., Kim K.M., Yoon J. BINOL_L-Based Chiral Receptors as Fluorescent and Colorimetric Chemosensors for Amino Acids. *J. Org. Chem.*, 2013, **78**(22), P. 11571–11576.
- [22] Li G., Xu C. Hydrothermal synthesis of 3D Ni_xCo_{1-x}S₂ particles/graphene composite hydrogels for high performance supercapacitors. *Carbon*, 2015, **90**, P. 44–52.
- [23] Zhao.Y., Song X., Song Q., Yin Z. A facile route to the synthesis copper oxide/reduced graphene oxide nanocomposites and electrochemical detection of catechol organic pollutant. *CrystEngComm*, 2012, **14**, P. 6710–6719.

Annealing effects on V_2O_{5-x} thin films deposited by non reactive sputteringD. Rachel Malini¹, R.Sivakumar², C. Sanjeeviraja^{3,*}¹Department of Physics, The American College, Madurai-625002, India²Directorate of Distance Education, Alagappa University, Karaikudi-630004, India³Department of Physics, A.C. College of Engg. & Tech., Karaikudi-630004, India

sanjeeviraja@rediffmail.com

PACS 68

DOI 10.17586/2220-8054-2016-7-3-547-552

Thin films of vanadium oxide (V_2O_{5-x}) were prepared by rf magnetron sputtering process and are heat treated to study the annealing effect. As-deposited thin films are amorphous in nature and crystallinity is improved by annealing the sample. Thin layers with high density and small grain size varying from 36 nm to 70 nm were seen in the FESEM images of as-deposited thin films. In the case of annealed thin films, it has been transformed to thin elongated rod like structure with 202.5 nm length and an average diameter of approximately 48 nm. Optical properties were studied by using UV-Vis-NIR spectrophotometer and the reduction in transmission in annealed thin films is due to the crystalline nature of thin films. Studies were done on the samples by taking photoluminescence and Laser Raman spectra.

Keywords: vanadium oxide, rf magnetron sputtering, annealing.

Received: 4 February 2016

Revised: 26 April 2016

1. Introduction

Vanadium pentoxide (V_2O_5), a transition metal oxide semiconductor, shows a wide range of applications in thin film form due to its multivalency, layered structure and wide optical band gap [1]. It is a promising compound for smart window applications, but the intercalation process is slow because of its low electrical conductivity and diffusion coefficient of ions [2–7]. Nanoparticle V_2O_5 thin films are used to overcome this issue by increasing the surface area and decreasing the diffusion distance [8]. In our study, the experimental details for preparing sputtered V_2O_{5-x} thin films and the effect of annealing over the prepared thin films were discussed.

2. Experimental

V_2O_{5-x} thin films were prepared on well cleaned Corning glass substrates (8 cm × 6 cm) by varying rf power as 150 W, 175 W and 200 W at room temperature. A target of 6 mm thickness and 50 mm diameter was obtained by pressing V_2O_5 powder (99.9 % purity) in a pelletiser which was then sintered to 300 °C for about 2 hrs. The following parameters were kept constant during deposition of samples by non reactive sputtering process: 30 minutes deposition time, 1.33×10^{-2} mbar argon gas pressure and 6 cm target-substrate spacing. As-deposited thin films were then annealed at 400 °C for 5 hrs. Structural properties of thin films were studied by XRD using a XPERT-PRO PANalytical diffractometer with $CuK\alpha$ radiation ($\lambda=1.5406 \text{ \AA}$). The morphology of samples was studied using FEI's Quanta 200 FEG field emission scanning electron microscope (FESEM) and optical studies were undertaken by UV-vis-NIR spectrophotometer (HR-2000, M/s Ocean Optics, USA). PL spectra of samples were recorded at room temperature by using 'Varian Cary Eclipse Spectrophotometer' and Raman spectra were taken by Laser Raman spectrometer (Acton SpectraPro 2500i, Princeton Instruments, Acton Optics & Coatings).

3. Results and Discussion

XRD patterns of as-deposited and annealed V_2O_{5-x} thin films deposited on glass substrates by varying rf power from 150 W to 200 W are shown in Fig. 1. X-ray pattern of the V_2O_5 target is also displayed for comparison. The target material exhibits 23 peaks corresponding to the orthorhombic V_2O_5 phase at $2\theta = 15.26^\circ$, 20.15° , 21.64° , 25.48° , 26.05° , 30.92° , 32.31° , 33.28° , 34.25° , 41.2° , 41.97° , 45.38° , 47.27° , 47.75° , 48.74° , 51.16° , 51.93° , 55.57° , 58.98° , 61.02° , 62.04° , 68.71° and 74.39° [JCPDS No: 89-2482]. It belongs to Pmmn space group having lattice parameters as $a = 11.544 \text{ \AA}$, $b = 3.571 \text{ \AA}$ and $c = 4.383 \text{ \AA}$. The maximum intensity with the height of 930.2 a.u. is displayed by the peak at $2\theta = 20.15^\circ$ which proves that the V_2O_5 target is oriented along (0 0 1) plane. The as-deposited V_2O_{5-x} thin films are gray in color [9]. XRD patterns of as-deposited thin films show very broad and diffuse patterns. There is no evidence for any diffraction peak and so these films are amorphous in nature. This shows that the plasma power of 200 W generated by the

rf was not enough for the growth of crystalline V_2O_{5-x} thin films in the absence of oxygen atmosphere during sputtering process [10]. With 0% oxygen content and V_2O_5 as target during sputtering process, the deposited thin films are devoid of long range atomic order and are amorphous in nature. Generally, crystalline V_2O_5 thin films are obtained by several authors by reactive sputtering under oxygen-argon mixture and also by choosing vanadium metal as target.

The annealed V_2O_{5-x} thin films deposited at low rf power are yellowish gray in color, whereas the samples prepared at high rf power are yellow in appearance, like V_2O_5 powder [11]. The annealed thin film deposited at 175 W rf power shows peaks at $2\theta = 17.71^\circ$ and 28.64° which are due to $(\bar{2} 0 1)$ and $(\bar{2} 0 2)$ plans of monoclinic VO_2 phase [JCPDS(31-1438)]. In the annealed thin film prepared at 200 W rf power, two peaks were observed at $2\theta = 12.58^\circ$ and 17.71° and are attributed to $(1 0 1)$ plane of orthorhombic V_2O_5 phase [JCPDS (85-2422)] and $(\bar{2} 0 1)$ plane of monoclinic VO_2 phase respectively. The crystallite size was calculated from the full width at half maximum (FWHM) of the V_2O_5 phase in the annealed thin films deposited at 200 W rf power and is 60 nm. The crystallite size is 57 nm and 79 nm for the VO_2 phase in the annealed thin films deposited at 175 W and 200 W respectively. This shows that the growth of VO_2 phase in the annealed thin films improves with increase in rf power and this is due to the lack of oxygen during the sputtering process.

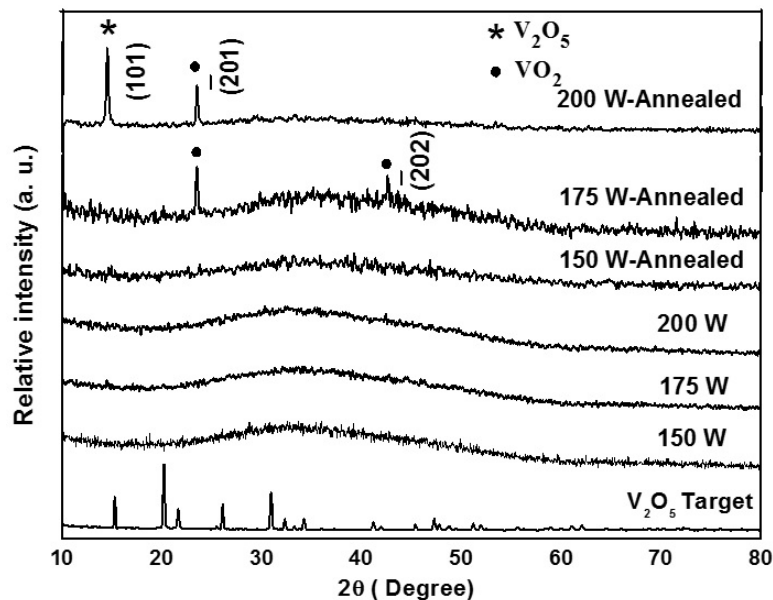


FIG. 1. XRD pattern of V_2O_5 target, as-deposited and annealed V_2O_{5-x} thin films

Figure 2 shows the typical FESEM micrographs of as-deposited and annealed V_2O_{5-x} thin films deposited at 200 W rf power. Thin layers with high density and small grain size varying from 36 nm to 70 nm are seen in FESEM images of as-deposited thin films. Unlike the as-deposited thin films, annealed V_2O_{5-x} thin films deposited at 175 W rf power contain individual and separate grains (not shown). The grain size of such annealed thin films increases with increase in rf power and the grain shape varies from small granular surface structure to elongated thin rectangular bars when rf power increases from 175 W to 200 W. The granular spherical shape grains show an average diameter of 324 nm in annealed thin films deposited at 175 W rf power. Annealed thin films deposited at 200 W rf power show thin elongated rod like structure with approximately 202 nm length and average diameter of 48 nm. Because of the formation of new bonds which results in densification, grain growth is encouraged in annealed thin films [12].

Figure 3(a) shows the transmission of as deposited and annealed thin films deposited by varying rf power over the wavelength range of 300 – 900 nm. V_2O_{5-x} thin films deposited at 150, 175 and 200 W rf power have transmittance values of 80 %, 84.1 % and 92.9 % respectively. The high transmission indicates that thin films deposited at 200 W rf power are weakly absorbing in the spectral range of 450 to 1000 nm and the decrease in transmission at $\lambda < 400$ nm is due to the fundamental absorption. These data are consistent with previous reports [13]. The transmittance values for the annealed samples are recorded as 61 %, 43.9 % and 30.7 %. The surface of annealed samples becomes rough, resulting in light loss by scattering and thus low transmittance [14,15]. In annealed thin films the absorption peak at around 350 nm was red-shifted with an increase in rf power [16].

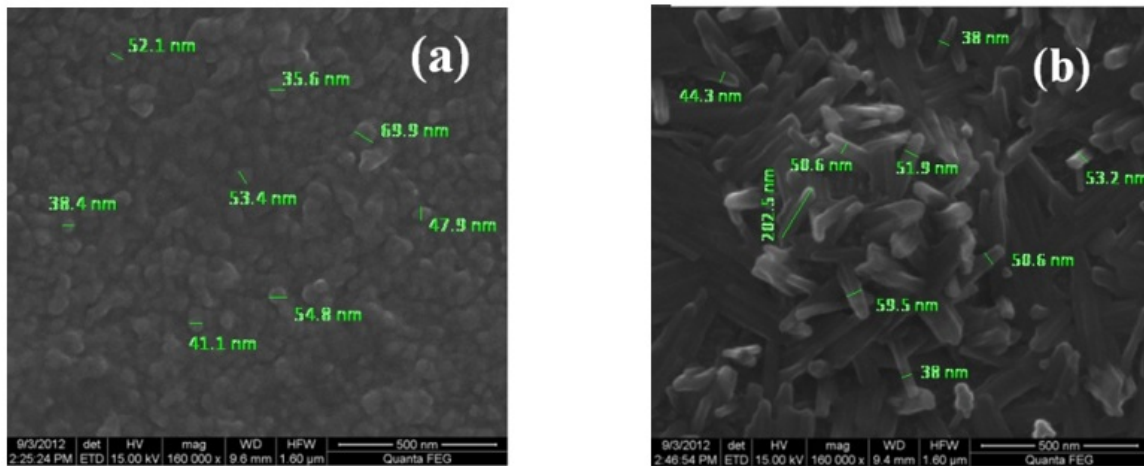


FIG. 2. FESEM images of (a) as-deposited and (b) annealed thin films at 200 W rf power

The experimental data were found to give a better fit when $(\alpha h\nu)^{1/2}$ was plotted against $h\nu$. This suggests an indirect allowed transition. Fig. 3(b) shows the relation between $(\alpha h\nu)^{1/2}$ and photon energy for as-deposited and annealed thin films prepared by varying rf power. E_g of as-deposited thin films increases as 2.10, 2.35 and 2.45 eV with increase in rf power. High rf power during deposition favors the formation of V_2O_5 phase in thin films by partially filling oxygen vacancies, thereby reducing localized states and hence the bandgap increases. The optical bandgap of annealed thin films decreases as 1.40, 1.26 and 1.18 eV with increase in rf power. Excess electrons are localized at the empty 3-d orbital of vanadium atoms which are closer to oxygen vacancy and thus localized states are developed in the bandgap and hence a decrease in bandgap energy [17].

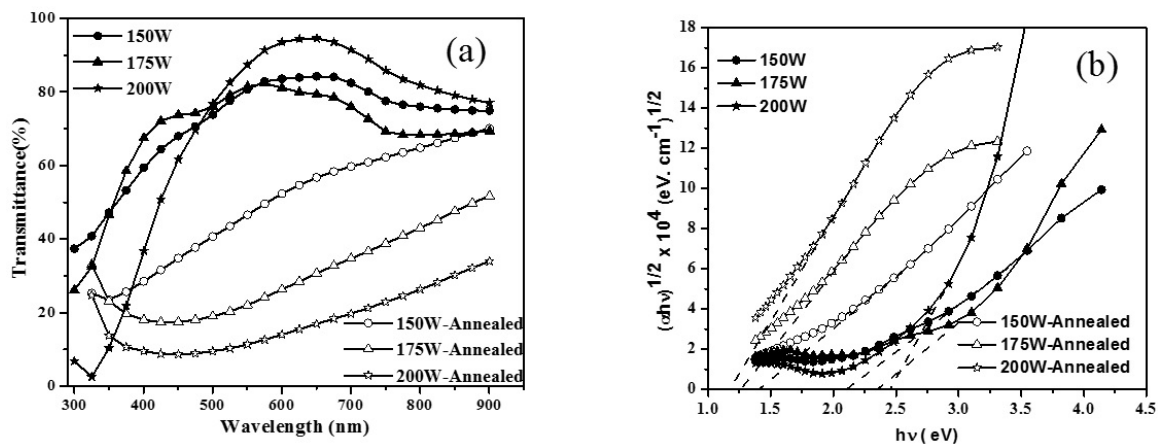


FIG. 3. (a) Transmittance spectra and (b) Optical bandgap of V_2O_{5-x} thin films

Figure 4(a) shows the PL spectra of V_2O_{5-x} thin films deposited at various rf power recorded at room temperature by using the instrument 'Varian Cary Eclipse Spectrophotometer' where the source is the Xe lamp. PL emission peaks of as-deposited thin films exhibit a blue shift when rf power increases. The presence of emission wavelength at around 600 nm for the excitation wavelength of 460 nm indicates the existence of defects on the surface of thin films as oxygen vacancies [18]. The optical bandgap energy values have been calculated from the emission wavelength and are obtained as 1.93, 2.05 and 2.3 eV with respect to 150, 175 and 200 W rf power. The calculated bandgap energy values are in good agreement with those obtained from UV-Vis-NIR spectrophotometer studies. The PL spectra of annealed thin films deposited at various rf power for the excitation wavelength of 460 nm were recorded at room temperature and are shown in Fig. 4(b). The PL emission peaks of annealed thin films exhibit a red shift by positioning at 749, 759 and 774 nm for 150, 175 and 200 W rf power respectively. From the emission wavelength, the energy bandgap values for thin films of 150, 175 and 200 W rf power during deposition have been calculated as 1.66, 1.64 and 1.60 eV respectively. The emission peak at around 759 nm

indicates that the samples could emit intensely visible light at room temperature and is due to defects such as oxygen vacancies which got involved during growth [19]. This result is confirmed by Yu-quan Wang [20] by fitting two Gaussian peaks in the PL spectrum centered at approximately 650 and 730 nm, which correspond to energies of approximately 1.82 and 1.68 eV, respectively. Since the band gap of V_2O_5 is approximately 2.24 eV, they deduced that these visible emissions are caused by oxygen defects.

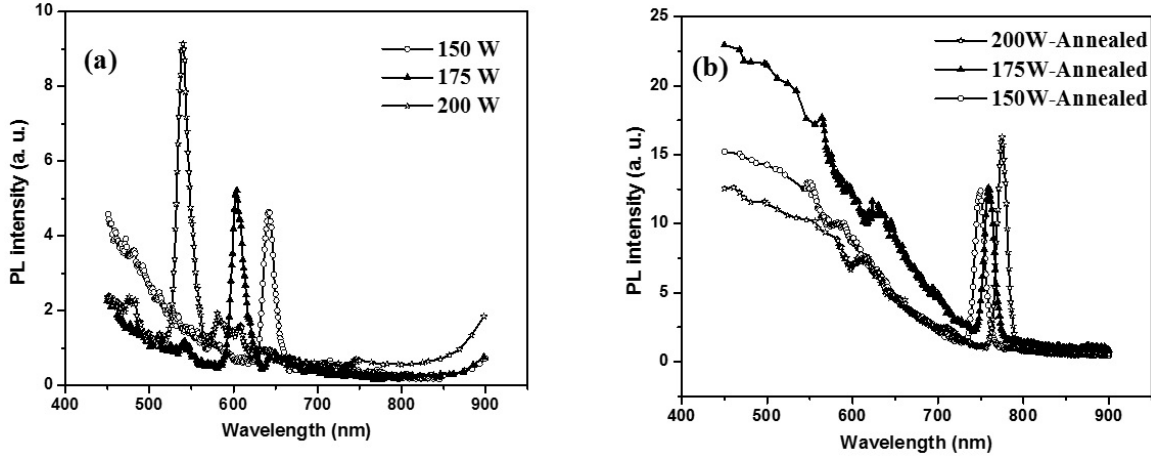


FIG. 4. (a) PL emission spectra of V_2O_{5-x} thin films deposited at various rf power and (b) their respective annealed samples

Figure 5(a) shows the Raman spectra of V_2O_{5-x} thin films deposited at different rf power along with that of V_2O_5 target material. The target material exhibits two sharp peaks at 785.99 cm^{-1} and 902.10 cm^{-1} which are due to the V–O–V stretching vibration mode [21] and the $V^{4+} = O$ bond which is created by the modification in $V^{5+} = O$ vanadyl oxygen stretching mode [22] respectively. The corner shared oxygens in common to the two pyramids exhibit another stretching mode as V_2-O and the peak corresponding to it is located at 702.84 cm^{-1} in the target material [23]. Two flat and small peaks are visible at 1004.63 cm^{-1} and 1071.81 cm^{-1} and a broad peak at 1175.34 cm^{-1} which corresponds to the terminal oxygen (V=O) stretching modes due to the unshared oxygen [24]. Raman spectra of as-deposited thin film prepared at 150 W rf power exhibits a peak at 1053.57 cm^{-1} which corresponds to the terminal oxygen (V=O) stretching mode due to the unshared oxygen. A flat peak is also observed at 943.12 cm^{-1} which is due to the $V^{5+} = O$ vanadyl oxygen stretching mode modification. Five peaks are observed in the Raman spectrum of thin film deposited at 175 W rf power and are located at 706.23 , 839.46 , 938.59 , 986.39 and 1051.30 cm^{-1} . The new peak at 705.87 cm^{-1} in the Raman spectrum is due to the stretching vibration of $V_2 - O$ bond [25]. The flat peak due to the modification in $V^{5+} = O$ vanadyl oxygen stretching mode to $V^{4+} = O$ appears as a sharp one with intensity of 107.96 a.u. at 938.59 cm^{-1} . The terminal oxygen stretching mode due to the unshared oxygen is responsible for the new Raman peak at 986.39 cm^{-1} . The emergence of the Raman inactive mode at 839.46 cm^{-1} again confirms the amorphous nature of the prepared thin film. The red shift of the peak due to the terminal oxygen (V=O) stretching mode from 1053.57 cm^{-1} to 1051.30 cm^{-1} with increase in intensity from 56.39 to 66.59 a.u. also confirms the structural disorder resulting in the amorphous nature of the thin films prepared. Six Raman peaks with low intensities are observed in the Raman spectrum of thin film deposited at 200 W rf power and are located at 773.41 , 863.36 , 900.97 , 944.25 , 993.18 and 1151.44 cm^{-1} . The first peak at 773.41 cm^{-1} is due to the V-O-V stretching vibration mode and the peaks at 900.97 and 944.25 cm^{-1} correspond to the $V^{4+} = O$ bond which is created by the modification in $V^{5+} = O$ vanadyl oxygen stretching mode. This modification is due to basic point defects in the V_2O_{5-x} crystal lattice i.e. the oxygen vacancies created by removing vanadyl oxygen and thereby generating reduced V^{4+} from V^{5+} ions. The seventh peak of the Raman spectrum corresponds to the terminal oxygen (V=O) stretching mode due to the unshared oxygen and is located at 1049.04 cm^{-1} with high intensity of 80.86 a.u.

Figure 5(b) shows Raman spectra of annealed thin films deposited at different rf powers. Apart from the two sharp peaks at 1007.98 and 1129.8 cm^{-1} due to $V^{5+} = O$ bond of terminal oxygen atoms, the Raman spectrum of annealed V_2O_{5-x} thin films deposited at 150 W rf power shows two low intensity peaks at 766.49 and 846.25 cm^{-1} . The peak observed at 846.25 cm^{-1} corresponds to infrared active mode and is Raman inactive for a well-crystalline V_2O_5 material. When a non-stoichiometric V_2O_5 thin film with structural disorders is analyzed, this mode becomes active [26]. The Raman spectrum of annealed thin films deposited at 175 W rf power shows

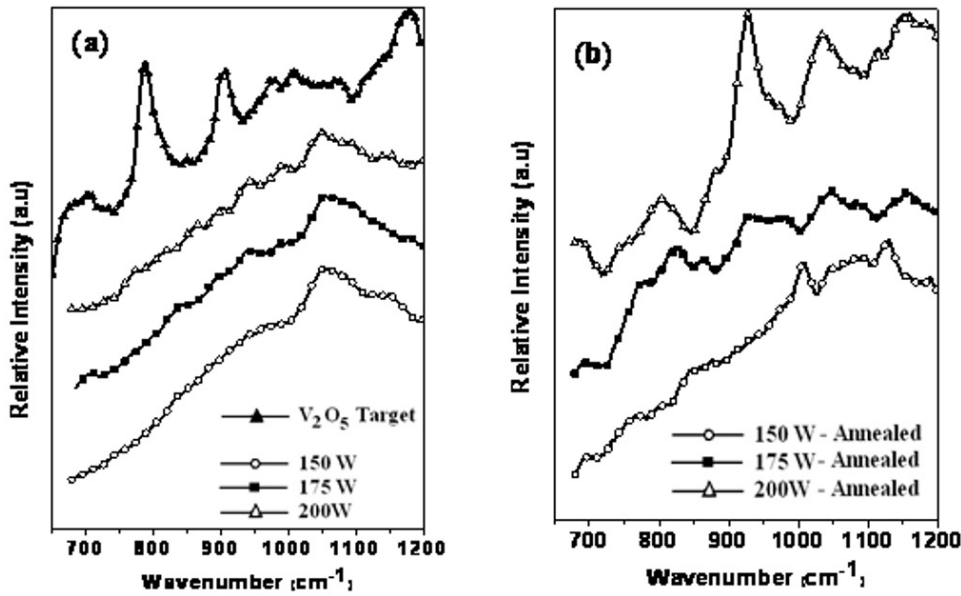


FIG. 5. (a) Raman spectra of V_2O_{5-x} thin films deposited at various rf power and (b) their respective annealed samples

four peaks at 824.11, 930.535, 1049.04 and 1158.36 cm^{-1} . The peaks corresponding to the stretching mode due to $V^{5+} = O$ bond of terminal oxygen atoms are shifted to high energy region at 1049.04 and 1158.36 cm^{-1} with increase in intensities and this shows that the annealed thin films are heading towards V_2O_{5-x} phase. Along with that, a peak due to $V^{4+} = O$ bond is also seen at 939.9 cm^{-1} which proves the presence of VO_2 in annealed thin films. The peak corresponding to the Raman inactive mode appears at 824.11 cm^{-1} . The absence of external low frequency modes at 104, 142 and 194 cm^{-1} indicates that the prepared thin films are lagging in layered V_2O_{5-x} crystalline structure. The Raman spectrum of annealed thin films deposited at 200 W rf power exhibits well resolved Raman lines which indicate the crystallinity of thin films. The high intensity Raman peak at about 928.15 cm^{-1} is related to the vanadyl stretching mode corresponding to $V=O$ bond in the crystal structure and this is attributed to the $V^{4+} = O$ bonds. These $V^{4+} = O$ bonds arise due to the direct conversion from $V^{5+} = O$ bonds or the breaking of the single oxygen bonds which involves V^{4+} ions or both. The shift of this peak towards low frequency range indicates the presence of structural disorder in the annealed thin films at high rf power and this is confirmed by the presence of the peak at 804.23 cm^{-1} which corresponds to the IR active mode. The two broad peaks at 1032.95 and 1151.32 cm^{-1} are assigned to the stretching mode due to $V^{5+} = O$ bond of terminal oxygen atoms on the surface clusters of annealed thin films. The generation of a new peak at 684.59 cm^{-1} is due to the stretching vibration mode of $V_2 - O$ bond in the $V-O-V$ disordered framework. If sufficient oxygen pressure was allowed during deposition, this peak would have exhibited a red shift and would be 706 cm^{-1} which is the stretching mode of the crystalline V_2O_{5-x} thin films arising due to the corner sharing oxygen atoms of two successive pyramids.

4. Conclusion

In this paper, annealing effects on V_2O_{5-x} thin films deposited by varying rf power have been studied. As-deposited thin films are amorphous in nature and their crystallinity is improved by annealing. Nanoscale grains are seen in as-deposited thin films and were then transformed into rectangular rods after annealing. The optical bandgap for annealed thin films decreases with increase in rf power and is due to development of localized states. PL spectra of as-deposited thin films show blue shift in emission peak at 600 nm with increase in rf power and annealed samples exhibit a reverse effect. Apart from the peak due to $V=O$ stretching mode, a Raman peak is observed at 928.1 cm^{-1} in annealed thin films deposited at 200 W rf power and is attributed to $V^{4+} = O$ bonds.

References

- [1] Rajendra Kumar R.T., Karunakaran B., et al. Structural properties of V_2O_5 thin films prepared by vacuum evaporation, *Mat. Sci. Semicon. Proc.*, 2003, **6**, P. 543–546.
- [2] Takahashi K., Wang Y., Cao G. Growth and electrochromic properties of single-crystal V_2O_5 nanorod arrays. *Appl. Phys. Lett.*, 2005, **86**, P. 053102-1–053102-3.
- [3] Ramana C.V., Hussain O.M., et al. Physical investigations on electron-beam evaporated vanadium pentoxide films. *Mater. Sci. Eng. B*, 1998, **52**, P. 32–39.
- [4] Fujita Y., Miyazaki K., Tatsuyama C. On the electrochromism of evaporated V_2O_5 films. *Jpn. J. Appl. Phys.*, 1985, **24**, P. 1082–1086.
- [5] Kim B.H., Kim A., et al. Energy gap modulation in V_2O_5 nanowires by gas adsorption. *Appl. Phys. Lett.*, 2008, **93**, P. 233101–233103.
- [6] Raible I., Burghard M., et al. V_2O_5 nanofibres: novel gas sensors with extremely high sensitivity and selectivity to amines. *Actuat. B*, 2005, **106** P. 730–735.
- [7] Moshfegh A.Z., Ignatiev A. Formation and characterization of thin film vanadium oxides: Auger electron spectroscopy, X-ray photoelectron spectroscopy, X-ray diffraction, scanning electron microscopy, and optical reflectance studies. *Thin Solid Films*, 1991, **198** P. 251–268.
- [8] Wang Y., Takahashi K., Shang H., Cao G. Synthesis and Electrochemical Properties of Vanadium Pentoxide Nanotube Arrays. *J. Phys. Chem. B*, 2005, **109**, P. 3085–3088.
- [9] Alaa A. Akl. Crystallization and electrical properties of V_2O_5 thin films prepared by RF sputtering. *Appl. Surf. Sci.*, 2007, **25**, P. 7094–7099.
- [10] Rachel Malini D., Sanjeeviraja C. Effect of RF power on electrochromic V-Ce mixed oxide thin films. *Electrochim. Acta*, 2013, **104**, P. 162–169.
- [11] Wu G., Du K., et al. Optical absorption edge evolution of vanadium pentoxide films during lithium intercalation. *Thin Solid Films*, 2005, **485**, P. 284–289.
- [12] Kingery W.D. in: W. Kingery (Ed). *Kinetics of High Temperature Process*. MIT Press, Cambridge, MA., 1959, P. 187.
- [13] Michailovits L., Hevesi Liem phan I., Varga Zs. Determination of the optical constants and thickness of amorphous V_2O_5 thin films. *Thin Solid Films*, 1983, **102**, P. 71–76.
- [14] Meng L.-J., Silva R.A., et al. Optical and structural properties of vanadium pentoxide films prepared by d.c. reactive magnetron sputtering. *Thin Solid Films*, 2006, **515**, P. 195–200.
- [15] Cui H.-N., Teixeira V., et al. Thermo-chromic properties of vanadium oxide films prepared by dc reactive magnetron sputtering. *Thin Solid Films*, 2008, **516**, P. 1484–1488.
- [16] Guan Z.S., Yao J.N., Yang Y.A., Loo B.H. Electrochromism of annealed vacuum-evaporated V_2O_5 films. *J. Electroanal. Chem.*, 1998, **443**, P. 175–179.
- [17] Ramana C.V., Hussain O.M., Srinivasulu Naidu B., Reddy P.J. Spectroscopic characterization of electron-beam evaporated V_2O_5 thin films. *Thin Solid Films*, 1997, **305**, P. 219–226.
- [18] Wu M.-C., Lee C.-S. Field emission of vertically aligned V_2O_5 nanowires on an ITO surface prepared with gaseous transport. *J. Solid State Chem.*, 2009, **182**, P. 2285–2289.
- [19] Wang Y.Q., Li Z.C., et al. Synthesis and optical properties of V_2O_5 nanorods. *J. Chem. Phys.*, 2007, **126**, P. 164701(1)–164701(3).
- [20] Wang Y.Q., Li Z.C., Zhang Z.J. Preparation of V_2O_5 thin film and its optical characteristics. *Front. Mater. Sci. China*, 2009, **3**, P. 44–47.
- [21] Subba Reddy Ch.V., Park K.-Il, et al. Simple preparation of V_2O_5 nanostructures and their characterization. *Bull. Korean Chem. Soc.*, 2008, **29**, P. 2061–2064.
- [22] Lee S.H., Cheong H.M., et al. Raman spectroscopic studies of amorphous vanadium oxide thin films. *Solid State Ionics.*, 2003, **165**, P. 111–116.
- [23] Chen W., Mai L., et al. Raman spectroscopic study of vanadium oxide nanotubes. *J. Solid State Chem.*, 2004, **177**, P. 377–379.
- [24] Lee S.H., Cheong H.M., et al. Improving the Durability of Amorphous Vanadium Oxide Thin-Film Electrode in a Liquid Electrolyte. *Electrochem. Solid-State Lett.*, 2003, **6**, P. A102–A105.
- [25] Julien C., Nazri G.A., Bergstrom O. Raman Scattering Studies of Microcrystalline V_6O_{13} . *Phys. Status solidi.B.*, 1997, **201**, P. 319–326.
- [26] Julien C., Guesdon J.P., et al. The influence of the substrate material on the growth of V_2O_5 flash-evaporated films. *Appl. Surf. Sci.*, 1995, **90**, P. 389–391.

Facile synthesis of (CdZn)Se nanocrystalline thin films via arrested precipitation technique (APT) for photovoltaic application

Chaitali. S. Bagade, Vishvnath. B. Ghanwat, Kishorkumar. V. Khot, Pallavi. B. Patil,
Rahul. M. Mane, P. N. Bhosale*

Materials Research Laboratory, Department of Chemistry, Shivaji University, Kolhapur 416004, India

*p.n.bhosale@rediffmail.com

PACS 81

DOI 10.17586/2220-8054-2016-7-3-553-557

Nanocrystalline (CdZn)Se thin films have been successfully synthesized via a simple and cost effective arrested precipitation technique. The deposition and synthetic strategy of (CdZn)Se thin films exert appreciable influence on the photovoltaic properties of solar cells. In this paper, systematic characterizations of optostructural, morphological, compositional and electrochemical properties have been carried out. The optical band gap was evaluated from UV-Vis-NIR spectra at wavelengths ranging from 400 – 1100 nm. X-ray diffraction (XRD) pattern reveals that the deposited film was nanocrystalline in nature and exhibited a cubic crystal structure. The dependency of microstructural parameters such as crystallite size has been studied. Scanning electron microscopy (SEM) images demonstrate that surface morphology was uniform, dense, smooth and well adhered to substrate surface. The as-deposited nanocrystalline (CdZn)Se thin film exhibits 0.61 % conversion efficiency at room temperature.

Keywords: (CdZn)Se, arrested precipitation technique (APT), thin films, semiconductor material, solar cells.

Received: 2 February 2016

Revised: 11 April 2016

1. Introduction

In recent years, the field of nanocrystalline semiconducting thin films is rapidly expanding. The increasing interest for these materials is due to the fact that these are characterized by properties which are substantially different from the corresponding ones for bulk semiconductors [1]. In this regard, group II-VI semiconductors are considered important technological materials due to their potential applications in optoelectronic devices [2]. Among these, cadmium zinc selenide (CdZn)Se is found to be an excellent material with a band gap value around 1.9 eV which makes it fairly interesting for the fabrication of solar cells through the photoelectrochemical route [3]. (CdZn)Se is a promising ternary material because of its tunable parameters, such as band gap and surface morphology. The most important applications of (CdZn)Se thin film is in solar cells, high efficiency thin film transistors, light emitting diodes, laser diodes and electroluminescent devices [4–7]. Various techniques have been used for the synthesis of (CdZn)Se thin films such as electrodeposition, chemical bath deposition (CBD), screen printing followed by sintering and metal organic chemical vapor deposition (MOCVD) [8–10]. One of the disadvantages of this technique is that some of them need sophisticated instrumentation along with vacuum and high temperature which increases the production cost of the material. However, the solution based deposition method, i.e. arrested precipitation technique offers the possibility of depositing thin films at low temperature under atmospheric conditions and at low fabrication cost. As a one step, environment friendly and low energy consumption aqueous technique, APT is based on controlled release of metal ions from metal complexes and reaction with chalcogen ions accordingly Ostwald ripening law [11].

2. Experimental

2.1. Deposition of thin film

We have developed a simple, rapid, low cost and environmentally friendly chemical method using nontoxic reagents for the deposition of proposed thin films because of its various advantages such as, large area deposition, relatively low temperature processes, no restriction on the use of substrate, reproducibility and most significantly no requirement of sophisticated equipment. A modified chemical deposition technique which is combination of CBD and controlled chemical growth process (CCGP) is employed. This modified technique is known as arrested precipitation technique (APT). It is based on the controlled release of metal and chalcogen ions and characterized by simple formulation, ease of set up and has the potential to replace

expensive energy and equipment demanding techniques. Additionally, surface morphology can be tuned by adjusting the pH of the bath solution, deposition time, temperature and the reagent concentration.

In a typical synthesis, 8 ml of 0.05 M [Cd-EDTA] and 12 ml of 0.2 M [Zn-EDTA] solution was taken in reaction beaker. The pH of bath was adjusted to 10.4 by dropwise addition of ammonia. Next, 20 ml of 0.25 M Na₂SeSO₃ solution was added to reaction bath with constant stirring. The total volume of reaction bath was adjusted to 50 ml by adding double distilled water then reaction mixture was stirred for 5 min to get homogeneous solution. Precleaned ITO glass substrates were immersed vertically close to the inner wall of reaction container and then kept at 50 °C temperature with constant substrate rotation 45 rpm and deposition time was kept 4 h. Various preparative parameters like pH, temperature, concentration and time were finalized at initial stage of deposition. After deposition, substrates were withdrawn from bath, sufficiently rinsed with double distilled water and dried at room temperature. The deposited thin film was uniform, peach in color and well-adhered to the glass substrate. This deposited thin film was used for subsequent investigations.

2.2. Characterizations of thin film

The thickness of the deposited thin films was measured by surface profiler (AMBIOS XP-1). A UV-Vis Spectrophotometer (Model: Shimadzu UV-1800) was used to record absorption spectra of deposited thin films in from 400 – 1100 nm. The structural properties of the thin films were studied using X-ray Diffractometer (Bruker AXS, D8 Model) using Cu K α ($\lambda = 1.5418 \text{ \AA}$) radiation for 2θ ranging from 10 ° to 80 °. Surface morphology and elemental analysis were examined using Scanning Electron Microscope (SEM) equipped with Energy Dispersive Spectroscopic (EDS) analyzer (JEOL-JSM-6360A). Photoelectrochemical (PEC) measurement was carried out by using (CdZn)Se thin film as photoanode in dark and under illumination using a 500 W tungsten filament lamp (intensity 30 mWcm⁻²) at electrochemical workstation (AUTOLAB PGSTAT 100 potentiostat). The photoelectrochemical cell was a two electrode system: (CdZn)Se film deposited on ITO substrate is a working electrode with active surface area of 1 cm² and graphite as counter electrode in sulphide/polysulphide as redox electrolyte.

3. Results and discussion

3.1. Thickness measurement

The thickness of the deposited thin film was found to be 730 nm. Thickness of the deposited films is controlled by two independent variables such as uniform growth and surface morphology. The process of precipitation of a substance in the solution depends on degree of supersaturation and formation of nucleus and its growth onto the substrate's surface.

3.2. Optical and structural analysis

Optical band gap energy of (CdZn)Se thin film was calculated by using the optical absorption spectra. The optical absorption spectra of deposited (CdZn)Se thin film was recorded from 400–1100 nm, as shown in Fig. 1(a). Electronic transition between valence and conduction bands starts at the absorption edge, corresponding to the minimum energy difference between the lowest energy of conduction band and the highest energy of valence band in material. Fig. 1(a) clearly shows that maximum optical absorption is observed at around 650–750 nm.

The band gap of (CdZn)Se thin film was determined by extrapolating straight line to the energy axis using equation (1)

$$\alpha = \frac{A(h\nu - E_g)^n}{h\nu}, \quad (1)$$

where ' α ' is absorption coefficient, ' $h\nu$ ' is photon energy ' A ' is a parameter that depends on the transition probability, ' h ' is planck's constant, ' E_g ' is optical band gap energy of the material and exponent ' n ' depends on nature of transition during absorption process. The value of n is 1/2, 3/2, 2, 3 for direct allowed, direct forbidden, indirect allowed and indirect forbidden transitions, respectively. The nature of the plots suggest a direct and allowed type of transition, since linear dependence is obtained at $n = 1/2$. The optical band gap value of (CdZn)Se thin film 1.91 eV was observed as shown in inset Fig. 1(a).

XRD pattern of (CdZn)Se thin film was carried out at room temperature in the range of 10 – 80 ° and shown Fig. 1(b). Broad and intense peaks in the XRD patterns confirm the nanocrystalline nature of thin film. XRD patterns of thin film exhibit peaks at 25.39 °, 42.17 °, 49.74 ° and 60.85 ° which are indexed to the (111), (220), (311) and (400) planes respectively of cubic CdSe (JCPDS card no. 19-0191). Also, the peaks at 12.47 °, 14.30 °, 20.13 °, 23.62 °, 29.32 ° and 31.83 ° are indexed to the (111), (200), (220), (311), (400) and (331) planes of cubic ZnSe (JCPDS card no. 02-0479). The XRD pattern of (CdZn)Se

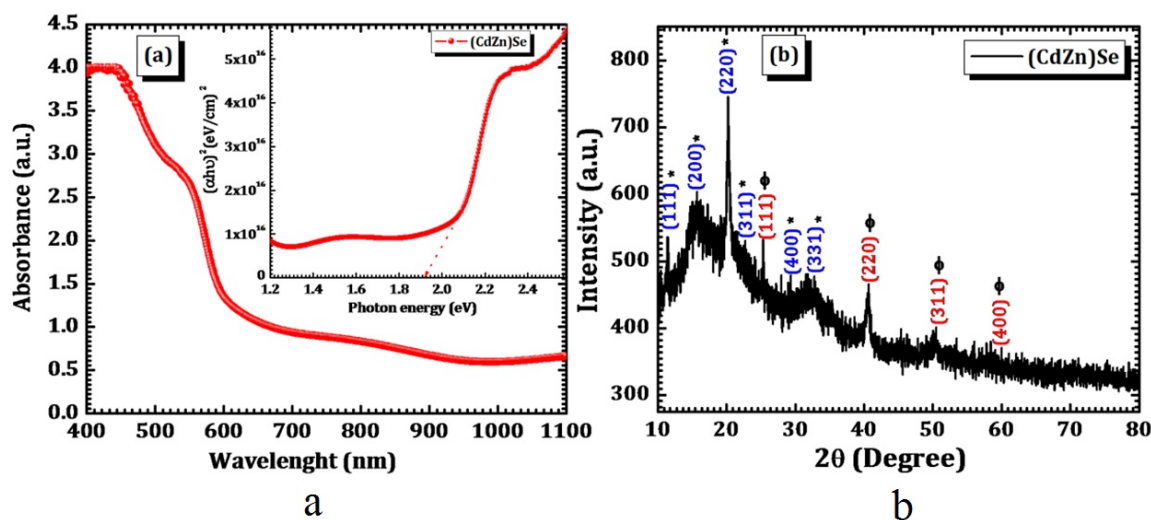


FIG. 1. (a) Optical absorption spectra and inset Fig shows Plots of $(\alpha h\nu)^2$ Vs. $(h\nu)$ (b) XRD pattern of (CdZn)Se thin film

nanocrystals was located between those for CdSe and ZnSe materials. Such phase formation of CdSe and ZnSe provides strong evidence for (CdZn)Se solid solution formation, which was in good agreement with the reported value [12, 13]. The average crystallite size was calculated from XRD patterns using Debye Scherrer's eq. (2)

$$D = \frac{0.94\lambda}{\beta \cos \theta}, \quad (2)$$

where ' λ ' is used X-ray wavelength (1.5406 Å), ' β ' is full width of half-maximum (FWHM) in radians and ' θ ' is Bragg's angle. The calculated crystallite size was 24 nm for the (CdZn)Se thin film.

3.3. Morphology and compositional analysis

In order to study the microstructures of (CdZn)Se thin films, scanning electron microscopy (SEM) was used. Fig. 2 shows high and low magnification SEM micro images of (CdZn)Se thin films. It shows formation of densely packed nanospheres like smooth homogenous surface morphology which was dispersed uniformly on the substrate surface. The presence of elements in deposited thin film was confirmed by EDS technique. Fig. 2(e) shows elemental distribution of the constituent elements for typical (CdZn)Se thin film. The elemental analysis was carried out only for Cd, Zn, and Se elements. The peaks at 3.55, 1.10 and 1.70 keV confirm the presence of Cd, Zn and Se in thin film, respectively [14].

3.4. Photoelectrochemical performance

The PEC performance of (CdZn)Se thin film was verified using a standard two electrode configuration in the dark and under an illumination of 30 mW/cm² light intensity and in 0.5 M sulfide/polysulfide redox electrolyte. After illumination, shifting of J-V curve in the fourth quadrant suggests that electrons were generated due to illumination, the magnitude of open circuit voltage increases with negative polarity towards (CdZn)Se electrode, indicating cathodic behavior of the photovoltage, which confirms that (CdZn)Se thin films are n-type. The current voltage (J-V) characteristics of glass/ITO/ (CdZn)Se 0.5 M polysulfide/graphite were measured. From the J-V measurements, the obtained value of J_{sc} was 1.162 mA/cm² and corresponding values of V_{oc} was 581 mV, respectively. Closely packed nanospheres improve the carrier transport mechanism and minimize the surface trap states. Such types of interconnected nanospheres provide higher effective surface area for light absorption. A conversion efficiency of 0.61% was achieved for (CdZn)Se thin film [15].

4. Conclusion

In conclusion, we report a facile chemical route for the deposition of (CdZn)Se thin film by using a simple and cost effective APT. From optical measurements, we can conclude that optical band gap was the direct allowed type, having a band gap energy 1.91 eV. X-ray diffraction pattern illustrated cubic crystal structure

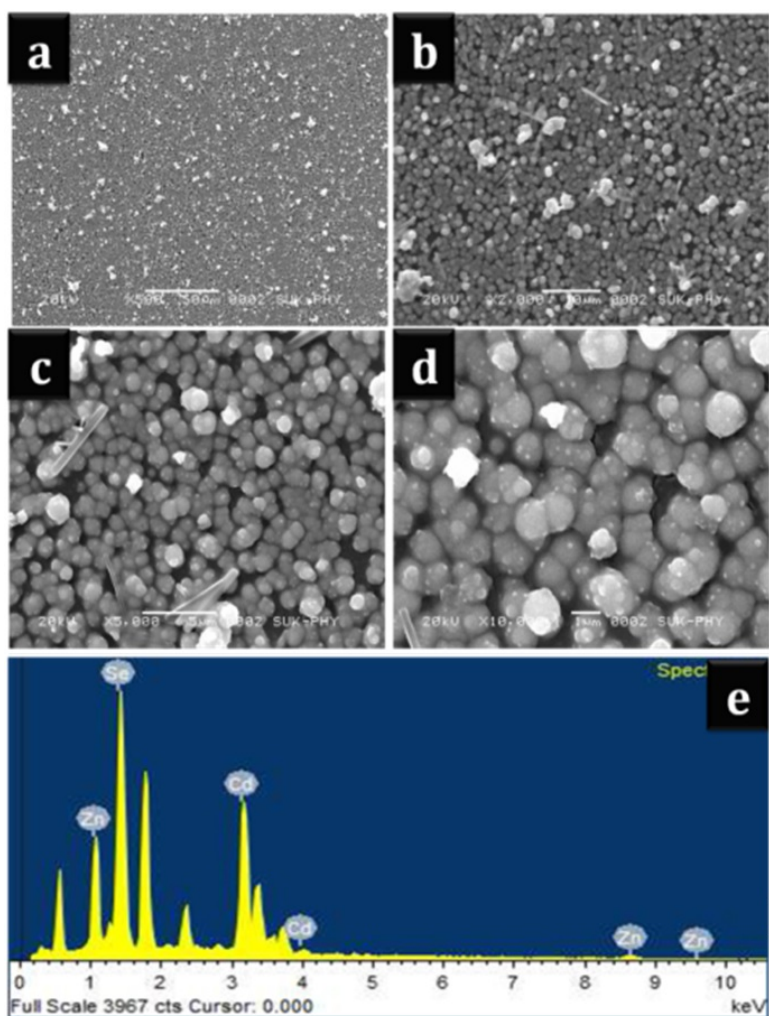


FIG. 2. (a-d) Low and high magnification SEM images and (e) EDS spectra of (CdZn)Se thin film

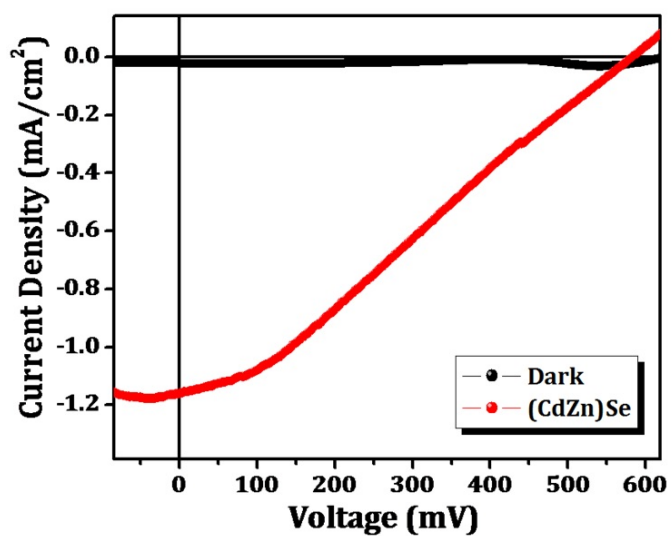


FIG. 3. $J - V$ characteristics of (CdZn)Se thin film in sulphide/polysulphide electrolyte

for both CdSe and ZnSe phases. SEM study illustrated that nanosphere like morphology for (CdZn)Se thin film was observed. Such morphology shows high efficiency due to large surface area for the absorption of light. EDS analysis shows presence of all elements (Cd, Zn and Se) in stoichiometric form. The highest conversion efficiency was obtained for (CdZn)Se thin film (0.61 %) thin film. Overall achieved results revealed that newly devised APT is a suitable method for the synthesis of different metal chalcogenide thin films.

Acknowledgement

One of the authors, Chaitali S. Bagade is very much thankful to Department of Science and Technology (DST), New Delhi for providing DST-INSPIRE fellowship for financial support (Registration No. IF140571). This work is also supported by the Priority Research Centre Program through the National Research Foundation of Korea (NRF) funded by the Ministry of Education, Science and Technology (2009-0094055).

References

- [1] Ubale U. Effect of complexing agent on growth process and properties of nanostructured Bi_2S_3 thin films deposited by chemical bath deposition method. *Mater. Chem. & Phys.*, 2010, **121**, P. 555–560.
- [2] Bagade C. S., Ghanwat V. B., Khot K. V., Bhosale P. N. Efficient improvement of photoelectrochemical performance of CdSe thin film deposited via arrested precipitation technique. *Mate. Lett.*, 2016, **164**, P. 52–55.
- [3] Zhai R., Wang S., Xu H. Y., Wang H., Yan H. Rapid formation of CdS, ZnS thin films by microwave-assisted chemical bath deposition. *Mater. Lett.*, 2005, **59**, P. 1497–1501.
- [4] Wu X., Yu Y., Liu Y., Xu Y., Liu C., Zhang B. Synthesis of Hollow $\text{Cd}_x\text{Zn}_{1-x}\text{Se}$ Nanoframes through the Selective Cation Exchange of Inorganic–Organic Hybrid ZnSe–Amine Nanoflakes with Cadmium Ions. *Angew. Chem. Int. Ed.*, 2012, **51**, P. 3211–3215.
- [5] Bagade C.S., Mali S.S., Ghanwat V.B., Khot K.V., Patil P.B., Kharade S.D., Mane R.M., Desai N.D., Hong C.K., Patil P.S., Bhosale P.N. A facile and low cost strategy to synthesize $\text{Cd}_{1-x}\text{Zn}_x\text{Se}$ thin films for photoelectrochemical performance: effect of zinc content. *RSC Adv.*, 2015, **5**, P. 55658–55668.
- [6] Akaltun Y., Yıldırım M.A., Atesn A., Yıldırım M. Zinc concentration effect on structural, optical and electrical properties of $\text{Cd}_{1-x}\text{Zn}_x\text{Se}$ thin films. *Mate. Res. Bull.*, 2012, **47**, P. 3390–3396.
- [7] Camargo-Gambo G.J., L. Pacheco J.S., Leon J.M. de, Conradson S.D., Hernández-Caldero I. Local structural characterization of Zn: Cd:Se ternary semiconductors. *Thin Solid Films*, 2005, **490**, P. 165–167.
- [8] Chavhan S.D., Mane R.S., Ganesh T., Lee W., Han S.H., Senthilarasu S., Lee S. H. Structural and optical properties of electrodeposited $\text{Cd}_{0.7}\text{Zn}_{0.3}\text{Se}$ thin films: Effect of annealing. *J. Alloys Compd.*, 2009, **474**, P. 210–213.
- [9] Suttrave D.S., Shahane G.S., Patil V.B., Deshmukh L.P. Micro-crystallographic and optical studies on $\text{Cd}_{1-x}\text{Zn}_x\text{Se}$ thin films. *Mater. Chem. Phys.*, 2000, **65**, P. 298–305.
- [10] Shan C.X., Fan X.W., Zhang J.Y., Zhang Z.Z., Wang X.H., Lu Y.M., Liu Y.C., Shen D.Z., Lu S.Z. Fabrication of ZnCdSe quantum dots under Stranski–Krastanow mode, *J. Cryst. Growth*, 2004, **265**, P. 541–547.
- [11] Mezrag F., Mohamed W.K., Bouariss N. The effect of zinc concentration upon optical and dielectric properties of $\text{Cd}_{1-x}\text{Zn}_x\text{Se}$. *Phys. B*, 2010, **405**, P. 2272–2276.
- [12] Cao J., Xue B., Li H., Deng D., Gu Y. Facile synthesis of high-quality water-soluble N-acetyl-l-cysteine-capped $\text{Zn}_{1-x}\text{Cd}_x\text{Se}/\text{ZnS}$ core/shell quantum dots emitting in the violet–green spectral range. *J. Colloid Interface Sci.*, 2010, **34**(8), P. 369–376.
- [13] Sheng Y., Weia J., Liu B., Peng L. A facile route to synthesize CdZnSe core-shell-like alloyed quantum dots via cation exchange reaction in aqueous system. *Mate. Res. Bull.*, 2014, **57**, P. 67–71.
- [14] Zhong X., Zhang Z., Liu S., Han M., Knoll W. Embryonic Nuclei-Induced Alloying Process for the Reproducible Synthesis of Blue-Emitting $\text{Zn}_x\text{Cd}_{1-x}\text{Se}$ Nanocrystals with Long-Time Thermal Stability in Size Distribution and Emission Wavelength. *J. Phys. Chem. B.*, 2004, **108**, P. 15552–15559.
- [15] Kharade S.D., Pawar N.B., Mali S.S., Hong C.K., Patil P.S., Gang M.G., Kim J., Bhosale P.N. Effect of copper content on optostructural, morphological and photoelectrochemical properties of $\text{MoBi}_{2-x}\text{Cu}_x\text{Se}_4$ thin films. *J. Mater Sci*, 2013, **48**, P. 7300–7311.

The study on ultrasonic velocities of $\text{Co}_x\text{Fe}_{3-x}\text{O}_4$ nanoferrofluid prepared by co-precipitation method

P. Chithralekha¹, C. Murugeswari², K. Ramachandran³, R. Srinivasan^{2,*}

¹Department of Physics, G. Venkataswamy Naidu College, Kovilpatti–628 502, India

²Department of Physics, Thiagarajar College, Madurai–625 009, India

³School of Physics, Madurai Kamaraj University, Madurai–625 021, India

p.lekha@yahoo.co.in, thirumalchandran@gmail.com, *r.srini2067@yahoo.co.in

PACS 47.65.C, 75.50.Mm

DOI 10.17586/2220-8054-2016-7-3-558-560

Nanoferrofluids of $\text{Co}_x\text{Fe}_{3-x}\text{O}_4$ were prepared by the chemical co-precipitation method by varying the value of x (0.2, 0.6 and 1.0 M). The structural and surface morphological investigations were done by X-ray diffraction (XRD) and SEM techniques respectively. The particle size calculated from the data of XRD, (3 1 1) plane revealed that the particle size increases with higher cobalt content and are in the range of 5 – 16 nm. The ultrasonic velocity of the aqueous carrier fluid and Cobalt ferrofluids was measured by varying the temperature from 30 – 70 °C. The ultrasonic velocities of magnetic nanoferrofluids decrease with concentration in the absence of magnetic field. The higher value for the nanoferrofluid's velocity compared to that of the carrier liquid in the absence of a magnetic field shows the influence of dispersed particles on the velocity of ultrasonic propagation.

Keywords: nanoferrofluid, co-precipitation, ultrasonic velocity.

Received: 5 February 2016

Revised: 4 April 2016

1. Introduction

Ferrofluids are stable colloidal dispersions of nanosized particles of ferro- or ferrimagnetic particles in a carrier liquid [1]. Among spinel ferrites, cobalt ferrite has attracted considerable attention in recent years due to its unique physical properties, such as high Curie temperature, large magnetocrystalline anisotropy, high coercivity, moderate saturation magnetization, large magnetostrictive coefficient, excellent chemical stability and mechanical hardness [2]. The physical and chemical properties of spinel nanoparticles are greatly affected by their synthetic route. For this reason, various methods have been reported in the literature for the preparation of these nanoscale spinel particles, e.g. the ceramic method, sol–gel, co-precipitation, solvent evaporation, hydrothermal, combustion, micro emulsion and citrate methods [3–7]. The magnetic properties of ferrites are directly related to the distribution of the cations over tetrahedral and octahedral lattice sites. Since the magnetic moments of the ions are ordered parallel within each sublattice and antiparallel between both sublattices, the difference in the magnetic moments between both sublattices gives magnetic moment to the ferrite crystal [8]. In the present work, attempts are made to investigate the change in the acoustic properties of magnetic fluids by increasing the concentration of cobalt in the spinel ferrite.

2. Experimental

Nanoferrofluids of $\text{Co}_x\text{Fe}_{3-x}\text{O}_4$ were prepared by the chemical co-precipitation method by varying the value of x (0.2, 0.6 and 1.0). Aqueous solutions of FeCl_3 , CoCl_3 and NaOH were prepared separately in the respective stoichiometric ratios. The NaOH solution was then added dropwise to FeCl_3 and CoCl_3 solutions separately and both were mixed with constant stirring using magnetic stirrer at 80 °C for 1 hr. The precipitate thus formed was isolated by centrifugation and washed several times with deionized water. The magnetic nanoferrofluids thus obtained were stabilized by the addition of surfactant and stirred at 80 °C for 1 hr. The resulting product was washed several times with deionized water to remove impurities and free radicals. The samples prepared at different values of x were characterized by XRD and SEM. Then, aqueous nanoferrofluids were prepared and ultrasonic velocity studies were carried out.

3. Results and Discussion

Figure 1 shows the XRD pattern of the samples. Series of characteristic peaks in the spectrum agree with standard CoFe_3O_4 XRD spectrum. The average crystalline size D of the particles from Scherer formula is in the range of 5 to 16 nm. The peaks at 30° (110), 45.4° (311) reveal that the presence of Fe_3O_4 [9]. The intensity of the peak increases with increased cobalt concentration. The characteristic peak at 40.25° appears due the presence of cobalt [10]. The SEM images of the samples are shown in Fig. 2.

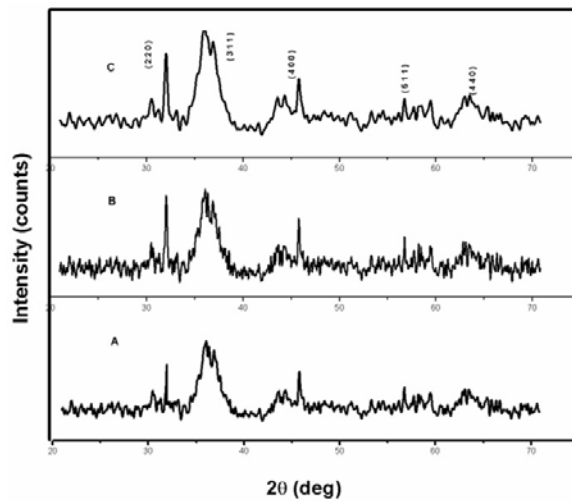


FIG. 1. The XRD pattern of $\text{Co}_x\text{Fe}_{3-x}\text{O}_4$ for (A) $x = 0.2$ M; (B) $x = 0.6$ M; (C) $x = 1.0$ M

The ultrasonic velocities of the nanoferrofluids for various values of x were measured by varying the temperature from 30 to 70°C . The variation of velocity with temperature of the nanoferrofluids is shown in Fig. 3. The ultrasonic velocity decreases with increased temperature for all values of x in the absence of magnetic field. The higher values of velocity for nanoferrofluids than that of the carrier liquid in the absence of magnetic field shows the influence of dispersed particles on the velocity of ultrasonic propagation. This indicates that the fluids of higher concentration are less compressible than those of lower concentration [11].

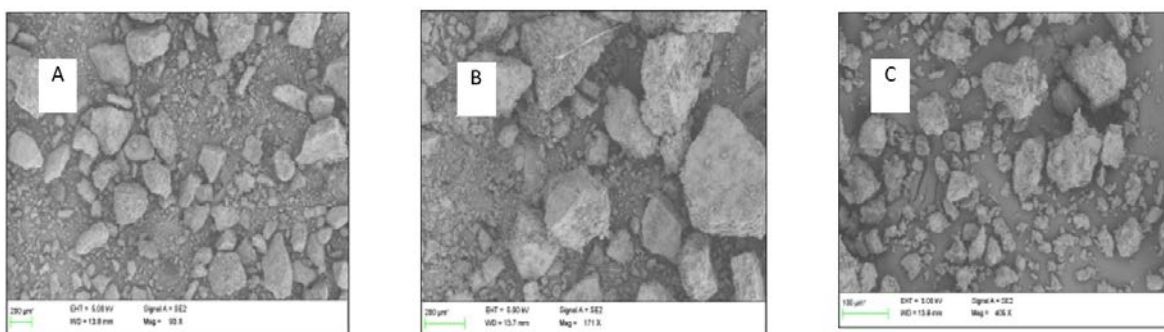


FIG. 2. The SEM images of $\text{Co}_x\text{Fe}_{3-x}\text{O}_4$ for (A) $x = 0.2$ M; (B) $x = 0.6$ M; (C) $x = 1.0$ M

4. Conclusion

Cobalt ferrite nanoferrofluids were prepared by the chemical co-precipitation method. The XRD pattern of the composite confirms the presence of cobalt containing magnetic phases without any additional phases. The SEM data shows that the formation of nanoparticles. The increase of ultrasonic velocity with cobalt is attributed to the increased compactness of the medium or reduction in free space between the components.

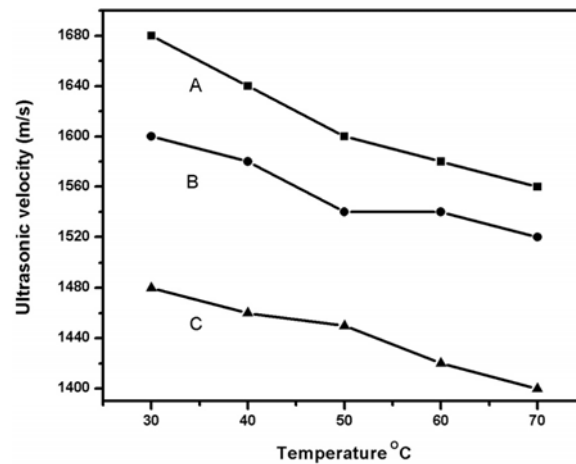


FIG. 3. The variation of ultrasonic velocity with temperature of $\text{Co}_x\text{Fe}_{3-x}\text{O}_4$ for (A) $x = 0.2$ M; (B) $x = 0.6$ M; (C) $x = 1.0$ M

References

- [1] Rosensweig R.E. *Ferrohydrodynamics*. Cambridge University Press, 1985.
- [2] Rosensweig R.E., Nestor J.W. and Timmins R.S. Rheology of transformer oil based ferrofluid. In Mater. Assoc. Direct Energy Convers. Proc. Symp. Chem. Eng. Ser. 1965, **5**, P. 104–106.
- [3] Papell S.S. Low viscosity magnetic fluid obtained by the colloidal suspension of magnetic particles. In U.S. Patent, 1965, **3**, P. 215–218.
- [4] Thomas J.R., *J. Appl. Phys.*, 1966, P. 372014.
- [5] Hess P.H. and Parker P.H. *J. Appl. Polym. Sci.*, 1966, P. 101915.
- [6] Rosensweig R.E. *J. Sci. American*, 1982, **247**(4), P. 136-138.
- [7] M. Motozawa, T. Sawada. *J. Magn. Mater.*, 2005, **289**, P. 66–68.
- [8] CheolGi Kim, Chong-Oh Kim, I. Dumitru, N. Lupu, and H. Chiriac *sensor letters*, 2007, **5**, P. 1–3.
- [9] Arunas Jagminas, Kęstutis Mažeika, Rokas Kondrotas, Marija Kurtinaitien, Aldona Jagminienė and Agnė Mikalauskaitė. *Int. J. Appl. Electromagnet. Mech*, 2014, **6**.
- [10] Ruo-Yu Hong, Jian-Hua Li, Shi-Zhong Zhang, Hong-Zhong Li, Ying Zheng, Jian-min Ding, Dong-Guang Wei. *J. App. Sur. Sci.*, 2009, **255**, P. 3485–3486.
- [11] Meaz T.M., Amer M.A. and El-Nimr M.K. *Egypt. J. Solids*, 2008, **31**(1).

Photoluminescence characteristics of nanocrystalline $\text{Ba}_{0.97}\text{Ca}_{0.03}\text{SO}_4:\text{Eu}$ by combustion method

P. Rubalajyothi, L. C. Nehru

Department of Medical Physics, School of Physics, Bharathidasan University,
Tiruchirappalli–620024, Tamilnadu, India
lcnehr@yahoo.com

PACS 61.43Gt, 88.20jj, 61.05cp, 61.50Lt

DOI 10.17586/2220-8054-2016-7-3-561-564

Nanocrystalline $\text{Ba}_{0.97}\text{Ca}_{0.03}\text{SO}_4:\text{Eu}$ powder has been prepared by combustion method. XRD shows orthorhombic structure, the lattice parameter values are $a = 8.836 \text{ \AA}$, $b = 5.440 \text{ \AA}$, $c = 6.859 \text{ \AA}$. The nanocrystalline powder $\text{Ba}_{0.97}\text{Ca}_{0.03}\text{SO}_4:\text{Eu}$ having a grain size of 47 nm, and also FTIR, PL, and three dimensional structure studies of the material and the results are presented in detail.

Keywords: $\text{Ba}_{0.97}\text{Ca}_{0.03}\text{SO}_4:\text{Eu}$, combustion method, XRD, computer software for structural bonding (JANA 2006, VESTA, PRIMA).

Received: 5 February 2016

Revised: 10 May 2016

1. Introduction

Thermoluminescence is the thermally stimulated emission of light from an insulator or semiconductor, following the previous absorption of energy from ionizing radiation such as gamma rays, X-rays, beta particles, alpha particles, neutrons and energetic ions. This phenomenon has been utilized for several applications. The main applications are in detection and measurement of absorbed radiation and dating of archaeological samples and detecting defects in solids. There are a number of commercially available TLDs for this purpose under different trade names the most popular are LiF:Mg,Cu,P , LiF:Mg,Ti , $\text{Ba}_{(1-x)}\text{Ca}_x\text{SO}_4:\text{Eu}$, $\text{K}_2\text{Ca}_2(\text{SO}_3)_4$, $\text{CaSO}_4:\text{Dy}$. Here, I have chosen the material $\text{Ba}_{(1-x)}\text{Ca}_x\text{SO}_4:\text{Eu}$, because this material is one that is having more prominence in the medical field. Here, calcium, sulfate and, barium materials were phosphorescent and these materials sensitivity and stability were high in the radiation dosimetry process. Sulfate is a common chemical in current everyday life and is used in a number of industrial processes. Sulfate is a major contributor to Climate change because when the light scattering it's efficiently increase the earth's albedo. CaSO_4 is another kind of chemical, mainly used in laboratory and industries. In precipitation processes, calcium sulfate is utilized to concentrate radioactive elements.

Photoluminescence (PL) is light emission from any form of matter after the absorption of photons. The observation of photoluminescence at a specific energy can be viewed as indication that the photon caused an excitation that populated an excited state associated with this transition energy. PL emission spectra of the nanomaterial without gamma irradiation, and the aim of this paper is to report on a preparations of $\text{Ba}_{0.97}\text{Ca}_{0.03}\text{SO}_4:\text{Eu}$ to prepare the new method and I have include this structure and hkl calculations were included.

2. Methods and details

The thermoluminescence properties of nanocrystalline $\text{Ba}_{0.97}\text{Ca}_{0.03}\text{SO}_4:\text{Eu}$ powder was successfully prepared by combustion method using a urea as fuel. Stoichiometric amounts of barium nitrate ($\text{Ba}(\text{NO}_3)_2$), calcium nitrate ($\text{Ca}(\text{NO}_3)_2 \cdot 4\text{H}_2\text{O}$), ammonium sulfate ($(\text{NH}_4)_2\text{SO}_4$) and doping material europium were dissolved in an aqueous solution of urea with constant stirring at room temperature. The solution was dried at $100 \text{ }^\circ\text{C}$ for 30 mins. After collect the powder to agate motor to grain and annealed at $500 \text{ }^\circ\text{C}$ for 1 h. The formation of the powder $\text{Ba}_{0.97}\text{Ca}_{0.03}\text{SO}_4:\text{Eu}$ material is confirmed by XRD taken at room temperature using PANalytical X-ray diffractometer with Cu target ($\text{Cu-K}\alpha$), line $\lambda = 1.54060 \text{ \AA}$ with step size $\Delta 2\theta = 0.05 \text{ }^\circ$.

3. Result

3.1. X-ray diffraction

In X-ray diffraction experiment, hkl values were obtained for the $\text{Ba}_{0.97}\text{Ca}_{0.03}\text{SO}_4:\text{Eu}$ powder sample. All the XRD peaks of the compounds have orthorhombic structure, as shown in Fig. 1. Hence, the lattice parameter is $a = 8.836$, $b = 5.440$, $c = 6.859$ values. The crystallite sizes were calculated using the Scherer formula. Based on this formula, the particle size was calculated to be 47 nm for the three dimensional structure for $\text{Ba}_{0.97}\text{Ca}_{0.03}\text{SO}_4:\text{Eu}$.

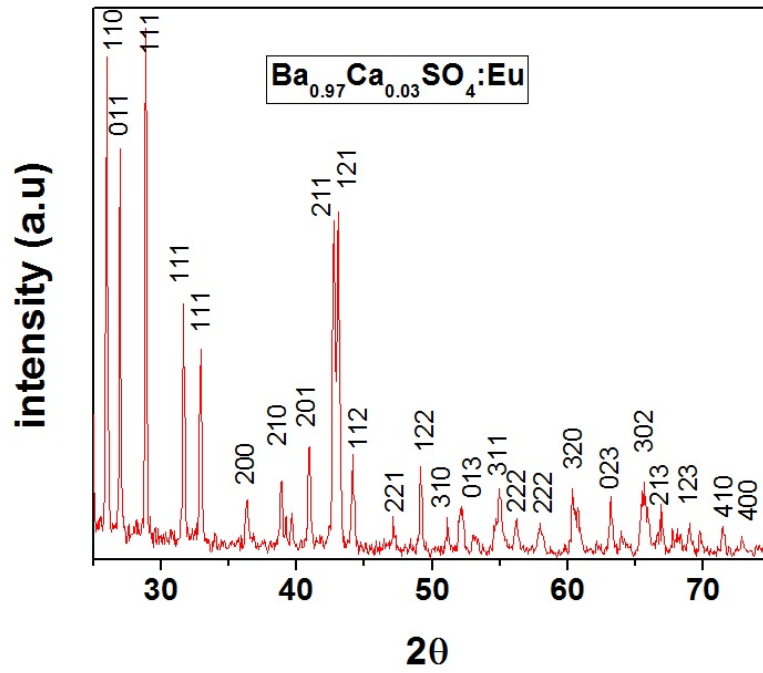


FIG. 1. X-ray Diffraction

TABLE 1. hkl calculation for $\text{Ba}_{0.97}\text{Ca}_{0.03}\text{SO}_4:\text{Eu}$

2θ	Θ	$\sin^2\theta$	$\sin^2\theta/k$	$h^2+k^2+l^2$	hkl
19.9735	9.986	0.029	1.9	2	110
22.7881	11.394	0.038	2.59	3	111
26.8557	13.427	0.053	3.56	4	200
31.5432	15.77	0.073	4.89	5	210
36.1701	18.085	0.096	6.41	6	211

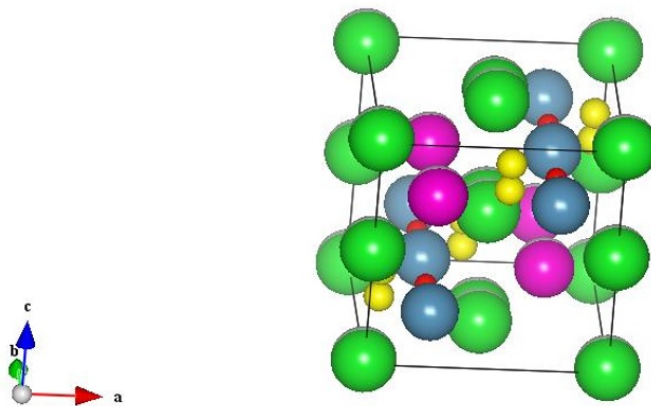


FIG. 2. By using the VESTA after the refinement method

The above diagram (Fig. 2) for $Ba_{0.97}Ca_{0.03}SO_4:Eu$ shows the three dimensional structure obtained by using the VESTA software. The green color represents the barium and blue represents the calcium and red represents the oxygen and yellow represents sulfur and magenta color represents the europium.

By using the following formula to calculate the electron density, we determined that the value is $0.08 \text{ e}/\text{\AA}^3$, meaning that this low electron mid bond density is ionic in nature:

$$\rho = 1/V f_0 \exp 2\pi i(hx + ky + lz),$$

where, v is the volume of the material, f_0 is the structure factor value by refinement method, hkl is the miller indices value, xyz is the cartesian co-ordinates.

3.2. Fourier transfer infrared spectroscopy

Fourier Transform Infrared (FTIR) Spectroscopy was also used to analyze the nanocrystalline $Ba_{0.97}Ca_{0.03}SO_4:Eu$ material. From this analysis, we confirmed the presence of many organic-based functional groups present in the $Ba_{0.97}Ca_{0.03}SO_4:Eu$ sample. In the FTIR spectrum showed peaks at 3437.72 cm^{-1} , 2925.03 cm^{-1} , 2351.56 cm^{-1} , 2064.43 cm^{-1} , 1643.72 cm^{-1} , 977.47 cm^{-1} , 639.14 cm^{-1} , 608.75 cm^{-1} , which are indicative of alcohols, phenols, alkanes, alkynes, carbonyls, aliphatic amines, alkyl halides, as shown in Fig 3.

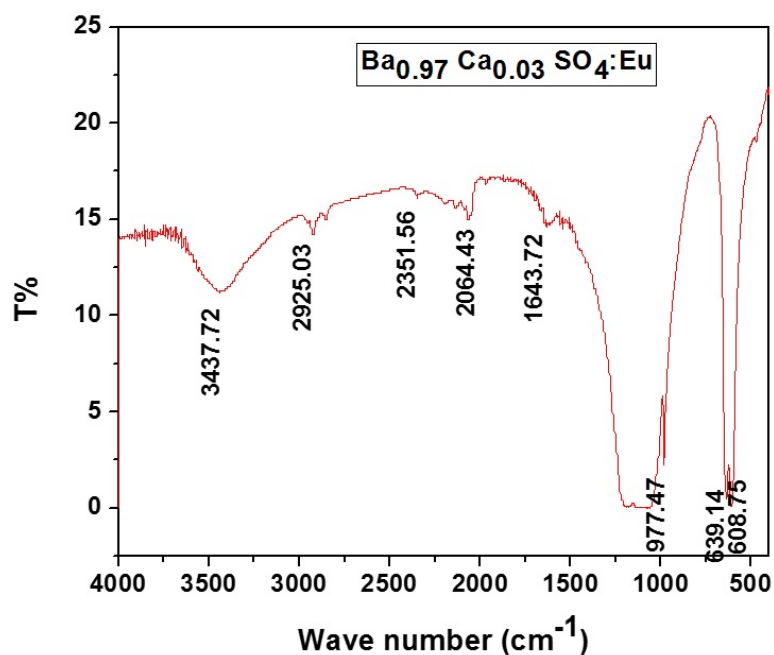


FIG. 3. Various functional group in FTIR

3.3. Photoluminescence

Figure 4 shows the PL emission spectra for un-irradiated nanocrystalline $Ba_{0.97}Ca_{0.03}SO_4:Eu$ with an excitation wavelength of 325 nm. The un-irradiated phosphor has six peaks at 378, 412, 441, 494, 520 and 595 nm. The peaks at 412, 441 and 494 nm may be attributed to the same Eu^{2+} emission arising due to the transition from eg to $t2g$ levels of the $4f65d$ configuration to $8S7/2$ levels of the $4f65d$ configuration but with Eu^{2+} occupying different lattice sites [2,6]. The peak at 520 and 595 nm suggest that europium also enters the lattice in its trivalent state. This peak may be assigned to the Eu^{3+} emission due to the transition $5D1 \rightarrow 7F1$ [4,7]. The disappearance of the 520 nm and 595 nm peak might be due to the conversion of Eu^{3+} to Eu^{2+} due to irradiation [1,3]. The disappearance of the 441 and 494 nm peak is quite surprising; however, it may be speculated that on irradiation, the 441 nm and 494 nm peak of Eu^{2+} might be shifted to the lower wavelength side to show its emission at 378 nm along with the existing one at 378 nm [8].

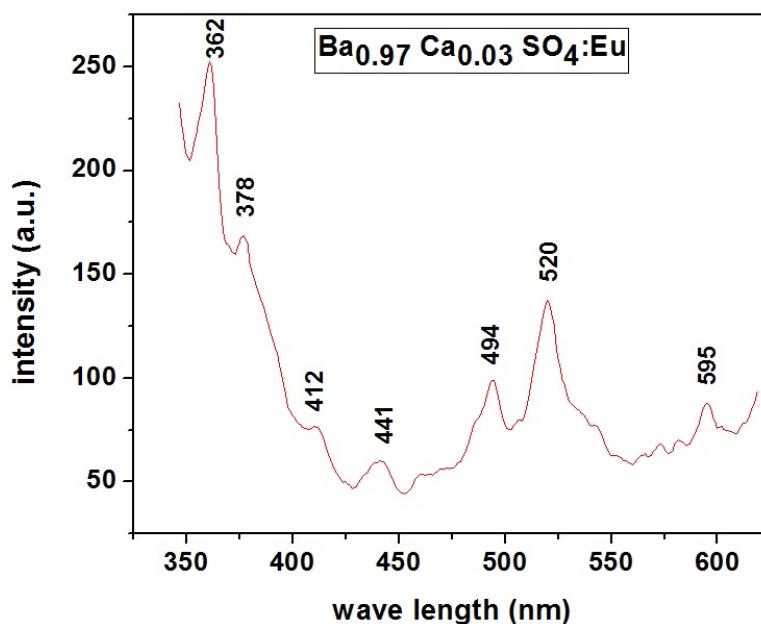


FIG. 4. Photoluminescence

4. Conclusion

Nanocrystalline Ba_{0.97}Ca_{0.03}SO₄:Eu powder has been prepared by the combustion method and subsequently confirmed by XRD. The Ba_{0.97}Ca_{0.03}SO₄ structure is orthorhombic in nature. The size of the Nanocrystalline is 47 nm. The size of the particle is calculated by using the Scherrer formula. Additionally, various organic-based functional groups are present in FTIR spectrum. The excitation wavelength is 325 nm for photoluminescence for the conversion of Eu²⁺ to Eu³⁺.

References

- [1] Merz J.L., Pershan P.S. Charge Conversion of Irradiated Rare-Earth Ions in CaF₂. II. Thermoluminescent Spectra. *Phys. Rev.*, 1967, **162**(2), P. 235.
- [2] Blasse G. *Luminescence in Inorganic Solids*. Plenum, New York, 1978, P. 457–494.
- [3] Bapat V.N. Thermoluminescence of CaF₂(Eu): influence of the presence of other lanthanide impurities. *J. Phys. C: Solid State Phys.*, 1977, **12**(19), P. 10L465–67.
- [4] Pode R.B., Dhoble S. Radiation-induced defects in Eu³⁺-activated yttrium vanadates. *J. Phys. D: Appl. Phys.* 1998, **31**(1), P. 146.
- [5] Xiong G., Pengfei W., Wai K.C., Engju C. Effect of γ -irradiation on structures and luminescent properties of nanocrystalline MSO₄:Eu_{x+3} (M = Ca, Ba, Sr, x = 0.001–0.005). *J. Phys. Chem. Solids*, 2000, **61**(1), P. 115–121.
- [6] Pandey A., Sonkawade R.G., Sahare P.D. Thermoluminescence and photoluminescence characteristics of nanocrystalline K₂Ca₂(SO₄)₃:Eu. *J. Phys. D: Appl. Phys.*, 2002, **35**(21), P. 2744–2747.
- [7] Esparza-Garcia A.E., Garcia-Hipolito M., Aguilar-Frutis M. A, Falcony C., Cathodoluminescent and Photoluminescent Properties of Al₂O₃ Powders Doped with Eu. *Phys. Status Solidi A*, 2002, **193**(1), P. 117–124.
- [8] Lochab S.P., Sahare P.D., Chauhan R.S., Numan S., Pandey A. Thermoluminescence and photoluminescence study of Ba_{0.97}Ca_{0.03}SO₄:Eu. *J. Phys. D: Appl. Phys.*, 2006, **39**(9), P. 1786–1792.
- [9] Rangeela Y.D., Doredrajit S.S. Synthesis and TL glow curve analysis of BaSO₄:Eu, Dy phosphor. *J. Luminescence*, 2012, **132**(6), P. 1575–1580.

Observation of insulating and metallic-type behavior in Bi_2Se_3 transistor at room temperature

V. Gunasekaran, G. H. Park, K. S. Kim, M. Suemitsu, H. Fukidome*

Research Institute of Electrical Communication, Tohoku University, 2-1-1, Katahira, Aoba-ku,
Sendai 980-8577, Japan

guna@riec.tohoku.ac.jp, *fukidome@riec.tohoku.ac.jp

PACS 72.20.-i

DOI 10.17586/2220-8054-2016-7-3-565-568

Topological insulators are a new class of electronic materials with promising device applications. In this work, multi-layer Bi_2Se_3 field effect transistors (FETs) are prepared by standard lithography followed by mechanical exfoliation method. Electrical characterization of the FET has been studied at room temperature. We observed both insulating and metallic-type transport behavior when device was gate-biased. Electron-phonon scattering plays a vital role in observing this behavior. We assume that this sort of behavior could be raised from the inherent metallic surface and semiconducting interior bulk properties of Bi_2Se_3 .

Keywords: bismuth selenide, topological insulator, transistors.

Received: 9 February 2016

1. Introduction

Recently, topological insulators (Bi_2Se_3 , Bi_2Te_3 and Sb_2Te_3) have attracted much attention because of their bulk band gap (0.3 eV) and spin-polarized surface states with conductive massless Dirac Fermions [1]. Interestingly, Bi_2Se_3 has rhombohedral crystal structure which consists of Se or Bi lattices in stacked manner with the sequence of Se-Bi-Se-Bi-Se. This forms a sheet-like structure in which the adjacent quintuple layers (QL) are bonded by van der Waals forces [2]. According to recent reports, Bi_2Se_3 has been found to have potential application in field effect transistors (FET), thermoelectric materials, low-power spintronics and opto-electronics. Particularly, Bi_2Se_3 nanowire FET exhibits superior current-voltage characteristics with a large On/off current ratio, well saturated output current, zero cutoff current, and sharp turn-on voltage [2–5]. These unique properties open up a new consideration of Bi_2Se_3 as a potential candidate in spintronics and nanoelectronics.

There are few reports available on electrical transport studies of Bi_2Se_3 nanowire transistor [3], epitaxial growth of Bi_2Se_3 thin films [4], ultra-thin Bi_2Se_3 thin film [6], and few-layer nano-plates [7]. All these transport studies were investigated in low-temperature environment. When an ultra-thin (thickness ~ 3.5 nm) sample with approximately 3 QL investigated, a strong insulating state was observed. However an improved conductance was observed for the samples with thicknesses of 6.5 nm to 14 nm [3].

Yet, up to now, much less attention has paid to investigations on room-temperature transport measurement of Bi_2Se_3 transistors. The reason behind that, since Bi_2Se_3 has gapless surface states, it could show surface metallic conduction however the bulk transport conduction cannot be easily identified at room temperature. As reported by H. Zhu et al, by tuning gate electric field at different temperatures, the bulk transport conduction can be isolated from the surface metallic conduction [3]. In this work, we fabricated multi-layer (ML) Bi_2Se_3 transistor (back-gated) and investigated their characteristics at room temperature. We observed both insulating and metallic-type transport behavior when the device was gate-biased.

2. Experimental

2.1. Sample preparation

High quality 2D n- Bi_2Se_3 crystals were purchased from 2D Semiconductors Co. Mechanical exfoliation method was used to remove the Bi_2Se_3 layers by peeling off, followed by transferring the layers into SiO_2/Si substrates (resistivity $\sim 1\text{--}15$ ohm cm^{-1}). Heavily p-doped silicon with a 90 nm thick thermally grown SiO_2 top layer was used as substrates. Before transferring the layers, the substrates were well cleaned ultrasonically with acetone, ethanol and DI water. ML Bi_2Se_3 flakes were visually identified by using an optical microscope and chosen for device fabrication. Further confirmation for the number of layers in the sample was verified using Raman spectroscopy. We measured the thickness of Bi_2Se_3 layer as 143 nm using Bruker (Model: Dektak XT) thickness measurement system.

2.2. Device fabrication

We used a standard photolithography processes to make an electrode pattern. Mask aligner instrument (SUSS MicroTec; Model: MJB4, GmbH, Germany) was used. The photoresist (PR) AZ 5214E was spin-coated over the sample and UV light was exposed through Cr mask. Electron-beam evaporation [Sanyu Electron Model: SVC-700, LEB/4G] method was used to make Ti/Au (10/30 nm) electrodes as source and drain and structured by lift-off using acetone. Silver contact was made to Si substrate as back-gate. Detailed lithographic processes are schematically shown in Fig. 1. The channels of these fabricated Bi₂Se₃ transistor are 10 μm in length and 12 μm in width. After fabrication, the electrical transport characteristics of the devices were analyzed with semiconductor device analyzer (Agilent Technologies, Model: B1500A). These measurements were carried out under ambient conditions.

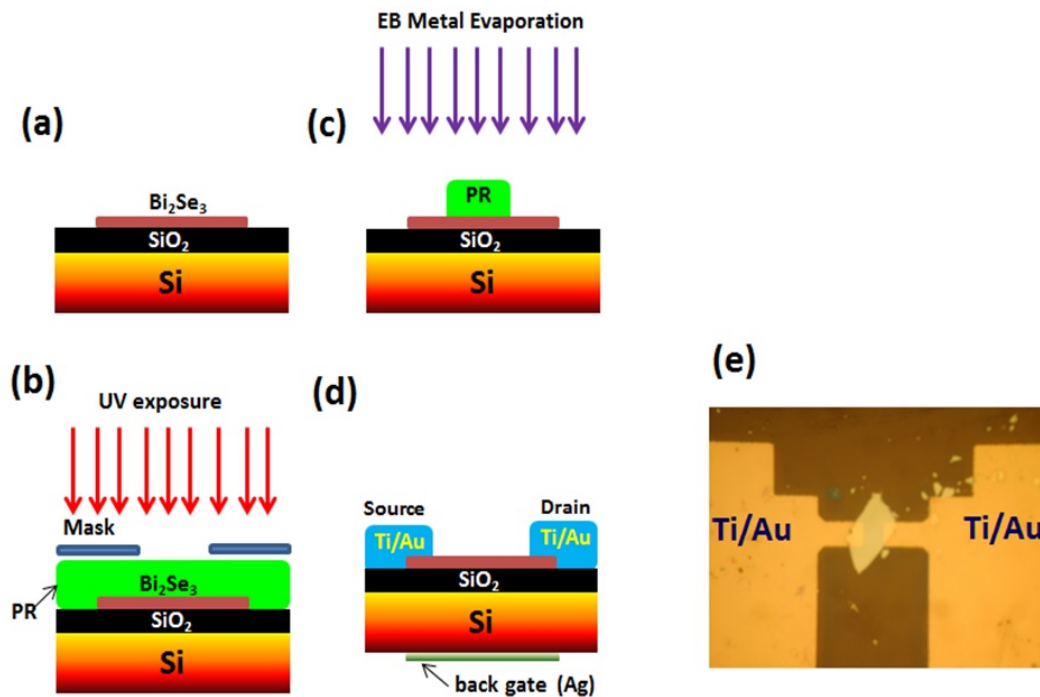


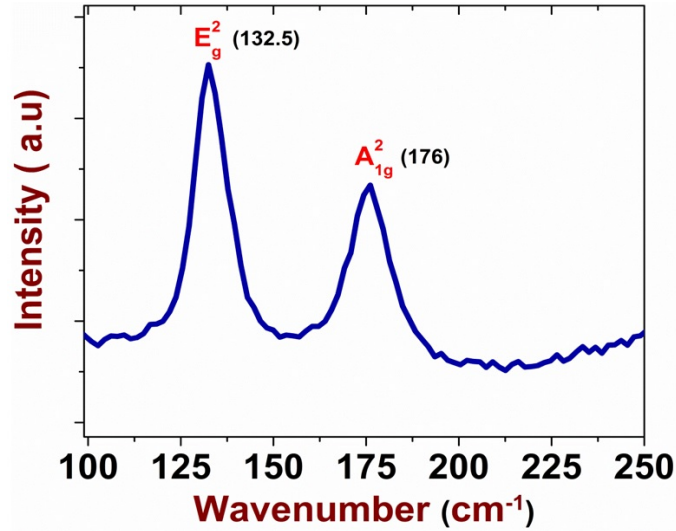
FIG. 1. (a) ML Bi₂Se₃ is transferred on SiO₂/Si substrate using mechanical exfoliation; (b) Photo-resist (PR) AZ 5214E is spincoated over the sample and UV exposure through Cr mask; (c) Evaporation of Ti/Au metals over the sample using electron beam evaporation method; (d) after lift-off process, the fabricated device with source, drain electrode pattern and back-gate (Ag electrode) configuration; (e) Optical image of fabricated FET device with Ti/Au electrodes

3. Results and discussion

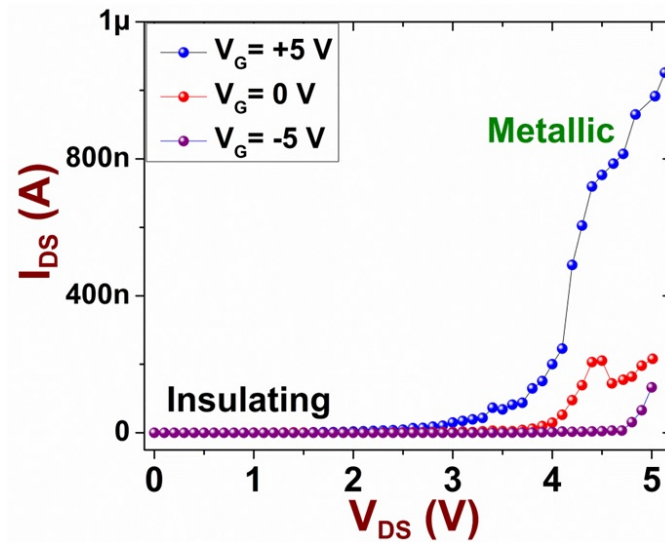
Figure 2 shows the Raman spectrum of ML Bi₂Se₃ in the range of 100 – 250 cm⁻¹. Raman spectroscopy is mainly used to identify and confirm the number of layers present in the sample [8,9].

We carried out Raman spectroscopy measurements using a micro-Raman spectroscopy system (model: Renishaw inVia) with a 514.5 nm laser excitation source. The power of incident laser was set as 35 mW and was focused through a 100× objective. Two characteristic peaks were observed at ~132.5 cm⁻¹ and ~176 cm⁻¹, which correspond to an in-plane mode (E_g^2) and an out-of-plane mode (A_{1g}^2) of Rhombohedral Bi₂Se₃ lattice vibrations respectively [10–12]. According to Zhao et al, the Raman active out-of-plane mode (A_{1g}^2) signal is strongly reduced in bulk Bi₂Se₃ crystal rather than strong sharp peak appeared for few layer QLs [13]. In our case of ML Bi₂Se₃ (thickness ~143 nm), a diminution in signal (A_{1g}^2) was observed as appeared in Ref. 13, which further confirms sample's multi-layer nature.

The n-Bi₂Se₃ field effect transistor (FET) characteristic measurements were conducted on a probe station. The drain-source current (I_{DS}) versus drain-source voltage (V_{DS}) under different gate bias (V_G) has been

FIG. 2. Raman spectra of ML Bi_2Se_3 flake

measured at room temperature and the results are shown in Figure 3. The applied gate voltage is changed from -5 V to 5 V in 5 V steps. The output characteristics show an insulating and metallic-type behavior when the gate biases (V_G) is varied. At low gate-voltage ($V_G < 0$), no remarkable increase in drain current was observed. While increasing gate-voltage, a significant increase in drain current was observed. A sharp increase in drain current can be seen at $V_G = 5$ V in Fig. 3. By tuning the gate voltage, a metallic-like behavior was observed [14].

FIG. 3. I_{DS} - V_{DS} under different gate bias at room temperature

According to previous reports on Bi_2Se_3 nano-wire FET, a metallic-like conduction was observed where mobility-temperature relationship plays a major role in minimizing electron-phonon scattering at low-temperature (77 K) [15,16]. However, in our case, we observed both insulating and metallic-like transport behavior under different gate bias at room-temperature. At low-gate voltage ($V_G < 0$), the electron-phonon scattering is a dominating factor which limits the electron conduction causing insulating behavior in Bi_2Se_3 channel [16]. However, when gate bias is increased, the induced electron conduction dominates which suppress the electron-phonon scattering resulting metallic-like characteristics. We believe that the evolution of this metallic-type behavior at room temperature is attributed due to strong suppression of surface phonon scattering which has been achieved through gate-tuning.

Our results are further evidenced by previous observations where a strong insulating state was found in ultra-thin Bi₂Se₃ crystals (3 QL thickness \sim 3.5 nm). But when the thickness of film is \sim 6 – 14 nm, a weakly insulating state was observed in Bi₂Se₃ thin films which is attributed mainly due to strong interlayer (top and bottom) couplings [3, 17–19]. This results in the absence of scattering which shows an increased contribution for the multi-layer ($>$ 100 nm) to the total carrier conduction. The amplitude of scattering and their related character as a function of thickness are associated with the topologically protected gapless surface states of Bi₂Se₃. Hence the electronic transport in ML Bi₂Se₃ is governed by both parallel surface and bulk contributions.

4. Conclusion

In conclusion, we have successfully fabricated ML *n*-Bi₂Se₃ FET and investigated their transistor characteristics at room temperature. Observation of both insulating and metallic transport in output characteristics further confirm that the intrinsic bulk bandgap nature and conductive surface states exist in Bi₂Se₃. Our findings may provide important guidance for the room-temperature transport studies on topological insulators.

Acknowledgement

This work was financially supported by the Grant-in-Aid for Scientific Research of Japan Society for the Promotion of Science (JSPS). The author (V. G.) extends sincere thanks to lab members Mr. Fuminori Sasaki, Mr. Keiichiro Tashima for their help in device fabrication and characterization.

References

- [1] Zhang H., Liu C.-X., et al. Topological insulators in Bi₂Se₃, Bi₂Te₃ and Sb₂Te₃ with a single Dirac cone on the surface. *Nat. Phys.*, 2009, **5**(6), P. 438–442.
- [2] Dresselhaus M.S., Chen G., et al. New directions for low-dimensional thermoelectric materials, *Adv. Mater.*, 2007, **19**, P. 1043–1053.
- [3] Zhu H., Richter C.A., et al. Topological insulator Bi₂Se₃ nanowire high performance field-effect transistors. *Sci. Rep.*, 2013, **3**, P. 1757.
- [4] Jerng S.K., Joo K., et al. Ordered growth of topological insulator Bi₂Se₃ thin films on dielectric amorphous SiO₂ by MBE. *Nanoscale*, 2013, **5**, P. 10618–10622.
- [5] McIver J.W., Hsieh D., et al. Control over topological insulator photocurrents with light polarization. *Nat. Nanotech*, 2012, **7**, P. 96–100.
- [6] Cho S., Butch N.P., Paglione J.P., Fuhrer M.S. Insulating Behavior in Ultrathin Bismuth Selenide Field Effect Transistors. *Nano Lett.*, 2011, **11**, P. 1925–1927.
- [7] Kong D., Dang W., et al. Few-Layer nanoplates of Bi₂Se₃ and Bi₂Te₃ with highly tunable chemical potential. *Nano Lett.*, 2010, **10**, P. 2245–2250.
- [8] Novoselov K.S., Geim A.K., et al. Electric field effect in atomically thin carbon films. *Science*, 2004, **306**, P. 666–669.
- [9] Novoselov K.S., Jiang D., et al. Two-dimensional atomic crystals. *Proc. Natl. Acad. Sci. U. S. A.*, 2005, **102**, P. 10451–10453.
- [10] Liu X., Smith D.J., et al. Structural properties of Bi₂Te₃ and Bi₂Se₃ topological insulators grown by molecular beam epitaxy on GaAs (001) substrates. *Appl. Phys. Lett.*, 2011, **99**, P. 171903–171906.
- [11] Dang W.H., Peng H.L., et al. Epitaxial heterostructures of ultrathin topological insulator nanoplate and graphene. *Nano Lett.*, 2010, **10**, P. 2870–2876.
- [12] Zhang J., Peng Z.P., et al. Raman spectroscopy of few-quintuple layer topological insulator Bi₂Se₃ nanoplatelets. *Nano Lett.*, 2011, **11**, P. 2407–2414.
- [13] Zhao S.Y.F., Beekman C., et al. Fabrication and characterization of topological insulator Bi₂Se₃ nanocrystals. *Appl. Phys. Lett.*, 2011, **98**, P. 141911.
- [14] Joen D.S., Burk D.E. MOSFET *electron* inversion layer mobilities—a physically based semi-empirical model for a wide temperature range. *IEEE Trans. Elec. Dev.*, 1989, **36**, P. 1515–1518.
- [15] Zhang Q., Iannaccone Q., Fiori G. Two-dimensional tunnel transistors based on Bi₂Se₃ thin film. *IEEE Elec. Dev. Lett.*, 2014, **35**(1).
- [16] Zhu H., Zhao E. Topological insulator Bi₂Se₃ nanowire field-effect transistors. *ECS Transactions*, 2014, **64**(17), P. 51–59.
- [17] Liu M., Chang C., et al. Electron interaction-driven insulating ground state in Bi₂Se₃ topological insulators in the two dimensional limit. *Arxiv:1011.1055*, 2010 [cond-mat.mtrl-sci].
- [18] Hirahara T., Sakamoto Y., et al. Anomalous transport in an n-type topological insulator ultrathin Bi₂Se₃ film. *Phys. Rev. B.*, 2010, **82**, P. 155309-6.
- [19] Steinberg H., Gardner D.R., Lee Y.S., Herrero P.J. Surface state transport and ambipolar electric field effect in Bi₂Se₃ nanodevices. *Nano Lett.*, 2010, **12**(10), P. 5032–5036.

Asymmetric molecular diode energy calculation using Extended Hückel and Parametric method

A. Mallaiah¹, G. N. Swamy², K. Padmapriya³

¹Research Scholar, JNTUA, Anthapuramu, A.P, India

²Department of EI&E, VR Siddhartha Engineering College, Vijayawada, A.P, India

³Department of ECE, JNTUK, Kakinada, A.P, India
malli797@gmail.com

PACS 31.15.bu, 73.40.Ei, 73.40.Cg, 81.07.Nb

DOI 10.17586/2220-8054-2016-7-3-569-574

The Electrical rectification properties of an asymmetric molecule's amine group and nitro group has been studied by placing the compound between two gold electrodes and using Extended Hückel, Parametric and non-equilibrium Green's function (NEGF) formalisms. The conductance of the device falls exponentially with an increased number of CH₂ moieties in the molecule. Current rectification was observed based on HOMO, LUMO gaps and potential drop across the molecules. The investigation of the spatial dispersion of frontier orbitals, the highest occupied molecular orbitals, lowest unoccupied molecular (HOMO-LUMO) of the molecule command the transmission of electrons in the molecule. The results demonstrate that, depending on the group of molecules and number of CH₂ moieties present, current shipping from left side of device to right side of device based on orbital energy gaps. Our findings demonstrate that a true molecular diode can be created, and thus miniaturize the electronic circuit's size to the Nano scale.

Keywords: HOMO, LUMO, orbital energy, molecular diode, NEGF.

Received: 18 February 2016. Revised: 11 May 2016. Final revision: 13 May 2016

1. Introduction

One of the most active fields in nanotechnology research is the fabrication of electronic circuits with Nano scale devices. Several research groups have been succeeded in fabricating Nano devices in form of rectifiers, switches, logic gates and flip flops in which active part of device is single molecule and metallic Nano wire [9].

Aviram and Ratner [1] suggested that a single molecule with a Donor bridge Acceptor (DBA) behaves as a diode when placed in an electric field. Electrons can move cathode terminal to acceptor, and electrons from donor and then transferred towards anode. The working principle of this device is similar to "valve" diode introduced by Shockley 65 years back. Such hybrid molecular electronic (HME) device comprising molecules embedded between electrodes of utilizing donor molecules NH₂, OH, CH₃, CH₂CH₃, acceptor molecules NO₂, CN, CHO, COR' where R' is an aliphatic chain [4].

The source of conductivity for a poly phenylene based chains is a set of π type orbitals that lie supra and infra the level of the molecule when it is of a planar or nearly planar geometry. In a planar conformation the π orbitals associated with each individual atom convergence or coupled in various combinations to create a set of extended π orbitals that crosses the length of the molecule. This occurs because there is a significant energetic advantage that arises from delocalizing valance electrons in orbitals that span or nearly span the length of the entire molecule. The low energy π orbital available in the molecule and high energy π orbital dissent somewhat they do have nodal planes (planes where the orbital vanish) pointed perpendicularly to the axis of a wire like molecule. The higher the energy of the orbital the more nodal planes it will contain [15].

A delocalized π orbital usually extended across one or more of the neighboring aromatic rings in the molecule as well as across other intervene multiply bonded groups can add or merge to form a number of larger moleculespanning π orbitals, each molecule bearing [4] a different nodal structure and energy. There are five possible asymmetric factors involved in the junction: electrode material; electrode shape; interface [6]; configuration of junction; and the nature of the molecular bridge. In this paper our discussion concerns the molecular bridge. Like semiconducting material the introduction of electron donating and electron receiving groups into the molecular wire can achieve the p-n junction like molecules. These materials have been exploited as the key electronic components with a light emitting diodes, transistors, sensor devices, photovoltaic solar cells.

Recently Nonequilibrium green's function (NEGF) formalism has become a powerful tool to explore electronic transportation [14] at a real molecular level due to the contribution by Datta and co-workers [7–9],

Ratner and co-workers [23–25], Di Carlo and co-workers [12], Xue and co-workers [10], Guo and co-workers [13], and so on. Although it has been used in a wide variety of systems, there is less concern on the effect of asymmetrically substituted groups in previous work. In the present work we will consider a series of model systems constructed by two sulfur atoms by a substituted molecule as shown in Fig. 1 and exploit the potential molecular rectification.

This paper organized as follows: In section 2 we give a brief description of the calculation method and structure of molecules. Section 3 shows the detailed analysis of the HOMO & LUMO energies between the sulfur atoms. The effect of the molecular orbitals and energies are analyzed. The HOMO, LUMO gap (HLG) and potential drop listed. A brief summary is given in Section 4.

2. Computational methods

2.1. Geometry optimization

We performed geometry optimization of the DBA diode nanowire. Our model includes sulfur atoms attached on each side of the molecule. The optimization was performed with the Argus Lab program [16–19] Austin Model 1 (AM1) in which the inclusion of enhanced and correlation function along with the polarization functions on heavier atoms and hydrogen's becomes correctly to report the nature of LUMO and other higher unoccupied orbitals. These serve as channels for electron tunnelling from acceptor to donor in an applied bias voltage. The electron transfer mechanism in the molecular system largely depends up on the spatial location [20] as well as spatial orientation of the frontier molecular orbitals. The molecular orbitals can be visualized using Argus Labs program. From the orbital HOMO, LUMO energy values, the potential drop (PD) across the molecule is calculated. This allows one to estimate if the system works like a rectifier when a suitable voltage applied to the molecule. At a suitable bias voltage the electron is loaded to the acceptor side (LUMO) and then it tunnels to the donor side (HOMO). This occurs when the rectifier molecule is in an instantaneous negatively-charged state.

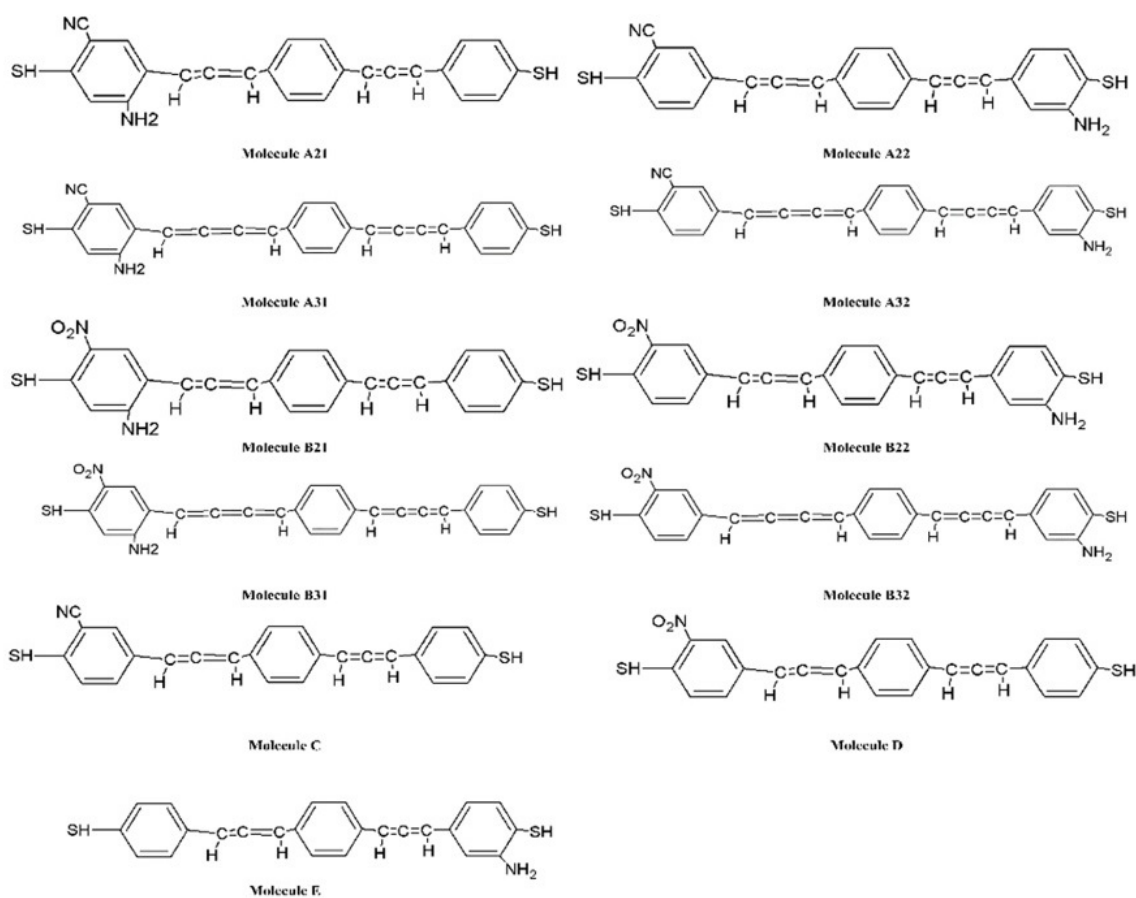


FIG. 1. Structure of donor π acceptor nanowire which consists of a unimolecular bridge

The molecular structures for DBA molecules A21, A22, A31, A32 were designed using CN and NH₂ molecules with same position of benzene ring and opposite sides of the benzene position having odd and even number of separation bonds, while structures B21, B22, B31, B32 structures with NO₂ and NH₂ molecules in addition to that C, D, E structures are shown in Fig. 1. All Structures' HOMO and LUMO energy gaps were optimized and calculated via parametric method 3 in Argus lab [20].

Above listed molecules the DBA remains almost linear with small difference of linearity. The rigid linear construction of the DBA present in these molecules may be assigned to the involvement of the sp-carbon atoms in the bonding which is one the essential measures for device applications [27].

3. Results and discussions

3.1. SP orbital energy levels

The property and relation of these molecules A, B, C, D and E were carried out using AM1 optimization on individual Donor and acceptor heterocycles, and all were optimized with same methodology. Table 1 displays the HOMO and LUMO energies HLG and potential drop across the molecules calculated using equation 1:

$$HLG = E_{HOMO} - E_{LUMO}, \quad (1)$$

where E_{HOMO} and E_{LUMO} energies of HOMO and LUMO respectively.

Figure 2 shows the orbital energy diagram from HOMO and LUMO levels of different structures connected CN, NO₂ and NH₂ molecular bridge at the same time in bridge energy levels observed with only acceptor molecule and donor molecule. Observation of table 1 results in the $n = 2$ carbon atom chains separated with 2 sp hybridization and observe Fig. 1 A21,A22,B21 AND B22 where the LUMO and HOMO are still distributed over almost the entire molecule. The case changes radically $n = 3$ two insulating groups move by 3.82 eV, 4.57 eV, so that direct overlap between the sulfur and the LUMO and HOMO do not distribute from left to right. From this observation, rectification is obtained for sp chains greater than or equal to 2.

TABLE 1. Orbital Energies of HOMO, LUMO, LUMO+1 for different molecules

Donor-Acceptor	Modal Name	HOMO (a.u)	LUMO (a.u)	LUMO+1 (a.u)	HLG# (a.u)	HLG (eV)	PD [§] (a.u)	PD (eV)
CN-NH ₂	A21	0.0283	-0.1589	-0.2368	0.1872	5.0940	-0.0779	2.1198
	A22	0.025	-0.1665	-0.2389	0.1915	5.2110	-0.0724	1.9701
CN-NH ₂	A31	-0.0431	-0.1836	-0.2484	0.1405	3.8232	-0.0648	1.7633
	A32	-0.0121	-0.1801	-0.2374	0.168	4.5715	-0.0573	1.5592
NO ₂ -NH ₂	B21	0.01313	-0.182	-0.2456	0.1951	5.3098	-0.0636	1.7306
	B22	-0.0055	-0.1834	-0.2462	0.1779	4.8409	-0.0628	1.7089
NO ₂ -NH ₂	B31	0.0198	-0.2299	-0.2582	0.2497	6.7947	-0.0283	0.7701
	B32	0.0109	-0.2373	-0.2448	0.2482	6.7539	-0.0075	0.2041
CN	C	0.021	-0.1707	-0.2464	0.1917	5.2164	-0.0757	2.0599
NO ₂	D	0.0076	-0.1872	-0.2507	0.1948	5.3008	-0.0635	1.7279
NH ₂	E	0.038	-0.1451	-0.2253	0.1831	4.9824	-0.0802	2.1824

#HOMO and LUMO energy gap (HLG) = |HOMO - LUMO|;

§Potential Difference (PD) = $E_{LUMO+1} - E_{LUMO}$

3.2. The shift of molecular orbital & transport analysis

The DBA molecule is connected between the electrodes i.e., donor is connected to the positive terminal and acceptor is connected to negative terminal and a suitable voltage is applied one electron will be entered to the molecule from the negative side. The enrolled electron inside the bridge will be placed in the LUMO of the molecule localized on the acceptor side. Then this electron tunnels in through the flexible bridge to the donor side and finally escapes to the anode through the unoccupied molecular orbital located on the donor side of the molecule. In a rectifying molecular bridge, this tunnelling process is largely controlled by the unoccupied orbitals (LUMO's are used for the electrical conduction inside the molecule).

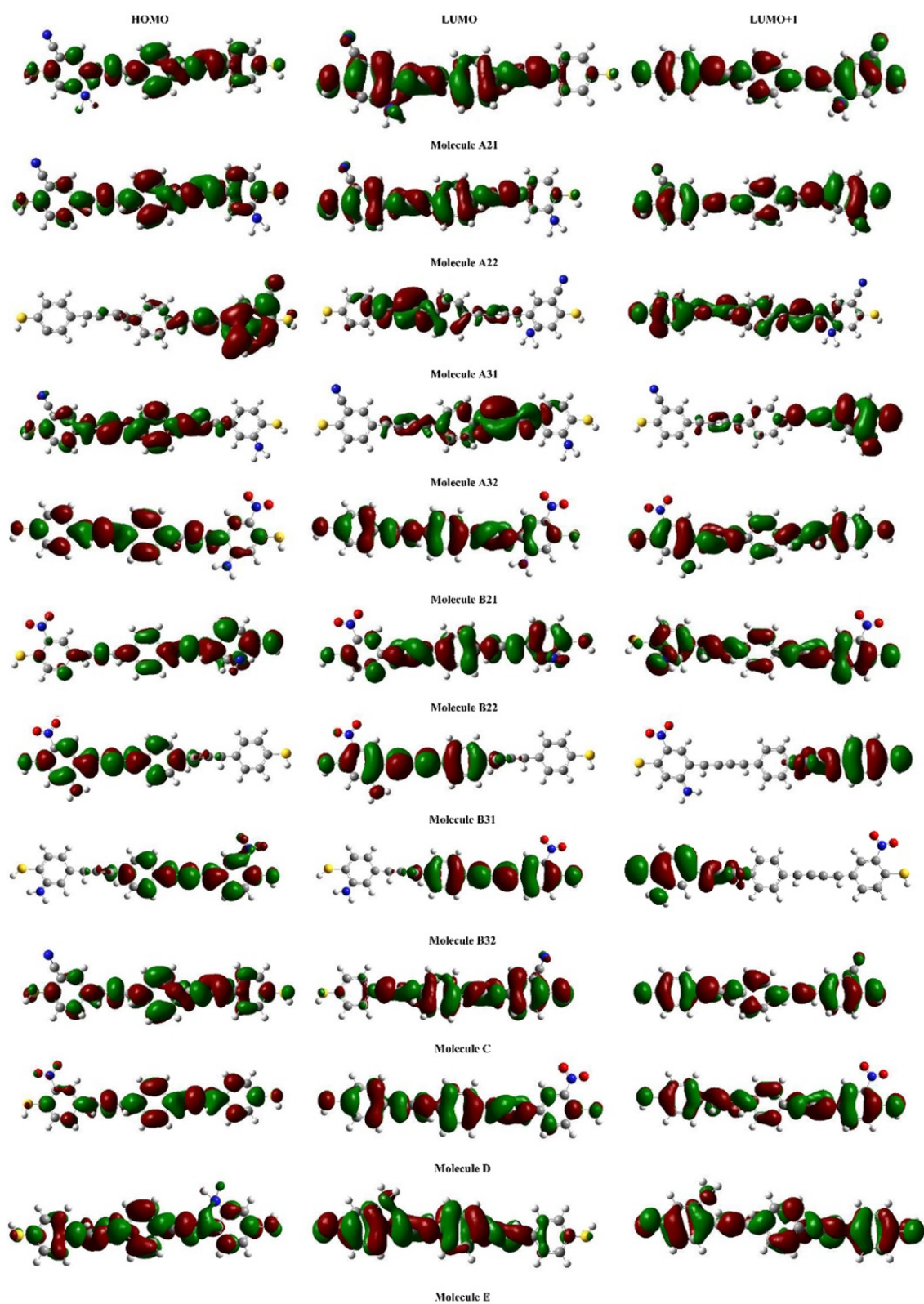


FIG. 2. Molecular Orbital pictures of HOMO, LUMO and LUMO+1 of different molecules

The abovediscussed bridge operation for electron transfer in both the reverse and forward directions of bias applied to the molecule in this study is described as follows: in the forward direction the applied positive energy required for raising is greater than the Fermi energy of the electron in the occupied level of the sulfur contact on the acceptor side, closely as high as the energy of the LUMO, which is located acceptor part of the molecule. The inserted electron from the sulfur contact to the acceptor part of the molecule can travel through the central bridge to the unoccupied molecular orbital present in the donor of the molecule and finally escape into the sulfur contact which is connected in the donor part of bridge. In a reverse bias condition for electron transfer from the donor to the acceptor part of the molecule through the central bridge, the applied voltage bias must be sufficient more to increase the Fermi energy of the sulfur contact on the donor side of the molecule, due to that it would match with the energy of the LUMO+1 situated on the donor part of the molecule. To maintain current flow through the molecule sufficient surplus voltage is given in the forward direction compared to the reverse direction bias voltage because that electron jumps from the LUMO+1 to the LUMO level.

TABLE 2. The calculated Muliken charge ranges, Total energy and dipole moment of molecular bridge

Modal Name	Muliken Charge Range (eV)	Total Energy (Kcal/Mol.)	Dipole Moment (Debye)
A21	-1.041 to 1.041	-1849.0303	16.3230
A22	-0.828 to 0.828	-1848.7505	18.0507
A31	-0.632 to 0.632	-1923.8167	12.4588
A32	-0.826 to 0.826	-1924.0890	13.7230
B21	-1.048 to 1.048	-1960.9553	11.6610
B22	-0.785 to 0.785	-1960.5074	15.0299
B31	-1.044 to 1.044	-2036.1977	12.1986
B32	-1.099 to 1.099	-2036.0312	14.6837
C	-0.630 to 0.630	-1794.1484	15.7409
D	-0.535 to 0.535	-1906.3258	10.7947
E	-1.045 to 1.045	-1757.5900	9.0366

Using population analyses, and as an effect of the rectifying properties of the molecular systems, the electron is transmitted through the molecule. The spatial position of the molecular orbitals plays an important role in accounting for electron transport in the molecule. The Potential Drop (PD) across the molecule gives information about the effectiveness of the DBA to behave as a rectifier when voltage is applied to the molecule. The PD value obtained from orbital energy values is as follows:

$$\text{Potential Drop (PD)} = \Delta E_{LUMO} = E_{LUMO+K} - E_{LUMO}; \quad k = 0, 1, 2, \quad (2)$$

where E_{LUMO} is the orbital energy localized on the acceptor side and E_{LUMO+K} is the orbital energy of the next unoccupied orbital (here it is LUMO+1), which is localized on the donor side of the molecule. The approximate PD across the proposed molecular rectifiers have been calculated using above equation 2 and listed in Table 2. The spatial location and orientations of frontier molecular orbitals are shown in Fig. 2 for molecules A,B,C,D,E, in which the two ends of the cumulenlic bridge acceptor and donor are connected via even and odd number double bonds.

4. Conclusion

The electron transport properties of molecular bridges containing amine group and nitro groups with odd and even number of double bonds and also varying position of the donor (NH₂) and acceptor (NO₂, CN) molecules energies were calculated using Extended Hückel and Parametric Methods. From our observations of energy HOMO, LUMO and HLG bridges having an odd number double bonds showed molecular conductance and should have utility as a molecular wire, heterocyclic with even number of double bonds work as a rectifying diode in a electronic circuits. Therefore, a pure static method based on EHT without calculating the current could be an alternative approach from the NEGF methods in studying or designing the novel molecular electronic devices.

Acknowledgement

The authors would like to thank Dr. K. Bhanuprakash, Chief Scientist, CSIR-ICT, Hyderabad, for encouragement and support throughout the period of this work and ECE Department, JNTUA, Ananthapuramu, Gudlavalleru Engineering College, Gudlavalleru, provided the computing facilities available to carry out the simulation work.

References

- [1] Aviram A., Ratner M.A. Molecular rectifiers. *Chemical Physics Letter*, 1974, **29**(2), P. 277–283.
- [2] Datta S. Nanoscale device modeling: the Green's function method. *Super lattices and Microstructures*, 2000, **28**(4), P. 253–278.
- [3] Datta S. *Electronic Transport in Mesoscopic Systems Cambridge University Press*. New York, 1996, 200 p.
- [4] Pradan M.R., Rajan E.G. A system engineering Approach to Molecular Electronics. *International Journal of Computer applications*, 2010, **3**(8), P. 14–23.
- [5] Fobelets K., Ding P., et al. Electrical Transport in Polymer-Covered Silicon Nanowires. *IEEE Transactions on Nanotechnology*, 2012, **11**(4), P. 661–665.
- [6] Jin-woo kim, Jeong-Hwan Kim, Russell Deaton. Programmable Construction of Nanostructures. *IEEE Nanotechnology Magazine*, 2012, **2**(3), P. 19–23.
- [7] Xia Y., Chu Z., Hung W.N.N. An Integrated Optimization Approach for Nano hybrid Circuit Cell Mapping. *IEEE Transactions on Nanotechnology*, 2011, **10**(6) P. 1275–1284.
- [8] Damle P.S., Ghosh A.W., Datta S. Unified description of molecular conduction: From molecules to metallic wires. *Physics Review B*, 2001, **64**(20), P. 201403-1–201403-4
- [9] Datta S., Tian W., et al. Current-Voltage Characteristics of Self-Assembled Monolayers by Scanning Tunneling Microscopy. *Physics Review Letters*, 1997, **79**(13), P. 2530–2533.
- [10] Xue Y., Ratner M.A. Microscopic study of electrical transport through individual molecules with metallic contacts. I. Band lineup, voltage drop and high field transport. *Physics Review B*, 2003, **68**, P. 115406
- [11] Song H., Kim Y., et al. *Observation of molecular orbital gating Nature Letters*, 2009, **462**(24), P. 1039–1043.
- [12] Pecchia A., Di Carlo A., et al. Incoherent electron-phonon scattering in octanethiols. *Nano Letters*, 2004, **4**(11), P. 2109–2114.
- [13] Wan C.C., Mozos J.-L., et al. Quantized conductance of Si atomic wires. *Physical Review B*, 1997, **56**(8), P. R4351–R4354.
- [14] Wang Z., Kadohira T., Tada T., Watanabe S. Nonequilibrium Quantum Transport Properties of a Silver Atomic Switch. *Nano Letters*, 2007, **7**(9), P. 2688–2692.
- [15] Xu Y., Shi X., et al. Conductance oscillation and quantization in monatomic Al wires. *Journal of Physics: Condensed Matter*, 2007, **19**(5), P. 056010.
- [16] Parlato F.R., Barra L., et al. Single molecule break junctions based on a perylene diimide cyano functionalized derivative. *Nanoscale Research Letter*, 2015, **10**, P. 305.
- [17] Yu Zhang L., Friesner R.A. Ab initio calculation of electronic coupling in the photosynthetic reaction center. *Proceedings of the National Academy of Sciences of the United States of America*, 1998, **95**, P. 13603–13605.
- [18] Thompson M.A., Glendening E.D., Feller D. The Nature of K+/Crown Ether Interactions: A Hybrid Quantum Mechanical-Molecular Mechanical Study. *The Journal of Physical Chemistry*, 1994, **98**(41), P. 10465–10476.
- [19] Thompson M.A., Schenter G.K. Excited States of the Bacteriochlorophyll b Dimer of Rhodospseudomonas viridis: A QM/MM Study of the Photosynthetic Reaction Center That Includes MM Polarization. *The Journal of Physical Chemistry*, 1995, **99**, P. 6374–6386.
- [20] Thompson M.A. QM/MMpol: A Consistent Model for Solute/Solvent Polarization. Application to the Aqueous Solvation and Spectroscopy of Formaldehyde, Acetaldehyde, and Acetone. *The Journal of Physical Chemistry*, 1996, **100**, P. 14492–14507.
- [21] Dewar M.J.S., Zoebisch E., et al. Development and use of quantum mechanical molecular models. 76. AM1: a new general purpose quantum mechanical molecular model. *Journal of the American Chemical Society*, 1985, **107**(13), P. 3902–3909.
- [22] Joachim C., Gimzewski J.K., Aviram A. Electronics using hybrid-molecular and mono-molecular devices Nature. *Macmillan Magazines Limited*, 2000, **408**, P. 541–548.
- [23] Tian W., Datta S., et al. Conductance spectra of molecular wires. *The Journal of Chemical Physics*, 1998, **109**(7) P. 2874–2882.
- [24] Xue Y.Q., Datta S., Ratner M.A. First-principles based matrix Green's function approach to molecular electronic devices: general formalism. *Chemical Physics*, 2002, **281**(2), P. 151–170.
- [25] Yaliraki S.N., Roitberg A.E., et al. The injecting energy at molecule/metal interfaces: Implications for conductance of molecular junctions from an ab initio molecular description. *The Journal of chemical physics*, 1999, **111**(15), P. 6997–7002.
- [26] Ghosh A.W., Datta S. Molecular conduction: paradigms and possibilities. *Journal of Computational electronics*, 2002, **1**(4), P. 515–525.
- [27] Amgad Ahmed Ali Abdul Manaf Hashim. Density functional theory study of atomic layer deposition of zinc oxide on grapheme. *Nanoscale Research Letters*, 2015, **10**, P. 299.



NANOSYSTEMS:

PHYSICS, CHEMISTRY, MATHEMATICS

Журнал зарегистрирован

Федеральной службой по надзору в сфере связи, информационных технологий и массовых коммуникаций

(свидетельство ПИ № ФС 77 - 49048 от 22.03.2012 г.)

ISSN 2220-8054

Учредитель: федеральное государственное автономное образовательное учреждение высшего образования

«Санкт-Петербургский национальный исследовательский университет информационных технологий, механики и оптики»

Издатель: федеральное государственное автономное образовательное учреждение высшего образования

«Санкт-Петербургский национальный исследовательский университет информационных технологий, механики и оптики»

Отпечатано в Учреждении «Университетские телекоммуникации»

Адрес: 197101, Санкт-Петербург, Кронверкский пр., 49

Подписка на журнал НФХМ

На первое полугодие 2017 года подписка осуществляется через

ОАО Агентство «Роспечать»

Подписной индекс 57385 в каталоге «Издания органов научно-технической информации»